ALMA MATER STUDIORUM - UNIVERSITÀ DI BOLOGNA

DOTTORATO DI RICERCA IN
INGEGNERIA BIOMEDICA, ELETTRICA E DEI SISTEMI

Ciclo XXXVI

Settore Concorsuale: 09/E4

Settore Scientifico Disciplinare: ING-INF/07

Distributed and Synchronized Measurements for the Wide-Area Observation of Electric Power Systems in Distorted and Low-Inertia Conditions

Supervisore:
Prof. Lorenzo Peretto

Co-supervisore:
Prof. Roberto Tinarelli

Coordinatore Dottorato:
Prof. Michele Monaci

Presentata da:
Federica Costa

Esame finale anno 2024

If you want to be sure,
don't measure twice.

C. Santschi

To my parents and Olli,
without whom I could have never achieved this.

Acknowledgements

First and foremost, I would like to thank my supervisor for all his precious advice and support during these years. Since the preparation of the Master's thesis until the end of my Ph.D., I am grateful for his constant encouragement, especially throughout some of the most difficult times. I cannot be thankful enough for the many opportunities I was offered that let me get out of my comfort zone: from the several international conferences I was able to attend to the work as a teaching assistant which, unexpectedly, I enjoyed more than I thought I would.

I would like to thank him also for the possibility he gave me to spend 10 months at the Swiss Federal Institute of Metrology in Bern, Switzerland. There I learned more than I could have possibly imagined in such a short time. I cannot thank all the people that I met there, both at work and outside, who welcomed me as part of the family. I dearly cherish the happy moments and the flabbergasting experiences with some special people who allowed me not to be so homesick.

I also have to thank my parents for their constant emotional, financial, and psychological support which never failed to be there since I moved to Bologna to attend the University when I was 19. I cannot thank them enough for always being present and putting up with me during some rough patches, albeit virtually. I cannot be grateful enough for the hours-long phone calls that helped, and still help me, so much, for always offering me a safe place to spend some time, for the "relaxing" post-exam summer trips, and, most importantly, for never stop believing in me.

I also would like to thank the rest of my family, my grandmas, and my friends for supporting me and cheering for me for all these years. All these people also helped me, in one way or another, to become a better person all-round.

Abstract

With the aim of heading towards a more sustainable future, there has been a noticeable increase in the installation of Renewable Energy Sources (RES) in power systems in the latest years. Besides the evident environmental benefits, RES pose several technological challenges in terms of scheduling, operation, and control of transmission and distribution power networks. Therefore, it raised the necessity of developing smart grids, relying on suitable distributed measurement infrastructure, for instance, based on Phasor Measurement Units (PMUs). Not only are such devices able to estimate a phasor, but they can also provide time information which is essential for real-time monitoring. This Thesis falls within this context by analyzing the uncertainty requirements of PMUs in distribution and transmission applications. Concerning the latter, the reliability of PMU measurements during severe power system events is examined, whereas for the first, typical configurations of distribution networks are studied for the development of target uncertainties.

The second part of the Thesis, instead, is dedicated to the application of PMUs in low-inertia power grids. The replacement of traditional synchronous machines with inertia-less RES is progressively reducing the overall system inertia, resulting in faster and more severe events. In this scenario, PMUs may play a vital role in spite of the fact that no standard requirements nor target uncertainties are yet available. This Thesis deeply investigates PMU-based applications, by proposing a new inertia index relying only on local measurements and evaluating their reliability in low-inertia scenarios. It also develops possible uncertainty intervals based on the electrical instrumentation currently used in power systems and assesses the interoperability with other devices before and after contingency events.

Keywords: phasor measurement unit, uncertainty, instrumentation, low-inertia power system, smart grid.

Sommario

Con l'obiettivo di puntare ad un futuro più sostenibile, negli ultimi anni si è registrato un notevole aumento nell'installazione di fonti energetiche rinnovabili (RES) nei sistemi elettrici. Oltre agli evidenti benefici ambientali, le RES pongono importanti sfide tecnologiche in termini di programmazione, funzionamento e controllo delle reti di trasmissione e distribuzione dell'energia elettrica. Pertanto, è emersa la necessità di sviluppare reti intelligenti, basate su un'adeguata infrastruttura di misure distribuite, ad esempio mediante unità di misura fasoriali (PMU). Tali dispositivi non solo sono in grado di stimare un fasore, ma possono anche fornire informazioni temporali, essenziali per il monitoraggio in tempo reale. Questa tesi si inserisce in questo contesto analizzando i requisiti di incertezza delle PMU nelle applicazioni in reti elettriche di distribuzione e trasmissione. Per quanto riguarda la seconda, viene esaminata l'affidabilità delle misure delle PMU durante gravi eventi nei sistemi elettrici, mentre per la prima vengono studiate le configurazioni tipiche delle reti di distribuzione per lo sviluppo delle incertezze di riferimento.

La seconda parte della tesi, invece, è dedicata all'applicazione delle PMU nelle reti elettriche a bassa inerzia. La sostituzione delle tradizionali macchine sincrone con RES prive di inerzia sta progressivamente riducendo l'inerzia complessiva del sistema, con conseguenti eventi più rapidi e gravi. In questo scenario, le PMU possono svolgere un ruolo fondamentale, nonostante non siano ancora disponibili né requisiti standard, né incertezze target. Questa tesi analizza approfonditamente le applicazioni basate sulle PMU, proponendo un nuovo indice di inerzia basato solo su misure locali e valutando la loro affidabilità in contesti a bassa inerzia. La tesi propone inoltre possibili intervalli di incertezza basati sulla strumentazione elettrica attualmente utilizzata nei sistemi di potenza e valuta l'interoperabilità con altri dispositivi prima e dopo eventi e guasti.

Parole chiave: sincrofasori, incertezza, strumentazione di misura, sistemi elettrici a bassa inerzia, reti intelligenti.

Contents

Acknowledgments i

Abstract iii

Sommario v

Introduction 1

1 Metrology Fundamentals Concepts: Definitions and Uncertainty Evaluation 7
- 1.1 Definitions in Metrology 7
- 1.2 Uncertainty in Measurements 9
  - 1.2.1 Type A Uncertainty Evaluation 10
  - 1.2.2 Type B Uncertainty Evaluation 11
  - 1.2.3 Measurements Modelling 15
  - 1.2.4 Monte Carlo Method 17
- 1.3 Metrological Traceability, Calibration and its Hierarchy 19
- 1.4 Discussion 20

2 Electric Instrumentation for Smart Grids 21
- 2.1 Introduction and State-of-the-Art 21
- 2.2 Phasor Measurement Units 23
  - 2.2.1 Synchrophasor Model 24
  - 2.2.2 Measurement Evaluation 26
  - 2.2.3 Synchrophasor Estimation Algorithms 27
- 2.3 Instrument Transformers 28
  - 2.3.1 Voltage Transformers 29
  - 2.3.2 Current Transformers 31
- 2.4 Low-Power Instrument Transformers 32
  - 2.4.1 Capacitive Dividers 33
  - 2.4.2 Rogowski Coils 34
- 2.5 Discussion 37

3 Calibration Infrastructure for Synchrophasors 39
- 3.1 Introduction and State-of-the-Art 39
- 3.2 Hardware Architecture 40
- 3.3 Software Architecture 41
  - 3.3.1 Steady-State Signals 41
  - 3.3.2 Dynamic Signals 44
- 3.4 Generation Stage Calibration Routine 48
  - 3.4.1 Magnitude Sweep 50
  - 3.4.2 Frequency Sweep 54

3.5 Acquisition Stage Calibration Routine 58
3.5.1 Frequency Sweep 60
3.6 Time Synchronization Evaluation 62
3.6.1 Testing Conditions 63
3.6.2 Results Analysis 68
3.7 Discussion 71

4 Uncertainty Contributions and PMUs' Reliability in Distribution and Transmission Power Systems 73
4.1 Introduction and State-of-the-Art 73
4.1.1 Examined Synchrophasor Estimation Algorithms 74
4.1.2 nRMSE Definition 77
4.2 Application of nRMSE for Contingencies Detection 80
4.2.1 Real-World Scenarios 80
4.2.2 Results Assessment 81
4.3 Target Uncertainty for Distribution Power Systems 85
4.3.1 Simulation Conditions 86
4.3.2 Results Evaluation and Comparison 89
4.4 Frequency Uncertainty Requirements in Transmission Power Systems Resynchronization 94
4.4.1 Power System Separations in Continental Europe 94
4.4.2 Frequency Uncertainty Analysis 98
4.5 Discussion 104

5 Power System Inertia Fundamentals and Models 107
5.1 Introduction and State-of-the-Art 107
5.1.1 Power System Stability 110
5.1.2 Fundamentals on Power System Inertia 111
5.2 Inertia Estimation Algorithms 114
5.2.1 Algorithms Classification 114
5.2.2 Challenges in Inertia Estimation 117
5.2.3 Swing-Equation Based Approach 118
5.3 Low-Inertia Power System Models 121
5.3.1 Distribution Power System Model 121
5.3.2 Transmission Power System Model 122
5.4 Discussion 123

6 PMUs in Low-Inertia Power Systems: Local Assessment and Interoperability 125
6.1 Metrological Perspective on Inertia Measurements 125
6.1.1 Testing Conditions 126
6.1.2 Results Assessment and Discussion 128
6.2 Local Evaluation of Inertia Variations 132
6.2.1 Power System Scenario 132
6.2.2 Results Discussion and Conclusions 135
6.3 Local Data Aggregation and Reliability 140
6.3.1 PMU Model and Power System Simulations 140
6.3.2 Results Evaluation 143
6.4 nRMSE for Renewable-Based Power Systems 147

6.4.1 Simulated Scenarios . . . 148
6.4.2 Results Assessment . . . 150
6.5 Electric Instrumentation Interoperability in Low-Inertia Conditions . 154
6.5.1 Simulation Specifications and Models . . . 155
6.5.2 Results Analysis . . . 157
6.6 Discussion . . . 162

Conclusions **165**

List of Acronyms **169**

List of Figures **179**

List of Tables **182**

Bibliography **183**

Introduction

Context and Motivation

From the Kyoto Protocol adopted in 1997 that first pursued the reduction and limitation of greenhouse gas emissions, a lot of work has been done and will have to be done in the next years in the field of sustainability [1].

The *2030 Climate Target Plan* promoted by the European Commission proposes to cut greenhouse gas emissions by at least 55% by 2030 and sets Europe on a responsible path to becoming climate neutral by 2050 [2]. In the meantime, though, it is necessary to ensure stable and affordable energy supplies, with the aim of providing universal energy access and enabling robust economic growth. This Plan sets out a cost-effective and economically productive pathway, resulting in a clean, and resilient energy economy dominated by Renewable Energy Sources (RES) like solar and wind instead of fossil fuels [3]. The main targets to be achieved by 2050 in the industry, power, transport, and buildings sectors are shown in Fig. 1.

In this context, the European Union (EU)'s Climate Plan proposes additional energy-related policies with the aim of further pushing utilities to install RES. It is worth mentioning the Strategic Energy Technology Plan that was launched in 2007. It is still ongoing and it aims at accelerating the deployment of green technologies. Its activities are clustered into 10 actions for research and innovation which address the whole innovation chain, from research to market uptake, and tackle both financing and regulatory frameworks [4].

Among climate directives, it is worth citing Directive 2018/2001/EC on the promotion of the use of energy from renewables. It pursues that 32% of the energy consumed within the EU comes from renewable-based sources by 2030. However, it is worth remarking that an intermediate target was set for 2020: the overall EU target for RES use had to be equal to 20% by the year 2020. Nevertheless, the

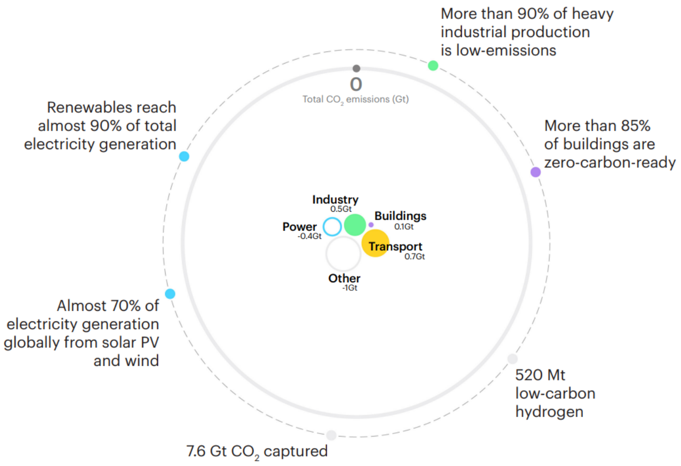

Figure 1: Objectives of the Climate Energy Plan promoted by the European Commission, showing the targets to be achieved by 2050 in various sectors. Source: [3].

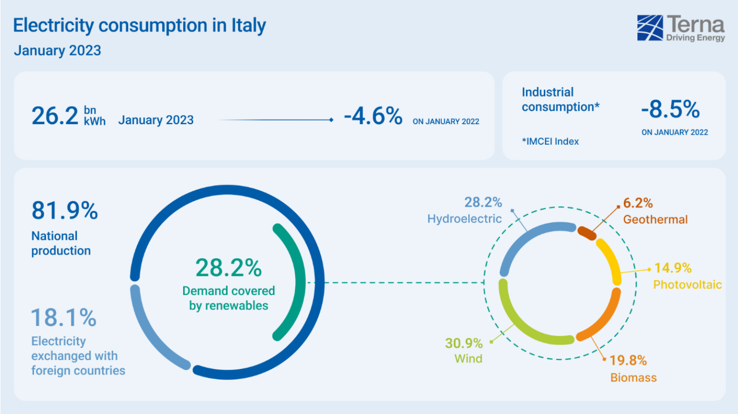

Figure 2: Energy consumption levels recorded in Italy in January 2023 by the Italian Transmission System Operator (TSO), Terna. It is worth highlighting that only 28.2% of the overall power production was based on renewable sources. Source: [7].

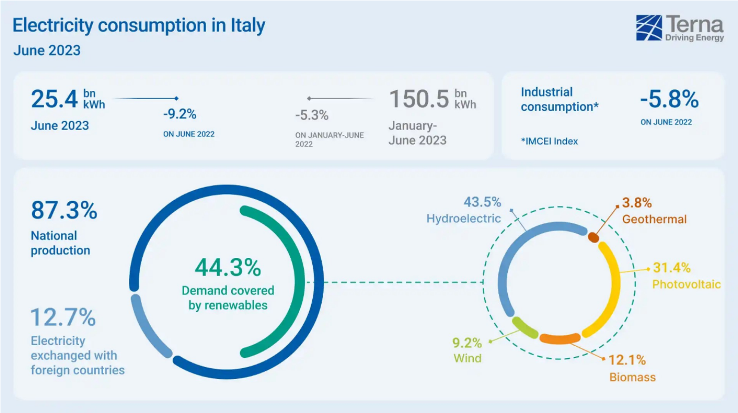

Figure 3: Energy consumption levels recorded in Italy in June 2023 by the Italian TSO, Terna. It is worth underlying that 44.3% of the overall power production was based on renewable sources. Source: [8].

Italian one was barely below the target, as it was equal to 17% [5].
In 2022, fossil-fuel-based energy still represented the majority of the energy produced in Italy constituting 63.9% of the total. The overall installed power was equal to 123.3 GW, resulting in an increase of 3% with respect to 2021. In more detail, 61.1 GW of those were RES which are equivalent to 50% of the total capacity, increasing by 5.3% in comparison to the previous year [6].
However, RES are subject to inherent volatility and seasonal trends which represent some of their intrinsic characteristics. As a matter of fact, it is worth noticing how the energy production relying on RES changes between the winter and the summer seasons. As an example, the Italian energy consumption in January and in June 2023 are shown in Fig. 2 and 3, respectively. While in June, RES constituted 44.3% of the overall power demand, in January they were 16% less. It can be also remarked how wind-based energy production represented the biggest share in the winter season with 30.9%, while it decreased to 9.2% in the summer. On the contrary, both hydroelectric and photovoltaic production increased significantly in the summer season representing almost 75% of all renewable-based production.

The last policy worth referencing is the Emission Trading Scheme. It was presented by the European Commission in July 2015 and its targets are in line with the EU's 2030 Climate and Energy policy framework. Indeed, it proposes to reduce emissions in the EU by 43% compared to 2005 [2, 9].

Besides the indisputable environmental benefits, all such ambitious targets pose several technological challenges that need to be tackled in a very limited time. Focusing only on the power sector, this transition is indeed going to require many changes in the operation of power networks, ranging from the system's down to the component's levels. Nonetheless, in the latest years, electric power systems have been continuously upgrading, increasing their degree of automation and capabilities of identifying and reacting to events that may trigger undesirable situations [10]. For such a reason, power grids have started to be referred to as *smart* grids, owing to their innovative *intelligent* operating conditions and features.

The next generation of smart grids shall indeed be represented by turnkey services while preserving the highest level of power delivery and power quality. In order to keep a high level of power quality, new schemes, procedures, and policies for the decentralization management of the power system are required. Furthermore, the roles and the responsibilities of sector actors such as distribution and transmission system operators, aggregators, as well as generators will change on a greatly increased importance, compared to the present situation.

Notwithstanding that, the final objective does not change: it entails the round-the-clock network stability and the uninterrupted delivery of power supply within specified quality standard levels, as the RES penetration increases. However, RES themselves threaten it by contributing to a worsening of the power quality and a progressive reduction of the system inertia, owing to the replacement of traditional machines. Hence, power systems are less resilient and more prone to contingencies and blackouts as recorded by some major system events that occurred in Arizona-Southern California in 2011 [11], in South Australia in 2016 [12], and in Odessa, Texas in 2022 [13], just to mention a few of them.

Consequently, it is evident how crucial it is the need of having a real-time picture of the system state in order to have updated, significant information on the possible criticality that may affect the correct operation of the networks. In this context, a pivotal role is played by power system measurements. In particular synchronized measurements performed by Phasor Measurement Units (PMUs) can definitely contribute to the delineation of a real-time, synchronized picture of the system state which can be used for the system operators in their daily activities.

However, with the advent of smart grids, measurement issues are turning into measurement challenges. Metrological issues in smart grids need more and even new answers, owing to RES which modified the traditional power flow.

Therefore, this Thesis falls within this framework by investigating the requirements and the performances of PMUs in modern electric power systems.
In more detail, systems characterized by distorted and low-inertia scenarios are examined, with the purpose of assessing the performance of state-of-the-art PMUs and investigating the contribution of other electric instrumentation such as Instrument Transformers (ITs) to the measurement uncertainty. A particular emphasis is given to the possible applications of PMUs in the local estimation of inertia and on their reliability, from a metrological perspective which is hardly ever considered in the recent literature besides that no international standards are yet available.
In the following, the Thesis outline is presented, then the main contributions are highlighted following their presentation order.

Thesis Outline

The Thesis is organized as follows:

Chapter 1 presents all the fundamental definitions and key concepts relative to the science of metrology. First of all, the most significant definitions are illustrated, as in the International Vocabulary of Metrology (VIM). Afterward, type A and B uncertainty evaluation methodologies are explained according to the Guide to the expression of Uncertainty in Measurements (GUM).

Chapter 2 depicts an overview of the main types of electric instrumentation that can be found in smart grids, focusing on PMUs and ITs. Specifically, it presents the basic concepts relative to PMUs and the requirements detailed in the relevant international Standard, i.e., IEC/IEEE 60255-118-1 [14]. The second part of the Chapter presents voltage and current ITs, as well as the new Low-Power Instrument Transformers (LPITs), highlighting their operating principles and their requirements shown in the Standards, i.e., the IEC 61869 series.

Chapter 3 illustrates the main components as well as hardware and software of the PMU calibrator present at the Swiss Federal Institute of Metrology (METAS). In this Chapter, tests concerning the stability of the generation and acquisition stages of the calibrator are performed in order to evaluate type A uncertainty. In addition, different time sources are tested to assess the performances of the calibrator in terms of synchronization and traceability to the reference units.

Chapter 4 describes the main advancements developed in this Thesis in the context of uncertainty contributions relative to PMU-based measurements at distribution and transmission levels. Regarding the first ones, target uncertainties are assessed, based on the typical elements constituting a measurement setup. Concerning transmission power systems, instead, both applications involve the investigation of the uncertainty of PMUs during system events. The first one involves the reliability of measurements; whereas, the second one pursues the requirements for the frequency uncertainty when performing secure maneuvers.

Chapter 5 introduces the fundamental concepts of power system stability and inertia. This is followed by a literature review, showing the most recent inertia estimation algorithms present in the scientific literature. From this analysis, the main unsolved problems are illustrated, focusing in more detail on the metrological ones. Afterward, among all possible routines, the method applied at a local level for the inertia estimation is presented. The last part of this Chapter presents two power system models which are used for the validation: one representative of a distribution grid, and the other of a transmission power system.

Chapter 6 presents some applications of PMUs for the local assessment of power system inertia in various scenarios. First of all, a metrological perspective is considered with the aim of establishing confidence intervals; second, from a local perspective, inertia is estimated by performing only single-node measurements. This is followed by an analysis of the measurement reliability in low-inertia scenarios and, consequently, on the possibility of merging data for the definition of local areas. The last part is dedicated to a study on the interoperability between measurements performed by different electric instrumentation in a low-inertia condition.

Contributions

In the following, the main contributions of this Thesis are organized in a bullet list, according to the order of appearance in their corresponding Chapters.

- Characterization of the stability of the generation and acquisition analog stages of a PMU calibrator capable of performing both steady-state and dynamic tests as illustrated in the IEC/IEEE 60255-188-1 Standard. Both hardware and software are described, in order to illustrate the specifications of the main components and the implementation of the test signals.
  In addition, a study on the effects of different time sources is performed. The contribution of this study is reflected in the assessment of the phase noise and time skew when time sources affected by different behaviors are applied.
- Establishment of the target uncertainty of a typical MV measurement chain, comprising PMUs and LPITs. The results indicate how even the lowest class of ITs' contributes so significantly to the overall uncertainty that the phase measurement is compromised. The outcomes of this study constitute a preliminary indication of the performances of PMUs in distribution grids.
- Evaluation of the required uncertainty for frequency measurements performed by PMUs at the transmission level after a system split. The results show that uncertainty constitutes an important indicator, which cannot be neglected, especially during dynamic conditions. The results propose the addition of such a quantity to the current policies.
- Establishment of confidence intervals for inertia estimations, based on the specification of modern in-field instrumentation. As a result, the obtained intervals happen to be non-negligible, especially for small power disturbances which are more challenging to be measured by ITs.
- Local assessment of inertia, based only on measurements performed at a single node using a novel indicator that takes into account power and frequency variations in time. The results indicate how the indicator can be helpful in discerning an event from a steady-state condition; plus, its magnitude is representative of the proximity to the fault location.
- Investigation of the reliability of PMU measurements in low-inertia systems, based on the Normalized Root Mean Square Error (nRMSE) index. The relation with the PMU reporting rate is deeply investigated.
- Aggregation of PMU measurements, according to their reliability index in a low-inertia distribution grid. Different transients and contingencies are simulated in order to assess the performances in various scenarios.
- Investigation of the interoperability between different instrumentation present in a low-inertia power system, specifically concerning PMUs and Power Quality (PQ) meters. The outcomes point out how the comparison between measurements obtained by different devices is not straightforward.

Chapter 1

Metrology Fundamentals Concepts: Definitions and Uncertainty Evaluation

When measuring the value of a quantity with a given measuring instrument, it is absolutely necessary to evaluate its associated uncertainty or measurement error. This Chapter aims at providing all the fundamental definitions and key concepts related to metrology which are necessary tools that are going to be applied in the following Chapters of the Thesis. To this purpose, the first part of this Chapter presents the most significant definitions as illustrated in the International Vocabulary of Metrology (VIM). This is followed by the evaluation of the uncertainty using type A and B methods, according to the Guide to the expression of Uncertainty in Measurements (GUM). Lastly, some insights into the metrological traceability and calibration hierarchy are provided at the end of this Chapter.

1.1 Definitions in Metrology

According to the International Vocabulary of Metrology (VIM), *metrology* is defined as *the science of measurement and its application, including all theoretical and practical aspects of measurement, whatever the measurement uncertainty and field of application* [15].

A *measurement* is defined as *the process of experimentally obtaining one or more values that can reasonably be attributed to a quantity together with any other available relevant information.*

In this context, the *measurand* is the quantity intended to be measured. While the *measurement result* is a set of values being attributed to a measurand together with any other available relevant information [15].

There exist many factors, or *influence quantities*, that affect the measurement result. According to [15], they are quantities that are not the measurand but affect the result of the measurement. For instance, climatic conditions (e.g., temperature, moisture, dust, etc. ...), electromagnetic waves (e.g., noise, disturbances, etc. ...), the operator who performs the measurement, as well as the measurement conditions and procedures (e.g., the length of the wires, the connections, and so on).

It is worth better describing the differences between *disturbances* and *noise*. The firsts are influencing quantities affecting the reading (i.e., the measurand value). They come from deterministic, known sources. For instance, depending on the application, the industrial frequency at 50 Hz, for power systems having such a rated frequency, can be a disturbance that is nearly impossible to be taken out. It is caused by lights, wires, and everything else connected to the grid that emits 50

Hz disturbance which couples with wires and probes for the measurement. That is the reason why during the calibration procedure, which will be better explained in Section 1.3, every National Metrology Institute (NMI) usually employs frequencies different from the rated one of the power system.

The *noise*, instead, is a pure random contribution that couples with the setup windings and probes. Contrarily to disturbances, noise comes from unknown sources; however, it is mostly attributable to thermal noise. Such noise is also known as *Johnson noise* and it arises when two metal components get together at a given temperature. Johnson noise is zero only at zero Kelvin (corresponding to $-273.15\,^{\circ}\mathrm{C}$), therefore is always present in a conducted or emitted way.

When taking into consideration all of these influence quantities, it is clear that it is of utmost importance that one has to ensure that they affect neither the repeatability nor the reproducibility of measurements.

When treating *repeatability*, the VIM refers to that as the closeness of agreement between the result of successive measurements of the same measurand performed under the *same* measurement conditions [15]. For instance, it can involve the following aspects: use of the same measurement procedure, measuring instruments, laboratory, and operators; it can involve short-time intervals between measurements to ensure the stability of the measurand, and so on.

On the other hand, *reproducibility* regards the closeness of agreement between the result of successive measurements of the same measurand performed under *different* measurement conditions (e.g., changing the measurement procedure, measuring instruments, laboratory, etc. ...). The objective of this consists in guaranteeing that a generic laboratory can obtain the same results as the other laboratories.

More in detail, the *method of a measurement* is the logical sequence of operations used in the performance of a measurement. On the other side, the *measurement procedure* is the set of operations used in the performance of measurement, according to the given method [15].

At this stage, it is also important to introduce three basic definitions that will be applied in the following Chapters.

Variance of a Random Variable (r.v.): the variance s^2 can be estimated as the squared deviation of the generic z_j observation from its expectation, equal to the mean value $\overline{z}$ as follows:

$$s^2(z_i) = \frac{1}{n-1}\sum_{j=1}^{n}(z_j - \overline{z})^2 \tag{1.1}$$

with the arithmetic mean $\overline{z}$ defined as:

$$\overline{z} = \frac{1}{n}\sum_{j=1}^{n} z_j \tag{1.2}$$

where z_j is the generic j^{th} observation of out a total of n observations.

Covariance: the covariance of two r.v. is the measure of their mutual dependence. It can be estimated by $s(y_i, z_i)$ obtained from n independent pairs of simultaneous observations as follows:

$$s(y_i, z_i) = \frac{1}{n-1}\sum_{j=1}^{n}(y_j - \overline{y})(z_j - \overline{z}) \tag{1.3}$$

where $\overline{y}$ and $\overline{z}$ are the arithmetic means of y and z computed as in Eq. (1.2).

Correlation coefficient: it is the measure of the relative mutual linear dependence of two r.v. and it is defined as:

$$r(y_i, z_i) = r(z_i, y_i) = \frac{s(y_i, z_i)}{\sqrt{s(y_i, y_i) \cdot s(z_i, z_i)}} = \frac{s(y_i, z_i)}{s(y_i) \cdot s(z_i)} \tag{1.4}$$

where $-1 \leq r(y_i, z_i) \leq 1$. A correlation coefficient equal to 1 indicates a total correlation between two r.v., whereas a coefficient of 0 indicates total uncorrelation.

1.2 Uncertainty in Measurements

As briefly illustrated in the aforementioned Section 1.1, there exists numerous *influence quantities* that may affect the measurand in a stronger or weaker way. This results in the need for performing repeated measurements in order to ensure the *repeatability* and *reproducibility* of a measurement. Obtaining a set of measurements per each measurand implies that a single measurement is not enough to represent the measurement result, but rather a new quantity has to be evaluated which is the *uncertainty*, clearly beside the measurement unit.

Before detailing the procedures of evaluating the uncertainty, it is worth underlying the difference between *error* and *uncertainty.*

An *error* is a deviation between the instrument's reading and the value of the measurand. It is a comparison between a reading and a reference value, performing simultaneously the same measurement of the measurand. Whereas, the *uncertainty* represents a lack of knowledge since it represents an interval in which the measurand value (i.e., the true value) falls with a given probability.

With the term *uncertainty* one refers to a parameter characterizing the dispersion of the values being attributed to a measurand, based on the information used. Measurement uncertainty includes components arising from systematic effects, such as components associated with corrections and values attributed to quantities of measurement standards. Sometimes estimated systematic effects are not corrected but, instead, associated measurement uncertainty components are incorporated [15].

The International Organization for Standardization (ISO) issued for the first time in 1993 the Guide to the expression of Uncertainty in Measurements (GUM) which represents an international standard, that is worldwide accepted and applied for correctly assessing the uncertainty [16].

The measurement uncertainty can be evaluated utilizing two different methodologies: type A or type B. Depending on the adopted procedure, the nature of different types of uncertainty is highlighted:

- *Type A* evaluation procedure emphasizes random uncertainty contributions.
- Whereas, by following *type B* procedure, sources that give rise to systematic contributions are consequently estimated. In this case, one can refer to them as *systematic errors* because they are constant (i.e., they behave as an offset) and they can be evaluated, by realizing a difference to a reference.

In order to evaluate the nature of the different uncertainties, the procedure illustrated in GUM is followed [16].

1.2.1 Type A Uncertainty Evaluation

This Section illustrates how to evaluate type A uncertainty which emphasizes contributions characterized by a random nature such as noise, disturbances, and other parameters changing in the environment as temperature, humidity, and so on.

The procedure starts with the acquisition of n measurements and the evaluation of the mean value as in Eq. (1.2), which is a correct and consistent estimation of the expected value μ in the presence of random contributions.

To estimate the variability of the mean, the Central Limit Theorem (CLT) is applied. It states that the average of n independent determinations of a r.v. having mean m and variance s^2 is a new r.v. having mean m and variance s^2/n which is n-times lower than the original distribution, as $n \to \infty$. Therefore, the variance s^2 of the n measurements is computed as follows:

$$s^2 = \frac{1}{n-1}\sum_{i=1}^{n}(x_i - m)^2 \tag{1.5}$$

However, according to the CLT, the variability of m is:

$$s_m = \frac{s}{\sqrt{n}} \tag{1.6}$$

where s is the standard deviation of the measurements.

Hence, one can build a Gaussian distribution centered around m having a standard deviation s_m, according to the CLT. The expected value μ cannot be known, but it is one of the means as the mean value is an unbiased estimator.

However, it must be recalled that CLT applies when the sample size n is sufficiently large or the n determinations of a r.v. follow a Gaussian distribution. In case n is not large enough, it is suggested to use the Student's t-distribution to estimate the type A uncertainty [16, 17].

The Student's t-distribution is a continuous probability distribution that generalizes the Gaussian distribution. Similarly to the latter, it is symmetric around zero and it is bell-shaped. Its pdf for a generic continuous r.v., t, is:

$$f(t) = \frac{1}{\sqrt{\nu\pi}} \frac{\Gamma\left(\frac{\nu+1}{2}\right)}{\Gamma\left(\frac{\nu}{2}\right)} \left(1 + \frac{t^2}{\nu}\right)^{-(\nu+1)/2} \tag{1.7}$$

where ν is the number of degrees of freedom which corresponds to the number of measurements $n-1$ and Γ is the Gamma function. Similarly to Eq. (1.6), the uncertainty can be evaluated as follows:

$$s_m = t_{\alpha,\nu} \cdot \frac{s}{\sqrt{n}} \tag{1.8}$$

where s is the standard deviation of the n measurements, t is the Student's t-distribution evaluated in α and ν, whose values are tabulated. The number of degrees of freedom is ν, while $\alpha = 1 - p$ is the percentile, which can be chosen as $p = 95\,\%$ corresponding to a $95\,\%$ confidence interval, for instance.

It is also worth underlying that the Student's t-distribution approaches a Gaussian one for $\nu \to \infty$ with $\mu = 0$ and $\sigma = 1$.

In either of the two cases presented in Eq. (1.6) or (1.8), the result of a measurement r can be rewritten, applying only type A methodology, as follows:

$$r = m \pm k \cdot s_m \tag{1.9}$$

where k is the coverage factor. It can be equal to $k = 1, 2, 3$ which corresponds respectively to 68.5, 95, and 99.73 % of the probability of including the true value in the defined confidence interval.

For the sake of clarity, Fig. 1.1 aims to illustrate this concept by presenting two distributions D1 and D2. D1 is regarded as the distribution of the true value having μ as the expected value, whereas D2 is one of the possible distributions that could be obtained by performing repeated measurements, having m as the mean value.

When fixing a coverage factor k, one is increasing the intersected area between the two curves, resulting in an ever-close match between the true value and the mean. It is worth noting that the great difference between the two Gaussian curves in Fig. 1.1 is intentional for the sake of clarity of the figure.

In general, the target consists of reducing as much as possible random contributions of uncertainty until they constitute a negligible quantity to systematic ones. This can be possible by increasing the number of measurements: the greater the number of measurements n, the lower the dispersion of data for the same probability, according to Eq. (1.6). However, it must be kept into account that when increasing n, it consequently increases the time required to perform measurements. Hence possible variations may occur in the measurand itself or in the environment. As a consequence, a good trade-off has to be found when selecting n.

1.2.2 Type B Uncertainty Evaluation

Type B method allows the evaluation of the uncertainty associated with the measurement result using a non-statistical approach, which is more general [16].

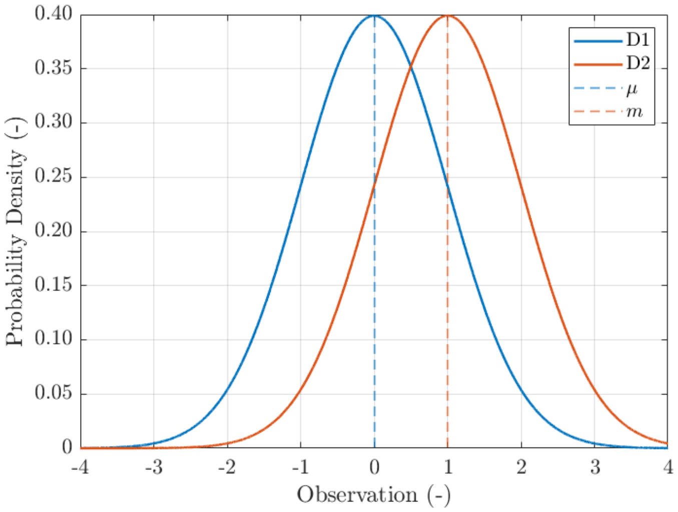

Figure 1.1: Distribution of the true value D1 and distribution of one of the means D2, in blue and red respectively. Their corresponding expected value μ and mean value m are represented by dashed blue and red lines.

For this purpose, for each measuring instrument and measuring operation, the relative accuracy specifications are associated, as well as the other systematic uncertainty contributions.

In theory, the type B method assumes that all the known systematic contributions have already been corrected (e.g., measurement method, measurement procedure, operator's mistakes if made repeatedly, etc. ...). However, this method cannot fully exclude contributions evaluated by the type A approach owing to the biased contributions present in the measurand itself.

To find the uncertainty to be associated with the reading of a measurement instrument, one has to consider two indices provided by the manufacturer: the gain error on the reading L, and the non-linearity error on the full-scale FS, both expressed in % and available in every instrument datasheet.

Let G be the instrument reading and G_{FS} the full-scale, then $\%L$ is used to calculate an error on the reading G that increases as G increases. The relationship between ΔG and G is constant though.

As illustrated in Fig. 1.2, the ideal instrument behavior is represented by the solid line bisector in blue, whereas the dotted line in red indicates the real behavior of the instrument. The blue and red dots represent the measurements obtained using an ideal and a real instrument, respectively.

The error on the reading can be computed as follows:

$$\%L = \frac{|b-1|}{1} \cdot 100 \tag{1.10}$$

where b is the angular coefficient of the real instrument curve and 1 is the angular coefficient of the ideal instrument curve, i.e., the bisector.

Whereas $\%FS$ is the index of non-linearity. It allows calculating of the maximum deviation between the indication of the instrument and the value of the measurand, verified by the manufacturer through the entire range of values that the instrument

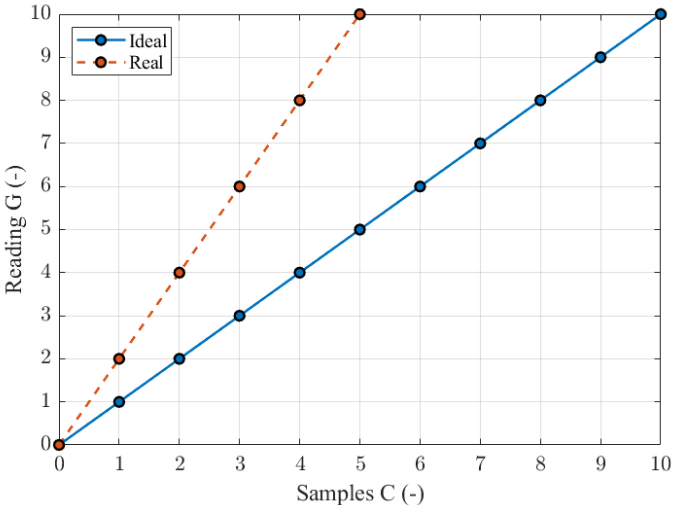

Figure 1.2: Ideal instrument behavior represented by a bisector, as a solid blue line, and real instrument behavior illustrated by a dotted red line. The angular coefficient between the two represents the gain, or reading, error.

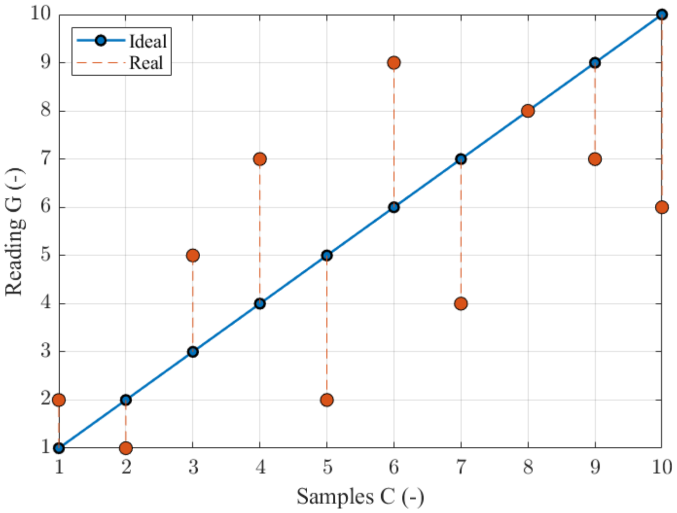

Figure 1.3: Ideal instrument behavior represented by a bisector, as a solid blue line, and real instrument measurements illustrated by solid red circles. The difference between each ideal and actual measurement is represented by a dotted red line.

can measure and normalized to the full-scale, G_{FS}, as shown in Fig. 1.3. This error is known as *non-linear* owing to the non-ideal behavior of the components present inside the instrument.

It is evaluated as:

$$\%FS = \frac{|G_i - C_i|^{max}}{G_{FS}} \cdot 100 \tag{1.11}$$

where for each sample C_i, G_i is the corresponding reading of the instrument.

The result of this procedure implies that one has to associate with the maximum error of the instrument every measurement. The worst case should always be considered for all uncertainty systematic contributions: no matter which instrument of the batch has the worst $\%L$ and $\%FS$, regardless of whether they belong to the same instrument.

Given the fact that the actual value of all systematic contributions and non-random contributions is not known, then one can treat them as r.v., and the minimum and/or maximum values are distributed according to a given probability. It means that the worst-case scenario does not have to be considered anymore, but rather two cases depending on whether the distribution is known.

In case the distribution is known, the manufacturer provides the probability distribution of the systematic error, then the uncertainty value is taken according to a given probability (e.g., 95 %) around the mean value m.

On the other hand, if that is not the case, then one has to assume that all contributions have the same probability so a uniform distribution is considered, according to the principle of maximum entropy. The standard deviation around the expected value m leads to:

$$\sigma = \frac{\%L}{\sqrt{3}} \approx 0.58 \cdot \%L \tag{1.12}$$

However, in general, one has to treat the combination of both reading and non-linear errors. It means that the actual measurements will not be placed around a bisector as in Fig. 1.3, but rather around the gain error straight line as in Fig. 1.2. This line, known as *best-fit line*, has to be determined as an approximation of the measurement points following the procedure described hereinafter.

Recalling that G_i is the generic i^{th} reading, $b \cdot c_i$ are the generic i^{th} values placed on the unknown best-fit line having b as an angular coefficient, then it is possible to write the expression of the least-square method as:

$$s = \sum_{i=1}^{N} (G_i - b \cdot c_i)^2 \tag{1.13}$$

As the objective consists in selecting the angular coefficient b such that s is the smallest, then the minimum can be found as:

$$\frac{ds}{db} = 2 \cdot \sum_{i=1}^{N} [(G_i - b \cdot c_i)(-c_i)] = 0 \Rightarrow b = \frac{\sum_{i=1}^{N} G_i \cdot c_i}{\sum_{i=1}^{N} c_i^2} \tag{1.14}$$

In conclusion, the type B uncertainty u_B affecting a given measured value due to the contribution of all systematic contributions of the measuring instrument is given by the following:

$$u_B = \frac{1}{\sqrt{3}} \left(\%L \cdot \frac{G}{100} + \%FS \cdot \frac{G_{FS}}{100} \right) \tag{1.15}$$

In Eq. (1.15), it is assumed that the distribution is not known, therefore the standard deviation of the uniform distribution is considered.

As a last step, the *combined uncertainty* u_C is evaluated, assuming that the two contributions u_A and u_B are independent, as follows:

$$u_C = \sqrt{u_A^2 + u_B^2} \tag{1.16}$$

According to the CLT, the sum of a given number of r.v. results in a new r.v. that tends to have a normal distribution. Hence, u_C represents its standard deviation with a certain coverage factor k. The quantity U is computed as:

$$U = k \cdot u_C \tag{1.17}$$

It is known as *combined expanded uncertainty* and it includes the probability of the measurement falling within the confidence interval, with a percentage depending on the value of k. The final measurement result can be then written as:

$$x = [m \pm U] \, (u.o.m.) \tag{1.18}$$

where u.o.m. indicates the unit of measurement, written inside round brackets.

1.2.3 Measurements Modelling

In many cases, a measurand Y is not measured directly but it is determined from N quantities $X_1, X_2, ..., X_N$ through a functional relationship f:

$$Y = f\left(X_1, X_2, ..., X_N\right) \tag{1.19}$$

The input quantities $X_1, X_2, ..., X_N$ can be viewed as measurands of different quantities: one can measure X_1 and calculate its associated expanded uncertainty, performing repeated observations.

An estimate of the measurand Y denoted by y is obtained by using input estimates $x_1, x_2, ..., x_N$ for the N quantities $X_1, X_2, ..., X_N$. It is worth recalling that the use of estimates is since one cannot perform infinite measurements. Besides, the performance of infinite measurement does not guarantee the evaluation of the true value, owing to biases. Therefore, the result of the measurement is given by:

$$y = f\left(x_1, x_2, ..., x_N\right) \tag{1.20}$$

In particular:

$$y = \overline{Y} = \frac{1}{n}\sum_{k=1}^{n} Y_k = \frac{1}{n}\sum_{k=1}^{n} f\left(X_{1,k}, X_{2,k}, ..., X_{N,k}\right) \tag{1.21}$$

where $X_{1,k}$ is the k^{th} reading of the input quantity X_1, and n is the total number of readings used for the estimate.

There exist two different scenarios that need to be considered when evaluating the combined standard uncertainty of Y, $u_{C,Y}$, from the measured input quantities $X_1, X_2, ..., X_N$ depending on whether the latter are correlated.

Uncorrelated input quantities: in case the input quantities are uncorrelated, then the combined uncertainty $u_C(y)$ is the positive square root of the combined variance $u_C(y)^2$ obtained considering the first-order Taylor's series of f:

$$u_C^2(y) = \sum_{i=1}^{N} \left(\frac{\partial f}{\partial x_i} \right)^2 \cdot u(x_i)^2 \tag{1.22}$$

$u_C(y)$ characterizes the dispersion of the values that could be attributed to the measurand Y. It is worth noting that the function f plays a key role, as it can increase or decrease the value of the input uncertainty associated with y.

The partial derivatives $\partial f/\partial x_i$ calculated with respect to each input quantity, are evaluated at $X_i = x_i$ and they are called *sensitivity coefficients*, c_i.

The change in y produced by a small Δx_i in the input estimate x is given by:

$$(\Delta y)_i = \frac{\partial f}{\partial x_i} \cdot \Delta x_i \tag{1.23}$$

Indicating that even if Δx_i is large, if $\partial f/\partial x_i = 0$ one does not have any contribution. If this change is generated by the input uncertainty, then $(\partial f/\partial x_i) \cdot u(x_i)$.

Therefore, the combined variance $u_C^2(y)$ can be seen as the following sum:

$$u_C^2(y) = \sum_{i=1}^{N} \left[c_i \cdot u(x_i) \right]^2 = \sum_{i=1}^{N} u_i^2(y) \tag{1.24}$$

Where in Eq. (1.24) the sensitivity coefficients c_i and the uncertainty associated with x_i, $u(x_i)$, are defined as in the following Eq. (1.25) and (1.26), respectively.

$$c_i = \frac{\partial f}{\partial x_i} \tag{1.25}$$

$$u_i(y) = |c_i| u(x_i) \tag{1.26}$$

It is worth noting that if the combined effect of the function non-linearity and uncertainty estimates is significant, then higher-order terms in Taylor's series must be considered.

Correlated input quantities: in case some of the X_i are significantly correlated, this effect needs to be taken into account. The expression for the combined variance $u_C^2(y)$ associated with the result of the measurement is the following:

$$\begin{aligned} u_C^2(y) &= \sum_{i=1}^{N} \sum_{j=1}^{N} \frac{\partial f}{\partial x_i} \frac{\partial f}{\partial x_j} u(x_i, x_j) = \\ &= \sum_{i=1}^{N} \left(\frac{\partial f}{\partial x_i} \right)^2 \cdot u^2(x_i) + 2 \cdot \sum_{i=1}^{N-1} \sum_{j=i+1}^{N} \frac{\partial f}{\partial x_i} \frac{\partial f}{\partial x_j} u(x_i, x_j) \end{aligned} \tag{1.27}$$

where x_i, x_j are the estimates of X_i, X_j and $u(x_i, x_j) = u(x_j, x_i)$ is the estimated covariance associated with x_i, x_j. The degree of correlation is the *correlation coefficient* which is calculated as in Eq. (1.3).

Picking out $u(x_i, x_j)$ and introducing Eq. (1.3), as well as the definition of *sensitivity coefficient* presented in Eq. (1.25), then Eq. (1.27) simplifies as:

$$u_C^2(y) = \sum_{i=1}^{N} c_i^2 u^2(x_i) + 2 \cdot \sum_{i=1}^{N-1} \sum_{j=i+1}^{N} c_i c_j u(x_i) u(x_j) r(x_i, x_j) \tag{1.28}$$

However, the expression shown in Eq. (1.28) considers the whole population. This is not the case because one always deals with a limited number of samples; for this reason, estimates have to be used. Rewriting Eq. (1.28) introducing estimates results in the following expression:

$$u_C^2(y) = \sum_{i=1}^{N} c_i^2 s^2(x_i) + 2 \cdot \sum_{i=1}^{N-1} \sum_{j=i+1}^{N} c_i c_j s(x_i) s(x_j) \overline{r}(x_i, x_j) \tag{1.29}$$

The procedure to evaluate the uncertainty, also known as Law of Propagation of Uncertainties (LPU), associated with a given measurement function can be summarized in the following steps:

- Definition of the quantity Y to be measured;
- Definition of the quantities $X_1, X_2, ..., X_N$ on which depend Y;
- Definition of the function f that links Y to $X_1, X_2, ..., X_N$;
- Association to each $X_1, X_2, ..., X_N$ an appropriate Probability Density Function (pdf) and then the corresponding uncertainty $u(x_1), u(x_2), ..., u(x_n)$;
- Application of these uncertainties to f to define $u_C^2(y)$ using Eq. (1.29).

It is worth underlying that this LPU can be applied if, at least, one of the following conditions is met:

- The analytical expression of f is available;
- The uncertainty contributions are in the same order of magnitude;
- The pdf of the measurand is normal.

However, this method is rather cumbersome from a computational point of view. There exists a numerical solution that can be implemented as an alternative, which is called *Monte Carlo method.*

1.2.4 Monte Carlo Method

The LPU illustrated in the previous section 1.2.3 of approximating the model with a first-order Taylor's series can be replaced, for different reasons, by the method illustrated in the Supplement I of the GUM which is the *Propagation of distributions using a Monte Carlo method* [18].

The Monte Carlo Method (MCM) entails the knowledge of the pdf of the input quantities; however, this can be easily verified. By using the CLT, one knows that the input quantities are characterized by a Gaussian distribution. Hence, it is enough to know the mean values m and their standard deviations $s_m/\sqrt{n}$ in order to apply the MCM.

The MCM provides an approximation of the pdf of the measurand, following the procedure illustrated hereinafter:

1. As a first step, one has to choose the M repetitions to perform the MCM;
2. Then, M samples are generated for each of the N input variables;
3. The model f to obtain the value of the input Y is applied;
4. The M values of Y are placed in an ascending order and approximate the cumulative pdf in output;
5. The measurand and its standard uncertainty are estimated;
6. Lastly, the shortest interval having a confidence level of 95% is determined, which corresponds to a coverage factor $k = 2$, for instance[1].

It is worth highlighting that the following applicability conditions need to be met in order to correctly apply the MCM:

- The function f has to be continuous in all x_i input quantities and in their neighborhood;
- The pdf of Y has to be continuous in the range where it is strictly positive, unimodal (i.e., meaning that it has just one value having a maximum probability), strictly increasing at the left side of the mode and strictly decreasing at the right of it. These conditions are needed to ensure that the shortest possible interval is determined.
- The expected value and the variance of Y exist;
- The number of iterations M is high enough.

Typical pdf selection for the input variables can consist of the choice of a rectangular (i.e., uniform), trapezoidal (i.e., it results from the combination of two uniform distributions), or Gaussian distribution.

In conclusion, it is worth underlying that the MCM needs to be repeated an increasing number of times M such that, at a certain point, the results are stable (i.e., they differ from a small value one from the other fixed a priori before the application of the method). The key point is that the difference between subsequent results must not depend on the value of iterations M that has been chosen.

---

[1] It is worth specifying that $k = 2$ can be applied only if the result is Gaussian, which is not always the case.

1.3 Metrological Traceability, Calibration and its Hierarchy

Before detailing the steps entailed in the metrological traceability, it is worth illustrating the concept of *quality*. It can refer to two different definitions: firstly, it is the capability of a product to satisfy the customer's requirements. Secondly, it can refer to the quality of a product, or production, comprising the capability of the production to keep constant its characteristics.

In order to assess quality, measurements are necessary. There is a common practice among companies to provide a certification of their product, and it is owing to many different reasons. For instance, it may be due to the need for buyers to be assured about the quality of a product, the inspection of the products from company A to company B, or the need for adaptation to the legislative system of the country in which the buyer uses the product.

The certification is provided by a third party which is usually an *accredited laboratory*. The certification of conformity is defined by ISO/IEC Guide 2 "Standardization and related activities - General vocabulary" as *the procedure by which a third party assesses that a product, process, or service complies with the established requirements* [19].

One of the fundamental aspects is established by the level of assurance required, which essentially corresponds to the confidence interval. Therefore every conformity certification has a calibration and a metrology subsystem that guarantees the *traceability* of the results with an uninterrupted chain.

In this context, the Western European Calibration Cooperation is an international committee that brings together members of various countries regarding the metrological reference of the product laboratories as well as rules and procedures to be used to assess the conformity of product characteristics.

The *traceability* is the property of the result measurement which consists of being able to refer it appropriate samples through an uninterrupted chain of comparisons. In other terms, it means that one has to be able to demonstrate that the accuracy of the instrument can be compared with the one of those in the primary metrology institutes. Generally, there exists one National Metrology Institute (NMI) in each country: INRIM in Italy, METAS in Switzerland, NPL in the UK, and so on.

In Fig. 1.4 the traceability sequence is illustrated: the NMI calibrates the accredited laboratory instrument, which provides calibrations for the generic industry instrument. In this way, if one is able to provide that the generic industry instrument refers to the one at the NMI in a chain without interruptions, then it is possible to obtain the ISO 9001 certifications, providing the quality of the products [20].

A *calibration*, according to the VIM, is the operation that, under specified conditions, establishes a relation between the quantity values with measurement uncertainties provided by measurement standards and corresponding indications with associated measurement uncertainties. In the second step, it uses this information to establish a relation for obtaining a measurement result from an indication [15].

According to the definition illustrated in [15], the presented procedure is also known

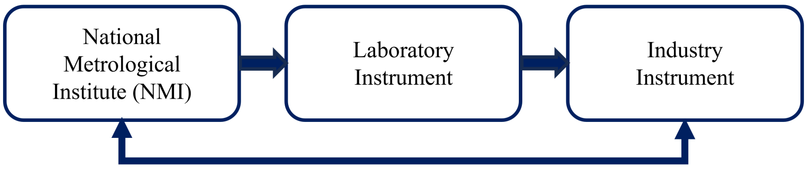

Figure 1.4: Traceability sequence illustrating the uninterrupted chain of comparison, starting from the NMI up to the generic industry instrument.

as *calibration hierarchy*. It is indeed a sequence of calibrations from a reference to the final measuring system, where the outcome of each calibration depends on the outcome of the previous calibration.

However, in this context, it is crucial to discern the concept of *calibration* between those of *verification* and *validation*.

Verification: is the provision of objective evidence that a given item fulfills specified requirements. In other terms, it is the confirmation that performance properties or legal requirements of a measuring system are achieved and that a target measurement uncertainty can be met. When applicable, measurement uncertainty should be taken into consideration [15].

On the other hand, *validation* is a verification where the specified requirements are adequate for an intended use [15].

1.4 Discussion

This Chapter presented all the fundamental concepts of metrology, ranging from the basic definitions to the evaluation of the combined uncertainty according to the GUM. The ending parts of this Chapter illustrated the MCM and the concepts of traceability and calibration hierarchy. More in detail, the latter is going to be applied in Chapter 3 for what regards a Phasor Measurement Unit (PMU) calibrator.

As a matter of fact, the specification of these definitions and the importance of the calibration hierarchy are critical concepts in metrology. All of these are going to be applied in the following Chapters, either with the fundamental procedures regarding the evaluation of uncertainty or with the application of the MCM.

Chapter 2

Electric Instrumentation for Smart Grids

This Chapter is intended to present an overview of smart grids and the main types of electric instrumentation that can be employed in this context. The first part of this Chapter presents the issues that modern power systems have to face and the role that could be played by electric instrumentation. Specifically, in this Thesis, the focus will be given to Phasor Measurement Units (PMUs) and to Instrument Transformers (ITs) because they are going to be employed in various applications developed in the next Chapters. Therefore, the first section is devoted to the basic concepts related to PMUs, their measurement evaluation, as well as their main applications, and their state-of-the-art. The last part, instead, presents both voltage and current transformers, as well as Low-Power Instrument Transformers (LPITs), focusing on their working principle and on the relevant international Standards.

2.1 Introduction and State-of-the-Art

The ongoing increase of Distributed Generation (DG), Plug-In Electric Vehicles (PEVs), microgrids, and power electronic components in power systems are kicking off new challenges that need to be tackled. Among these, DG affects both the planning and the operation of the network, as well as stability issues, especially at the transmission level. Additionally, the so-called Converter-Interfaced Generation (CIG) is decoupled by the power system via power electronic converters which, in general, do not contribute to the system's rotational inertia[1].

Furthermore, uncontrolled PEVs charging systems can lead to a violation of the lower limit for the voltage and the overloading of the distribution system. Whereas harmonic injection from power electronic components such as electric drives, Distributed Energy Resources (DER) and PEVs inverters can increase the overall Total Harmonic Distortion (THD) index, modifying conventional voltage and current level patterns. The latter must stay within certain fixed limits, according to the relative Standards EN 50160 and IEEE 519, respectively [21, 22].

Therefore, traditional power systems are required to become *smart* and transition towards dynamic, resilient networks commonly referred to as *smart grids*. An example of a smart grid is depicted in Fig. 2.1, highlighting all the main actors which

---

[1] The term "Converter-Interfaced Generation" indicates a particular type of "Distributed Generation", usually produced by renewable energy sources, which is interfaced to the power system via a dedicated power electronic converter. However, since the majority of DG has its own power conversion stage, the two terms are often used interchangeably in this Thesis.

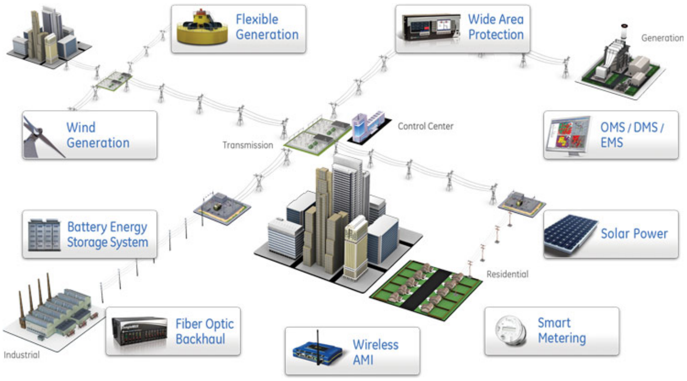

Figure 2.1: Example of a smart grid, including DERs and a wide-area monitoring system. Source: [23]

may play a role in this scenario, from flexible generation to smart metering.

In light of the above, it is clear that urgent modifications and improvements need to be performed in modern power systems in order to make them more resilient and flexible, from both the operational and planning point of view.

In this context, a recent device called Phasor Measurement Unit (PMU) has been developed. In general, PMUs are regarded as a valuable resource in the framework of Wide Area Monitoring, Protection, Automation and Control (WAMPAC) for the management of distribution grids. Among their several applications, the most relevant ones concern the real-time monitoring and measuring of relevant quantities for the correct behavior of distribution and transmission networks.

Firstly, dynamic monitoring and protection are related to the detection of an islanding operation of DG in order to avoid issues such as the reclosing out of synchronism or a Temporary Overvoltage (TOV) produced by the CIG itself which act as a standalone generator: this can be performed by two PMUs providing their measurements to a voltage angle difference algorithm [24]. Moreover, PMUs can also be efficient in the monitoring of electromechanical transients as synchronous generators are used in both conventional centralized and distributed generation [25–27].

As far as fault location and detection are concerned, an important role can be played by PMUs since they can compare pre- and post-fault data in order to detect the moment in which the transient condition has started, taking advantage of the sampling windows [28, 29]. Indeed, they can be optimally placed using optimization algorithms to minimize costs and ensure complete observability of the network at the same time [30, 31].

It is also worth recalling that all of these effects are reflected on more “traditional” instrumentation as well. As briefly anticipated, owing to the large-scale presence of both CIG and PEVs inverters in the network, the harmonic levels are noticeably higher, causing a strong impact on distribution and transmission systems [32].

Therefore, both Distribution System Operator (DSO) and Transmission System Operator (TSO) have to keep into account this effect on the performances of other electrical instrumentation, such as Instrument Transformer (IT) which is strongly subject to these counter effects.

The high levels of harmonic pollution, and consequent THD, are noticeably affecting the performances of ITs. Additionally, the effect of multiple influence quantities is

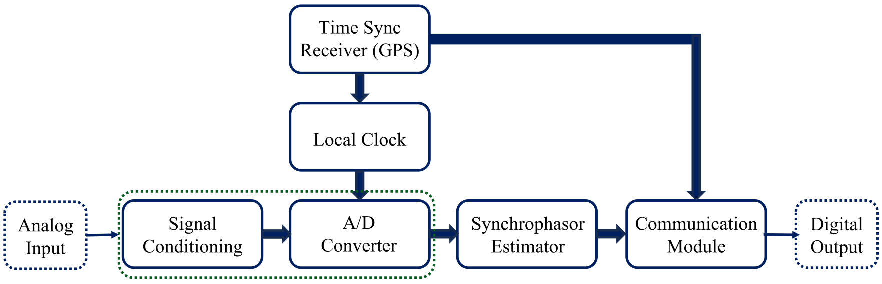

Figure 2.2: Block diagram of a PMU including its main components. Dashed blue blocks and thin arrows indicate analog/digital inputs/outputs, whereas the green dashed block highlights the DAQ components.

not often well known nor detailed in the relevant Standard [33–35].

For these reasons, PMUs and ITs are the two main types of electric instrumentation that are examined in this Thesis. Therefore, the next Sections present their main characteristics, their basic equations, and the key concepts derived from their relevant international Standards in order to provide all the necessary background before elaborating on their applications and development of new features, which are detailed in the next Chapters of this Thesis.

2.2 Phasor Measurement Units

A Phasor Measurement Unit (PMU) is a measurement device that is able to provide synchronized voltage and current phasors, also known as *synchrophasors*. Specifically, not only can a PMU measure the amplitude and phase of the phasor, but it is also able to estimate its frequency and its Rate Of Change Of Frequency (ROCOF), using a time synchronization necessary to tag each measurement with the corresponding time instant [36].

The block diagram comprising the main components constituting a PMU is shown in Fig. 2.2. In the figure, the main blocks and connections are represented by solid, thick blue lines and arrows; whereas, dashed blue blocks and thin arrows indicate analog/digital inputs/outputs. The green dashed block highlights the Data Acquisition Board (DAQ) components.

Examining Fig. 2.2, the first blocks consist of the acquisition of the analog voltage and current input signals. These are processed in a DAQ board, which usually comprises a signal conditioning stage, including an anti-aliasing filter, and an Analog to Digital Converter (ADC) with a sampling rate usually varying from 12 to 128 samples per cycle of the nominal power frequency which is either 50 or 60 Hz. In particular, the ADC is locked with a local clock that receives a Pulse Per Second (PPS) from a time synchronization receiver. The latter is a Global Positioning System (GPS) which is required to time-stamp the PMU measurements.

The sampled data is then processed by an estimator algorithm that is able to reconstruct the acquired phasor. It is worth noting that the IEC/IEEE 60255-118-1 Standard (briefly referred to as PMU Std hereinafter), which is the relevant Standard for PMUs, provides just a suggested algorithm based on a low-pass filter. However, each manufacturer is free to develop its own estimation routine as long as it is compliant with the requirements illustrated in [14].

For these reasons, there exists a large number of algorithms presented in the literature and compliant with the PMU Std requirements. An overview of the most significant ones is presented in Section 2.2.3, while Section 4.1.1 presents the rationale behind the choice of three of such algorithms, as well as their key characteristics. However, as it will be better explained in the following Chapters, the objective of this Thesis does not consist either in the development of enhanced versions of the considered PMU algorithms or in the development of completely new ones, but rather it focuses on the performance evaluation of consolidated routines in specific scenarios and applications which can be ever-more found in the field.

The last step in the block diagram of the PMU involves the communication of the computed synchrophasors through a digital communication network to higher-level applications, either a Phasor Data Concentrator (PDC) or a control room, at a rate of 10 up to 100 or 120 frames per second, respectively for power systems having a rated frequency of 50 or 60 Hz, according to [14]. Once again, it is worth highlighting the synchronization of the communication with the GPS, to ensure the association of a time stamp to each phasor as shown in Fig. 2.2.

The time tag associated with each measurement consists of three numbers: a Second Of Century (SOC), a Fraction of a Second (FRACSEC) count, and a message time quality flag [14]. This time tag is sent out with the phasors, thus if a phasor information packet arrives at the PDC out of order, the phasor time response can still be assembled correctly. Whereas, if the GPS pulse is not received for a while, then the time-tagging error may result in significant phase errors [37].

The collection of synchrophasor data from several PMUs in a PDC is able to create a system-wide measurement set that provides a time-stamped picture of the power system state. At this point, there exist several applications ranging from state estimation to fault location presented in the literature [38–44]. However, in this Thesis, the focus is on applications in distribution and transmission power systems, as well as in low-inertia power grids. More specifically, Chapters 4 and 6 present such applications, highlighting the role of uncertainty as well as the PMUs' reliability and interoperability with other electric instrumentation.

Apart from the PMU Std, there are other IEEE Standards providing guidelines and requirements for both PMUs and PDCs. The IEEE Standards C37.242 [45] for synchronization, calibration, testing, and installation of PMUs and C37.247 [37] for PDC requirements have been recently published to specify the performance and the functional requirements of typical PMUs and PDCs. In view of the realization of a smart grid, it is worth highlighting that PDCs may also interface directly to either upper-level PDCs or to a Supervisory Control And Data Acquisition (SCADA) system [14, 25, 37, 46]. This is to highlight that, despite the next Sections refer just to the PMU Std, there exists other relevant International Standards which are worth citing for the sake of completeness.

2.2.1 Synchrophasor Model

The most recent PMU Std defines the synchrophasor convention and the time-tagging process as well as provides a definition of an accuracy measure and the requirements for measurement performance under both steady-state and dynamic conditions [14]. According to the PMU Std, PMUs can be classified into two classes of performances: P-Type (typical for Protection applications requiring a fast response) and M-Type (typical for Measurement ones requiring high precision).

This Section presents an overview of the most relevant definitions and indices to evaluate the performance of PMUs according to [14].

The time-domain representation of a sinusoidal signal is commonly defined as:

$$x(t) = X_m \cos(\omega t + \varphi) \tag{2.1}$$

Whereas its corresponding phasor representation is represented as follows:

$$\overline{X} = \frac{X_m}{\sqrt{2}} \cdot e^{j\varphi} = \frac{X_m}{\sqrt{2}} \left(\cos(\varphi) + j\sin(\varphi)\right) = X_r + jX_i \tag{2.2}$$

Where the magnitude is the Root-Mean Square (rms) ($X_m/\sqrt{2}$) of the waveform peak value and the value of φ is the instantaneous phase angle relative to a cosine function at the nominal system frequency synchronized to the UTC. It is also important to notice that this phasor is defined for the angular frequency ω which is a function of the power system rated frequency, f_0, following this relation:

$$\omega = 2\pi f_0 \tag{2.3}$$

A PMU shall calculate and be capable of reporting frequency and ROCOF, thus for this measurement the following standard definitions have to be used. Given a sinusoidal signal, as shown in:

$$x(t) = X_m \cos\left[\psi(t)\right] \tag{2.4}$$

The frequency $f(t)$ is defined as in:

$$f(t) = \frac{1}{2\pi}\frac{d\psi(t)}{dt} \tag{2.5}$$

Whereas the ROCOF is defined as follows:

$$ROCOF(t) = \frac{df(t)}{dt} \tag{2.6}$$

Synchrophasors are always computed in relation to the system's nominal frequency, f_0. If the cosine argument is represented as in the following equation, introducing Eq. (2.3), results in:

$$\psi(t) = \omega_0 t + \varphi(t) = 2\pi f_0 t + \varphi(t) = 2\pi\left[f_0 t + \frac{\varphi(t)}{2\pi}\right] \tag{2.7}$$

Therefore, the equation for the frequency becomes:

$$f(t) = f_0 + \frac{d\left[\frac{\varphi(t)}{2\pi}\right]}{dt} = f_0 + \Delta f(t) \tag{2.8}$$

where $\Delta f(t)$ is the deviation of the frequency from the nominal one. The ROCOF expression simplifies as follows:

$$ROCOF(t) = \frac{d^2 \frac{[\varphi(t)]}{2\pi}}{dt^2} = \frac{d\left[\Delta f(t)\right]}{dt} \tag{2.9}$$

2.2.2 Measurement Evaluation

According to the PMU Std, the theoretical values of a synchrophasor representation of a sinusoidal and the values obtained from a PMU may include differences in both amplitude and phase, due to both the measurement chain and uncertainties on the time synchronization. Theoretically, they could be separately specified as amplitude and phase errors but, in the Standard and in common practice, they are considered together in a single quantity called Total Vector Error (TVE).

The TVE is an expression of the difference between a “perfect” sample of a theoretical synchrophasor and the estimate given by the unit under test at the same instant of time. The value is normalized and expressed as per unit or percent of the theoretical phasor. It is defined as:

$$TVE(n) = \sqrt{\frac{\left[\hat{X}_r(n) - X_r(n)\right]^2 + \left[\hat{X}_i(n) - X_i(n)\right]^2}{\left[X_r(n)\right]^2 + \left[X_i(n)\right]^2}} \tag{2.10}$$

Where $\hat{X}_r(n)$ and $\hat{X}_i(n)$ are the sequences of estimates given by the PMU under test of the real and imaginary parts of the phasor, respectively. Whereas, $X_r(n)$ and $X_i(n)$ are the sequences of the theoretical values of the input signal at the instants of time n. It is worth highlighting that these theoretical values can be determined only in certain well-defined situations, such as at constant frequency or at a calibration stage of the device [14].

For the sake of completeness, Fig. 2.3 presents a graphical representation of TVE as illustrated in the PMU Std. The ideal synchrophasor is indicated with X, while the measured one with $\hat{X}$. The projections along the horizontal and vertical axes indicate the real and imaginary components of the two vectors represented by subscripts r and i, respectively, following the same notation used in Eq. (2.10).

The frequency and ROCOF measurements shall also be evaluated with the criteria defined in [14]. The frequency and ROCOF errors are the absolute value of the difference between the theoretical and the measured values, indicated by the subscripts t and m, and given in Hz and Hz/s, respectively. The Frequency Error (FE) is defined as in:

$$FE = |f_t - f_m| \tag{2.11}$$

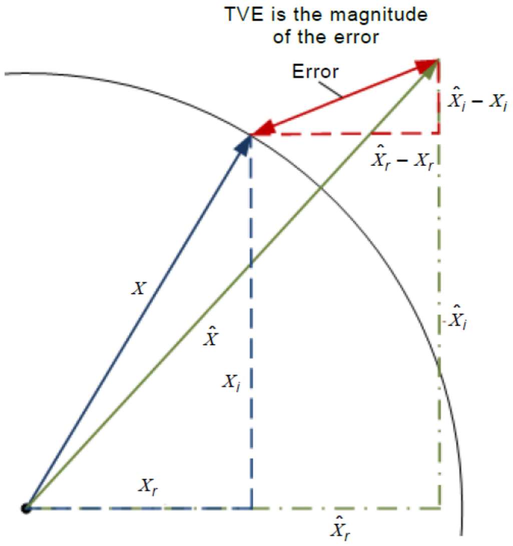

Figure 2.3: Graphical representation of TVE real and imaginary components in red: the ideal and the measured phasor components are illustrated in blue and green, respectively. Source: [14].

While the ROCOF Error (RFE) is defined as:

$$RFE = \left| \frac{df_t(t)}{dt} - \frac{df_m(t)}{dt} \right| \tag{2.12}$$

Synchrophasor measurements shall be synchronized to UTC time with accuracy sufficient to meet the requirement of PMU Std. In particular, a phase error of 0.01 rad, corresponding to 0.57°, in the synchrophasor measurement will cause 1 % TVE which is the maximum steady-state error allowed in [14]. In case the phase error can be entirely attributed to a time error, it is worth noticing that 0.01 rad corresponds to a time error of ±26 μs for a 60 Hz system and ±31 μs for a 50 Hz system.

The PMU Std provides all information, requirements, and limits as well as the necessary details on how to perform steady-state and dynamic tests for PMU compliance [14]. Nevertheless, PMU Std limits are omitted here for the sake of brevity. However, Chapter 3 briefly presents in Section 3.3 the steady-state and dynamic signals modeled for the compliance tests. Plus, the most relevant pieces of information are reported in the following Chapters 4 and 6 when referring and comparing results to the limits illustrated in the PMU Std is required.

2.2.3 Synchrophasor Estimation Algorithms

As illustrated in the previous Section 2.2.1, the PMU Std [14] does not provide specific details on the synchrophasor estimator algorithm to be implemented in PMUs, but rather it proposes one based on a FIR low-pass filter. Likewise, the window length, the sampling rate, the estimates reporting rate, as well as the measurement accuracy are all distinctive to each PMU device. Therefore, several alternatives have been investigated and reported in the scientific literature [47].

For such a reason, alternatives to the Discrete Fourier Transform (DFT) have been investigated and reported in the scientific literature. In general, two main algorithm categories can be distinguished: DFT-based and non-DFT-based ones.

Examining the first category, the classic DFT-based methods work well when the system frequency f_0 is close to the nominal frequency; however, significant errors arise when the frequency drifts from f_0, owing to the spectral leakage. For this reason, much effort has been made to improve the accuracy of such algorithms under off-nominal frequency conditions. Among these, it is worth referencing to Iterative Interpolated Discrete Fourier Transform (i-IpDFT) approaches [48–50], to dynamic DFT ones [51], to Phase-Locked Loop (PLL) based approaches [52], or even to those based on the Taylor Fourier Transform (TFT) such as the Compressive Sensing Taylor-Fourier Model (CS-TFM) [53].

On the other hand, many non-DFT-based algorithms are based on a Kalman Filter (KF) which are typically characterized by low latencies. It is worth remarking on Taylor-KFs [54] and Adaptive and Extended KFs [55, 56]. A smaller number of other approaches are based on different techniques such as Taylor Weighted Least-Squares [57] or wavelets [58], which are able to first discriminate discontinuities, followed by an adaptive window algorithm to estimate the phasor quantities.

Given the broadness of the topic comprising several techniques, comparative studies between DFT and KF-based algorithms are typically performed, as in [59, 60]. The analyses are based on simulations to evaluate and compare the performance of the estimators. It is shown that KFs are optimal for harmonic rejection and for tracking large-frequency deviations occurring in power systems, contrary to DFT-based ones, which suffer from leakage issues. On the other hand, DFT approaches do not suffer from instabilities, in contrast to KFs, and they are generally simpler than the latter, resulting in a significantly lighter computational burden [47, 59].

In light of the above, in this Thesis three different algorithms are utilized: the algorithm suggested by the PMU Std, one based on the i-IpDFT, and lastly the CS-TFM. These are going to be employed in Chapters 4 and 6 in the practical applications. Their main characteristics and performances are presented in Section 4.1.1, whereas specific implementation and parameter details are provided for each individual application.

2.3 Instrument Transformers

In order to perform measurements on MV and HV power systems, it is required to use an Instrument Transformer (IT) which can either be a Current Transformer (CT) or a Voltage Transformer (VT).

Traditional ITs are slowly being replaced by the so-called LPITs, however, this Section aims at presenting the basic concepts relative to ITs. General concepts for VTs and CTs as well as their construction are detailed, together with their most relevant equations. This is followed by the illustration of ratio and phase errors and the consequent classes according to the relevant Standards. The last part of this Chapter presents two of the most commonly used LPITs, specifically showing one typology for current and one for voltage applications.

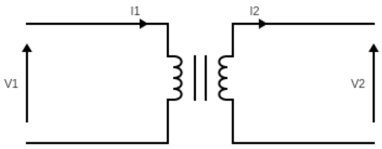

Figure 2.4: Model of an ideal transformer, omitting all parasitic parameters.

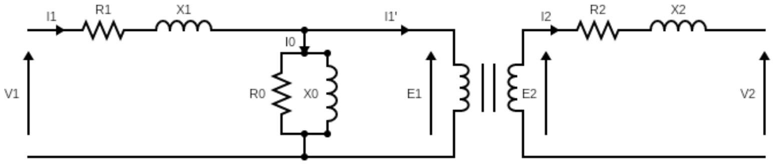

Figure 2.5: Model of a real transformer, including longitudinal primary and secondary parameters as well as non-idealities in the ferromagnetic core represented by the transversal parameters on the primary side.

2.3.1 Voltage Transformers

Before illustrating the key equations related to VTs, it is worth recalling the topology of an ideal transformer which is shown in the scheme of Fig. 2.4. For an ideal transformer, the basic relation between the voltage V, current I, and the number of turns N between the primary and secondary, indicated by subscripts 1 and 2, is the following:

$$\frac{V_2}{V_1} = \frac{N_2}{N_1} = \frac{I_1}{I_2} \tag{2.13}$$

However, real transformers have a more complex behavior which can be represented by adding longitudinal parameters on both the primary and secondary sides and transversal parameters on the primary side. The resulting model of a real transformer is shown in Fig. 2.5.
This is valid for every transformer, which can be found in the field, hence for both instrument and power ones. Nevertheless, since this Section focuses only on VTs, the following concepts are valid only for VTs. In a similar way, the following Section 2.3.2 will illustrate the key concepts relative to CTs.

In general, when measuring a secondary voltage $\overline{V_2}$, assuming to use an ideal voltmeter, the withdrawn current $\overline{I_2}$ is equal to zero. Hence, $\overline{E_2} = \overline{V_2}$ since the voltage drop over the secondary longitudinal parameters is null, referring to Fig. 2.5. However, $\overline{V_1} \neq \overline{E_1}$ both in module and in phase, owing to the transversal and longitudinal parameters on the primary side, representing the non-idealities in the windings and in the ferromagnetic core.

In order to minimize these differences, there exist two possible solutions. First, it is possible to act on the minimization of the $R_1 + jX_1$ term by increasing the cross-section of the conductor and reducing the number of turns. Alternatively, the reduction of the current $\overline{I_0}$ withdrawn by transversal parameters can be a valid option. Plus the latter is usually the easiest one to accomplish. Hence, since $\overline{I_0}$ is proportional to the magnetic flux Φ, $\overline{I_0}$ can be limited by over-sizing the ferromagnetic core or by increasing the number of turns. It means choosing a lower value

Table 2.1: Voltage ratio error ε_u and phase displacement $\Delta\varphi$ in % and in crad, respectively, for inductive VTs as defined in IEC 61869-3. Adapted from [61].

Class	Ratio Error ε_u (±%)	Phase Displacement $\Delta\varphi$ (± crad)
0.1	0.1	0.15
0.2	0.2	0.3
0.5	0.5	0.6

of maximum flux density in the range of $B_{max} = 0.6 \div 0.7$ T, rather than the most common choice which is $B_{max} = 1.5$ T. In this way, by reducing $\overline{I_0}$, the magnitude and phase differences on the primary side are minimized.

In this context, it is worth recalling that there exists a series of international Standards dedicated to VTs that define their accuracy classes. More in detail, IEC 61869-3 and -5 present the requirements for inductive and capacitive VTs, respectively [61, 62]. They define the ratio error and the phase displacement which are the maximum error on the module and on the phase, respectively, that can be obtained in each class[2]. The ratio error, or voltage error, is indicated by ε_u and it is expressed in percent, according to the following equation:

$$\varepsilon_u = \frac{k_r \cdot U_s - U_p}{U_p} \cdot 100 \tag{2.14}$$

where k_r is the rated transformation ratio, whereas U_p and U_s are the actual primary and secondary voltages, respectively [61, 62]. The phase displacement, instead, is indicated by $\Delta\varphi$ and it is defined as:

$$\Delta\varphi = \varphi_s - \varphi_p \tag{2.15}$$

where φ_s and φ_p are the secondary and primary voltage phase angles, respectively. It can be expressed in minutes (min) or in centiradians (crad).

Table 2.1 presents the limits of the voltage ratio error and phase displacement for inductive VTs, as defined in the IEC 61869-3 standard [61]. Similarly, Table 2.2 presents the same limits but referring to capacitive VTs [62]. It is worth noting that for both typologies of VTs accuracy classes having worse performances are available, i.e., class 1.0 and 3.0. However, they are omitted here as they are not so commonly used for in-field applications. Additionally, for the sake of brevity, the phase displacement $\Delta\varphi$ is indicated only in crad.

---

[2] For ITs, the terms *phase displacement* and *phase error* can be used interchangeably. However, for analog-output LPITs the phase displacement is not always coincident with phase error, as in some cases it may include variable and fixed components such as phase offsets and delay times [63].

Table 2.2: Voltage ratio error ε_u and phase displacement $\Delta\varphi$ in % and in crad, respectively, for capacitive VTs as defined in IEC 61869-5. Adapted from [62].

Class	Ratio Error ε_u (±%)	Phase Displacement $\Delta\varphi$ (± crad)
0.2	0.2	0.3
0.5	0.5	0.6

2.3.2 Current Transformers

The same reasoning performed for the analysis of VTs is replicated for deriving useful information about the key equations and the behavior of CTs.

In contrast to VTs which work in open-circuit, CTs work in short-circuit. Typically, it is required to reduce the measured current $I_2 < I_1$, hence $N_1 > N_2$ according to Eq. (2.13). In addition, *ring- or window-type* CTs have usually just $N_1 = 1$, resulting in a secondary current I_2/I_1 equal to $1/N_2$.

However, $\overline{I_2} \neq 0$ but $\overline{V_2} = 0$ because of the short-circuit. On the secondary, there is still a voltage $\overline{E_2}$ which is equivalent to the voltage drop over the secondary longitudinal parameters $R_2 + jX_2$. On the primary, instead, there are both $\overline{I_0}$ and the secondary current referred to primary $\overline{I_1'}$. Once again, it is the current $\overline{I_0}$ over the transversal parameters that gives rise to the ratio and phase errors. It is crucial to minimize it, as it is summing up to the current $\overline{I_1'}$ which is the one to be measured. To reduce $\overline{I_0}$, it is necessary to over-size the ferromagnetic core or the winding cross sections, as for VTs. It is also important to minimize the voltage drop over the parameters $R_2 + jX_2$ to reduce $\overline{E_2}$ which reflects as a small $\overline{V_1}$ on the primary.

The presented description refers to *wound-type* CTs which are indeed based on the usual working principle of transformers. Instead, *ring- or window-type* ones are characterized by a 1 or 5 A output and rated power of 5 to 15 VA.

An important criticality that is typical for CTs entails safety. Since the secondary side of a CT works in short-circuit, in case it opens there will be a $N \cdot V_1$ voltage at the transformer terminals which is extremely dangerous for both the operator and the transformer which may saturate. It is then mandatory to install surge arresters in order to protect the CT, the other instrumentation, and the operators.

Additionally, CTs may suffer from over-shootings due to possible resonances and non-linearity at the knee point in the magnetic hysteresis cycle. Moreover, their range of applications typically excludes power quality measurements owing to their limited bandwidth. In this sense, their accuracy class cannot be considered valid anymore. From a more practical point of view, instead, they are bulky and heavy, making their in-field installation rather challenging.

For these reasons, in MV applications CTs are slowly being replaced by Rogowski Coils (RCs), while for voltage measurements VTs are being substituted by voltage dividers, in particular by Capacitive Dividers (CDs). Nevertheless, in HV applications VTs and CTs are still widely used for insulation reasons.

In a similar way to Eq. (2.14), in the following the ratio error, expressed in percent, for a CT is evaluated:

Table 2.3: Current ratio error ε_i and phase displacement $\Delta\varphi$ in % and in crad, respectively, for CTs as defined in IEC 61869-2. Adapted from [64].

Class	Ratio Error ε_i (±%)			Phase Displacement $\Delta\varphi$ (± crad)		
	20%	100%	120%	20%	100%	120%
0.1	0.2	0.1	0.1	0.24	0.15	0.15
0.2	0.35	0.2	0.2	0.45	0.3	0.3
0.5	0.75	0.5	0.5	1.35	0.9	0.9

$$\varepsilon_i = \frac{k_r \cdot I_s - I_p}{I_p} \cdot 100 \tag{2.16}$$

where k_r is the rated transformation ratio, while I_p and I_s are the actual primary and secondary currents, respectively [64]. The phase displacement, instead, is computed as in Eq. (2.15), considering, though, the secondary and primary current phase angles instead of the voltage ones.

Similarly to what has been reported for VTs, the following Table 2.3 presents the current ratio error and the phase displacement as defined in the IEC 61869-2 standard for each accuracy class. However, for the sake of brevity, the phase displacement is illustrated only in crad, and the highest available class (i.e., class 1.0) is omitted. The three percentages, 20 %, 100 %, and 120 %, indicate the percentage of the rated current. For the sake of brevity, the lowest percentage, corresponding just to 5 % of the rated current, is omitted from Table 2.3, however, it is present in the IEC 61869-2 Standard [64].

2.4 Low-Power Instrument Transformers

Nowadays, there exists a new type of IT which is the so-called Low-Power Instrument Transformer (LPIT): it could be either a Low-Power Voltage Transformer (LPVT) or a Low-Power Current Transformer (LPCT). These devices are a new version of traditional ITs, based on a different technology and having a limited amount of output power, which is usually less than 5 VA. These advancements are possible, due to the replacement of traditional electro-mechanical protection relays with electronic-based ones that require a limited amount of power.

Among their main features, it is worth recalling they can be used for power quality measurements, having a bandwidth ranging from 20 up to 150 kHz. They also have higher accuracy and new protection functions (e.g., bi-directional power plow assessment which is particularly relevant in the case of DG). They are also convenient from an installation point of view, as they are much lighter and compact in comparison with traditional ITs, hence they could better fit in in-field applications characterized by a limited space.

Among the most common LPCTs, it is worth focusing the attention on RCs. Whereas, among LPVTs, instead, there exist capacitive, resistive, and optical VTs. The first ones are often used in MV up to 27 kV, while the latter are used especially in HV since they have a good accuracy up to 0.1 %. There are also combined LPITs which

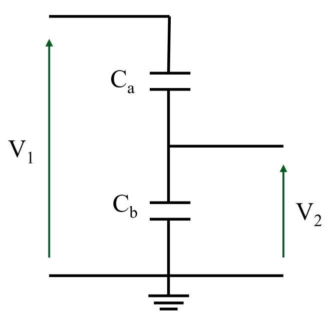

Figure 2.6: Structure of an ideal LPVT made up of a capacitive divider, comprising only two ideal capacitors C_a and C_b and no parasitic components. The input and output voltages and indicated by subscripts 1 and 2, respectively.

are usually made up of a capacitive LPVT and a RC: capacitive LPVT are preferred because they have insulation in them by definition, thus they can be installed outdoors or in gas-insulated substations.

The reference international Standards for such devices is still the IEC 61869 series: more specifically the IEC 61869-10 for LPCT and IEC 61869-11 for LPVT, respectively, [65, 66].

2.4.1 Capacitive Dividers

In spite of their name, voltage dividers are not inherently *transformers* since they are not based on magnetic core induction, but rather on resistors, capacitors, and inductors. Nonetheless, they are commonly referred to as LPITs.

This Section deals with CDs only, since they are widely used nowadays for several in-field applications. They consist of a divider comprising, ideally, two capacitors whose relation is the following:

$$V_2 = V_1 \cdot \frac{C_a}{C_a + C_b} \tag{2.17}$$

A simplified structure of a CD is represented in Fig. 2.6 where all parasitic components are omitted as a first approximation.

In in-field applications, utilities usually specify the equivalent capacitance C_e between the HV terminal and ground as $C_e = C_a + C_b$ which is generally less than 20 pF in order to avoid loading all dividers installed in the field.

To obtain $V_2 \ll V_1$, it is necessary that $C_a \ll C_b$ hence Eq. (2.17) can be approximated as:

$$V_2 \approx V_1 \cdot \frac{C_a}{C_b} \approx \frac{\overline{Z_b}}{\overline{Z_a}} \tag{2.18}$$

However, more complex expressions with respect to the one shown in Eq. (2.18) can be derived when parasitic effects represented by resistors and inductors are taken into account in the model of a capacitor.

Table 2.4: Voltage ratio ε_u and phase errors $\Delta\varphi$ in % and in crad, respectively, for LPVTs as defined in IEC 61869-11. Adapted from [66].

Class	Ratio Error ε_u (±%)			Phase Error $\Delta\varphi$ (± crad)		
	80 %	100 %	120 %	80 %	100 %	120 %
0.1	0.2	0.1	0.1	0.15	0.15	0.15
0.2	0.2	0.2	0.2	0.3	0.3	0.3
0.5	0.5	0.5	0.5	0.6	0.6	0.6

CDs present many advantages, among those it is worth recalling their bandwidth. The latter can reach up to tens of hundreds of kHz, therefore CDs are suitable for Partial Discharge (PD) measurements. They are also characterized by very good linearity in a wide range of measurements and, with respect to resistive dividers, CDs do not dissipate power [67].

Nonetheless, they present a few drawbacks which may discourage their use. As a matter of fact, it is worth reminding that they do not work in DC conditions, as traditional VTs, since capacitors behave as open circuits for zero frequencies. Moreover, their behavior changes as the frequency increases. More in detail, it is worth assessing the input impedance $\overline{Z_i}$: for resistive dividers, the input impedance is constant, albeit the effect of the parasitic capacitances increases at higher frequencies. However, for CDs the input impedance $\overline{Z_i}$ reduces, as the frequency, represented by ω, increases following this relation:

$$\overline{Z_i} = \frac{1}{j\omega\, C_a} + \frac{1}{j\omega\, C_b} = \frac{j\omega\, C_a + j\omega\, C_b}{j\omega\, C_a \cdot j\omega\, C_b} = \frac{1}{j\omega\, C_{eq}} \tag{2.19}$$

Where C_{eq} indicates the equivalent input capacitance of the CD.

For what concerns the accuracy requirements defined in the international standard, instead, it is worth mentioning first of all how to evaluate ratio and phase errors. The voltage ratio ε_u and the phase errors $\Delta\varphi$ can be computed as shown in Eq. (2.14) and Eq. (2.15), respectively. For the sake of completeness, Table 2.4 presents the limits illustrated in the IEC 61869-11 standard. However, they align with those shown in Table 2.1 and Table 2.2 concerning VTs.

In the case of LPVTs, though, three different percentages of the rated voltage are shown and they refer to 80, 100, and 120 %, respectively, according to [66]. In the same way as what has been presented for VTs and CTs, higher classes as 1.0 and 3.0 are present in the Standard, but they are omitted. Similarly, phase error values are expressed only in crad.

2.4.2 Rogowski Coils

Nowadays, RCs are one of the most used types of LPCTs for current measurements and their basic structure is represented in Fig. 2.7.

The unknown current $i(t)$ is not measured directly, but rather it is proportional to the output voltage $u_s(t)$. Their relation can be derived starting with Ampere's Law which is recalled as follows:

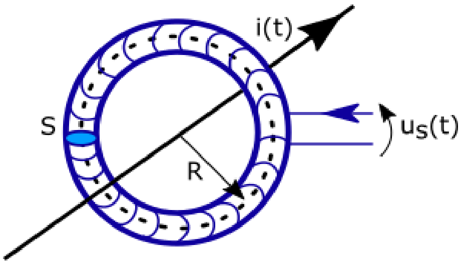

Figure 2.7: Structure of a Rogowski coil, having a radius R and a cross-section S. The output voltage at the terminals $u_s(t)$ is proportional to the derivative of the measured current $i(t)$. Source: [68].

$$\oint_l \overline{H} \cdot \overline{dl} = i \Rightarrow \oint_l H \cos(\alpha)\, dl = i \tag{2.20}$$

Where dl is the infinitesimal length of the RC, while l is the total length. α is the angle included between the infinitesimal length dl and the magnetic field $\overline{H}$.

The definition of flux density B, applied to the infinitesimal area of the RC, is:

$$\delta B = \mu_0 H \cos(\alpha) \tag{2.21}$$

where $\mu_0 = 4\pi \times 10^{-7}$ is the magnetic permeability of the vacuum in H/m.

Instead, the infinitesimal surface δA can be computed as:

$$\delta A = S \cdot n \cdot dl \tag{2.22}$$

where S is the infinitesimal cross-section of the winding and n is the number of turns per unit length of the RC.

Recalling the definition of flux $\delta\varphi$ passing through a generic infinitesimal surface δA, and introducing Eq. (2.21) and (2.22):

$$\delta\varphi = B \cdot \delta A = \mu_0 H \cos(\alpha) A \cdot n \cdot dl \tag{2.23}$$

Integrating the infinitesimal flux $\delta\varphi$ expressed in Eq. (2.23) over the entire area A of the RC results in:

$$\varphi = \oiint_A \overline{B} \cdot \hat{n}\, dA \Rightarrow \varphi = \int \delta\varphi = \mu_0 \cdot n \cdot S \oint_l H \cos(\alpha) dl \tag{2.24}$$

Introducing Ampere's Law shown in Eq. (2.20) in Eq. (2.24), the result is:

$$\varphi = \mu_0 \cdot n \cdot S \cdot i \tag{2.25}$$

Applying Lenz's Law to Eq. (2.25) results in:

$$u_s(t) = -\frac{d\varphi}{dt} = -\mu_0 \cdot A \cdot n \frac{di(t)}{dt} \tag{2.26}$$

where $u_s(t)$ is the output voltage measured at the terminals of the RC. Therefore, it is necessary to integrate Eq. (2.26) in time to obtain an output voltage $u_s(t)$ directly proportional to the input current $i(t)$ as:

$$i(t) = -\frac{1}{\mu_0 \cdot A \cdot n} \int u_s(t)dt \tag{2.27}$$

Some important characteristics can be derived by looking at Eq. (2.27). First of all, in the phasor domain, the measuring current presents a phase displacement of $-\pi/2$ with respect to the output voltage. Second, it is clear that RCs do not work in DC conditions as the $di(t)/dt$ is null. However, they work for AC signals; specifically, for a given current, the output voltage $u_s(t)$ increases as the frequency of the measured current $i(t)$ increases. Hence, RCs are suitable for measuring high currents but having a low frequency, or low currents but at high frequencies.

Some comments are worth mentioning for what concerns the realization aspects of RCs. In order to get high performances, it is important to meet at least this criterion: RCs should be realized with a uniformly distributed high density of turns. As the voltage $u_s(t)$ is proportional to the number of turns per unit length n, then increasing n implies an increase in the sensitivity of the RC. This also guarantees a limited number of gaps in between windings which reduces the probability of measuring external unwanted magnetic fields.

It has also to be underlined that geometrical parameters owing to the physical realization of the RC play an important role. Since inductive or capacitive parameters may prevail one over the other, it is crucial, at the developing stage, to test RCs in frequency to ensure a constant transfer ratio.

Considering the advantages of RCs, first, it must be said that they are not affected by any ferromagnetic influence: as the core is realized in a non-ferromagnetic material such as air or plastic, there is no increase in μ due to the ferromagnetic material. Owing to their linear behavior in a wide working range and no saturation at all, they can be suitably employed for both metering and protection in which the range of currents must be extended up to fault currents that may reach up to a few kA.

However, their realization implies that external magnetic fields which may couple with the coil are also measured. This may represent an important issue in three-phase power systems where the magnetic field produced by nearby phases can be coupled and measured on the phase under test. Nevertheless, if RCs are realized with high winding symmetry, then the same unwanted voltages may cancel out, reducing this effect.

From a practical perspective, RCs are small, compact in size, and light in comparison to traditional bulky CTs. They are also flexible as they can simply be wrapped around the cables, making their installation much easier and more convenient.

For what concerns the disadvantages, the most relevant negative feature is that the output voltage of the RC, $u_s(t)$ is proportional to the derivative of the measured current $di(t)/dt$. Hence, it means that an integrating circuit is required; plus, the latter requires a supply voltage which sometimes could represent an issue, especially in applications where physical and/or safety reasons could represent a major con-

Table 2.5: Current ratio ε_i and phase errors $\Delta\varphi$ in % and in crad, respectively, for LPCTs as defined in IEC 61869-10. Adapted from [65].

Class	Ratio Error ε_i ($\pm$%)			Phase Error $\Delta\varphi$ ($\pm$ crad)		
	20%	100%	$K_{pcr} \cdot I_{pr}$	20%	100%	$K_{pcr} \cdot I_{pr}$
0.1	0.2	0.1	0.1	0.24	0.15	0.15
0.2	0.35	0.2	0.2	0.45	0.3	0.3
0.5	0.75	0.5	0.5	1.35	0.9	0.9

cern. Moreover, as previously anticipated, RCs are very sensitive to the physical and electrical environment (e.g., the position of the primary conductor, external electric fields, temperature, etc. ...). In this context, it is often necessary to carry out preliminary studies on the location of the RC to avoid collecting invalid measurements. It is also relevant not to underestimate the *side effect*, which occurs when a RC is not placed centrally with respect to the cable axis. This effect can lead to a change in the ratio because of the different field deployments around the coil. Lastly, in an ideal condition, the temperature should not represent an issue for RCs realized a high number of turns and minimal gaps in between the windings; however, this is not always true in practical cases as demonstrated in [69–71].

Finally, it is worth mentioning some pieces of information for what regards the accuracy classes in the relevant international standard. Similarly to what has been presented for CTs, it is possible to apply Eq. (2.16) and Eq. (2.15) in order to evaluate the ratio and the phase errors of a LPCT, respectively. For passive LPCTs, the IEC 61869-10 standard applies.

Table 2.5 illustrates the ratio and phase errors for three different accuracy classes and for three percentages of the rated current. More in detail, I_{pr} is the rated primary current, while K_{pcr} is the rated extended primary current factor. Given the linear characteristics, the same passive LPCT can be used within a wide range of primary current values. The standard values for the K_{pcr} are 5, 10, 20, 50, and 100. However, the selection of proper primary and secondary rated values is done according to the input limits of the measuring or protection equipment [65].

2.5 Discussion

This Chapter presented the problems that modern power systems are facing nowadays and the electrical instrumentation that can play a key role in this context.

In the presented scenario, two of the most relevant instrumentation are shown: PMUs and ITs. They are deeply discussed, highlighting their basic concepts, working principles, and key parameters to assess their measurement evaluation, as well as some of the limit values illustrated in the relevant International Standards.

Some insights are also provided for what concerns the challenges that these instruments have to face in the upcoming future and their most common applications, which are discussed in the next Chapters of this Thesis.

Chapter 3

Calibration Infrastructure for Synchrophasors

The development of ever-performing PMUs is prompting the necessity of realizing suitable calibrator infrastructures operating at least one order of magnitude better concerning the PMU under test. In this context, it is worth analyzing the performance of each stage of a PMU calibrator: from the stability of its analog input and output modules to the time synchronization. For these reasons, this Chapter illustrates the hardware and software architecture of the PMU calibrator present at the Swiss Federal Institute of Metrology (METAS), in Switzerland. In this context, the first part of this Chapter presents the software required to generate waveforms and developed according to the PMU Std for steady-state and dynamic compliance tests. The second part, instead, is dedicated to the evaluation of the stability of the generating and acquisition stages, and the effects of various time sources on the calibrator performance.

3.1 Introduction and State-of-the-Art

In the beginning, PMUs were conceived for traditional transmission systems which are power systems inherently characterized by quite stable conditions [72]. In the future, though, PMU applications will be extended to distribution systems and reduced inertia operating conditions as it will be described in more detail in Chapters 4 and 6. Consequently, the reduced line lengths, the higher R/X ratios, and the unstable as well as bidirectional power demand profiles imply a much finer resolution in the PMU phase, frequency, and ROCOF measurements [73, 74].

To tackle such challenges, a wide range of PMU algorithms has been recently proposed to be able to achieve TVEs in the order of 0.01% [49, 53]. However, such a performance enhancement suggests a consequent improvement of the calibration infrastructure itself. The calibration shall present reference values whose accuracy is at least one order of magnitude better than the measurement values, for instance, a TVE in the order of 0.001% [75]. It would correspond to a worst-case phase error of 10 μrad or a time delay of 32 ns at 50 Hz, in case no other errors on the amplitude are observed. In this context, it is worth highlighting how this error could be caused by either a skew between the generation and re-acquisition stages or by a combination of erroneous estimates on the frequency and the phase [76].

The implementation of such demanding performance targets poses several challenges as already discussed in the scientific literature [77–82]. The aim of this Chapter does not involve either the uncertainty contributions related to the generation and re-acquisition of the test waveforms or the processing routines necessary for the

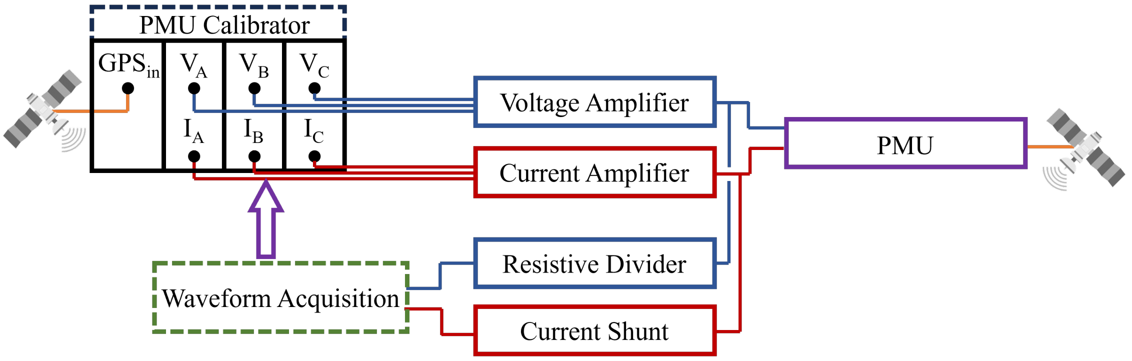

Figure 3.1: Simplified block diagram of the PMU calibrator infrastructure present at the Swiss Federal Institute of Metrology (METAS) in Bern, Switzerland. Voltage signals and related components are shown in blue, current-related ones in red, and timing ones are in orange. The PMU acquisition stage is shown as a simplified dotted block in green.

extraction of the reference values. It rather focuses on the assessment of the stability of the generation and acquisition stages of the PMU calibrator which represents a fundamental step to be taken prior to any further analysis. The last part of this Chapter, instead, is dedicated to a specific analysis of the effect of different time reference sources on the performance of the calibrator. They can affect both the accuracy of the reference sampling frequency and phase angle, as well as timestamps in the retrieved measurements.

For the sake of completeness, fundamental concepts concerning the hardware components and the software are presented. As a matter of fact, in Section 3.2 the hardware architecture of the calibrator is described, detailing each of its components and their main functions and characteristics. Section 3.3, instead, presents the software that has been developed for its application in the calibrator. More in detail, this description focuses only on how steady-state and dynamics test signals are developed according to the PMU Std.

The calibration routine of the generation stage is described in Section 3.4 where the stability of the generating modules is assessed. On the other hand, the acquisition stage is evaluated in Section 3.5. Similarly to the previous Section, a frequency sweep is performed. The last part of the Chapter, in Section 3.6, is devoted to the examination of the effects of different time sources on the PMU calibrator.

3.2 Hardware Architecture

In this Section, the main elements constituting the PMU calibration infrastructure present at the Swiss Federal Institute of Metrology (METAS) in Bern, Switzerland are described and their most relevant characteristics are illustrated.
Fig. 3.1 represents a simplified block diagram of the PMU calibrator whose elements are described as follows.

- NI PXI-1042Q, comprising three NI 4461 modules, one per phase so that three-phase signals can be evaluated and/or replicated. Each has two analog input and output channels to acquire both voltage and current signals simultaneously. The three modules rely on sigma-delta ADCs which introduce a non-constant phase displacement owing to its intrinsic operating principle.

Besides this difficulty, the second one consists in the fact that the ADC is not multiplexed, meaning that the contributions need to be individually assessed and compensated accordingly. For this reason, it is envisioned to rely on an external ADC, the NI BNC-2090A, which is based on resistors. Therefore, its phase displacement is constant and can be more easily assessed and compensated for. Lastly, the timing module, i.e., NI 6653, is better described in Section 3.6.

- OMICRON CMA 156 6 Phase Current Amplifier. It is both a voltage and a current amplifier. For what concerns the voltage side, a gain of 50 is set, while for the current a gain of 5. It is assumed that a complete frequency response of the amplifier is known. More specifically, the amplifier is regarded to have its gain (which is slightly different from 50, and from 5 for the current side) and its own group delay (slightly different from 0, as well). In addition, it is assumed that the amplifier does not distort the frequency of the signal. Hence, this device can be considered a linear, passive element in the measurement chain whose gain and group delay can be assessed. It has a band-pass frequency of 150 kHz, which is particularly useful for step compliance tests.
- Resistive voltage divider. Two handcrafted devices are available: one having a 1 : 40 ratio for a maximum 240 V rms voltage; the other features a 1 : 300 ratio for a maximum 1000 V rms voltage.
- Fluke A40B AC precision current shunt. It is a 10 A shunt, having a maximum rated current of 5 A rms and a maximum of 200 % of the rated current has to be tested according to the PMU Std for steady-state signals. An important feature of such current shunt models is that their output is fixed at 0.8 V for the nominal current input. Thus, in case changes in the setup are required, it is sufficient to keep the ADC operating in a fixed range of 1 V since the shunt output will never exceed 0.8 V.

Fig. 3.2 illustrates some of the detailed components constituting the calibrator infrastructure. On the top shelf, the OMICRON Daneo 400 hybrid signal analyzer is shown, as it is envisioned to treat sample values according to the IEC 61850 Standard. On the middle shelf, the main controller is present including the timing modules (NI 6653 and NI 6682) and the three analog input/output cards (NI 4461). On the bottom shelf, the external ADC is located, together with a computer used to control the whole measurement chain in LabVIEW environment.

3.3 Software Architecture

This Section illustrates the most relevant characteristics of the software, focusing on the generation and modeling of the test waveforms described in the PMU Std. For the sake of clarity, Section 3.3.1 presents the formulations used for steady-state signals, while in Section 3.3.2 dynamic tests are detailed.

3.3.1 Steady-State Signals

This Section presents the set of steady-state tests that need to be performed according to the PMU Std and, consequently, the signals that are modeled. In order to do

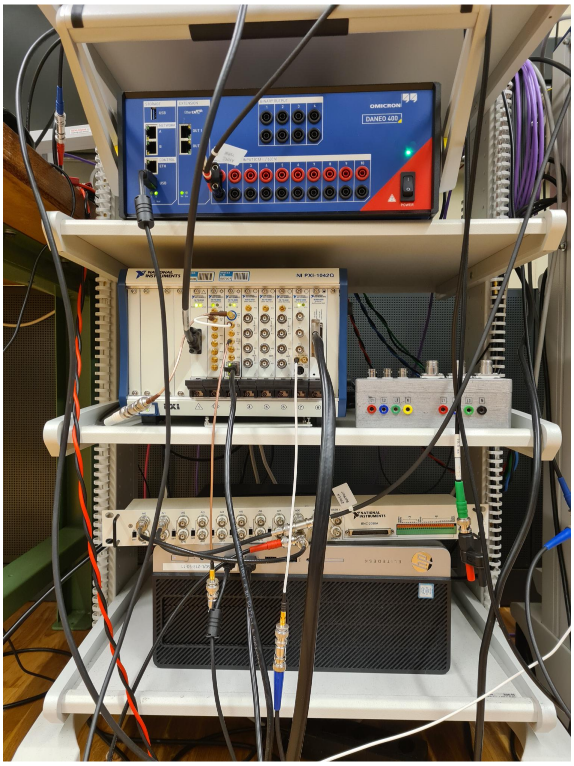

Figure 3.2: PMU Calibrator infrastructure present at the Swiss Federal Institute of Metrology (METAS) in Bern, Switzerland. Only some of its components are shown: a signal analyzer (top shelf), a real-time controller including time and analog input/output modules (middle shelf), and an external ADC (bottom shelf).

so, such waveforms are modeled in MATLAB environment to emulate testing conditions for both 50- and 60-Hz rated system signals, and for P- and M-class PMUs. To ensure maximum generalization, the sampling frequency f_s is chosen equal to 18 kSa/s and the time duration of each test is 12 s. By doing that, it is guaranteed that leakage effects are avoided for all possible signal frequencies under test.

After the modeling of the waveforms in MATLAB, according to the sets of equations that are going to be described in the following, a matrix is created for both steady-state and dynamic signals. It features a number of rows equal to the total number of samples, based on f_s and the test time length, and a number of columns equal to 7. The first six represent the three-phase voltage and three-phase current signals, while the last presents only 1 or 0 values. They are used as a flag to activate or deactivate the ongoing test. The matrix is saved as a .tdms file, which is lighter than a .txt file, and it is read in LabVIEW by the PMU calibrator which generates the corresponding samples.

The PMU Std evaluates five different influence quantities at a time in the context of steady-state signals: frequency, voltage and current magnitudes, harmonic distortion, and Out-Of-Band Interference (OOBI).

For what regards the signal frequency, the set of equations shown in Eq. (3.1) is considered: X_m is the rated signal amplitude in V before the amplification stage, and φ_0 is the initial phase in rad, assumed equal to 0 for the sake of simplicity. Whereas f_t is the frequency under test in Hz whose value is varied for each testing condition. The set of $X_a(t)$, $X_b(t)$, and $X_c(t)$ represent a generic three-phase time-varying signal which can hold true for either voltage or current waveforms just by replacing the variable X. For P-class compliance tests, an interval of ±2 Hz must be considered around the rated frequency according to [14]. Whereas, for M-class tests the interval extends to ±5 Hz. All frequencies within such ranges are simulated, by introducing different f_t in Eq. (3.1) with a step of $\Delta f = 0.5$ Hz.

$$\begin{aligned} X_a(t) &= X_m \cdot \cos\left(2\pi f_t t + \varphi_0\right) \\ X_b(t) &= X_m \cdot \cos\left(2\pi f_t t + \varphi_0 - 2/3\pi\right) \\ X_c(t) &= X_m \cdot \cos\left(2\pi f_t t + \varphi_0 + 2/3\pi\right) \end{aligned} \tag{3.1}$$

For what concerns the voltage magnitude, the three-phase voltage is shown in Eq. (3.2) where f_n is the system-rated frequency in Hz and V_p represents a percentage in V of the nominal voltage before the amplification stage. According to the PMU Std, two different ranges must be considered for P- and M-class compliance. For the first, the voltage percentage has to span from 80 % to 120 %, while from 10 % to 120 % for the latter. Voltage steps ΔV of 20 % are considered in both scenarios. It is worth highlighting that during this test, the current is simulated as a three-phase set at nominal conditions (i.e., nominal magnitude and frequency).

$$\begin{aligned} V_a(t) &= V_p \cdot \cos\left(2\pi f_n t + \varphi_0\right) \\ V_b(t) &= V_p \cdot \cos\left(2\pi f_n t + \varphi_0 - 2/3\pi\right) \\ V_c(t) &= V_p \cdot \cos\left(2\pi f_n t + \varphi_0 + 2/3\pi\right) \end{aligned} \tag{3.2}$$

Similarly to the voltage one, the current magnitude test consists of supplying a three-phase signal having a percentage of the rated current value. Eq. (3.2) is still valid, just by replacing the V variable with I. In this case, though, P- and M-class ranges match perfectly and they span from 10 % to 200 % of the rated current. In an analogous way to the previous case, steps of $\Delta I = 20\,\%$ are considered.

Harmonic distortion tests are evaluated by applying a single harmonic at a time whose magnitude is 1 % for P-class tests, while 10 % for M- ones. The set of equations is shown in Eq. (3.3), where X_m and f_n are the rated signal magnitude in V before its amplification and frequency in Hz; instead, φ_0 is the initial phase in rad equal to 0. The harmonic amplitude factor k_x is either 1 % or 10 %, while the harmonic order is n. All the harmonics up to $n = 50$ are tested, however particular relevance is given to common voltage and current harmonics indicated in the relevant power quality standards as in [21] and [22], respectively.

$$\begin{aligned} X_a(t) &= X_m \cdot \cos\left(2\pi f_n t + \varphi_0\right) + X_m k_x \cdot \cos\left(2\pi n f_n t + \varphi_0\right) \\ X_b(t) &= X_m \cdot \cos\left(2\pi f_n t + \varphi_0 - 2/3\pi\right) + X_m k_x \cdot \cos\left(2\pi n f_n t + \varphi_0 - 2/3n\pi\right) \\ X_c(t) &= X_m \cdot \cos\left(2\pi f_n t + \varphi_0 + 2/3\pi\right) + X_m k_x \cdot \cos\left(2\pi n f_n t + \varphi_0 + 2/3n\pi\right) \end{aligned} \tag{3.3}$$

The last steady-state test involves the verification of OOBI. According to the PMU Std, given the PMU reporting rate R_r and the power system rated frequency f_n, it is possible to calculate the interval within which f_n is changed. For $R_r \leq 100$ fps, the test frequency interval f_t is included between $f_n \pm 0.1 \cdot (R_r/2)$. Alternatively, for $R_r > 100$ fps, the interval is $f_t = f_n \pm 5$. The bandpass frequency bounds can be computed as $\pm R_r/2 + f_n$ for all R_r reporting rates. At this stage, it is possible to evaluate the frequencies below the passband as $f_n - R_r/2 - (0.1 \cdot 2^k)$ for $k = 0, 1, 2, ...$ until $f \leq 10$ Hz. On the other hand, the frequencies above the passband can be assessed as $f_n + R_r + (0.1 \cdot 2^m)$ for $m = 0, 1, 2, ...$ until $f \geq 2 \cdot f_n$ Hz. By rounding them to the next integer value and sorting them in ascending order, it is possible to retrieve the set of interfering frequencies used to test each frequency f_t in the previously obtained test interval. This process is repeated for all possible R_r and for the two system-rated frequencies $f_n = 50$ Hz and 60 Hz.

The set of equations can be represented as follows:

$$\begin{aligned}
X_a(t) &= X_m \cdot \cos\left(2\pi f_t t + \varphi_0\right) + X_m k_x \cdot \cos\left(2\pi n f_{int} t + \varphi_0\right) \\
X_b(t) &= X_m \cdot \cos\left(2\pi f_t t + \varphi_0 - 2/3\pi\right) + X_m k_x \cdot \cos\left(2\pi f_{int} t + \varphi_0 - 2/3\pi\right) \\
X_c(t) &= X_m \cdot \cos\left(2\pi f_t t + \varphi_0 + 2/3\pi\right) + X_m k_x \cdot \cos\left(2\pi f_{int} t + \varphi_0 + 2/3\pi\right)
\end{aligned} \tag{3.4}$$

In Eq. (3.4), X_m represents the rated value of the signal in V before its amplification, φ_0 is the initial phase in rad and it is equal to 0. The nominal frequency f_n is replaced by f_t which represents the set of frequencies to be tested. Each interference frequency is indicated by f_{int}, while its amplitude factor k_x is equal to 10 % for all $R_r \geq 10$ fps. It is also worth recalling that no requirements are set for P-class PMUs and for M-class ones having a $R_r < 10$ fps. In this test, PMUs are compliant with the Std when their TVE is less or equal to 1.3 %. On the other hand, all steady-state tests required a TVE of 1 % as per [14].

3.3.2 Dynamic Signals

In this Section, the dynamic test waveforms are presented. They are required to be generated, and consequently re-acquired, by the PMU calibrator. In the following, the five tests are described and the maximum TVE limits expected by the PMU Std are reported. The dynamic tests include amplitude and phase modulation, frequency ramp, and amplitude and phase steps, as treated in [14].

The first dynamic test that is considered is amplitude modulation. Such a test is performed at rated signal magnitude X_m and rated power system frequency f_n. The amplitude modulation factor k_x is equal to 0.1 for all tests, while the phase modulation factor k_a is equal to 0. The modulation frequency f_m is varied from a lower-bound of 0.1 Hz to an upper-bound of $R_r/10$ or 2 Hz for P-class PMUs, or from 0.1 Hz to $R_r/5$ or 5 Hz for M-class ones. For instance, for a PMU having a $R_r = 50$ fps, this implies that tests are carried out for all f_m ranging from 0.1 to 5.0 Hz in the widest range. This test does not vary its maximum TVE which is equal to 3 % for both P- and M-class PMUs [14].

The set of equations is shown in Eq. (3.5) where all variables have already been defined. It is worth noticing that the initial phase φ_0 has been omitted for the sake of brevity, as it is always assumed equal to 0 rad.

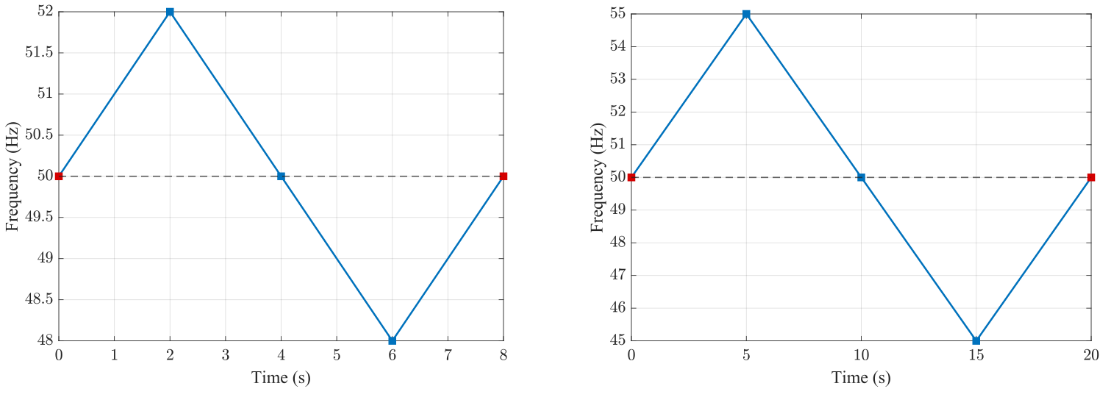

(a) (b)

Figure 3.3: Frequency as a function of time (solid blue line) during dynamic ramp tests for a 50-Hz signal, as illustrated in [14]. Blue markers indicate an idle time of 1 s, while red ones of 2 s. P-class frequency ramp is shown in (a), whereas M- one in (b). The horizontal dashed black line indicates the nominal system frequency.

$$\begin{aligned} X_a(t) &= X_m \cdot [1 + k_x \cdot \cos(2\pi f_m t)] \cdot \cos[2\pi f_n t + k_a \cdot \cos(2\pi f_m t - \pi)] \\ X_b(t) &= X_m \cdot [1 + k_x \cdot \cos(2\pi f_m t)] \cdot \cos[2\pi f_n t - 2/3\pi + k_a \cdot \cos(2\pi f_m t - \pi)] \\ X_c(t) &= X_m \cdot [1 + k_x \cdot \cos(2\pi f_m t)] \cdot \cos[2\pi f_n t + 2/3\pi + k_a \cdot \cos(2\pi f_m t - \pi)] \end{aligned} \tag{3.5}$$

Similarly to amplitude modulation, phase modulation tests rely on the same set of equations shown in Eq. (3.5). Such tests are performed at the same conditions (i.e., rated signal magnitude and frequency, identical test ranges concerning the modulation frequency f_m, and maximum TVE of 3 % for both classes). However, the amplitude modulation factor k_x is equal to 0, while the phase one is $k_a = 0.1$.

Frequency ramp tests consist of generating a linear frequency ramp at rated signal magnitude X_m and starting at the nominal power system frequency f_n. The three-phase signal is represented by the equations shown in Eq. (3.6). In addition to the parameters previously defined, R_f represents the constant frequency ramp rate in Hz/s, which is equivalent to $df(t)/dt$.

$$\begin{aligned} X_a(t) &= X_m \cdot \cos\left(2\pi f_n t + \pi R_f t^2\right) \\ X_b(t) &= X_m \cdot \cos\left(2\pi f_n t - 2/3\pi + \pi R_f t^2\right) \\ X_c(t) &= X_m \cdot \cos\left(2\pi f_n t + 2/3\pi + \pi R_f t^2\right) \end{aligned} \tag{3.6}$$

The ramp rate R_f is equal to ±1 Hz/s for both PMU classes; however, for P-class ones the ramp range is ±2 Hz, while for M- ones is lesser than $R_r/5$ or 5 Hz. For instance, for a 50 Hz power system signal, Fig. 3.3 reports the frequency trend as a function of time, represented by a solid blue line, for the P-class in (a) and the M-one in (b). Square blue markers indicate idle time instants of 1 s during which the PMU calibrator generates the corresponding frequency before inverting the slope. Red markers, instead, indicate the same idle time, but equal to 2 s in order to ensure the extinction of all transients at the beginning and at the end of the test. It is also worth recalling that the max TVE is equal to 1 % for both classes [14].

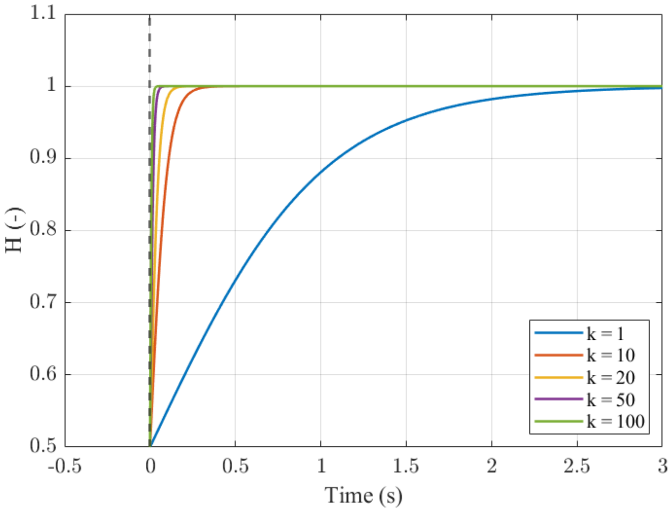

Figure 3.4: Heaviside function for positive values of time only, computed for five increasing values of k. The dashed black line represents the vertical asymptote.

According to [14], the three-phase waveforms that can replicate the amplitude step tests can be written as follows:

$$\begin{aligned} X_a(t) &= X_m \cdot [1 + k_x u(t)] \cdot \cos\left[2\pi f_n t + k_a u(t)\right] \\ X_b(t) &= X_m \cdot [1 + k_x u(t)] \cdot \cos\left[2\pi f_n t - 2/3\pi + k_a u(t)\right] \\ X_c(t) &= X_m \cdot [1 + k_x u(t)] \cdot \cos\left[2\pi f_n t + 2/3\pi + k_a u(t)\right] \end{aligned} \tag{3.7}$$

In Eq. (3.7), besides the already defined nominal signal magnitude X_m and rated frequency f_n, $u(t)$ is the unit step function and k_x and k_a represents the magnitude and phase step size, respectively.

However, it must be kept into account that the unit step is a non-differentiable function. This represents a critical issue when re-acquiring the waveform because differentiability is a mandatory condition to perform interpolation[1]. To solve this issue, the Heaviside function is used. It is a differentiable function and its analytical expression is the following:

$$H(t) = \frac{1}{1 + e^{-2kt}} \tag{3.8}$$

The time variable is indicated by t, while k is a coefficient that represents the steepness of the step. As a matter of fact, the higher k, the more the step tends to be an ideal one. This is shown in Fig. 3.4 in which five increasing values of k are plotted as a function of positive values of time.

At this stage, it is possible to re-write Eq. (3.7) by introducing the Heaviside function shown in Eq. (3.8) and $k_a = 0$ to simulate an amplitude step:

---

[1] Besides, if an ideal step were applied, the output would still not be ideal owing to the bandwidth limit of the amplifier. The complete description of the acquisition stage of the PMU calibrator and the consequent interpolation are presented in Section 3.5

$$\begin{aligned}
X_a(t) &= X_m \cdot \left[1 + \frac{k_x}{1+e^{-k(t-T_t)}}\right] \cdot \cos\left(2\pi f_n t\right) \\
X_b(t) &= X_m \cdot \left[1 + \frac{k_x}{1+e^{-k(t-T_t)}}\right] \cdot \cos\left(2\pi f_n t - 2/3\pi\right) \\
X_c(t) &= X_m \cdot \left[1 + \frac{k_x}{1+e^{-k(t-T_t)}}\right] \cdot \cos\left(2\pi f_n t + 2/3\pi\right)
\end{aligned} \tag{3.9}$$

Apart from X_m and f_n already defined and still equal to rated conditions even in this case, k_x is equal to ±0.1 according to [14], and $k = 100$ represents the steepness of the step as shown in Fig. 3.4. Lastly, T_t is the time-to-half-value, evaluated with respect to the asymptotic value to infinity of the function.

Two different expressions can be obtained from Eq. (3.9) depending on t:

$$X_a(t) \approx \begin{cases} (X_m + k_x) \cdot \cos\left(2\pi f_n t\right), & \text{if } t \geq T_t \\ X_m \cdot \cos\left(2\pi f_n t\right), & \text{otherwise} \end{cases}$$

Despite the fact that the analytical formulation ensures the correct modeling of an amplitude step, another criticality needs to be tackled before the implementation into the PMU calibrator.

First, it must be recalled that such tests are necessary to evaluate the response and delay time of the PMU, as well as its under/overshoot response. However, focusing only on the first ones, it has to be considered that the PMU response and its delay times are generally much smaller in comparison to its reporting rate which can reach up to $R_r = 100$ fps for 50-Hz signals. Hence, it is unlikely that the PMU data points will occur at the specified measurement points, marking it improbable to determine them with a single-step test.

To solve this issue, amplitude steps can be interleaved: it means that by applying a step at different time instants, a time-varying reporting is obtained. Afterward, measurements can be combined to provide a step response result whose resolution is less than the reporting interval.

The PMU Std proposes $n = 10$ as the number of interleaved steps to consider [14]. Hence, for the sake of generality of the purpose of the calibrator, this value is chosen. Tests last 10 s and $T_t = 2$ s is the time at which the 10 % amplitude step takes place. An interval of ±10 ms is considered around T_t for interleaving, with a difference between subsequent steps Δt_t being 2 ms, corresponding to 5 steps before and 5 after T_t. The same rationale is followed for negative amplitude steps.

Similar considerations are valid for the phase step test, which is the last dynamic compliance test presented in the PMU Std. In this case, it is still necessary to introduce the Heaviside function shown in Eq. (3.8) into Eq. (3.7) in order to simulate a step on the phase. For the sake of completeness, the three-phase signal is reported as follows:

$$\begin{aligned} X_a(t) &= X_m \cdot \cos\left[2\pi f_n t + \frac{k_a}{1+e^{-k(t-T_t)}}\right] \\ X_b(t) &= X_m \cdot \cos\left[2\pi f_n t - 2/3\pi + \frac{k_a}{1+e^{-k(t-T_t)}}\right] \\ X_c(t) &= X_m \cdot \cos\left[2\pi f_n t + 2/3\pi + \frac{k_a}{1+e^{-k(t-T_t)}}\right] \end{aligned} \tag{3.10}$$

In a similar way to the amplitude, the angle step of ±10° occurs at $T_t = 2$ s. Five steps are interleaved before and after T_t every $\Delta t_t = 2$ ms, so that $n = 10$ is ensured. The magnitude step size k_x is zero, while the phase one k_a is $\pm\pi/18$ and the steepness of the step k is 100. Different requirements in terms of delay and response times as well as for over/undershoot are envisioned for P- and M-class PMUs which are omitted here for the sake of brevity [14].

3.4 Generation Stage Calibration Routine

This Section illustrates the main characteristics of the generation stage of the calibrator as well as the magnitude and frequency tests performed in order to evaluate the stability of the PMU calibrator itself.

A block diagram depicting these fundamental steps is shown in Fig. 3.5.
First of all, starting from the left-hand side, the user sets the parameters required in LabVIEW environment. Based on these, the .tdms files generated in MATLAB and described in the previous Section 3.3 are played. This results in a matrix containing all waveform samples which can be generated as analog low-voltage and low-current signals by the PXI itself[2]. Afterward, such signals are sent to two Keysight 3458A digital multimeters working in different configurations.

The first one works in Master mode, while the second is in Slave mode. The Master orders the Slave to start sampling, sharing the same 10 MHz clock. In this context, it is worth noticing that a small time difference can be assessed. It represents a discrepancy between the transmission of the trigger and the actual triggering event. Nevertheless, it can be measured and compensated accordingly. By using the multimeters in the described configuration, it is possible to assess the phase difference between the two low-voltage signals. First, the voltage phase is assessed against the current one for the same phase of the three-phase signal. Afterward, this difference is evaluated against the other two phases.

It is worth recalling that when used in “DC mode”, the measurements taken by the two 3458A multimeters can be traced back to the realization of the Volt [83].

The steps necessary to perform the stability assessment of the PMU calibrator can

---

[2] For the sake of clarity, it is worth recalling that the NI PXI 1042Q is not able to generate analog currents. However, in the following treatise, they are referred to as *current* signals nonetheless for a better distinction from voltage ones.

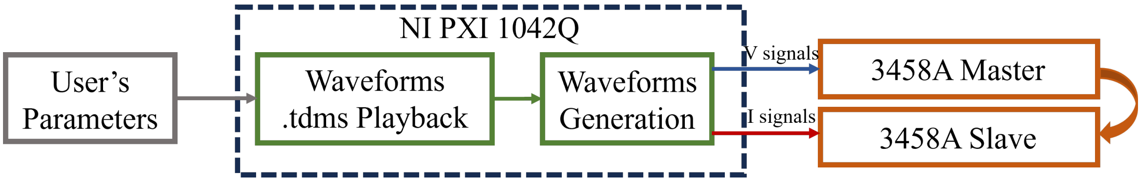

Figure 3.5: Block diagram of the fundamental steps and devices required for the evaluation of the generating stage of the PMU calibrator.

be summarized as follows. First of all, magnitude and frequency sweeps are applied in order to span across the entire voltage and current ranges, as well as the frequency one as envisioned in the PMU Std [14].

By placing the two multimeters at low signal levels, it is possible to assess the goodness of the digital-to-analog converter. As a matter of fact, this corresponds to the stability of the calibrator itself in the generation of the waveforms as no amplifiers or dividers/shunts are introduced at this stage.

Based on the previous outcomes, as no other sources of uncertainty are introduced in the chain, the mean value can be corrected, since it can be regarded as an offset. The remainder represents a contribution akin to a type A estimate as its nature stems only from random contributions.

For each test, $n = 15$ measurements are performed, hence the mean value and the corresponding standard deviations are computed according to Eq. (1.2) and Eq. (1.5), respectively. Owing to the rather limited number of measurements, the type A estimate is evaluated considering the inverse of the Student's t-distribution as described in Section 1.2.1 and shown in Eq. (1.8).

Considering $k = 2$, which results in a CI having a probability p of 95 %, then the percentile α which can be computed as $1-p$ is equal to 0.05. The number of degrees of freedom, instead, is $\nu = 14$, having considered $n = 15$ for all tests illustrated in the following. Hence, Eq. (1.8) results in:

$$s_m = t_{0.05,14} \cdot \frac{s}{\sqrt{15}} \tag{3.11}$$

Afterward, the obtained mean values are adjusted according to the correction factors of the 3458A multimeters. It is worth clarifying that once the samples are acquired, they are linearly fitted in a sinusoidal signal in order to retrieve the amplitude, phase, and frequency. Therefore, k_x, k_φ, and k_f represent the amplitude error, the phase delay, and the frequency offset to be corrected, respectively.

The measured mean values of the frequency f in Hz, voltage or current x in V[3], and phase φ in min are indicated by a $\hat{}$, while the corrected ones present a subscript c. The correction factors, represented with k, have a subscript that corresponds to the

---

[3] For the sake of completeness, it is worth clarifying that albeit they are referred to as *current channels*, their stability is established by measuring the corresponding voltage. For this reason, the unit of measurement is V in the following Tables and Figures.

relative quantity under test.
They can be summarized in the following set of equations:

$$\begin{aligned} f_c &= \hat{f} \cdot (1 - k_f) \\ x_c &= \hat{x} \cdot k_x \\ \varphi_c &= \hat{\varphi} - (60 \cdot k_\varphi) \end{aligned} \tag{3.12}$$

The corrected mean values shown in Eq. (3.12) are used to evaluate the error with respect to the reference one as follows:

$$\begin{aligned} e_f &= \frac{f_c - f_{ref}}{f_{ref}} \\ e_x &= \frac{x_c - x_{ref}}{x_{ref}} \\ e_\varphi &= \varphi_c - \varphi_{ref} \end{aligned} \tag{3.13}$$

These values are usually very small in the order of parts per million (ppm). Once assessed, they can be compensated accordingly as they constitute a quantifiable offset in the measurements.

For what concerns the phase difference, instead, it is usually more common to assess the phase displacement between the two channels. Consequently, the corresponding phase delay can be evaluated, rather than the single voltage or current phase φ. The phase displacement $\Delta\varphi$ can be computed as the point-by-point difference between the phase measured on the voltage φ_v and on the current channels φ_i.
The phase delay t_d, expressed in s, is computed as:

$$t_d = \frac{\Delta\varphi}{2\pi f_c} \tag{3.14}$$

The result of this process consists of the compensation of the mean value of the error and the evaluation of the type A contribution. Consequently, bar graphs can be plotted centered around zero and having as upper and lower-bound values the uncertainty, computed starting from the standard deviation of a 95 % CI. This process is repeated twice: once performing a magnitude sweep across all possible excitation levels at rated frequency, then a frequency sweep is carried out including the most severe cases at rated signal levels.

3.4.1 Magnitude Sweep

This Section presents the assessment of the uncertainties characterizing the generating stage of the PMU calibrator by performing a magnitude sweep.

The list of tests is shown in Table 3.1. The first column shows the excitation value in percentage. Such values are chosen based on the worst-case scenarios of the voltage and current magnitude tests for P- and M-class PMUs, according to the PMU Std. As a matter of fact, according to [14], M-class voltage magnitude tests require

Table 3.1: Calibration routine tests performed for the generation stage. Based on all possible excitation levels expressed in %, reference voltage V_{ref} and current I_{ref} values are determined. The reference frequency is set at 50 Hz, while both phases are set to 0 min.

Excitation (%)	f_{ref} (Hz)	V_{ref} (V)	$\varphi_{v,ref}$ (min)	I_{ref} (V)	$\varphi_{i,ref}$ (min)
30	50	1.38	0	0.3	0
40	50	1.84	0	0.4	0
50	50	2.30	0	0.5	0
60	50	2.76	0	0.6	0
70	50	3.22	0	0.7	0
80	50	3.68	0	0.8	0
90	50	4.14	0	0.9	0
100	50	4.60	0	1.0	0
120	50	5.52	0	1.2	0
150	50	6.90	0	1.5	0
200	50	7.00	0	2.0	0

testing over a range spanning from 10 % to 120 % of the rated voltage. Similarly, M-class current magnitude tests span over a range from 10 % to 200 % of the rated current. Based on this, the excitation values are chosen such that the largest testing range for M-class PMUs is covered.

As a reference frequency, f_{ref}, a 50 Hz signal is considered as it is the common power system frequency in Europe. For the sake of brevity, only such results are presented. However, the same procedure is valid for 60-Hz signals.

Both voltage and current reference phases, $\varphi_{v,ref}, \varphi_{i,ref}$, are set equal to 0, as the objective entails the assessment of the phase displacement $\Delta\varphi$ in min and the corresponding phase delays t_d in s.

The reference voltages V_{ref} are set based on the rated voltage V_n which is 230 V and on the gain of the amplifier which is equal to 50. Similarly, considering a rated current I_n of 5 A and the gain of the current amplifier equal to 5, the reference values are chosen according to:

$$\begin{aligned} V_{ref} &= \frac{V_n}{50} \cdot \frac{E}{100} \\ I_{ref} &= \frac{I_n}{5} \cdot \frac{E}{100} \end{aligned} \tag{3.15}$$

where the excitation is briefly indicated as E.

In this context, it is worth recalling that I_{ref} values are translated into voltage reference values at this calibration stage. Second, for an excitation of 200 % the corresponding V_{ref} would be equal to 9.2 V according to Eq. (3.15). However, such value cannot be generated by the NI 4461 card, hence V_{ref} is manually set equal to 7.00 V which is the maximum output available. In any case, this approximation does not affect the calibration routine as voltage magnitude tests equal to 200 % are not included in the PMU Std [14].

The results of the magnitude sweep are presented as follows.

First of all, the frequency errors computed using Eq. (3.13) are plotted as a function of the excitation, which is expressed as a percentage of the rated value. The results

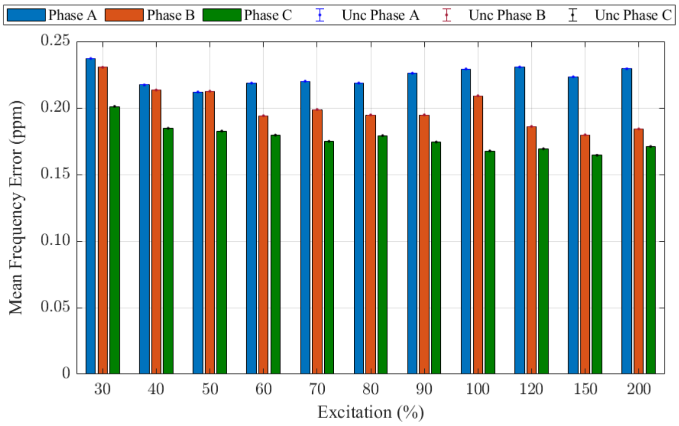

Figure 3.6: Results of the magnitude sweep in regard to the frequency. The mean value of the error (in ppm) is indicated by solid bars, while the corresponding uncertainty intervals are shown by smaller vertical bars on top (in ppm). The results of phase A are shown in blue, those of phase B in red, and phase C in green, as a function of the excitation expressed in % of the rated value.

concerning the three phases are shown in Fig. 3.6 in which the solid bars indicate the mean value of the frequency error expressed in ppm. The smaller vertical bars on top, instead, represent the uncertainty interval computed according to Eq. (3.11). The choice of expressing all type A estimates in ppm stems from the fact that all these results are rather small. In order to properly represent them and perform easier comparisons among each other, it has been chosen to use such a measurement unit. Nevertheless, it should not be left out of consideration the correlation of these outcomes with the PMU Std [14]. It is also worth recalling that a single value of frequency is applied to the PMU Calibrator; however, this value is not constrained to be the same on all three phases. Rather the objective of this test consists of the assessment of the frequency generation by the three different PXI cards.

However, as previously disclosed, it can be assumed that the mean error value can be compensated, conversely to the uncertainty. For this reason, Fig. 3.7 presents only the uncertainty intervals for the three phases, for various levels of voltage excitation. As this assumption can be regarded as valid in most of the cases, the figures shown hereinafter will present only the uncertainty interval. Hence, they will show a mean value equal to zero in spite of the fact that non-zero errors were assessed during the calibration routine for all quantities under test.
The results shown in Fig. 3.7, which essentially illustrate a zoomed portion around the vertical bars of Fig. 3.6, represent the frequency uncertainty intervals. As a matter of fact, such intervals are minimal as they are below 0.5 ppm for all possible excitation levels. This indicates the stability of the generated frequency by the PMU calibrator even for non-rated signals.

Fig. 3.8 and Fig. 3.9, instead, present the uncertainty intervals with regard to the voltage and current magnitude, respectively. The first comment concerns low values of the excitation: in such cases, similar results are obtained in the three phases. Whereas, as the level of excitation increases, the uncertainty intervals tend to differ from one phase to the other. Still, this variation is in the range of a few tens of ppm and is most likely due to non-linearities. Lastly, even though the voltage uncertainty intervals are much larger than the current ones, in all cases the maximum recorded uncertainty is below 80 ppm. This can be regarded as a very small interval if compared to the order of magnitude of the quantities to be measured.

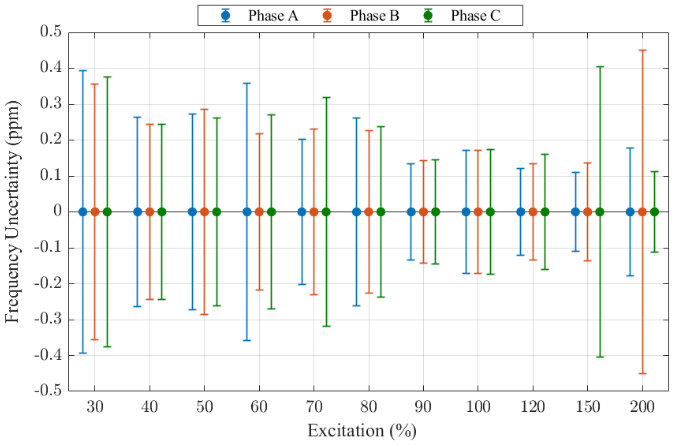

Figure 3.7: Results of the magnitude sweep in regard to the frequency. The 95 % confidence intervals are shown as vertical bars (in ppm). The results of phase A are shown in blue, those of phase B in red, and phase C in green, as a function of the excitation expressed in % of the rated value.

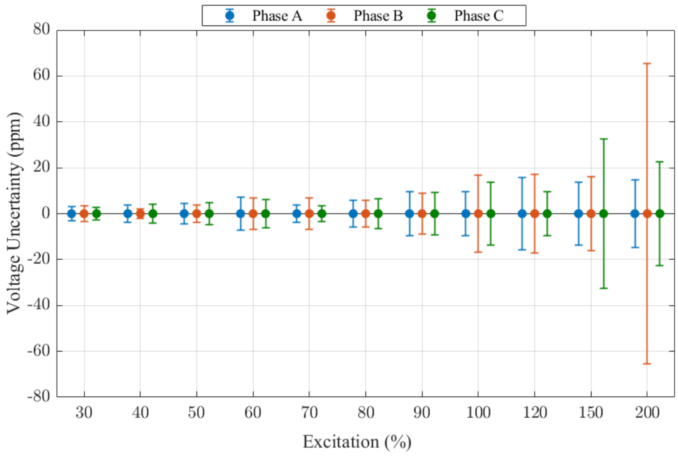

Figure 3.8: Results of the magnitude sweep illustrating the uncertainty intervals of the voltage magnitude. The 95 % confidence intervals are shown as vertical bars (in ppm). The results of phase A are shown in blue, those of phase B in red, and phase C in green, as a function of the excitation expressed in % of the rated value.

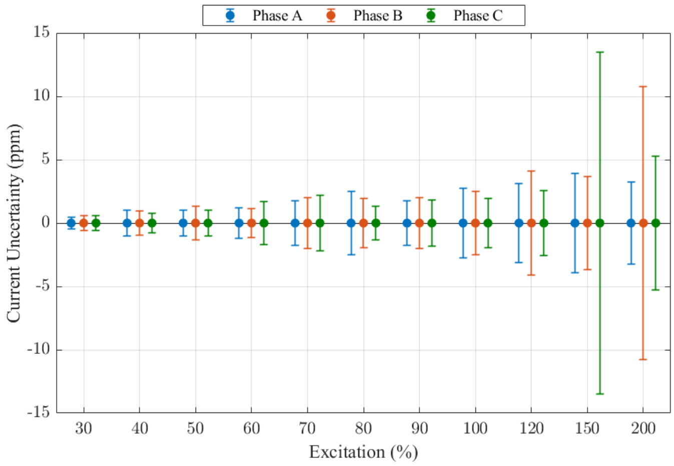

Figure 3.9: Results of the magnitude sweep illustrating the uncertainty intervals of the current magnitude. The 95 % confidence intervals are shown as vertical bars (in ppm). The results of phase A are shown in blue, those of phase B in red, and phase C in green, as a function of the excitation expressed in % of the rated value.

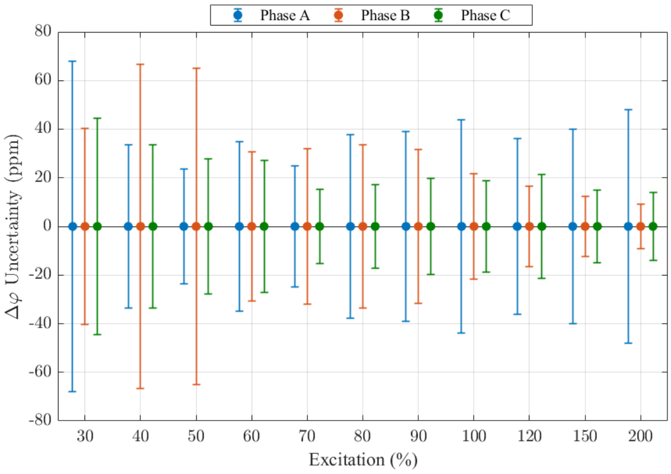

Figure 3.10: Results of the magnitude sweep illustrating the uncertainty intervals of the phase difference $\Delta\varphi$. The 95 % confidence intervals are shown as vertical bars (in ppm). The results of phase A are shown in blue, those of phase B in red, and phase C in green, as a function of the excitation expressed in % of the rated value.

In conclusion, Fig. 3.10 presents the uncertainty intervals of the phase difference $\Delta\varphi$ expressed in ppm. It is worth noting that $\Delta\varphi$ is calculated as the point-by-point difference between the voltage and current phases, for each phase A to C.
Hence, in comparison with the other results, in this case, the intervals do not tend to increase as the level of excitation increases. But rather the uncertainty is included within 50 ppm for all $E \geq 60\,\%$; however, higher bounds are reached on phases A and B at excitation levels equal to 30 %, 40 %, and 50 %.

This result concludes the analysis of the uncertainty intervals obtained by spanning across all input signal magnitudes at the rated frequency of 50 Hz. The presented results constitute a preliminary starting point for the evaluation of the overall measurement chain uncertainty of the PMU calibrator.

3.4.2 Frequency Sweep

This Section presents the evaluation of the uncertainty characterizing the generating stage of the PMU calibrator by spanning across all possible frequencies.

The list of tests is shown in Table 3.2. The first column illustrates the frequencies under test in Hz. Similarly to what is carried out for the magnitude sweep, 50 Hz is considered as the rated frequency. The rationale behind the choice of such values centered around 50 ± 5 Hz is to be found on the requirements for M-class PMUs as per [14]. As shown in Section 3.3.1, the PMU Std requires that the signal frequency is tested in an interval of ±2 Hz for P-class PMUs, while of ±5 Hz for M- ones. For the sake of generality of the purpose of the PMU calibrator, the frequency sweep is performed across the largest interval. A step of 1 Hz is selected in between the frequencies under test in order to ensure a rather fine resolution. Without loss of generalization, the same considerations hold true for 60-Hz signals.
The second column, instead, presents the excitation which is equal to 100 % for all possible frequencies as rated signals are expected in such a scenario.
The next two columns present the reference voltage magnitude V_{ref} in V and phase $\varphi_{v,ref}$ in min. In the last two, instead, the reference current magnitude I_{ref} and its corresponding reference phase $\varphi_{i,ref}$ are shown in V and min, respectively. As dis-

Table 3.2: Calibration routine tests performed for the generation stage based on all possible test frequencies included in the PMU Std for M-class PMUs. The excitation level is considered equal to 100%, hence voltage and current reference values are the nominal ones, prior to their corresponding amplification stages. Both reference phases are equal to 0 min.

Frequency (Hz)	Excitation (%)	V_{ref} (V)	$\varphi_{v,ref}$ (min)	I_{ref} (V)	$\varphi_{i,ref}$ (min)
45	100	4.60	0	1.0	0
46	100	4.60	0	1.0	0
47	100	4.60	0	1.0	0
48	100	4.60	0	1.0	0
49	100	4.60	0	1.0	0
50	100	4.60	0	1.0	0
51	100	4.60	0	1.0	0
52	100	4.60	0	1.0	0
53	100	4.60	0	1.0	0
54	100	4.60	0	1.0	0
55	100	4.60	0	1.0	0

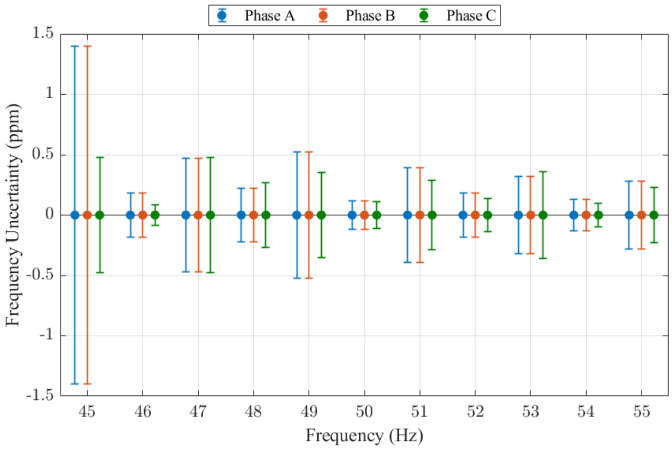

Figure 3.11: Results of the frequency sweep in regard to the frequency. The 95 % confidence intervals are shown as vertical bars (in ppm). The results of phase A are shown in blue, those of phase B in red, and phase C in green, as a function of the frequency expressed in Hz.

closed previously, the reference phase is selected equal to 0 for the sake of simplicity. Whereas, voltage and current reference values are computed according to Eq. (3.15) prior to their corresponding amplification stages.

The results of the frequency sweep are presented as follows, similar to what has been done for the magnitude ones.
First of all, the frequency uncertainty intervals for a 95 % CI are shown in Fig. 3.11. The results are included within ±0.5 ppm for all frequencies, apart from the lowest frequency, $f = 45$ Hz, which presents an interval of ±1.5 ppm. Apart from the latter, these results are similar to those shown in Fig. 3.7 where the maximum uncertainty was included within ±0.5 ppm. More in detail, for an $E = 100\,\%$ at $f = 50$ Hz the magnitude and frequency sweeps provide very similar results.

The voltage uncertainty intervals are shown in Fig. 3.12. For all frequencies, the uncertainty is included within ±20 ppm. However, for a $f = 45$ Hz, phase A shows a rather significant increase which exceeds ±30 ppm. For the rated 50 Hz frequency, at rated excitation, these results are aligned with those shown in Fig. 3.8. However,

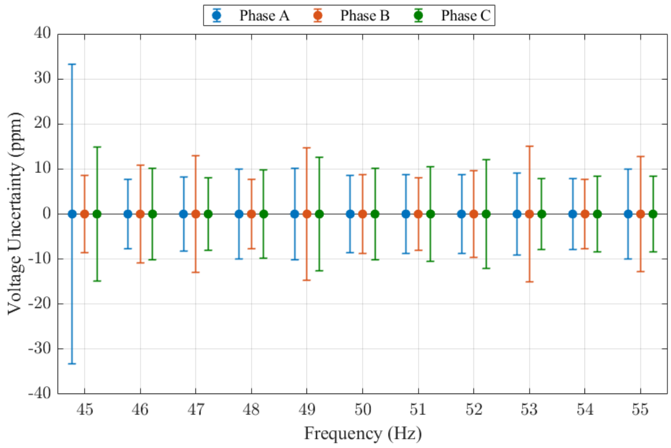

Figure 3.12: Results of the frequency sweep illustrating the uncertainty intervals of the voltage magnitude. The 95 % confidence intervals are shown as vertical bars (in ppm). The results of phase A are shown in blue, those of phase B in red, and phase C in green, as a function of the frequency expressed in Hz.

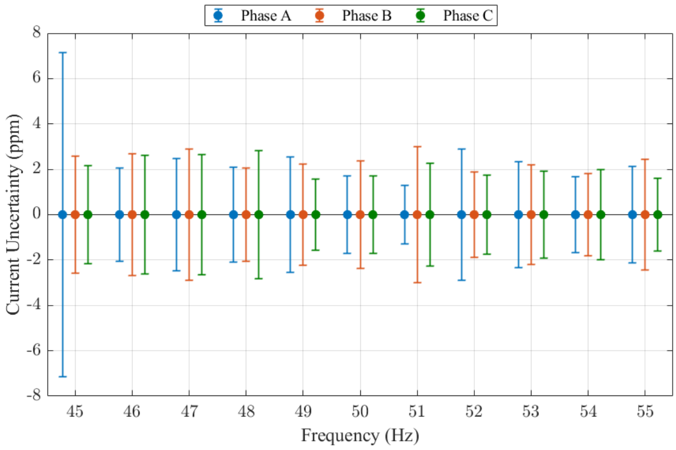

Figure 3.13: Results of the frequency sweep illustrating the uncertainty intervals of the current magnitude. The 95% confidence intervals are shown as vertical bars (in ppm). The results of phase A are shown in blue, those of phase B in red, and phase C in green, as a function of the frequency expressed in Hz.

it is evident how the magnitude sweep is more affecting the performances as the voltage uncertainty reached up to ±80 ppm at 200 % excitation level.

The results concerning the current uncertainty intervals are presented in Fig. 3.13. In a similar way to what has been observed in Fig. 3.12, phase A at 45 Hz presents a higher uncertainty with respect to the other results. However, in this case, a much lower uncertainty is assessed as it is included within ±4 ppm for all phases across the frequency range under test. Comparing Fig. 3.9 with these results, it can be concluded that similar intervals are obtained across the whole excitation range; nevertheless, larger ones are observed at high excitation levels, i.e., 150 % and 200 %. This confirms the higher dependency of the magnitude uncertainty on the excitation value rather than on the signal frequency.

The last results entail the assessment of the phase displacement $\Delta\varphi$ between voltage and current phases, computed as described in Section 3.4.1. The outcomes are shown in Fig. 3.14 in which $\Delta\varphi$ is plotted as a function of the frequency. In the same way as observed in Fig. 3.10, these uncertainty intervals are not constant across the whole range under test. Additionally, they also vary from one phase to the other. In Fig. 3.10, higher intervals were assessed for low values of the excitation, although in

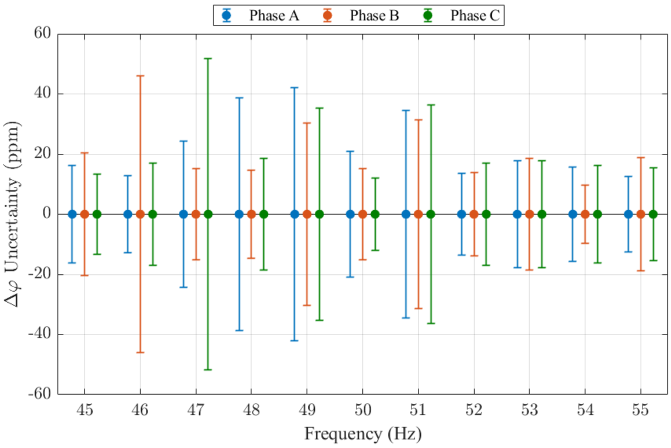

Figure 3.14: Results of the frequency sweep illustrating the uncertainty intervals of the phase difference $\Delta\varphi$. The 95 % confidence intervals are shown as vertical bars (in ppm). The results of phase A are shown in blue, those of phase B in red, and phase C in green, as a function of the frequency expressed in Hz.

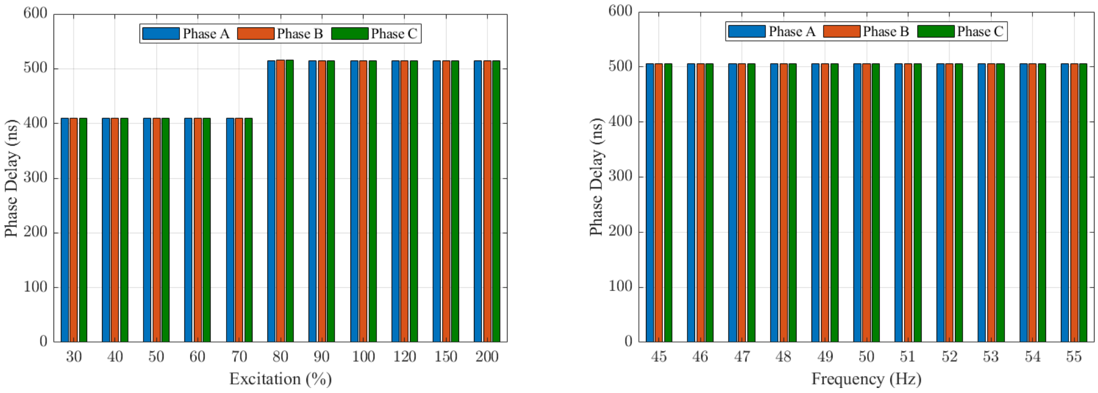

(a) (b)

Figure 3.15: Phase delay mean values expressed in ns as a result of the magnitude sweep in (a) and of the frequency sweep in (b). All results of phase A are in blue, those of phase B in red, and phase C in green, as a function of the excitation expressed in % of the rated value in (a) and of the frequency in Hz in (b).

Fig. 3.14 higher uncertainty intervals can be observed for some frequencies below 50 Hz and for $f = 51$ Hz. Whereas, at higher levels, the uncertainty interval is rather constant within ±20 ppm.

Lastly, the phase delay in time t_d is computed according to Eq. (3.14) for both magnitude and frequency sweeps. The objective entails the establishment of possible dependency of t_d on the two variables under test. The results are expressed in ns and are shown in Fig. 3.15(a) for what concerns the magnitude sweep, and in (b) for the frequency one. When the power system rated frequency is supplied, two different levels of group delay are assessed as the excitation range increases. As a matter of fact, for $E \leq 70\,\%$, a delay in the order of 400 ns is observed. Whereas, for higher values of E, t_d increases by roughly 100 ns. On the contrary, when the system signals are at rated excitation (i.e., $E = 100\,\%$), the computed phase delay is constant and in the order of 500 ns across the whole frequency range.

This concludes the evaluation of the generating stage of the PMU calibrator with the establishment of 95 %-CIs for the most significant signal quantities. The results illustrate the performances of the digital-to-analog converter in the generation of ideal signal waveforms, evaluated as a function of magnitude and frequency sweeps.

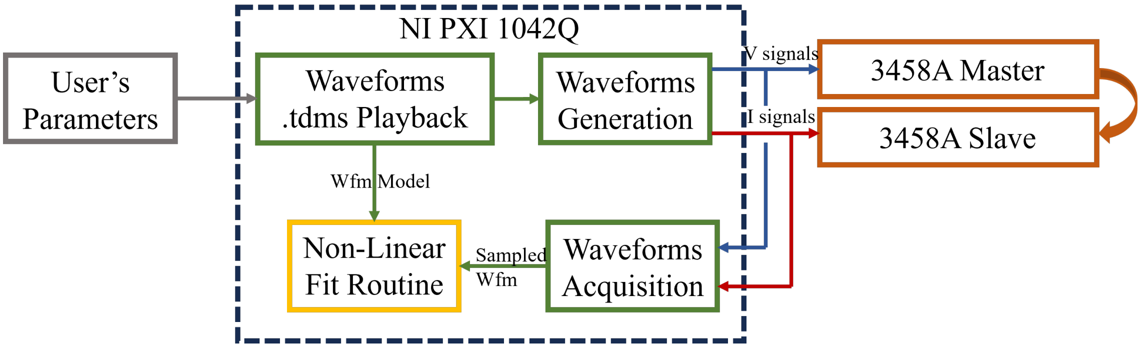

Figure 3.16: Block diagram of the fundamental steps and devices required for the evaluation of the acquisition stage of the PMU calibrator.

3.5 Acquisition Stage Calibration Routine

This Section presents the principal characteristics of the acquisition stage of the PMU calibrator as well as the frequency sweep tests that were carried out to assess the stability of the calibrator itself.

A block diagram illustrating the main steps is shown in Fig. 3.16. In a similar way to what is shown in Fig. 3.5, each block is analyzed from the left-hand side. The first row, however, is identical to the one presented in Section 3.4 but is recalled for the sake of completeness. First of all, the user sets the required parameters in LabVIEW. Consequently, .tdms files are generated and played as described in Section 3.3. Low-voltage and current signals are acquired by the two Keysight 3458A multimeters working in Master and in Slave mode, respectively.

This completes the assessment of the generation stage as already described in Section 3.4. In addition to this, in order to evaluate the acquisition, re-acquisition of the generated low-voltage and current signals is necessary. This is performed by the ADC indicated as the *Waveform Acquisition* block in Fig. 3.16. This results in a series of samples corresponding to the re-acquired waveform. In the future developments of this work, they will be automatically fitted by means of a non-linear routine for all possible test signals and compared with respect to the waveform model originally developed in MATLAB. However, at the current stage, given the simplicity of the waveforms under test, they are fitted considering the following expression:

$$x(t) = A \cdot \cos(2\pi f t + \varphi) + \xi \tag{3.16}$$

Based on Eq. (3.16), the amplitude A in V, frequency f in Hz, phase φ in rad, and DC component ξ in V are fitted. Comparing these results with those measured by two 3458A digital multimeters, it results that all the errors that can still be observed depend only on the ADC stage and on the non-linear fit. However, it is reasonable to assume that the latter constitute an almost-negligible contribution as mathematical errors are generally minimal in comparison to the ADC ones.
As a matter of fact, having already corrected the mean value of the error as described in Section 3.4, the remainders are only owing to the non-idealities, and consequent incorrect acquisition, of the waveforms caused by the digital-to-analog stage.

Without loss of generality, the same procedure and testing conditions (e.g., number of tests, coverage factor, etc. ...) described in Section 3.4 still apply. Analogously,

Table 3.3: Calibration routine tests performed for the acquisition stage based on possible test frequencies included in the PMU Std for M-class PMUs. Five different excitation levels are considered, hence the corresponding voltage and current reference values are computed, prior to their corresponding amplification stages. Both reference phases are equal to 0 min.

Frequency (Hz)	Excitation (%)	V_{ref} (V)	$\varphi_{v,ref}$ (min)	I_{ref} (V)	$\varphi_{i,ref}$ (min)
45	30	1.38	0	0.3	0
	50	2.30	0	0.5	0
	70	3.22	0	0.7	0
	100	4.60	0	1.0	0
	200	7.00	0	2.0	0
47	30	1.38	0	0.3	0
	50	2.30	0	0.5	0
	70	3.22	0	0.7	0
	100	4.60	0	1.0	0
	200	7.00	0	2.0	0
50	30	1.38	0	0.3	0
	50	2.30	0	0.5	0
	70	3.22	0	0.7	0
	100	4.60	0	1.0	0
	200	7.00	0	2.0	0
52	30	1.38	0	0.3	0
	50	2.30	0	0.5	0
	70	3.22	0	0.7	0
	100	4.60	0	1.0	0
	200	7.00	0	2.0	0
55	30	1.38	0	0.3	0
	50	2.30	0	0.5	0
	70	3.22	0	0.7	0
	100	4.60	0	1.0	0
	200	7.00	0	2.0	0

the objective consists of retrieving the standard deviations, akin to type A estimates, computed according to Eq. (1.8); hence, mean values are not thoroughly examined as done for the generation stage.

The complete set of tests carried out to evaluate the acquisition stage of the PMU calibrator is shown in Table 3.3. This includes a combination of the tests presented in Tables 3.1 and 3.2. In this analysis, five different levels of voltage and current excitation are considered, hence the corresponding reference values are computed according to Eq. (3.15). The reference phase values, i.e., $\varphi_{v,ref}$ and $\varphi_{i,ref}$, are assumed equal to 0 rad. They are still presented in Table 3.3 for the sake of completeness as their values are evaluated and accordingly fitted in the following treatise for all signals under test.

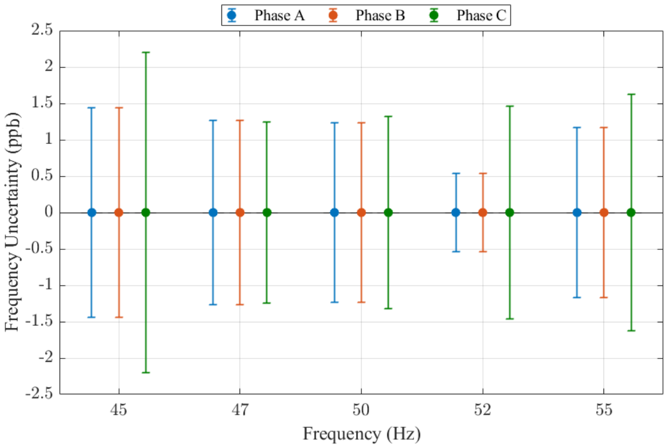

Figure 3.17: Results of the frequency sweep in regard to the frequency. The 95 % confidence intervals are shown as vertical bars (in ppb). The results of phase A are shown in blue, those of phase B in red, and phase C in green, as a function of the frequency expressed in Hz.

3.5.1 Frequency Sweep

In this Section, the main results concerning the frequency sweep are presented. For the sake of brevity, only a fixed value of voltage and current excitation is considered, namely an excitation of 100 % is examined for the first and of 30 % for the latter. The entire frequency range is spanned, as shown in Table 3.3.

It is worth recalling that this is done for the sake of conciseness. Nevertheless, it must be kept into consideration that this procedure should be repeated twice: first performing a complete magnitude sweep, then a frequency one to ensure a full characterization over the entire operating range of the PMU calibrator.

Similarly to the analysis presented in Section 3.4, the first results shown in Fig. 3.17 illustrate the frequency uncertainty assessed over the entire range under test and expressed in part per billion (ppb). These results refer to the 95 % CI and confirm the correct assessment of the frequency through the fit routine.

Having examined the frequency, the fit allows us to estimate the amplitude A of the signal. This procedure is repeated twice, for both voltage and current channels on all three phases of the calibrator. The results shown in Fig. 3.18 present the voltage uncertainty for a 95 % CI expressed in ppm. In spite of the fact that the uncertainty slightly varies among the three phases and as a function of the frequency, the maximum values obtained in this test are still included within 60 ppm.

In a similar way, Fig. 3.19 illustrates the uncertainty intervals of the current as a function of the frequency during the establishment of the stability of the acquisition stage. Conversely to the results of Fig. 3.18, the maximum current uncertainty interval is confined within 2 ppm. The current fluctuations among the three phases are much more limited with respect to the voltage ones, besides the fact that they are smaller in amplitude. This confirms the necessity of characterizing each individual stage of the PMU calibrator.

As a last point, the uncertainty on the phase of the voltage is assessed across the frequency range under test. It is worth highlighting that the current one is omitted only for the sake of brevity. Fig. 3.20 presents such results. More specifically, in (a) the uncertainty intervals are shown and expressed in ppb for the three phases.

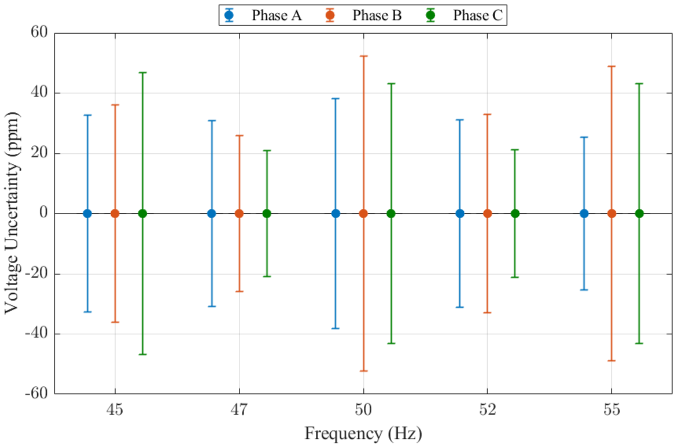

Figure 3.18: Results of the frequency sweep illustrating the uncertainty intervals of the voltage magnitude. The 95 % confidence intervals are shown as vertical bars (in ppm). The results of phase A are shown in blue, those of phase B in red, and phase C in green, as a function of the frequency expressed in Hz.

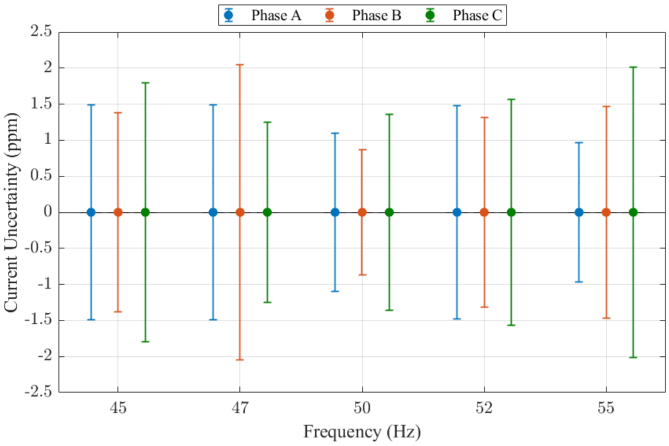

Figure 3.19: Results of the frequency sweep illustrating the uncertainty intervals of the current magnitude. The 95 % confidence intervals are shown as vertical bars (in ppm). The results of phase A are shown in blue, those of phase B in red, and phase C in green, as a function of the frequency expressed in Hz.

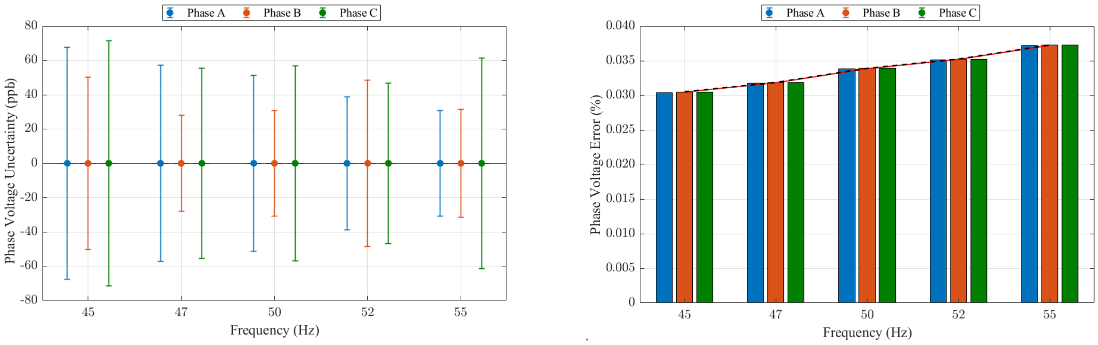

(a) (b)

Figure 3.20: Phase error of the voltage as a result of the frequency sweep. In (a) the uncertainty on the phase is expressed in ppb, instead (b) presents the errors as mean values in %. In addition, the black and red dotted line indicates a linear trend. All results of phase A are in blue, those of phase B in red, and phase C in green.

Noticeable variations can be observed among the three phases for a single frequency and for the same phase at different frequencies. On the other hand, in (b) the mean errors in the estimation of the phase voltage are expressed in %, rather than in ppm given their high values with respect to their corresponding uncertainty.
It can be clearly denoted how the three phases share comparable results, despite the varying uncertainty intervals. Additionally, it is worth noticing how such errors increase linearly with the frequency for all phases. As a matter of fact, a linear trend-line can be computed, having a coefficient of determination, or R^2, equal to 0.9952. Fig. 3.20(b) illustrates a dotted black and red trend-line in regard to the results of phase B shown in red in the same figure. Comparable trend lines can be determined for the other two phases but are omitted for the sake of clarity.
Nevertheless, it is worth recalling that such mean errors constitute a fixed offset which can be accordingly compensated once assessed, similarly to what was discussed for the generation stage presented in Section 3.4.

This concludes the analysis of the frequency sweep in regard to the acquisition stage of the PMU calibrator. In spite of being limited to a single excitation level for voltage and current signals, the presented results point out the variability of the uncertainty intervals across various phases and frequency ranges. This represents a preliminary analysis that could not only be further extended to the whole excitation range but also to more complex signals such as the steady-state and dynamic signals required by the PMU Std. In addition to the necessity of having an automatic fit of the generated values by means of the non-linear routine.

3.6 Time Synchronization Evaluation

This Section presents a comparison between four different time synchronization sources on a PMU calibrator, based on the paper presented at the IEEE International Symposium on Precision Clock Synchronization for Measurement, Control, and Communication (ISPCS) held in London, England in September 2023 [76].

In this analysis, the focus is only on the synchronization, namely on the internal time base and its alignment with respect to UTC. Based on its internal time base, usually comprising a 10 MHz clock, the calibrator defines the sampling frequency of

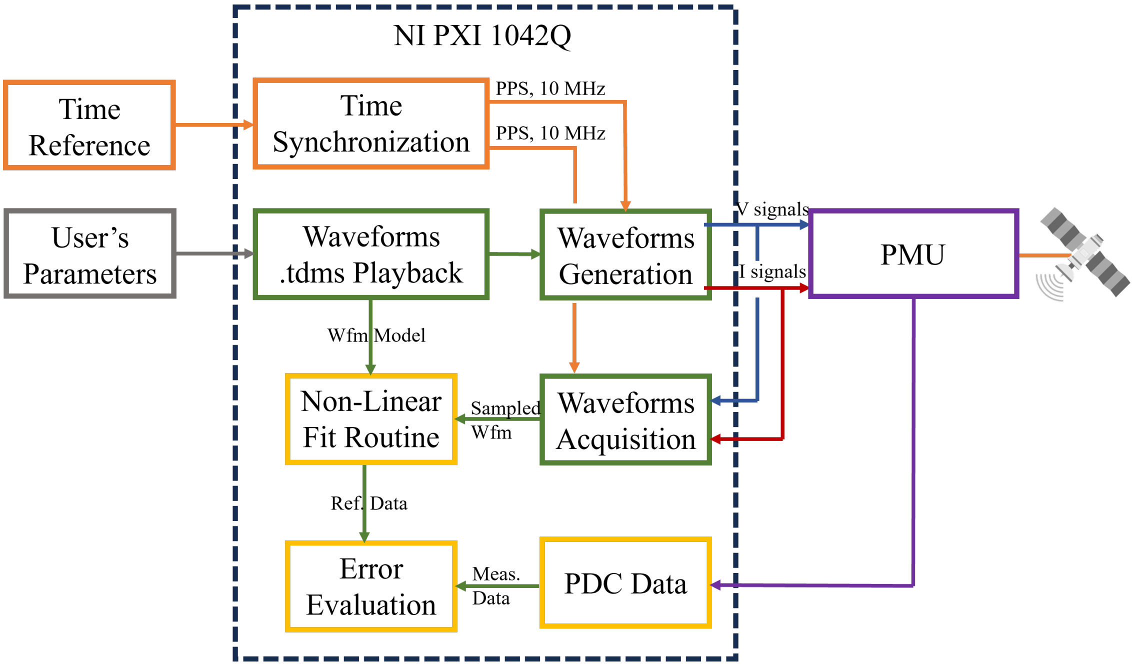
NI PXI 1042Q
Time Reference
Time Synchronization
PPS, 10 MHz
PPS, 10 MHz
User's Parameters
Waveforms .tdms Playback
Waveforms Generation
V signals
I signals
PMU
Wfm Model
Non-Linear Fit Routine
Sampled Wfm
Waveforms Acquisition
Ref. Data
Error Evaluation
Meas. Data
PDC Data

Figure 3.21: Complete block diagram of the fundamental steps and devices required in a PMU calibrator. While the generation and acquisition stages shown in green have been already presented in the previous Sections, in this part the focus is on the time synchronization blocks illustrated in orange.

the generated and re-acquired waveforms. In a similar way, trigger signals, generally consisting of a PPS, should be traceable and aligned to UTC. While the first aspect affects the accuracy of the reference frequency and phase angle value, the second may result in an erroneous comparison between the calibrator reference values and the time-stamped measurements of the device under test.
For the sake of completeness, Fig. 3.21 presents a block diagram of the PMU calibrator, comprising all its fundamental components already presented in the previous Section of this Chapter. The generation and acquisition stages have been thoroughly described and characterized in Sections 3.4 and 3.5, respectively. On the other hand, this Section focuses only on the time blocks illustrated in orange.

The objective entails the determination of how different time sources affect the performance of the PMU calibrator. Additionally, as this work has been developed at the Swiss NMI (METAS), a second aim consists of ensuring the traceability to the fundamental measurement unit, i.e., the physical realization of the second.

Section 3.6.1 illustrates the specifications on how the time synchronization is realized in the PMU calibrator. In addition, the testing conditions and the measurement setups are illustrated together with their main characteristics. Lastly, Section 3.6.2 presents the most significant results and proposes some future developments.

3.6.1 Testing Conditions

In addition to the hardware architecture presented in Section 3.2, this Section provides additional details concerning the time synchronization and its dissemination in the adopted setup. Moreover, the four tests performed to verify the effects of different time sources are thoroughly described as follows.

In a PMU calibrator, synchronization plays a crucial role, as generation and re-

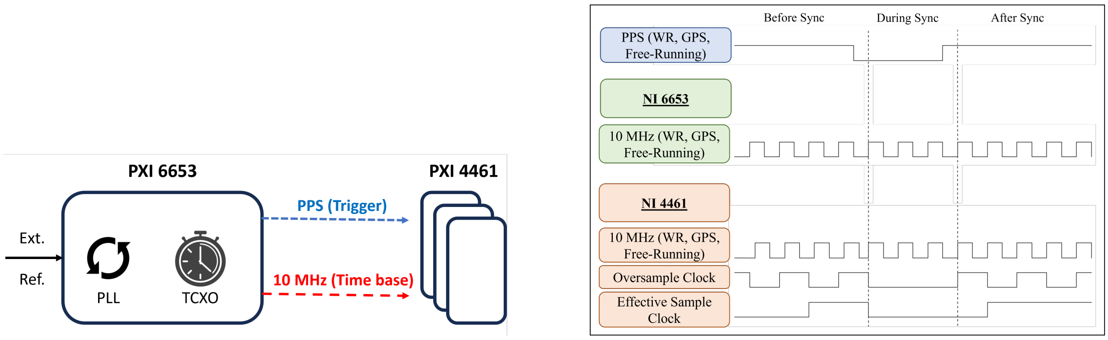
PXI 6653
PXI 4461
Ext.
Ref.
PLL
TCXO
PPS (Trigger)
10 MHz (Time base)
Before Sync
During Sync
After Sync
PPS (WR, GPS, Free-Running)
NI 6653
10 MHz (WR, GPS, Free-Running)
NI 4461
10 MHz (WR, GPS, Free-Running)
Oversample Clock
Effective Sample Clock

(a) (b)

Figure 3.22: Distribution of the time reference in the PMU calibrator showing in (a) how the NI 6653 board can be disciplined by an external reference. Then, it distributes the time information in terms of trigger signals and time-bases. In more detail, (b) presents the interaction between the NI 6653 and NI 4461 cards in terms of the 10 MHz time base and effective clock. Adapted from [76].

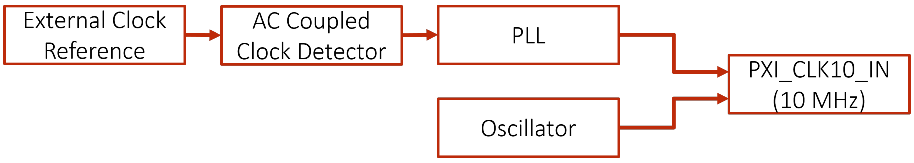
External Clock Reference
AC Coupled Clock Detector
PLL
Oscillator
PXI_CLK10_IN (10 MHz)

Figure 3.23: Block diagram of the basic working principle of the NI 6653 time module when a PLL is used to generate an equivalent 10 MHz time base from a generic external reference.

acquisition processes shall share the same time base and be synchronous. As a matter of fact, the 10 MHz time base affects the sampling frequency, hence the correct acquisition of the generation and re-acquisition of the signals. The PPS signal, instead, operates as a trigger and guarantees the alignment to UTC(CH). Therefore it impacts the starting of the acquisition, as an incorrect synchronization may result in an erroneous initial phase of the estimated synchrophasor. The test waveform generation shall be aligned to integer second transitions since the measurements of the PMU under test are typically time-stamped via GPS or similar synchronization protocols. Thus, to address these requirements, it is necessary to reference the PMU calibrator with a high-quality 10 MHz time base and a reference PPS signal.

In order to account for both, the PXI chassis of the PMU calibrator hosts two different modules: one NI 6653 timing and synchronization module, and three NI 4461 dynamic signal acquisition modules, as shown in Fig. 3.22(a).

The NI 6653 controls the three NI 4461 boards based on an external time reference. To do this, two different options are available: it is possible to either overwrite the time base or discipline it using a PLL and a temperature-compensated crystal oscillator (TCXO), which is an internal clock at 10 MHz.
In the latter, the external time reference is sent to a clock detector which locks to a PLL. This information is then used by the TCXO to generate an equivalent 10 MHz time base, as shown in Fig. 3.23. In spite of the limited benefits of this option, relying on such a general-purpose PLL allows to adopt any time reference (10 MHz, PPS, PTP, etc. ...) and generate an equivalent 10 MHz from it. Hence, it ensures the testing of a wider range of tests which would not be possible instead.

Having clarified the rationale behind such a choice for controlling the NI 4461 boards, it is then worth better analyzing the interaction between the latter and the NI 6653 board. The NI 4461 analog input/output modules are necessary to acquire and generate three-phase signals having a range of ±12 V. As discussed in Section 3.2, the analog input channels rely on a sigma-delta ADC with a 24-bit resolution which does not allow the direct control of the sampling since it generates independently its own sampling frequencies. As a matter of fact, it requires an oversampling and then filtering and consequent downsampling in order for the sampling frequency to be equal to 18 kSa/s which is the sampling rate at which the PMU calibrator works[4]. The sampling rate can be "controlled" by resetting the counter registers on the first rising edge, for instance, as shown in Fig. 3.22(b). In spite of the limited control possibilities on the sampling frequency, it is expected that it varies very little in this range. This assumption can be regarded as true since compliance tests according to the PMU Std generally last only a few seconds [14]. More in detail, Fig. 3.22(b) illustrates three stages: before, during, and after the synchronization, highlighting the role of the NI 6653 board on the three NI 4461 modules.

It is worth emphasizing that the NI 6653 module represents the only solution to distribute time among the other modules in the PXI. The skew of the output clock and trigger is guaranteed not to exceed 500 ps, while the delay between the external time reference and the equivalent 10 MHz time base is maximum ±1 ns.

For what regards the tests, four different testing configurations are considered and listed in the following:

- **Test A**: The PMU calibrator operates in free-running mode. More specifically, using this configuration it is possible to evaluate the 10 MHz time base produced by the PXI 6653 module itself.
- **Test B**: The reference clock is provided by a GPS receiver that disciplines the PXI 6653 time base.
- **Test C**: The internal time base of the PXI 6653 module is overridden by a cabled distribution of the 10 MHz directly derived from UTC(CH).
- **Test D**: The internal time base of the PXI 6653 module is overridden by a 10 MHz time-base produced by a WR ZEN - Time Provider. The WR ZEN is locked via a dedicated optical fiber to UTC(CH).

More in detail, Fig. 3.24 presents a block diagram of the configurations adopted in Test A and B, where the *External Clock Reference* block is highlighted in green. In this context, the latter is adapted based on the settings adopted in each test, i.e., no external clock is used in Test A while a GPS receiver is used in Test B.
Similarly, Fig. 3.25 illustrates the block diagram of the configurations used in Test C and D, which are both traceable to UTC(CH). In this scenario, conversely to Fig. 3.24, an extra stage is required to employ the traceable time reference in the NI 6653 card. While in Test C a cabled distribution of the 10 MHz clock is amplified, in Test D a WR is locked via an optic fiber cable.

---

[4] The 18 kSa/s frequency is normally considered as the PMU calibrator sampling frequency as it is an integer multiple of both 50 and 60 Hz signals.

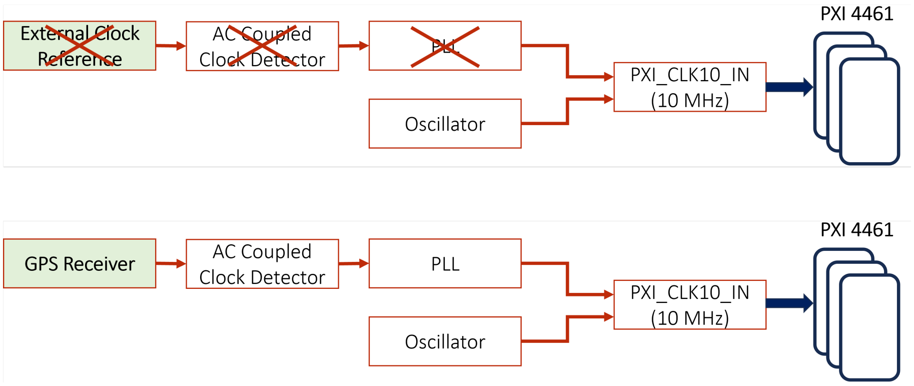
~~External Clock Reference~~
~~AC Coupled Clock Detector~~
~~PLL~~
Oscillator
PXI_CLK10_IN (10 MHz)
PXI 4461
GPS Receiver
AC Coupled Clock Detector
PLL
Oscillator
PXI_CLK10_IN (10 MHz)
PXI 4461

Figure 3.24: Block diagram of the basic working principle and settings adopted in Test A (upper) and B (lower), highlighting the specific external clock reference in the green-shaded block.

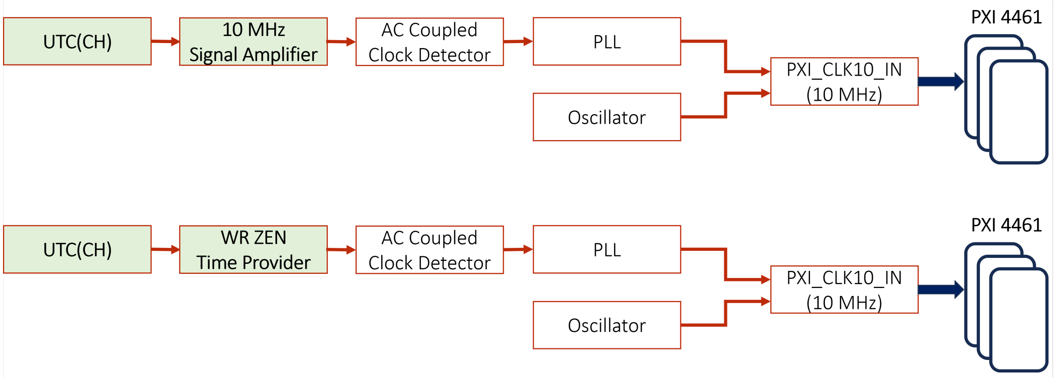
UTC(CH)
10 MHz Signal Amplifier
AC Coupled Clock Detector
PLL
Oscillator
PXI_CLK10_IN (10 MHz)
PXI 4461
UTC(CH)
WR ZEN Time Provider
AC Coupled Clock Detector
PLL
Oscillator
PXI_CLK10_IN (10 MHz)
PXI 4461

Figure 3.25: Block diagram of the basic working principle and settings adopted in Test C (upper) and D (lower), both traceable to UTC(CH), highlighting the specific external clock reference in the green-shaded block. An additional step is included to clarify the different settings between the two tests.

It is also worth noticing that both Fig. 3.24 and 3.25 are adapted from Fig. 3.23 for the sake of clarity and better comprehensibility.

While Tests A and B rely on time references that do not descend from a metrological realization of absolute time, Tests C and D are fully traceable to UTC(CH). Therefore, it is worth further clarifying this with the block scheme in Fig. 3.26 which illustrates the dissemination of time in METAS. In the blue area, the physical realization of the second using the Cesium fountain is carried out in the underground lab of METAS. From this, the PPS and the 10 MHz time base can be derived. Afterward, they are distributed to the other laboratories in METAS. On the right-hand side of Fig. 3.26, a 10 MHz signal is distributed via cable to the Electrical Power and Energy Laboratory where the PMU calibrator is located. However, in order to compensate for the attenuation caused by the long distance, a signal amplifier is required. This represents the configuration adopted for Test C.

Conversely, on the left-hand side of the same figure, the PPS and 10 MHz time base are locked to a WR Grandmaster. The latter is connected via an optic fiber to a WR Switch which has 18 ports, allowing for 17 other devices to be interfaced to it. At the Switch, two WR devices are connected: WR01 which is the device under test as it disciplines the PMU calibrator. Instead, WR02 is the reference device as it provides the UTC reference signal. The two WR devices are aligned with a skew lower than 400 ps considering a 95 % CI, obtained with a coverage factor equal to 2. This latter configuration describes in more detail the setup adopted for Test D.

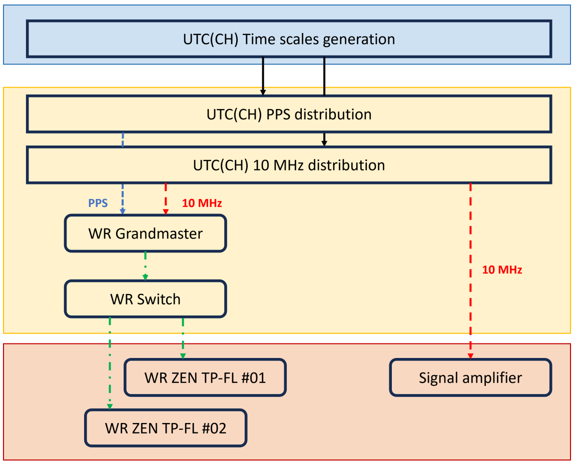
UTC(CH) Time scales generation
UTC(CH) PPS distribution
UTC(CH) 10 MHz distribution
PPS
10 MHz
WR Grandmaster
WR Switch
10 MHz
WR ZEN TP-FL #01
Signal amplifier
WR ZEN TP-FL #02

Figure 3.26: Dissemination of time reference in METAS, tracing back to the physical realization of the second. Blue, red, and yellow areas represent the realization, distribution, and final exploitation of the time itself, respectively. Blue and red arrows concern PPS and 10 MHz signals, respectively, while green ones account for fiber optic connections. Adapted from [76].

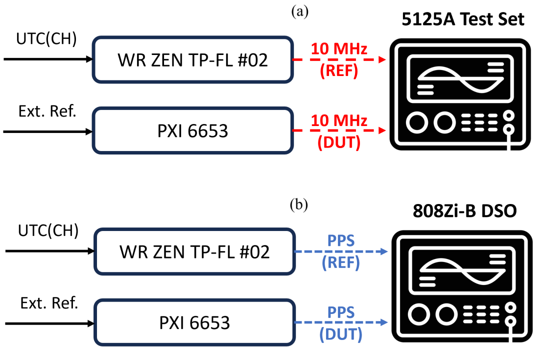
(a)
5125A Test Set
UTC(CH)
WR ZEN TP-FL #02
10 MHz
(REF)
Ext. Ref.
PXI 6653
10 MHz
(DUT)
(b)
808Zi-B DSO
UTC(CH)
WR ZEN TP-FL #02
PPS
(REF)
Ext. Ref.
PXI 6653
PPS
(DUT)

Figure 3.27: Block scheme illustrating the measurement setup employed for the phase noise in (a) and time skew assessment in (b). Source: [76].

However, it is worth highlighting that for both Tests C and D, WR02 is the reference device for phase noise and skew assessment. For both Tests, the red area shown in Fig. 3.26 indicates the final exploitation of the time.

In all four configurations, the PMU calibrator performance is characterized in terms of phase noise of the 10 MHz time base and time skew of the PPS signal in comparison to UTC(CH). For the sake of clarity, Fig. 3.27 shows the two measurement setups. As already disclosed, in both cases the reference is provided by WR02 indicated by the acronym *REF*, while the signal under test indicated as *DUT* is the output of the NI 6653 in the four settings.

In Fig. 3.27(a), the phase noise measurement is performed with a 5125A Phase Noise and Allan Deviation Test Set. For each configuration, the phase noise power spectral density is assessed between 100 mHz and 1 MHz. In Fig. 3.27(b), instead, the time skew measurement is evaluated by means of a Teledyne Lecroy Wavemaster 808Zi-B 8 GHz oscilloscope. On both scope channels, the occurrence of the PPS signal is detected in correspondence with a vertical positive front of the square wave. To optimize the accuracy of the measurement results, the oscilloscope time base is overridden by the 10 MHz output of the WR02.
For each test configuration, the statistical distribution of the PPS skew is examined with respect to UTC(CH). Additionally, to guarantee a statistically relevant sample,

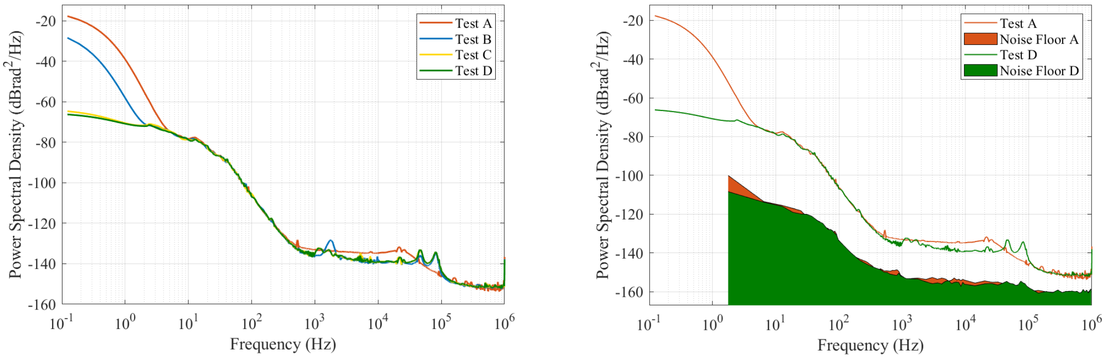

(a) (b)

Figure 3.28: In (a), the power spectral density of the phase noise is shown as a function of the frequency of the 10 MHz time base supplied to the PMU calibrator in Tests A, B, C, and D. In addition, (b) illustrates the noise floor (filled area) only for Tests A and D. Source: [76].

measurements are performed for two entire consecutive days, corresponding to over 150 thousand PPS transitions for each test configuration.

3.6.2 Results Analysis

This Section illustrates the most significant results obtained for the four different configurations described in the previous Section. First of all, the outcomes of the phase noise for what concerns the 10 MHz time base are analyzed as follows.

Fig. 3.28(a) shows the power spectral density of the phase noise for Tests A to D as a function of the frequency. At a glance, it can be observed an improvement from Test A to D as expected owing to the improved external time reference.
Test A represents a benchmark as its results account for the internal behavior of the PXI itself. The contribution of the GPS shown in the results of Test B provides an improvement of 10 dB in the low-frequency domain, i.e., up to 10 Hz. As foreseen, an even more noticeable improvement can be assessed when the PXI is disciplined by a 10 MHz derived from UTC(CH) in Test C and D. However, such improvement is not as evident as expected since a plateau can be noticed at high frequencies. This is most likely caused by the PXI structure, more precisely by the PLL inside, which tends to limit the performance of the 10 MHz. As a matter of fact, a better distinction was expected between the four tests, rather than a convergence mostly in the range comprised between 10 and 1000 Hz.
For the sake of clarity, in the following, only the results obtained in Test A and D are analyzed since they can be considered as the worst and the best-case scenarios. For this reason, Fig. 3.28(b) presents the power spectral density of Test A and D, together with their corresponding noise floor limited in frequency at 2 Hz, due to the instrument sampling rate. The noise floor quantifies the internal noise bias of the 5125A Test Set and establishes a sort of resolution limit on the current measurement. These results indicate that the noise floor is well below the phase noise, hence it ensures the accuracy of the measurement result.

The following analysis, instead, concerns the results of the PPS skew with respect to UTC(CH). Based on the same rationale used for presenting the phase noise results, Fig. 3.29 shows only the statistical distributions obtained from Test A and D.

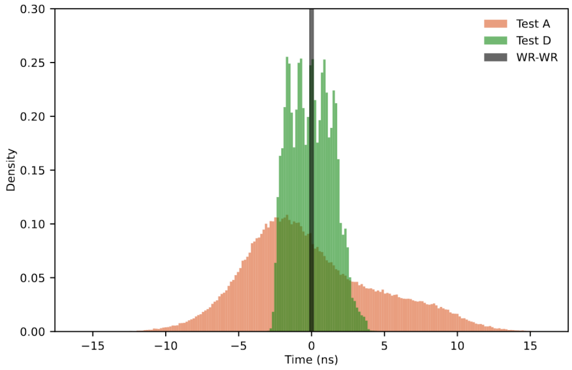

Figure 3.29: Statistical distribution of the PPS skew measurements with respect to UTC(CH) assessed in Tests A and D. The black vertical bar represents the variability between WR01 (the device under test) and WR02 (the reference one). Source: [76].

However, additionally to this, a third test case is considered. It is shown as a black vertical bar and its purpose entails the observation of the time skews of the two PPS generated by the comparison between WR01 and WR02.
Concerning this last test, it can be concluded that they coincide, apart from their uncertainty which is less than 400 ps for a 95 % CI, obtained by selecting $k = 2$.
Whereas, regarding Test A and D, a more evident improvement in terms of range can be noticed in comparison to the phase noise results of Fig. 3.28. The distribution of Test A, shown in red, is asymmetric as it ranges from -10 to $+15$ ns, and resembles a combination of two or more Gaussians. Hence, it depends on the drifting itself.
The histogram obtained for Test D, instead, is comparable to a uniform distribution mostly centered around 0. The skew between the WR switch and the UTC(CH) PPS is in the sub-ns range. In this sense, it can be concluded that the two are perfectly locked and its contribution to the skew of the PMU calibrator PPS is negligible. The spikes that can be noted across the entire range depend on the quantization of the PXI which is equal to 1 ns. However, as previously disclosed, they are unavoidable since the NI 6653 board represents the only way to distribute time in the PXI-based PMU calibrator. From these results, the Allan deviation can be evaluated for the three configurations under test, as it is commonly used to assess the stability and the accuracy of clock sources.

The Allan deviation computed for Test A, D, and the WR to WR comparison is shown in Fig. 3.30 in red, green, and black, respectively.
Concerning the latter, it can be observed that it is in the order of 10^{-17} which means that it is mostly related to numerical noise.
On the other hand, the improvement between Test A and D is evident, especially for long time periods greater than 10^2 s. However, it is worth recalling that compliance tests performed in the PMU calibrator generally last a few seconds. Therefore, comparing Test A and D results in the range up to 10^1, it can be noticed how they almost match perfectly. This represents a drawback in the application of a higher-performing time reference: the improvements are not as distinguishable as expected in the effective utilization range.

As a last evaluation, Fig. 3.31 presents the evolution in the time domain of the PPS skew measurements over an interval of 4 hours. The results of the WR comparison are consistent with the previous outcomes shown in Fig. 3.30. As a matter of fact, noise is observed in an interval comprised within 100 ps, which represents a negligi-

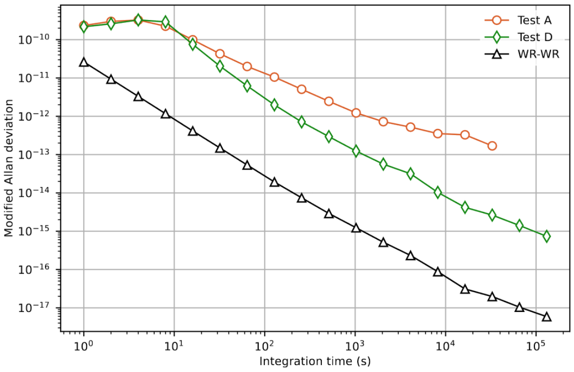

Figure 3.30: Allan deviation of the PPS skew measurements with respect to UTC(CH) in Tests A and D. The black line indicates the results of the WR against WR comparison. Source: [76].

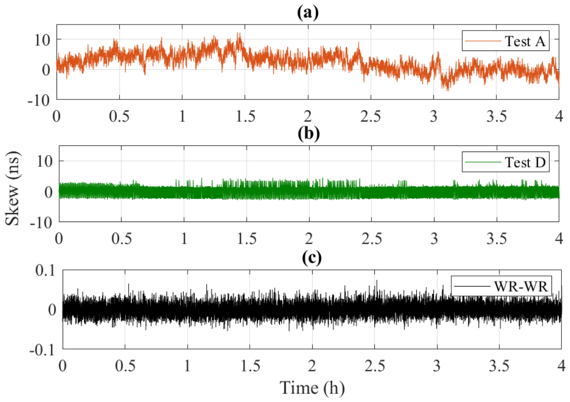

Figure 3.31: PPS skew measurements in the time domain assessed for Test A in (a), Test D in (b), and for the WR to WR comparison in (c). Source: [76].

ble skew with respect to UTC(CH).

Test A, instead, is clearly the least stable among the three. Variations are even exceeding 10 ns and are strongly fluctuating over time. Since no specific pattern is followed, a random-walk model could be used to replicate it. Lastly, for what concerns Test D, it can be concluded that it is rather stable in time and its oscillations are within 5 ns. To replicate them, a uniform distribution could exploited.

The presented results have an evident impact on the PMU calibrator. In terms of spectral purity of the generated test waveforms, Tests C and D promise a significant reduction of the phase noise, particularly in the frequency range up to 10 Hz. However, such performance enhancement is currently limited by the PLL of the PMU calibrator itself. Indeed, apart from very low frequencies, the phase noise power spectral density is nearly independent of the external reference. On the other hand, the disciplining of the calibrator reference clock with higher-quality references not only allows for improving the stability of the internal trigger but also ensures its alignment with respect to UTC(CH) and its direct traceability. It is particularly interesting to notice how the uncertainty decreases from nearly 15 to 3 ns. Nevertheless, such contributions can be considered negligible with respect to the delays introduced by the analog front end of the PMU under test. Hence, they represent a valid benchmark for the traceability of the PMU calibrator.

Further developments of this work could consist in the characterization of the PLL behavior or in the override of the internal clock of the NI 6653 module. Additionally, it could be worth replacing the three NI 4461 with digital signal acquisition modules that could allow direct control of the sampling rate to an external reference.

3.7 Discussion

The ever-increasing performances of PMUs are prompting the necessity of developing suitable calibration infrastructures. For this reason, in this Chapter, both the software and the hardware architecture of a PMU calibrator are analyzed. More emphasis is given to the realization of the test signals according to the PMU Std and to the illustration of the main components of the calibrator.

In addition to this, a particular focus is given to the analysis of the stability of its generation and acquisition stages, as the assessment of their characteristics is required for each application. Based on this, magnitude and frequency sweeps are carried out in order to span across the entire range of operation of PMUs.

The last part of this Chapter is dedicated to the estimation of the calibrator infrastructure in terms of time synchronization. In order to do that, different time sources are considered and accordingly tested to assess the impact on both phase uncertainty and traceability of the reference values. As a matter of fact, the overall aim of this Chapter entailed the evaluation and the prospective improvement of the different stages of a typical PMU calibrator.

Chapter 4

Uncertainty Contributions and PMUs' Reliability in Distribution and Transmission Power Systems

This Chapter illustrates the applications in distribution and transmission power systems relative to Phasor Measurement Units (PMUs) which have been developed in the Thesis. The Chapter provides a first introduction to the state-of-the-art of PMUs, detailing the adopted estimation algorithms and the reliability index. Afterward, the latter is applied both at MV and at HV levels in order to assess the trustworthiness of PMU measurements in case of real-world contingencies. The next part of the Chapter is dedicated to the role of uncertainties in typical MV and at HV applications. The first is related to a typical MV measurement chain, while the second refers to the frequency uncertainty requirements for the resynchronization of Continental Europe synchronous areas, after a power system split. The rationale behind these is to provide some useful insights and guidelines for DSOs and TSOs.

4.1 Introduction and State-of-the-Art

As pointed out in the previous Chapters, the ever-increasing installation of RES at various levels of power systems is prompting the necessity of developing a distributed measurement infrastructure. In the latest years, PMUs proved to be particularly useful in this context as they can allow the aggregation and comparison of their data acquired at different power system nodes based on their time stamps [36].

Besides the various applications for which PMUs can be used, detailed in Section 2.1, these devices are also being used in power systems that are ever more characterized by power electronic components. In addition to CIG, there exist an increasing number of High Voltage Direct Current (HVDC) links and Flexible Alternating Current Transmission System (FACTS) devices [84–86]. Additionally, the installation of RES also at HV transmission levels is making transmission power grids much less resilient than they inherently used to be. It is worth recalling the latest famous South Australia and the Arizona-Southern California blackouts that occurred in 2016 and 2011, respectively [11, 12].

To this purpose, it is ever more relevant to assess the power quality and the reliability of PMU measurements in renewable-based power systems. For this reason, Section 4.2 evaluates the reliability of PMU measurements by means of an index, as the nRMSE. Two real-world HV scenarios are studied: the first one entails the South Australia blackout, while the second involves a modified version of the IEEE 39-bus power system, including the presence of RES at the transmission level [87]. It must be noted that, in spite of the strong presence of RES, this Section does not aim either at evaluating the power system inertia or at correlating such measurements with a reduction of inertia. This part is studied in Chapter 5 and applied in Chapter 6, specifically in Section 6.4 for what concerns the application of nRMSE [88].

In this scenario, it must be also highlighted that the PMU Std has been originally envisioned for traditional transmission networks that are generally characterized by long lines, and stable conditions owing to their meshed structures. However, lately, PMUs have started being deployed by DSOs at the distribution level. Such MV power systems are quite different from HV ones: they are constituted by shorter lines, characterized by higher R/X ratios, especially for urban cable lines. Consequently, PMUs shall be capable of measuring lower phase angles and frequency differences among the different nodes [28, 89, 90]. However, the overall uncertainty of the PMU-based measurement chain does not depend only on the PMU itself, but rather it is a combination of all the uncertainties introduced by the components present in the measurement chain. To this purpose, the objective of Section 4.3 is to evaluate a realistic CI of typical MV PMU-based measurement chains [91].

Lastly, it is worth noticing that not only are PMUs used in a pre-contingency stage characterized by steady-state conditions, but they are also employed in the gradual reconnection of loads and portions of the power system during its restoration [92, 93]. Similarly to load reconnection after Under-Frequency Load Shedding (UFLS) operations, comparing PMU measurements in different areas allows for identifying the most suitable time instant to perform power system maneuvers, such as areas reconnection [94, 95]. However, there are no current works published in the literature that present the impact of the uncertainty of frequency measurements during severe power system conditions, such as resynchronization after a power system split. Additionally, for what concerns the regulatory framework proposed by the European Network of Transmission System Operators for Electricity (ENTSO-E), some aspects still need to be tackled. Based on these considerations, this topic is studied by analyzing two power system events, presented in Section 4.4. They occurred in Croatia and in France in 2021, both resulting in the splitting of Continental Europe (CE) into two separate synchronous areas [96, 97]. The objective of this part does not involve either the re-definition or challenges ENTSO-E policies. It rather proposes to evaluate the impact of estimation uncertainty in the frequency estimates, to ensure a secure resynchronization which is yet to be fully investigated [98].

Before presenting the main outcomes of such research, Section 4.1.1 illustrates the three main synchrophasor estimation algorithms used for PMUs, presenting their main features as well as pros and cons. These algorithms are also going to be used in inertia-related applications in Chapter 6. Section 4.1.2, instead, is intended to illustrate the nRMSE before its application in this Chapter. In the following, the main results presented in papers [91, 98, 99] are detailed and discussed.

4.1.1 Examined Synchrophasor Estimation Algorithms

The previous Section 2.2.3 presented an overview of the most common PMU algorithms, while this Section focuses only on the three routines that have been chosen for the various applications.

They are taken from the recent literature on synchrophasor estimation and are representative of both P- and M-class of the PMU Std [14][1]. Their main characteristics and the rationale behind their choices are thoroughly explained in this Section. In particular, the routines considered are the PMU Std reference algorithm for P-class [14], the CS-TFM [53], and the i-IpDFT [49]. The last two have been utilized in P- and M-class configurations, as they are compliant with both classes of the PMU Std, contrary to the PMU Std reference algorithm [14].

For the sake of simplicity, these three algorithms which are going to be used in Chapter 4 and 6 are referred to as follows:

- **PMU A**: PMU Std reference algorithm, only P-class configuration is available as illustrated in the PMU Std.
- **PMU B**: CS-TFM algorithm, both P- or M-class configurations are available. The M-class version of the CS-TFM is referred to as PMU D.
- **PMU C**: i-IpDFT algorithm, both P- or M-class configurations are available. Similarly to PMU B, the M-class version of the i-IpDFT-based PMU is referred to as PMU E.

It is worth emphasizing that the goal of this Thesis involves neither developing nor improving a specific PMU estimation algorithm, but rather it aims at assessing the performance of different routines that are compliant with the PMU Std and which constitute already well-established routines, proven to be particularly effective in specific power system conditions.

For the sake of clarity, in the following a brief description of the three selected PMU models is provided, highlighting their main advantages and disadvantages.

PMU A: its algorithm is inspired by the one presented in PMU Std reference algorithm for P-class and it relies on a three-nominal cycles sliding window. The filter consists of a triangular-weighted Finite Impulse Response (FIR) filter whose pass bandwidth is centered around the power system rated frequency and it covers the expected variation range of the fundamental frequency (e.g., from 47 to 52 Hz for a 50 Hz power system, according to [21]).

PMU A relies on a static signal model, meaning that its model parameters are the magnitude and phase of the phasor associated with the fundamental component. The frequency and ROCOF are estimated as finite difference derivatives of the phase estimates, considering values before and after the reporting time instant. However, in this way, they are always delayed by one sample with respect to the corresponding phasor. The main advantage of PMU A lies in its low complexity, resulting in a straightforward implementation in industrial controllers. Nevertheless, the hypothesis of stationary signals is hardly ever verified, especially in modern power systems which are strongly characterized by fast dynamics. This follows that the estimates of PMU A tend to show a smoother and slightly delayed trend with respect to the instantaneous value.

---

[1] As a matter of fact, the M-class of the PMU presented in the Standard can be seen only as a different configuration of the P-class, since actually just the filter changes. However, for the sake of clarity, P- and M- configurations are specified for each model under test.

PMU B: it is based on [53] that consists of an optimized formulation of [100] in which the algorithm has been upgraded for the optimal deployment in industrial controllers. In this model, not only is it possible to compute the phasor associated with a given frequency but also its first- and second-order Taylor expansion terms can be evaluated, corresponding to the frequency and ROCOF, respectively. Consequently, in contrast to PMU A which has just two parameters, PMU B has six: the phasor magnitude and its corresponding phase plus their first- and second-order time derivative as computed in the reporting time instant.

In this context, it is worth highlighting a first advantage in comparison to PMU A: the instantaneous frequency and ROCOF can be directly computed, without any filtering effect or delay introduced by finite differences. Other advantages result from a direct consequence of the adoption of a dynamic model: as a matter of fact, Taylor Fourier Transform (TFT)-based approaches include higher-order derivative terms which are particularly beneficial in the case of non-stationary conditions. On the other hand, it has been demonstrated that prior knowledge of the frequency of the most significant components is required, to prevent the TFT from suffering from uncompensated spectral leakage and, hence, inaccurate estimates [74].

Taking as a reference the PMU Std requirements, it has been already evaluated that the CS-TFM shows a worst-case response of 56.4 ms in the presence of amplitude and phase steps, and worst-case frequency and ROCOF errors equal to 3.88 mHz and 189 mHz/s. respectively, for what concerns the harmonic distortion test.

PMU C: it is derived from the Iterative Interpolated Discrete Fourier Transform (i-IpDFT) algorithm. This algorithm adopts an iterative routine whose target is to minimize both long- and short-range spectral leakage: the first one is due to the decaying lobes of the non-zero negative image component, while the latter is produced by the interference of close components, e.g., harmonics and inter-harmonics. As in [49], the i-IpDFT is compliant with both P- and M-class requirements.

As for the other DFT-based approach, the i-IpDFT relies on a static signal model and it has three parameters: the magnitude, phase, and frequency of the fundamental component. The ROCOF, instead, is computed as a finite difference between two subsequent frequency estimates. The i-IpDFT presents excellent performances in quasi-stationary conditions, owing to its static model which provides the best stationary approximation of the signal in the observation interval. On the contrary, i-IpDFT shows a significant performance degradation in dynamic conditions.

In order to achieve the M- configurations of PMU B and C, indicated by letters D and E, respectively, the observation interval is enlarged from three to five cycles of the nominal power system frequency, while the other parameters are unaltered. The longer observation interval results in a finer spectral resolution (from 16.6 to 10 Hz for 50 Hz signals and from 20 to 12 Hz for 60 Hz signals)[2].

---

[2] The frequency spectral resolution is computed as the reciprocal of the windowing period.

This is reflected in the performance of PMU B which shows a more effective rejection of spurious injections, whereas for PMU C a finer resolution corresponds to a larger separation between the DFT bins, resulting in a faster time to converge.

4.1.2 nRMSE Definition

In order to assess the reliability of PMUs measurements, a reliability index already presented in the literature is considered [101, 102]. For the sake of completeness, this Section presents the most relevant key concepts of nRMSE, as well as the steps needed for its application, jointly with its main advantages.

First of all, in power systems theory, a generic voltage or current signal can be represented considering the following non-linear dynamic model:

$$x(t) = A \cdot (1 + \varepsilon_A(t)) \cdot \cos\left(2\pi f t + \varphi + \varepsilon_\varphi(t)\right) \tag{4.1}$$

where A, f, and φ represent the amplitude, the frequency, and the initial phase of the fundamental component of the signal $x(t)$, respectively. Instead ε_A and ε_φ account for the amplitude and the phase dynamics with sinusoidal, linear, or quadratic trends varying with the time variable t, respectively.

In a real-world scenario, it is reasonable to assume that the signal at the PMU terminals consists of these three components:

$$y(t) = x(t) + \eta(t) + \xi(t) \tag{4.2}$$

where η represents the harmonic and inter-harmonic terms (i.e., the narrow-band terms), while ξ accounts for the wide-band contributions, such as uncorrelated Gaussian noise, decaying DC trends, or transients[3].

At first, the PMU acquires the input signal at a constant sampling rate f_s, expressed in Sa/s or Hz, which is locked to the UTC time reference, as follows:

$$y[n] = y(t = nT_s) \tag{4.3}$$

where $n = 0, ..., N_s$ represents the sample series having N_s as the total length. Instead, $T_s = f_s^{-1}$ is the sampling period, in s.

For each sample n of the series, the PMU produces an estimate, indicated by a ˆ hereinafter, of the phasor ($\hat{p}$), frequency ($\hat{f}$), and ROCOF ($\hat{R}_f$) associated with the

---

The latter is evaluated as 3 or 5 times, respectively for P- and M-class PMUs, the nominal power system rated period which is equal to 20 ms and 16.6 ms for 50 and 60 Hz power systems, respectively.

[3] Despite that a clear distinction can be made in theory, in practical cases there will always be ambiguity in discerning the different terms.

fundamental component. The three quantities can be evaluated following this set of equations as in Eq. (4.4):

$$\begin{aligned} \hat{f}(t) &= \frac{d\hat{\varphi}(t)}{dt} \\ \hat{R}_f(t) &= \frac{d^2\hat{\varphi}(t)}{dt^2} \\ \hat{p} = \hat{A} \cdot \exp&\Big\{j \cdot \Big[2\pi \left(\hat{f} - f_0\right) t\Big] + \hat{\varphi}\Big\} \end{aligned} \tag{4.4}$$

in which f_0 indicates the power system rated frequency, which is either 50 or 60 Hz, and it is specified for each application, presented in the following Sections.

Among the several online metrics for the assessment of reliability, Normalized Root Mean Square Error (nRMSE) is the one that has been utilized in the following[4]. The rationale behind such a choice relies on the fact that nRMSE presents a particularly easy implementation and a low computational burden. However, similar results can be achieved using other metrics such as the Goodness of Fit (GoF).
It is worth clarifying that, despite other metrics being available and well-established in the scientific literature, the objective of this Section does not entail the comparison of such a metric with others. It rather focuses on a deeper study and specific application of nRMSE in different power system operating scenarios.

Based on the PMU estimates shown in Eq. (4.4), it is possible to reconstruct the equivalent time-domain trend of the input signal as:

$$\hat{y}[n] = \hat{A} \cdot \cos\left(2\pi \hat{f} n T_s + \hat{\varphi} + \pi \hat{R}_f \left(nT_s\right)^2\right) \tag{4.5}$$

The nRMSE is defined as the squared root of the squared difference between the reconstructed and the acquired samples, i.e., the residuals, of the signal:

$$nRMSE = \frac{\sqrt{\sum_n \left(\hat{y}[n] - y[n]\right)^2}}{N_s} \tag{4.6}$$

where the normalization for the total sample length N_s allows for an unbiased comparison between PMUs having different window lengths.

Based on these considerations, it can be stated that nRMSE is a definition of the discrepancy between the sample series acquired by the PMU before data processing and its reconstructed phasor representation. In this way, nRMSE indicates the signal energy that has been neglected, i.e., owing to the inconsistencies between the phasor model and the sample series.

---

[4] In this Thesis, the term *reliability* is to be intended with a *trustworthiness* accent. Hereinafter, *reliability* is indeed used to indicate the dependability of measurements in various conditions, rather than the reliability of equipment from a statistical point of view which is the usual definition of the term. For this specific reason, the two can be regarded as synonyms in the remainder of this work.

In this context, it is also important to underline the major differences that run between the two alternative metrics of PMU measurement reliability: TVE and nRMSE. On one hand, the TVE is a single-point value that accounts for the actual estimation errors but cannot be computed online as it requires an a priori knowledge of the reference values, e.g., during a calibration stage. On the other hand, the nRMSE quantifies the energy neglected by the phasor representation static formulation, hence it can be evaluated continuously at any time.

Among its advantages, it is worth underlying that, since nRMSE is defined in the time domain, it does not introduce any prior assumptions on the PMU model. Moreover, as previously anticipated, the computation of the nRMSE does not require any prior knowledge of the reference values, such as the TVE, FE, or RFE that would make any in-field applications impossible. Additionally, it can be easily integrated into many window-based PMU algorithms, as the sample time series $y[n]$ is already available inside the PMU, just after the data acquisition stage. As aforementioned, the nRMSE takes into account any contribution that is not mapped in the model of estimated synchrophasor at the fundamental frequency. It is worth mentioning, for instance, the measurement noise and other narrow-band interferences (e.g., harmonics) which are present only in the time series, but they are not mapped in the reconstructed phasor. Other significant discrepancies can be assessed, for instance, during transient events in which the definition of the synchrophasor cannot be regarded as true anymore. In this way, nRMSE accounts for the so-called *definitional uncertainty*, meaning that it can estimate the inconsistencies between the synchrophasor model as defined in Eq. (4.2) and the acquired signal as in Eq. (4.5)[5]. Lastly, from an operative perspective, it is interesting to observe that the nRMSE has a limited impact on the overall computational complexity. Previous applications on real-time processors have proved how its computation time is nearly two orders of magnitude lower than the PMU estimation itself. Hence, it is reasonable to consider it a negligible contribution to the overall reporting latency [99, 101, 102].

In light of the above, it is clear such a reliability index can be beneficial in the analysis of particular power system scenarios. For this purpose, the next Section of this Chapter 4 presents an application of that in the latency identification of transients and contingencies, as a function of the PMU reporting rate. In Chapter 6, instead, nRMSE is applied to low-inertia power systems in order to both aggregate power system regions based on their values. Additionally, the aim involves retrieving a relation between loss of inertia and reliability of PMU measurements, once again based on the obtained values of nRMSE.

---

[5] It is worth noting that the definitional uncertainty could also be included in the model used to estimate synchrophasor, frequency and ROCOF. Hence, according to this hypothesis, in case there was a disturbance already included in the model, theoretically it would not add any definitional uncertainty. However, the nRMSE is likely to be related to the definitional uncertainty. Therefore, there could be errors in the signal model that increase the nRMSE but do not result in estimation errors, owing to orthogonality to each other. Based on this rationale and without loss of generality, the nRMSE is not modified to account for any disturbance hereinafter.

4.2 Application of nRMSE for Contingencies Detection

This Section presents an application of the described reliability index, nRMSE, in the detection of contingencies based on the paper presented at 25th IMEKO TC4 Symposium "Measurement of Electrical Quantities" held in Brescia, Italy in 2022, for which I was awarded a Best Paper Award [99]. Two real-world scenarios are considered: the first one relies on the South Australian blackout, while the second one is based on one of the most notorious IEEE benchmark grids, which is the IEEE 39-bus transmission system [12, 103].

The objective consists of evaluating the reliability of PMU-based measurements and the sensitivity of nRMSE in real-world scenarios. The effects of the PMU reporting rate in the identification of contingencies is assessed and possible amendments to the PMU Std are finally suggested.

The two real-world scenarios together with the description of the PMU model are detailed in Section 4.2.1, while the results are discussed in Section 4.2.2.

4.2.1 Real-World Scenarios

PMU Model: the computation of the nRMSE is strongly dependant on the PMU estimation algorithm. For this reason, in this application, PMU B is utilized. As presented in Section 4.1.1, PMU B is based on a dynamic algorithm which makes it particularly suitable in challenging power system conditions, besides being compliant with both P- and M-classes. More specifically, for this application, only the P-class configuration is used since this application entails a contingency, hence a protection application, rather than a metrology one. The sampling rate f_s is equal to 18 kSa/s and the observation window spans over three cycles of the nominal power system frequency.[6] The latter corresponds to 50 or 60 ms for the test scenarios having a 50 or a 60 Hz rated power system frequency, respectively. Four different reporting rates R_r are used spanning from the minimum up to the maximum ones allowed in the PMU Std, i.e., $R_r = 10$ fps is considered as the lowest value, while $R_r = 100$ fps or $R_r = 120$ fps is the highest for 50 or 60 Hz power systems, respectively [14].

Scenario I: as a first case, the well-known South Australia blackout that occurred on September 28th, 2016 is examined [12]. Before the contingency, most of the generating power was based on RES, specifically wind power. This is a typical operating condition for the South Australian power system, as illustrated in the Introduction. However, owing to extreme weather conditions, three transmission

---

[6] This sampling rate value is an integer multiple of both 50 and 60 Hz, i.e. the possible values of nominal frequency for all the considered test cases in Chapters 4 and 6. In the following, when omitted, it is implicitly assumed $f_s = 18$ kSa/s.

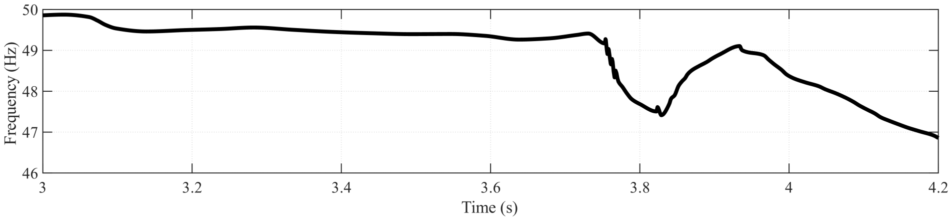

Figure 4.1: Portion of the frequency profile recorded during the South Australia blackout on September 28th, 2016. The contingency occurs at $t = 3.75$ s. Source: [12, 99].

lines tripped and initiated a sequence of cascaded faults. Consequently, the South Australia region was suddenly separated from the rest of the transmission system and the frequency started collapsing with an average ROCOF of -6.25 Hz/s. In less than 1 s, the remaining generation facilities tripped causing the blackout of the entire region. In this first scenario, a signal portion of 1.2 s is studied, where the contingency starts at $t = 3.75$ s, as shown in Fig. 4.1.

Scenario II: the second scenario is based on a modified version of the IEEE 39-bus system, which is representative of the New England power system. It comprises 10 synchronous machines and its initial conditions can be found in [103].

As discussed in [87], the modified version of the power system consists of the replacement of four synchronous generators by wind turbines having equivalent rated power, but characterized by a null contribution to the overall power system inertia. Moreover, the traditional static loads have been replaced by dynamic models which can represent in a more realistic manner load frequency and voltage responses [104]. Additionally, an Under-Frequency Load Shedding (UFLS) routine is implemented in each bus, based on PMU and ROCOF measurements.
The complete power system model, together with the PMUs and UFLS routine, have been developed in MATLAB/Simulink environment and then implemented in OPAL real-time simulator.

In this scenario, several generators are tripped resulting in an overall loss of power of 1.5 GW. The test waveforms consist of 2.0 s: the generators are tripped at $t = 0.15$ s, producing damped oscillations lasting for nearly 0.6 s before the UFLS scheme takes place around $t = 0.8$ s. The latter initializes a second transient condition before reaching a new steady-state operation. In this way, it is possible to investigate the nRMSE evolution in three different operating conditions.

It is particularly relevant to notice that, despite the fact that both scenarios are characterized by a stronger or weaker presence of RES, this application is not illustrated in Chapter 6. The motivation lies on the fact that nRMSE is used neither for the assessment of the impact of CIG nor for the gathering of local measurements based on the nRMSE. Conversely, the latency in the detection of real-world power system contingencies is evaluated, as a function of the PMU reporting rate.

4.2.2 Results Assessment

Scenario I: The results of the first real-world scenario are shown in Fig. 4.2. The latter presents in the upper graph the frequency profile recorded during the South Australia blackout, whereas, in the bottom part, the nRMSE is computed for four different reporting rates using PMU B: $R_r = 10, 25, 50, 100$ frames per seconds (fps).

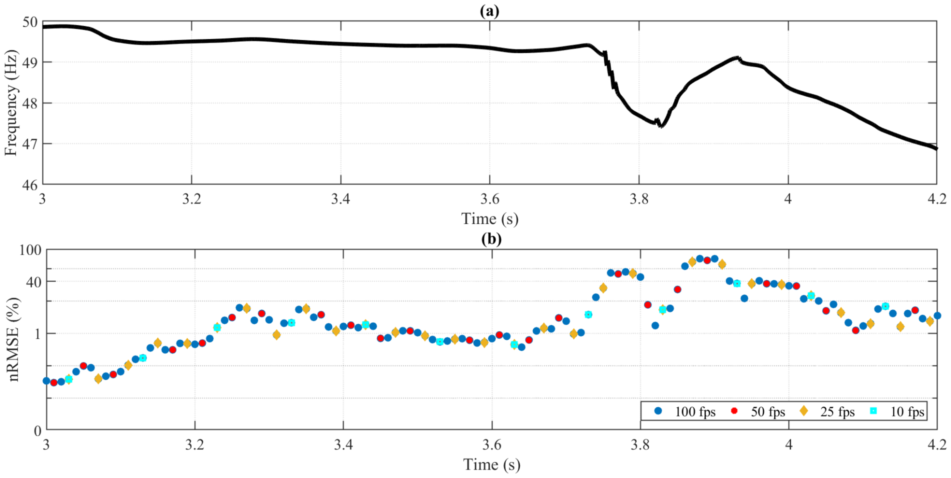

Figure 4.2: Results of the real-world scenario I: **(a)** Portion of the frequency profile recorded during the South Australia blackout on September 28th, 2016. **(b)** nRMSE expressed in % and computed using PMU B in P-class configuration for four different reporting rates R_r. Source: [12, 99].

As depicted in Fig. 4.2, lower values of R_r do not necessarily affect the numerical computation of the nRMSE. Nevertheless, the delay is inversely proportional to R_r: the higher R_r, the faster the detection of a transient condition which can be promptly assessed in order to take suitable counter-measures. When PMU B is used with low values of R_r, it can be barely noticed something erroneous in the measurements' reliability: only after 55 ms an increase in the nRMSE is observed. Whereas, high values of R_r can easily track the frequency drop with a detection time in the order of a few ms. Nonetheless, this contingency is particularly severe for the power system since in less than 1 s the system was in a blackout condition. Hence, a prompter detection could surely help but it does not guarantee the restoration of the system operation [12]. In this specific case, the definitional uncertainty is caused by the assumptions that the phasor magnitude is constant and its phase is parabolic.

Scenario II: Before presenting the nRMSE results, it is worth assessing power and voltage variations, as well as the ROCOF, that are measured during the entire sequence of events. Voltage and active power variations, respectively indicated with ΔV and ΔP, are computed as a finite difference of subsequent measurements. They are shown in Fig. 4.3 in blue and in red, respectively, and they are expressed in per-unit values in order to ensure an easier comparison. It can be clearly distinguished that the generators trip at $t = 0.15$ s, resulting in an immediate voltage variation, but a rather slower power one. The damped oscillations last until $t = 0.8$ s when the UFLS scheme is triggered. This time instant corresponds to a new strong ΔV which presents a smoother trend and a faster time to reach again null value again at the end of the transient. On the contrary, ΔP oscillations are slightly delayed with respect to ΔV ones: they present a trend that dampens slower than and only once at the end of the observation interval.

Fig. 4.4, instead, presents the ROCOF measured by P-class PMU B during the same event. The two events (i.e., the generators' tripping and the activation of the UFLS scheme) can be easily distinguished. Despite the fact that the first event is much stronger than the second one, both result in a sequence of damped oscillations that tends to bring back the power system to steady-state conditions.

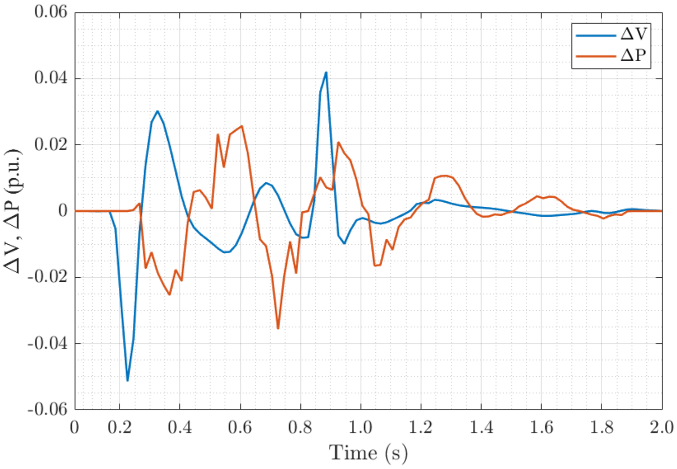

Figure 4.3: Results of the real-world scenario II: Voltage and active power variations, indicted as ΔV and ΔP in blue and red, respectively. They are both expressed in per-unit values.

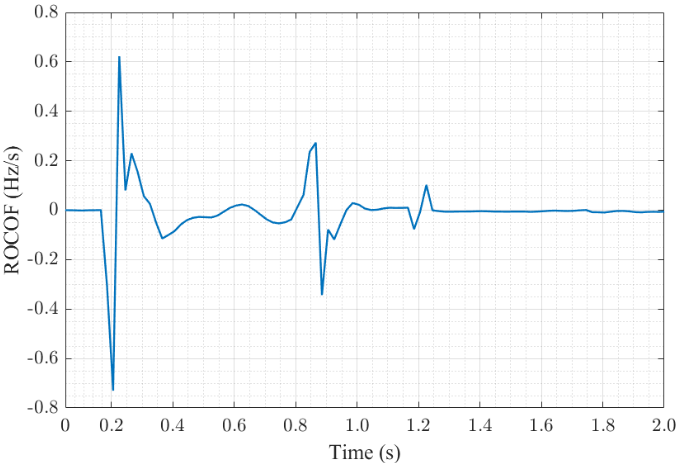

Figure 4.4: Results of the real-world scenario II: ROCOF expressed in Hz/s, measured during the entire sequence of events using P-class PMU B.

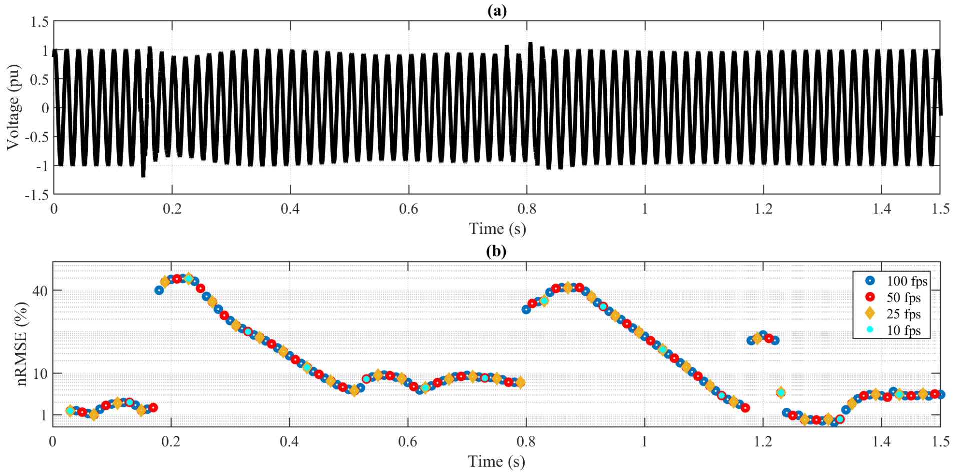

Figure 4.5: Results of the real-world scenario II: **(a)** Voltage profile in per unit value recorded during the contingency events in the modified IEEE 39-bus system. **(b)** nRMSE expressed in % and computed using PMU B in P-class configuration for four different reporting rates R_r. Source: [99].

Table 4.1: nRMSE detection latency, expressed in ms, as a function of the PMU reporting rate R_r in the two real-world scenarios under test. Source: [88].

R_r (fps)	Scenario I	Scenario II
10	n.a.	115
25	85	95
50	65	75
100	55	65

The results of the second scenario in terms of nRMSE are presented in Fig. 4.5. In particular, the upper graph illustrates the time trend of the voltage profile, expressed in per unit, recorded during the sequence of contingencies. Three different parts can be identified: a steady-state condition before $t = 0.15$ s, a sequence of time-damped oscillations, and a last series of events triggered by the UFLS scheme after $t = 0.8$ s. Looking at Fig. 4.5(b), the results of the nRMSE for the four R_r are shown. It can be noted that, once again, the nRMSE can easily discern steady-state from transient conditions. Moreover, the trend of the nRMSE in time provides further information regarding the restoration of the power system to a stable pre-fault condition, aligning with the results shown in Fig. 4.3.

Similarly to Scenario I, the PMU reporting rates strongly affect the responsiveness in the identification of contingency. For the sake of completeness, Table 4.1 summarizes the time latency expressed in ms in the detection of the contingency condition, as a function of R_r. The results of Fig. 4.2(b) and 4.5(b) are confirmed by the delays shown in Table 4.1: the higher the R_r, the fastest the contingency detection.

However, as shown in Table 4.1, considering the threshold equal to 40 % suggested in [101] results in a non-applicable (n.a.) result for what concerns R_r = 10 fps in Scenario I. In the other cases, instead, the detection time is inversely proportional to R_r. An extension of the study on the required threshold is carried out in Section 6.4 for renewable-based power systems [88].

Lastly, in view of integrating PMU data in more sophisticated control strategies, two possible amendments can be proposed to the packet structure, shown in Fig.

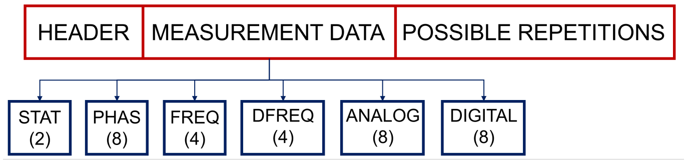

Figure 4.6: Measurement data packet structure as defined in [105]. Source: [99].

4.6 based on the IEEE C37.118.2 Synchrophasor Data Transfer for Power Systems [105]. The first one is based on the application of PMUs in local control centers: PMUs can detect bad data internally and use a single extra bit as a Boolean flag equal to 1 to indicate potential bad data. The second possible amendment, instead, can consist in the transmission of the nRMSE itself as possible useful information in case of a more centralized approach.

It is worth highlighting that none of these amendments would compromise the packet size in any relevant way, nor it would require excessive effort from computation and transmission capabilities.

4.3 Target Uncertainty for Distribution Power Systems

As anticipated at the beginning, the aim of this Chapter entails the establishment of uncertainty requirements for PMU measurements at various power system levels. For this reason, the objective of this Section is to define the accuracy requisites in order to achieve significant results, considering the typical distribution power systems' characteristics and those of PMU-based measurement chains. This Section illustrates the work presented at the 12th International Workshop on Applied Measurements for Power Systems (AMPS) held in Cagliari, Italy in 2022 [91].

On one hand, a typical PMU-based measurement chain is thoroughly described from the IT up to the synchrophasor estimation algorithm evaluated in the PMU. Different configurations, varying the IT class, and the PMU characteristics, are created. This results in a set of typical uncertainties obtained applying MCM.

On the other hand, conventional distribution network characteristics are considered, with the objective of creating a dataset of possible combinations including various cable lengths, loads, and ampacities. In this context, typical voltage displacements in terms of magnitude and phase are assessed at the end of such lines.

By comparing the uncertainties introduced by a PMU-based measurement chains with those of a distribution network, it can be determined the target uncertainty required in order to perform reliable measurements. They can constitute a useful insight for DSOs in order to achieve dependable and useful measurements.

Section 4.3.1 presents the simulation conditions, i.e., the measurement chain and the MV lines specifications, as well as the details of the MCM. Whereas, Section 4.3.2 illustrates and discusses the outcomes of this study.

4.3.1 Simulation Conditions

Uncertainty sources of the measurement chain: Four main elements can be identified in a typical PMU-based chain: an IT (in particular, a LPVT is considered in this application), a DAQ system (specifically, the focus is on the characteristics of a typical commercial ADC), a time synchronization source needed for the locking the PMU, and a PMU itself.

Having presented the four elements under study, at this stage, it is needed to detail more precisely the uncertainty sources, which are listed as follows:

- The accuracy performances of ITs and LPITs are detailed in the IEC 61869 Standard as described in Chapter 2. However, in this study, the focus is only on LPVTs which are illustrated, first in general and then in specific, in Sections 2.4 and 2.4.1, respectively. In this specific application, all three accuracy classes of 0.1, 0.2, and 0.5 are considered [63, 66]. They correspond to a ratio error of 0.1 %, 0.2 %, and 0.5 %, respectively. For what concerns the phase displacement, instead, they correspond to ±0.15 crad, ±0.3 crad, and ±0.6 crad, respectively. It is worth noticing that these values refer only to the rated voltage; for lower values, the limits become less strict therefore the impact on the overall uncertainty would be less significant, as shown in Table 2.4. In order to ensure conservative results, only rated conditions are examined, corresponding to 100 % of the rated voltage in Table 2.4.

- For what concerns the second element of the measurement chain, a commercial off-the-shelf DAQ board is studied; however, a particular focus is given to the specifications of the ADC. Each manufacturer provides typical performance indices such as the non-linearity error, the offset, and noise which all corrupt the quality of the digitalized signal. In this case, the most relevant parameters of a generic device are considered: it features a 24-bit ADC, a full-scale voltage of ±10 V, a 70 μV_{rms} input noise[7], ±0.03 % and ±0.008 % gain and offset errors, respectively, when the DAQ system works in typical operating conditions, which corresponds to $(25 \pm 5)^{\circ}$C according to the datasheet.

- PMUs can rely on different time sources, however, they are characterized by different characteristics and performances. In this study, three of them are considered: GPS, Precision Time Protocol (PTP), and Inter-Range Instrumentation Group timecode B (IRIG-B). They all have an uncertainty associated with the time information necessary for locking the PMU. Their typical uncertainties are in the range of ±10 to ±100 ns, ±500 ns, and ±500 ns, respectively, according to the literature [106]. However, in order to ensure conservative results, the worst-case scenario is considered hence ±100 ns is selected. These time uncertainties are reflected on a phase-angle offset in the estimation of the synchrophasor, affecting the final result, regardless of the accuracy of the PMU estimation algorithm. It is important to recall, as disclosed in Section 2.2.2, that it is sufficient to assess a time synchronization

---

[7] As a fair assumption, the noise introduced by the DAQ can be considered as a constant contribution over the observation window.

Table 4.2: Test configurations comprising different combinations of the sources of uncertainty under test.

Configuration	LPVT class	Time Sync	TVE
T1	0.1	GPS	0.01 %
T2	0.5	GPS	0.1 %
T3	0.5	GPS	0.01 %
T4	0.2	PTP	0.1 %
T5	0.1	PTP	0.1 %
T6	0.5	IRIG-B	1 %

error of 31.8 μs or 26.5 μs for 50 Hz and 60 Hz signals, respectively, to obtain a TVE of 1 %, assuming null errors on both the magnitude and phase estimation provided by the algorithm. The latter is the maximum error value allowable according to the PMU Std in steady-state conditions [14].

- The PMU algorithm itself adds its contribution to the previous sources in the measurement chain. In steady-state conditions, the maximum permissible error is a TVE of 1 % which can be constituted of a magnitude error of 1 % without any other sources of error. Alternatively, it can be derived from a 0.01 rad phase error, without any other sources of error. Nevertheless, it must be highlighted that in the literature there exists a huge number of algorithms that feature a TVE well below the PMU Std requirements, as the ones illustrated in Section 4.1.1. However, without loss of generality, three different TVE values are considered: 1 %, 0.1 %, and 0.01 % which can represent the worst- and one of the possible optimal cases that can be found in the literature. In the three cases, the entire percentage is first associated only with the magnitude and then with the phase angle only.

Given the complexity of the model and the significant number of sources of uncertainty, based on the theory presented in Chapter 1, it is considered reasonable to apply MCM following the procedure detailed in Section 1.2.4.

Therefore, in the following, the MCM is repeated for a total of $M = 10^5$ trials and is applied with increasing complexity: first of all, each contribution is examined individually. Secondly, different configurations, comprising a mixed range of uncertainties, are combined together in order to create different setups which can be found in the field. In this regard, it is important to notice that such an approach may yield a rather conservative target uncertainty since the different contributions are considered statistically independent and uncorrelated.

For the sake of clarity, Table 4.2 summarizes the six tests including different combinations of the four sources of uncertainty present in the measurement chain under test, from the LPVT up to the PMU and its sources for time synchronization[8].

---

[8] For the sake of conciseness, the ADC has been omitted in Table 4.2, as it is reasonable to consider that the DAQ is always the same in each of the six configurations. For this reason, the DAQ is simulated without changing the data previously described.

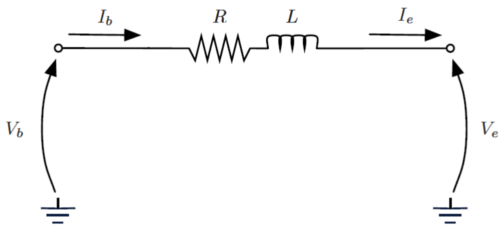

Figure 4.7: Configuration of a simplified π model of a distribution grid, including only longitudinal resistive and inductive parameters. Source: [91].

It is also worth noting that the selected configurations are a trade-off between ideal and realistic measurement chains. As a matter of fact, in distribution networks, ITs having an accuracy class better than 0.5 are seldom available, as they are generally used for particular applications at HV level. Similar considerations hold for the synchronization source, which mainly depends on the PMU location and on the GPS availability, especially in urban areas.

The reference value at the end of the measurement chain is a 9 V rms voltage, having a 0 rad phase. This waveform is corrupted by all sources of uncertainty and the synchrophasor is extracted. Afterward, the MCM is applied M times and, lastly, the mean value and the 95 %-Confidence Interval (CI) are assessed.

Distribution network characteristics: To consider realistic configurations of a distribution network, a portion is studied as between two nodes b and e supplying a load at its terminals, as shown in Fig. 4.7. A first approximation consists in assuming that the load is concentrated at the end of the line, and not distributed along it. It is also worth noting that the considered model is a simplified version of the traditional π model of a line. Since distribution power systems are typically characterized by short lines, i.e., less than 60 km, it is then reasonable to neglect transversal parameters, as their withdrawn current is minimal. In this way, parasitic capacitances and conductances per unit length can be generally omitted for short-distance cable lines. In the same way, it can be reasonably assumed that the reactive longitudinal parameters are only constituted by the inductive component.

The first objective consists in obtaining typical resistances and reactances values per unit length at 50 Hz and at the operating temperature of distribution power system cables, retrieved from different manufacturers and for various cable insulations.

To this purpose, eight cables produced by different manufacturers have been selected, based on the technical specifications in their commercial catalogs. They either feature a Hard Grade Ethylene Propylene Rubber (HEPR) or a Cross-linked Polyethylene (XLPE) insulation. Regardless of the insulation type, they are both characterized by an operating temperature of 90 °C, and their laying is in-ground flat and in-ground, for single- and three-core cables, respectively. As for the cross-section, 70 and 120 mm^2 have been selected as they are extremely common in distribution grids. The most relevant specifications are illustrated in Table 4.3.

The second objective, instead, involves the evaluation of the magnitude offset and the phase displacement introduced by the considered MV lines configurations. To this purpose, different scenarios are created to test every cable in various power system conditions. Three different lengths of 1, 10, and 20 km, respectively indicated as

Table 4.3: Characteristics of MV cables considered for a typical distribution network scenario.

Cable	Type	Insulation	Cross Section (mm^2)
C1	Single Core	HEPR	70
C2	Single Core	XLPE	70
C3	Three Core	HEPR	70
C4	Three Core	XLPE	70
C5	Single Core	HEPR	120
C6	Single Core	XLPE	120
C7	Three Core	HEPR	120
C8	Three Core	XLPE	120

D1, D2, and D3, are investigated. Then, a Power Factor (PF) first equal to 0.8 and then to 1 is examined; lastly, two powers for the burden are obtained starting from the 100 % and the 50 % of the cable ampacity expressed in A.

The described testing conditions are assessed for a 50-Hz, 20 kV rms, $\varphi = 0$ rad voltage at the upstream terminal b, leading to a new downstream voltage to be measured at terminal e, referring to Fig. 4.7. The latter has a phase angle $\Delta\varphi$, in rad, and a percentage voltage magnitude ΔV, in %, compared to the reference one which is examined in the next Section 4.3.2 presenting the results. Once again, the aim entails the assessment of these ΔV and $\Delta\varphi$ variations and their comparison with respect to the typical uncertainties introduced by the MV chain. Comparing these two leads to the determination of the target uncertainty required to perform reliable in-field measurements.

4.3.2 Results Evaluation and Comparison

This Section presents the results obtained from the simulated scenario described in the aforementioned part. First of all, the results obtained considering individually all the sources of uncertainty are presented.

Uncertainty of the measurement chain: Table 4.4 reports the mean value, $\overline{x}$, and the 95 %-confidence semi-interval, σ_{si95}, for both voltage magnitude and phase angle results, respectively in V and rad. In the first column, the considered source of uncertainty is specified.

A first observation concerns the three synchronization sources, whose errors affect only the phase of the estimated synchrophasor. Hence, since the voltage magnitude is not affected, it presents a $-$ for both $\overline{x}$ and σ_{si95}. In absolute terms, instead, the GPS presents the smallest results in terms of uncertainty, as expected.

A second comment regards the tests varying the TVE value. As briefly presented in the previous paragraphs, in the first test the TVE is associated entirely with the voltage magnitude, while in the second one with the phase angle[9]. For this

---

[9] It is worth recalling that a similar result could have been obtained using a complex random variable where magnitude variations are modeled with a Gaussian distribution,

Table 4.4: Results of the 10^5 trials obtained applying MCM considering each source of uncertainty individually in a typical MV measurement chain. Source: [91].

Source	Voltage Magnitude (V)		Phase Angle (rad)	
	$\overline{x}$	σ_{si95}	$\overline{x}$	σ_{si95}
GPS	-	-	0	$3 \cdot 10^{-5}$
PTP	-	-	0	$1 \cdot 10^{-4}$
IRIG-B	-	-	0	$1 \cdot 10^{-4}$
TVE 1%	9.09	-	0.01	-
TVE 0.1%	9.009	-	0.001	-
TVE 0.01%	9.0009	-	0.0001	-
ADC	9.000	$2 \cdot 10^{-3}$	0	$1 \cdot 10^{-6}$
0.1 IT	9.000	$8 \cdot 10^{-3}$	0	$1 \cdot 10^{-3}$
0.2 IT	9.00	$2 \cdot 10^{-2}$	0	$3 \cdot 10^{-3}$
0.5 IT	9.00	$4 \cdot 10^{-2}$	0	$5 \cdot 10^{-5}$

reason, they present alternatively null errors on the phase and on the magnitude, respectively. It is also worth mentioning that for all tests, the TVE is used as a fixed value rather than a random variable. Hence, the results in Table 4.4 show the resulting value after the addition of the TVE percentage to the reference signal; thus, the significant digits are purely defined by the TVE contribution itself.

Moving on to the ADC analysis, a single test has been performed including simultaneously the gain, non-linearity errors, and the noise level previously illustrated. It can be interesting to notice that the ADC is the least impacting element of the measurement chain: this can be derived by analyzing the σ_{si95} of magnitude and phase which are the smallest among all possible cases.

Lastly, the three classes of LPVTs are examined. The σ_{si95} reduces by almost one order of magnitude moving from class 0.1 to class 0.5; in contrast, the phase is in the order of some mrad for the three classes. These results indicate that LPVTs are the biggest contributions to the overall uncertainty, not only in terms of magnitude but also concerning the phase. Hence, the choice of the most suitable VT plays a major role in all PMU-based applications[10].

Having examined the results of the effects of the individual sources of uncertainty, the MCM is applied to the six configurations illustrated in Table 4.2. The results of the MCM application are shown in terms of voltage and phase angle results in Table 4.5. As expected, the results of test T1 show the best outcomes in terms of σ_{si95} on both magnitude and phase. On the other hand, test T6 provides the worst results among all six configurations. In more detail, it can be noted a difference of roughly one order of magnitude between the accuracies of the two tests. Nonetheless, it

---

while phase ones with a Rayleigh distribution. However, the adopted method is more conservative as the worst case for both variables is selected.

[10] In this study, the terms “LPVT” and “VT” as used interchangeably for the mere reason that they are characterized by identical limits at the rated voltage, according to the Standard and as shown in Tables 2.1, 2.2 and 2.4.

Table 4.5: Results of the 10^5 trials obtained applying MCM considering the six configurations, as detailed in Table 4.2, including a combination of the sources of uncertainty in a typical MV measurement chain. Source: [91].

Configuration	Voltage Magnitude (V)		Phase Angle (rad)	
	$\overline{x}$	σ_{si95}	$\overline{x}$	σ_{si95}
T1	9.001	$9 \cdot 10^{-3}$	0	$1 \cdot 10^{-3}$
T2	9.01	$4 \cdot 10^{-2}$	0	$5 \cdot 10^{-3}$
T3	9.00	$4 \cdot 10^{-2}$	0	$5 \cdot 10^{-3}$
T4	9.01	$2 \cdot 10^{-2}$	0	$3 \cdot 10^{-2}$
T5	9.009	$9 \cdot 10^{-3}$	0	$2 \cdot 10^{-3}$
T6	9.09	$4 \cdot 10^{-2}$	0	$1 \cdot 10^{-2}$

must be underlined that test T1 represents an ideal measurement chain that can be hardly found in the field owing to the rare installation of VTs having a 0.1 class which is often a costly solution dedicated only to particular measurement conditions. Consequently, test results obtained from the configurations T2 and T3 can represent a more realistic network condition. However, they also indicate an unavoidable accuracy reduction achievable with those configurations. Nonetheless, the better performances of the synchrophasor estimation algorithm, simulated as a difference of one order of magnitude in the TVE, is negligible in terms of final accuracy due to the major contribution of the 0.5 class LPVT. Lastly, the results of configurations T4 and T5 point out that with a 0.1 class VT, it is possible to better discern the effect of the other sources of uncertainty.

Distribution network specifications: Considering the cable configurations detailed in Table 4.3 and the scenarios for typical MV distribution networks presented in the previous Section, several tests have been performed. To obtain more conservative results, the errors at the two terminals of the line are supposed to be uncorrelated. Once again, it is worth recalling that the objective entails the assessment of the variation of the voltage magnitude and phase angle at the end of a typical MV line, indicated by ΔV and $\Delta \varphi$ and expressed in % and in rad, respectively.

First of all, the results of the phase angle variation $\Delta \varphi$ are illustrated. Fig. 4.8 presents $\Delta \varphi$, in rad, for the eight cable configurations, C1 to C8 listed on the horizontal axis, as a function of three distances D1, D2, and D3. The results relative to D1 are depicted in blue on the left vertical axis, whereas those of D2 and D3 are on the right vertical axis and are shown in yellow and red, respectively. Specifically, the results of Fig. 4.8 are relative to a test condition characterized by a cable ampacity, A, equal to 100 % and two PF equal to 0.8 and 1, respectively in (a) and (b).

Similarly, Fig. 4.9 presents the results obtained applying the same testing conditions as those shown in Fig. 4.8, but they are relative to a halved ampacity of the cables under test, in which A = 50 %.

In the following, the results of the voltage magnitude variations ΔV, in %, are shown. More in detail, Fig. 4.10 presents the results relative to a cable ampacity A of 100 %, for the eight cable configurations and for the three possible lengths D1 (in blue on the left vertical axis) and D2, D3 (in yellow and red, on the right vertical axis, respectively).

In a similar way to what is shown in Fig. 4.9, Fig. 4.11 presents the same results

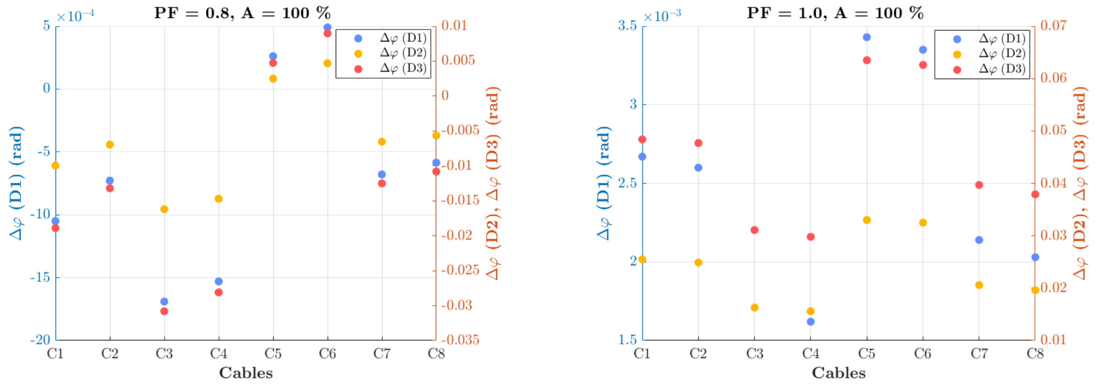

(a) (b)

Figure 4.8: Results of the $\Delta\varphi$, in rad, measured for the eight cable configurations shown in Table 4.3 having an ampacity A of 100%, for PF = 0.8 in (a) and for PF = 1 in (b). Results for D1 cable length are shown on the left vertical axis (blue dots), while D2 and D3 lengths are on the right vertical axis (yellow and red dots, respectively). Source: [91].

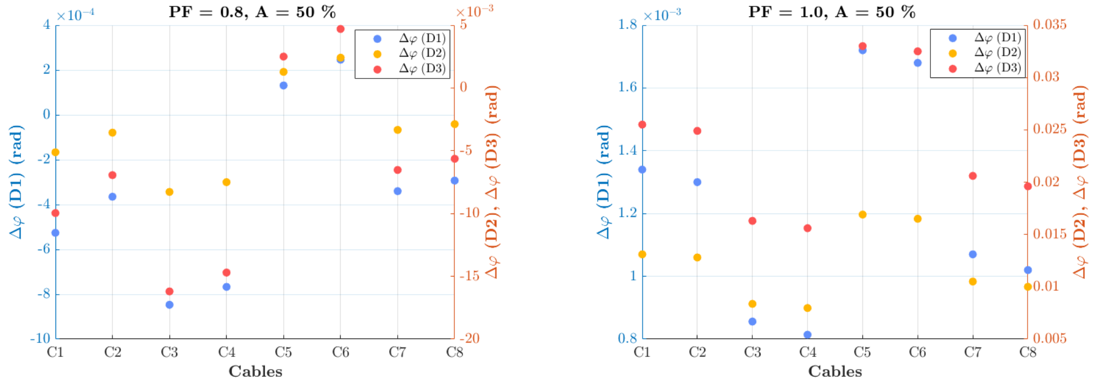

(a) (b)

Figure 4.9: Results of the $\Delta\varphi$, in rad, measured for the eight cable configurations shown in Table 4.3 having an ampacity A of 50%, for PF = 0.8 in (a) and for PF = 1 in (b). Results for D1 cable length are shown on the left vertical axis (blue dots), while D2 and D3 lengths are on the right vertical axis (yellow and red dots, respectively). Source: [91].

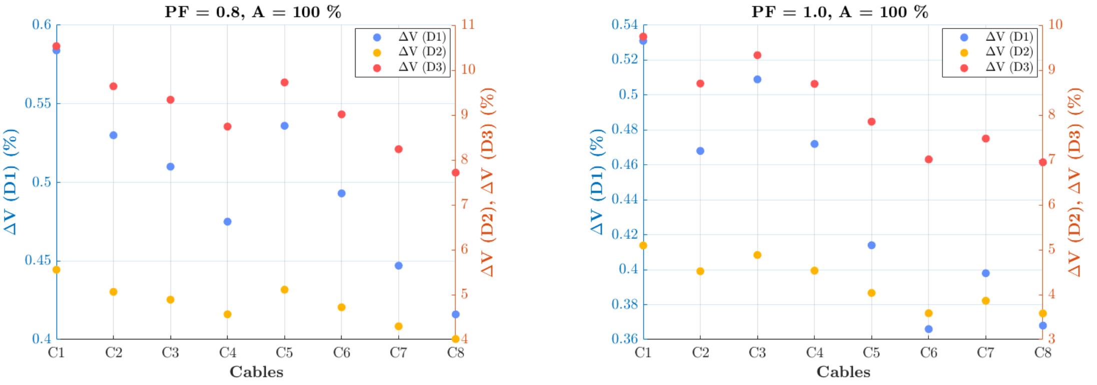

(a) (b)

Figure 4.10: Results of the ΔV, in %, measured for the eight cable configurations shown in Table 4.3 having an ampacity A of 100%, for PF = 0.8 in (a) and for PF = 1 in (b). Results for D1 cable length are shown on the left vertical axis (blue dots), while D2 and D3 lengths are on the right vertical axis (yellow and red dots, respectively). Source: [91].

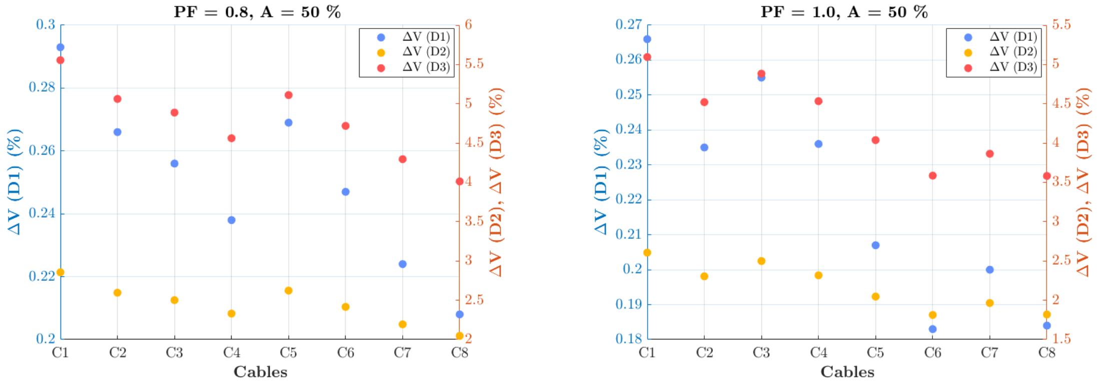

(a) (b)

Figure 4.11: Results of the ΔV, in %, measured for the eight cable configurations shown in Table 4.3 having an ampacity A of 50%, for PF = 0.8 in (a) and for PF = 1 in (b). Results for D1 cable length are shown on the left vertical axis (blue dots), while D2 and D3 lengths are on the right vertical axis (yellow and red dots, respectively). Source: [91].

but for a reduced cable ampacity of 50 %.

The main comments that can be derived at a glance from Fig. 4.8, 4.9, 4.10, and 4.11 concern the line lengths: the longer the line, the higher the voltage drops in terms of both magnitude and phase angle. Second, it has to be kept in mind that each cable, C1 to C8, is characterized by different parameters, hence the effect on the overall impedance slightly changes from one cable to the other. Lastly, the 100 % ampacity is the most severe case for the cable and the network, however, the quantities to be assessed are the highest, thus this implies that it is easier to measure them.

After having presented the results of the MCM in Table 4.5 and the magnitude and phase angle variations shown from Fig. 4.8 to Fig. 4.11, some useful conclusions can be drawn comparing these together. First, no major issues can be identified in the measurements of the synchrophasor magnitude. This result can be drawn by examining the worst-case scenario relative to the ΔV: it corresponds to the smallest achievable ΔV which is shown in Fig. 4.11(b). In this case, $\Delta V \approx 0.18\,\%$ for D1 in configuration C6. Projecting this result to the considered reference values, i.e., 20 kV rms voltage, one obtains a few tens of V which can be easily measured, given the worst-case results shown in Table 4.5 applying the MCM.

Conversely, the estimation of the synchrophasor phase angle still represents an unresolved tricky challenge that cannot be easily unraveled. The reason has not to be found either in the synchrophasor estimation algorithm (i.e., corresponding to the worst-case TVE) or in the quality of the time synchronization. As previously described, the main source of error comes from the IT.

In this regard, the worst configuration consists of an inductive load having a PF = 0.8 with either A = 100 % or A = 50 % cable ampacity. In such cases, the phase difference $\Delta\varphi$ is particularly small, i.e., in the order of a few hundred μrad. Additionally, even in the best configuration as shown in Fig. 4.8(b), having PF = 1.0 and A = 100 %, $\Delta\varphi$ is in the order of few mrad. Comparing these results to the best measurement chain configuration, despite being rather ideal, i.e., T1, whose results are illustrated in Table 4.5, the 95 %-confidence semi-interval, σ_{si95}, is in the order of 10^{-3} rad. Consequently, the measurement uncertainty is comparable to or even bigger than the measurand value, making it unfeasible for any inference or deduction based on the measurement results. This aspect must be taken into high consideration when aggregating and comparing measurements taken at different nodes of the same distribution network. Many PMU-based applications relying on the $\Delta\varphi$ information, such as fault location or SE, may yield inaccurate results when a PMU is installed at the distribution level owing to the characteristics of the power system itself and its measurement chains. It is then necessary to account for the associated measurement uncertainty both in the selection of the nodes of interest and in the evaluation of the measurement results.

4.4 Frequency Uncertainty Requirements in Transmission Power Systems Resynchronization

The previous Section 4.3 presented a study of the required target uncertainty for PMU-based measurements at the distribution level. However, PMUs were originally conceived for TSOs and they are often installed at the transmission power system level. Especially for TSOs, it is of utmost importance to ensure a proper exchange of information with other TSOs, mainly in case of contingencies. However, in the last years, two major events caused by anomalous conditions led to the splitting of Continental Europe (CE) into two synchronous areas.

Based on this, this Section aims at presenting a study on the importance of the accuracy of the frequency estimates in transient conditions, more specifically during the resynchronization of the CE area. Relying on such information, it is possible to identify more suitable conditions for resynchronization operations. Not only should the frequency deviation between the two areas be considered, but it is also necessary to take into account the respective measurement uncertainties.

This research stems from a set of policies and operational guidelines released by the European Network of Transmission System Operators for Electricity (ENTSO-E). In particular, according to the Emergency Operations Policy (briefly referred to as EOP, hereinafter), the frequency deviation between the two areas shall not exceed 200 mHz at the moment of the reconnection. As a matter of fact, this policy is rather conservative and guarantees a smooth and secure system operation [107]. However, this approach does not take into consideration the uncertainty contributions inherent in any PMU-based measurement system. Based on this rationale, this study proposes to investigate the frequency uncertainty requirements at the transmission level, during particularly severe and dynamic conditions.

In the following, Section 4.4.1 presents the considered PMU synchrophasor algorithms as well as the two test cases, specifying the power system's conditions before, during, and after the splitting from CE. Section 4.4.2, instead, discusses the frequency uncertainty that characterizes the two scenarios during the resynchronization. The next two Sections present the main results illustrated in [98].

4.4.1 Power System Separations in Continental Europe

PMU settings: in this study, all three PMU models detailed in Section 4.1.1 are taken into account. More specifically, both P- and M-class versions are used.

This choice stems from the fact that, in such a dynamic condition, it should be more reasonable to rely on P-class PMUs since they are specifically designed for protection purposes. However, for the sake of completeness, also M-class ones are examined, as they could provide more accurate results. For all PMUs, the sampling frequency is set equal to 12 kSa/s, and the reporting rate is 50 fps. The latter relies on the fact that both scenarios took place in Europe where the power system's rated frequency is 50 Hz. Higher reporting rates, i.e., 100 fps, are allowed, however, they are unlikely to be used in practical applications.

In the following, power system signals representative of each area are considered. Nevertheless, in the absence of waveform recorders, the power system signals are reconstructed based on the official ENTSO-E reports [96, 97].

In more detail, the time profiles are interpolated using a non-linear fit routine based on a shape-preserving piece-wise cubic polynomial [44]. This allows the reconstruction of the time-varying power signal without any discontinuities. Moreover, given the analytical formulation of the frequency resulting from the interpolation, it is possible to retrieve the corresponding phase and ROCOF profiles by means of integration and derivation, respectively.

This method allows for defining the ground-truth values for phasor, frequency, and ROCOF at each time instant. Evidently, this is not an exact reproduction of the real-world event and may risk overfitting the estimation results presented in the original reports. Based on the knowledge of ground-truth values, the actual PMU estimation errors can be assessed and compared with the expected uncertainty as given by the PMU Std [14].

In order not to rely only on purely simulated signals, but rather to reproduce the uncertainty contributions of the PMU analog front-end, the test waveforms are corrupted with an additive, uncorrelated noise with a SNR of 80 dB. Such a value of SNR has been chosen based on the fact that measurements performed at the transmission system level are generally characterized by lower levels of noise.

Test Case I

In this part, the first test case is detailed, presenting the power system status before, during, and after the contingency. The idea is to provide an all-around vision of the system state, highlighting the causes that led to the system split from the CE. Lastly, a post-fault analysis is presented: an error and uncertainty analysis is carried out on frequency estimates based on PMU measurements in the two CE areas. The first contingency took place on January 8th, 2021 in Ernestinovo, Croatia [96].

Pre-Fault Power System Status: on the day of the contingency, the power system was characterized by a high active power flow from the East to the West region. This situation was influenced by warm weather and Orthodox Christmas holidays in Southeast Europe, thus resulting in very low power demand, as well as a cold spell characterized by high demand in Northwest Europe. This condition led to an overall lower demand than usual in the Balkan Peninsula and a high power export from this area to CE of around 3900 MW.

In addition, the high-voltage 110 kV overhead line connecting substation Majdanpek 1 to Majdanpek 2 was switched off due to a circuit breaker failure in Majdanpek

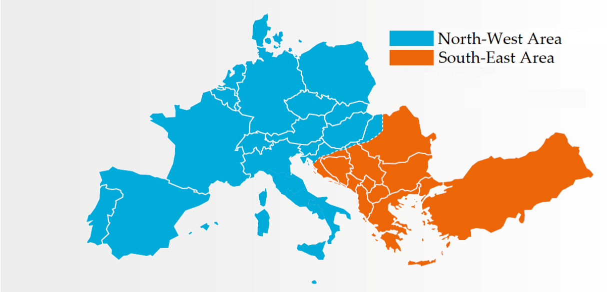

Figure 4.12: Synchronous areas resulting from the transmission power system split that occurred on January 8th, 2021. Two areas can be identified: a Northwest and a Southeast one, indicated in blue and red, respectively. Source: [96, 98].

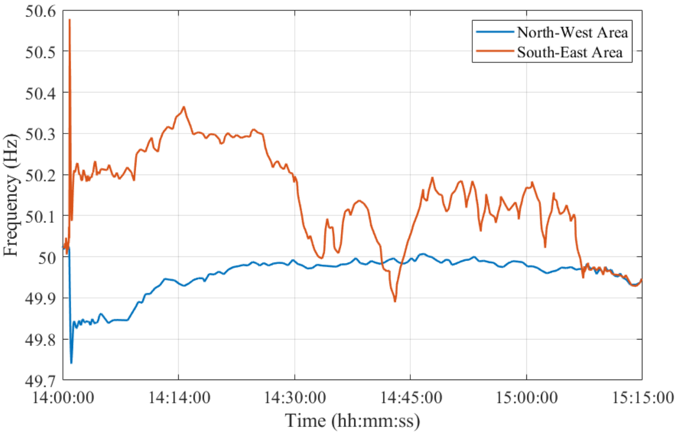

Figure 4.13: Time-varying frequency trends obtained from the interpolation algorithm in the North-West (NW) and South-East (SE) synchronous areas for the entire contingency duration, shown in blue and red, respectively. Source: [96, 98].

1. The power grid topology was not altered after the scheduled outage, counting on control room supervision of the power flows through the busbar coupler, protected by an over-current relay [96, 98].

Contingency and Post-Fault Analysis: based on the previous considerations, it can be easily drawn that the operation of the transmission system was on edge. As a matter of fact, a single outage was sufficient to drive the system to exceed the transient stability limit. Indeed, at 14:04:25.9 Central European Time (CET), the busbar coupler overload protection in Ernestinovo, Croatia led to a cascade of events. This led to the tripping of protections in other Croatian substations, in Serbia, Romania, and Bosnia and Herzegovina.

After 15 s, the stabilization was already reached owing to the following countermeasure actions, both automatic and manual. Among these, there was the activation of Frequency Control Response (FCR) in both the Northwest and Southeast areas. Nevertheless, after the trip of a second element, i.e., the Subotica-Novi Sad transmission line at 14:04:48.9 CET, the two areas started to separate due to angular instability. The resulting split of the CE is shown in Fig. 4.12.

The separation phenomena were characterized by a very fast voltage collapse at all substations close to the line of separation and by a gradual difference in the frequencies of the two areas. Indeed, the frequency was increasing in the Southeast area and decreasing in the Northwest area, as presented in Figure 4.13. For the sake of brevity, the first is referred to as NW, whereas the latter as SE hereinafter.

More specifically, frequency peaks of 50.6 Hz and 49.74 Hz were assessed in the SE and NW areas, respectively, as in Figure 4.13. ROCOF values reached up to 300 mHz/s and −60 mHz/s in the SE and NW areas, respectively.

Test Case II

The second test case also deals with the splitting of CE into two synchronous areas. However, this contingency occurred on July 24th, 2021 in Moux, France. For the sake of brevity, Test Case II relies on the same specifications and hypotheses presented for the first one, thus they are omitted.

Pre-Fault Power System Status: On the day of the contingency, a fire broke out in the Moux area, in the south of France at approximately 13:30:00 CET. During the organization of the firefighting efforts, the fire department acknowledged that two 400 kV transmission lines connecting Baixas–Gaudière were located in the fire area. However, these lines remained energized despite a request to the French TSO (RTE) to switch them off. In addition, there was a rather high power flow of 2544 MW from France to Spain.

Contingency and Post-Fault Analysis: The sequence of events that led to the splitting of the CE into two areas started with the tripping of differential protection caused by a two-phase fault at a substation in Baixas, France at 16:33:12.0 CET. The frequency, voltage, and load of the transmission elements remained within normal values, as expected after an N-1[11]. However, the N-1 criterion was no longer fulfilled after this event, which is why the Spanish TSO (REE) and RTE agreed to reduce the exchange between France and Spain. Nevertheless, the next two trips occurred before this reduction became effective.

The second event occurred at 16:35:23.8 CET with the trip of 400 kV Baixas-Gaudière line 1. After this second line trip, the voltage started collapsing: a voltage degradation was visible and its phase angle difference started increasing. The coils started to be disconnected, and the first generation was lost.

The third event occurred at 16:36:37.0 CET, initiated by the trip of the Argia-Cantegrit line. This tripping caused the loss of synchronism between France and the Iberian Peninsula, after which, the only possible defense action was to split the system. However, the frequency in the Iberian Peninsula started to drop even before the three remaining interconnection lines between Spain and France had tripped. There was a total load shed of 4872 MW of which 3561 MW was from REE. The resulting split of the CE is shown in Fig. 4.14.

More specifically, the nadir frequency measured in the middle of the Iberian Peninsula was 48.681 Hz, whereas, the maximum local ROCOF was measured at the Hernani substation in Spain and it was equal to −1.03 Hz/s.

---

[11] According to the Article 3(2)(14) of the ENTSO-E Network Code on System Operation, the N-1 criterion *is the rule according to which the elements remaining in operation within a TSO's control area after the occurrence of a contingency are capable of accommodating the new operational situation without violating operational security limits* [108].

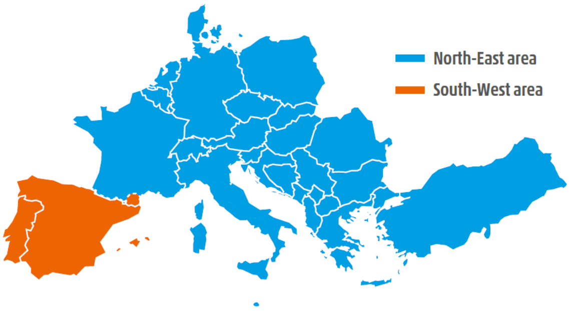

Figure 4.14: Synchronous areas resulting from the transmission power system split that occurred on July 24$^{\text{th}}$, 2021. Two areas can be identified: a North-East and a South-West one, indicated in blue and red, respectively. Source: [97, 98].

4.4.2 Frequency Uncertainty Analysis

Test Case I

In the PMU-based frequency uncertainty analysis, one PMU per synchronous area is considered. For what concerns the NW area, PMU measurements obtained at the substation located in Ernestinovo/Krsko, Croatia are evaluated. Whereas, for what concerns the SE Area, PMU measurements at the substation in Hamitabat, Turkey are considered.

Not only is the objective to establish a frequency estimate in the two areas by means of PMUs having different dynamic performances, but also to evaluate their errors in transient conditions. Based on this, it would be possible to set a more robust and rigorous criterion for resynchronization. Specifically, in Test Case I, only the resynchronization procedure which lasted from 15:00:00 CET until 15:15:00 CET is considered. The reconnection of the SE Area to the CE was successfully accomplished at 15:07:31.6 CET.

The frequency error f_e measured in Hz is computed as follows:

$$f_e = f_p - f_t \tag{4.7}$$

where f_p, in Hz, represents the frequency measured by the PMU and f_t, in Hz, is the ground-truth frequency regarded as a reference and obtained from the interpolation. As a first step, the method used to assess the accuracy of the frequency estimates involves the analysis of the error distributions, as depicted in Fig. 4.15.

For the sake of readability, only the distributions of P-class PMU A and B are displayed, but similar considerations hold for the other models. The two histograms represent the statistical distributions of the frequency errors, f_e, computed according to Eq. (4.7) and produced by PMU A and B in green and pink, respectively. The results are clearly characterized by quite different variation ranges. The worst-case error is limited to 0.4 and 0.1 mHz for PMU A and B, respectively. As expected, PMU B proves to be more accurate thanks to the higher noise rejection and improved dynamic capabilities. Nonetheless, both PMU models are compliant with the PMU Std limit for off-nominal frequency conditions, which is 10 mHz [14].

Having verified the compliance with the PMU Std despite the dynamic conditions, the following analysis aims at correlating these results with the maximum frequency tolerance indicated in ENTSO-E EOP at the resynchronization stage [107].

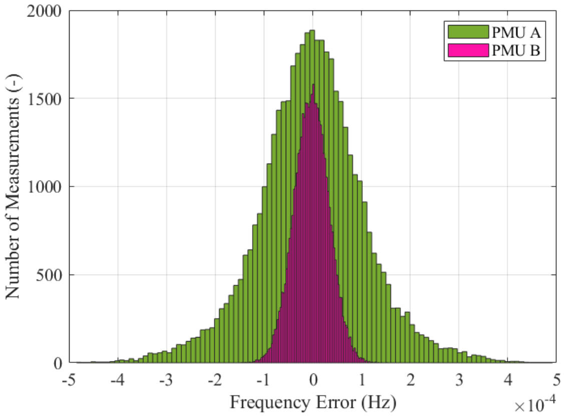

Figure 4.15: Test Case I: Distribution of the frequency error obtained using P-class PMU A and B, in green and pink, respectively. Such errors have been computed in the SE synchronous area during the resynchronization to CE. Source: [98].

As a matter of fact, despite the different error variation ranges, the PMUs' frequency profiles provided are comparable. In this regard, Fig. 4.16 and 4.17 show the measured frequency during the reconnection operation: for each measurement, a vertical error bar indicates the corresponding error with respect to the ground-truth value evaluated according to Eq. (4.7). This analysis is carried out for all five PMU models: Fig. 4.16 presents the results relative to P-class PMU models only, while Fig. 4.17 illustrates those of M-class.

Although the resynchronization was successfully accomplished at 15:07:31.6 CET, it can be noted that at this time the frequencies, jointly with their corresponding uncertainty bandwidths in the two synchronous areas, are still not perfectly overlapping. However, this is the first time instant during which the two frequencies intersect. They are within the maximum tolerance of ±200 mHz to 50 Hz, as indicated in ENTSO-E EOP [107]. Indeed, they fall within a maximum difference of 50 mHz. It is worth recalling what ENTSO-E suggests in this policy, approved on September 26th, 2017: to resynchronize as securely as possible, ENTSO-E indicates that both systems must be in a stable state, and both frequencies must be near 50 Hz, with a maximum tolerance of ±200 mHz to 50 Hz. Based on this rationale, this threshold is compared with the PMU frequency uncertainties. The same reasoning holds true for Test Case II which is presented in the following Section.

Moreover, it can be interesting to notice that from the resynchronization time instant onwards, the two frequencies together with their uncertainties perfectly overlap, guaranteeing a correct power system synchronization. It is interesting to observe how both P- and M-class PMU results align almost perfectly with those presented in [96]. It is thus reasonable to say that this test case is characterized by dynamics that can be easily captured by any P-class PMU. The use of M-class ones does not produce relevant changes in the estimates, as depicted in Fig. 4.17, but may be considered if higher distortions are expected.

From this incident, ENTSO-E derived a couple of recommendations, among which two of them are worth mentioning. Firstly, the substation topology should be chosen in such a way that the power flow through the busbar coupler is as low as possible. Secondly, it should be mandatory to include outages of any transmission elements in the contingency lists, including busbar couplers.

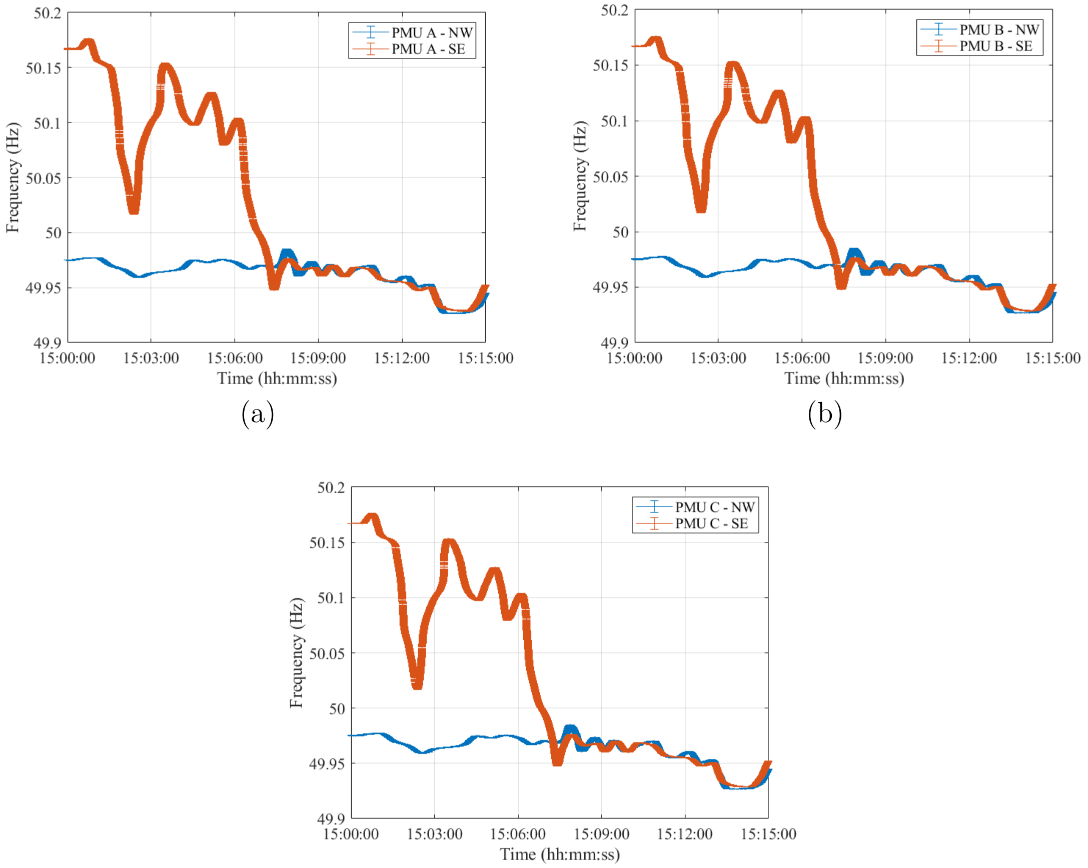

(a) (b)

(c)

Figure 4.16: Test Case I: Uncertainty on the frequency estimates recorded during the resynchronization phase using PMU A (a), B (b), and C (c) in P-class configuration according to the PMU Std in the NW and SE synchronous areas in blue and red, respectively. Source: [98].

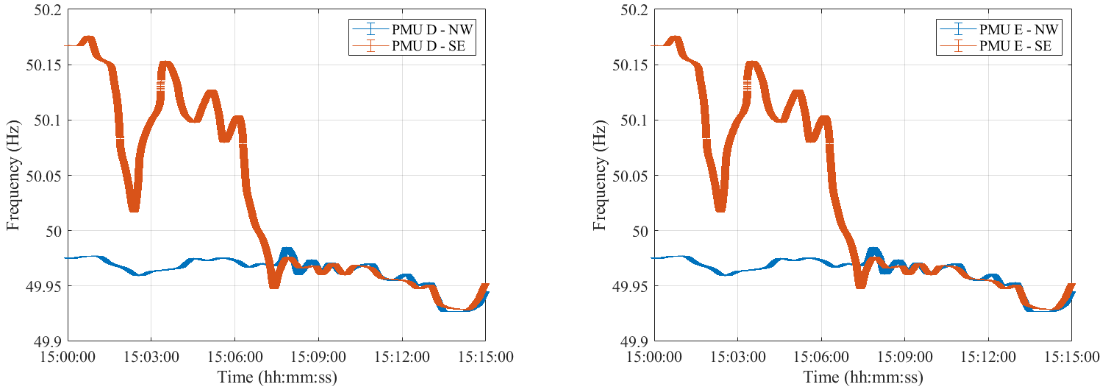

(a) (b)

Figure 4.17: Test Case I: Uncertainty on the frequency estimates recorded during the resynchronization phase using PMU D (a), and E (b), corresponding to the M-class configuration of PMU B and C, respectively, according to the PMU Std in the NW and SE synchronous areas in blue and red. Source: [98].

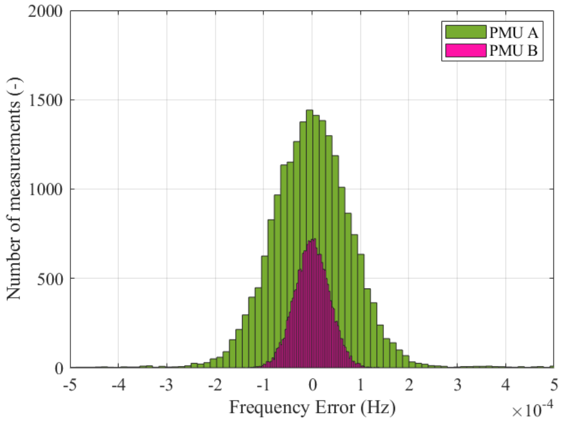

Figure 4.18: Test Case II: Distribution of the frequency error obtained using PMU A and B, in green and pink, respectively. Such errors have been recorded during the fault sequence leading to the splitting of CE. Source: [98].

Test Case II

Similar to the analysis carried out in the previous section, one PMU per synchronous area is considered in Test Case II. For what concerns the Northeast Area, in the following, the PMU measurements obtained at the substation located in Saucats, France are analyzed. Regarding the Southwest Area, instead, PMU data at the substation in LaCereal, Spain are examined. For the sake of brevity, the first is referred to as NE, while the latter as SW hereinafter.

Given the complexity of this Test Case, with respect to the previous one, both the frequency estimates and their errors are assessed in two transient conditions: during the fault sequence and during the resynchronization. More in detail, the first includes a time interval lasting from 16:35:00 CET until 16:42:00 CET during which the second and third faults occurred, leading to the splitting of the CE. Afterward, the PMU dynamic responses are evaluated during the resynchronization procedure which lasted from 17:09:00 CET until 17:09:30 CET. The reconnection of the SE area to the CE was successfully accomplished at 17:09:00 CET.

Similar to Test Case I, as a first step, the two error distributions are investigated to assess the accuracy of the frequency estimates, as shown in Fig. 4.18. Results of PMU A and B are indicated in green and pink, respectively. The two histograms refer to the measured frequency errors in the NE synchronous area during the fault sequence leading to the splitting of CE. For the sake of completeness, it is worth recalling that they are obtained by applying Eq. (4.7). Even in this case, in a like manner to the results of Fig. 4.15, PMU A and B present quite different variation ranges despite their mean values being the same. Namely, PMU A has worse dynamic performance with a worst-case frequency error of 0.5 mHz. whereas PMU B presents the same distribution width as in the previous case, i.e., spanning around ±0.1 mHz, indicating the robustness of its estimation algorithm.

The results of Fig. 4.18 align quite well with those presented in [97]: the frequency nadir of 48.68 Hz is correctly detected by both PMUs. Despite the overlapping of the results of PMU A and B, it is worth noting that the first one presents a much wider error bandwidth for the same frequency estimation.

Fig. 4.19 presents the frequency trends measured by PMU A and B during the 2$^{\text{nd}}$ and 3$^{\text{rd}}$ faults that led to the power system splitting. It can be clearly observed that

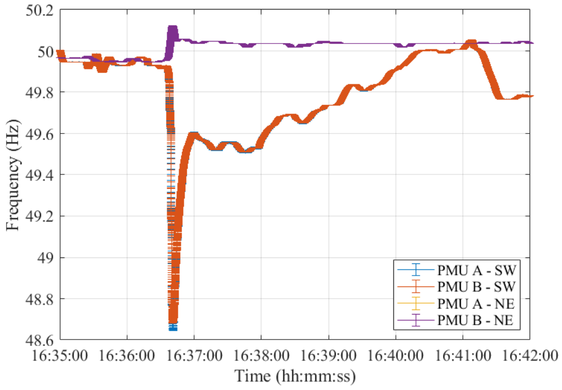

Figure 4.19: Test Case II: Uncertainty on frequency estimates obtained using PMU A and B during the 2nd and 3rd faults, leading to the system separation in both SW and NE synchronous areas. Source: [98].

at the beginning, the two frequencies oscillate around their rated value of 50 Hz. Despite their error bandwidth overlapping for several seconds, this is not a suitable time instant to perform the resynchronization owing to the strong fluctuations. As a matter of fact, just a few seconds after, at 16:36:37 CET, the third event occurred. It led to the splitting of the CE into two separate areas. From this time instant onward, the two frequencies started diverging in opposite directions and never intersect for the following minutes.

The resynchronization occurred at 17:09:00 CET. The frequencies measured in the two synchronous areas by the five PMU models are shown in Fig. 4.20 and 4.21, illustrating 30 s after the resynchronization, for P- and M-class respectively.

It can be noted how at the beginning of the resynchronization procedure, the two frequencies, comprising their error bandwidths, are approximately within the ±200 mHz threshold suggested by the ENTSO-E EOP [107]. Nevertheless, after the successful resynchronization, the two frequencies show a behavior that is clearly in contrast to what has been observed for Test Case I. In fact, the two do not overlap as in the previous scenario, but rather the frequency in the separated area, i.e., SW, starts oscillating around its rated value of 50 Hz. Just at the end of the 30 s transient, it can be concluded that the two frequencies are superimposing.

From this first observation, it can be immediately determined that not only should the frequency be taken into account when performing power system maneuvers but its uncertainty is of utmost importance as well. As a matter of fact, the uncertainty holds relevant information that should not be neglected, especially before performing emergency maneuvers or counteractions such as in these two test cases.

From this second incident, ENTSO-E derived several recommendations. Among these, they suggest implementing overload protections with a 1 to 5 min threshold that will be complemented with special protection scheme functionality, e.g., based on a centralized load shedding scheme. Second, ENTSO-E proposes the coordination of protection against loss of synchronism with the protection schemes of neighboring systems coordinated by the relative national TSOs. Plus, in light of the events that happened during this event, they advise improving the communication chain in case of external conditions impacting the system operation.

A final comment holds true for both test cases examined in this study. From the

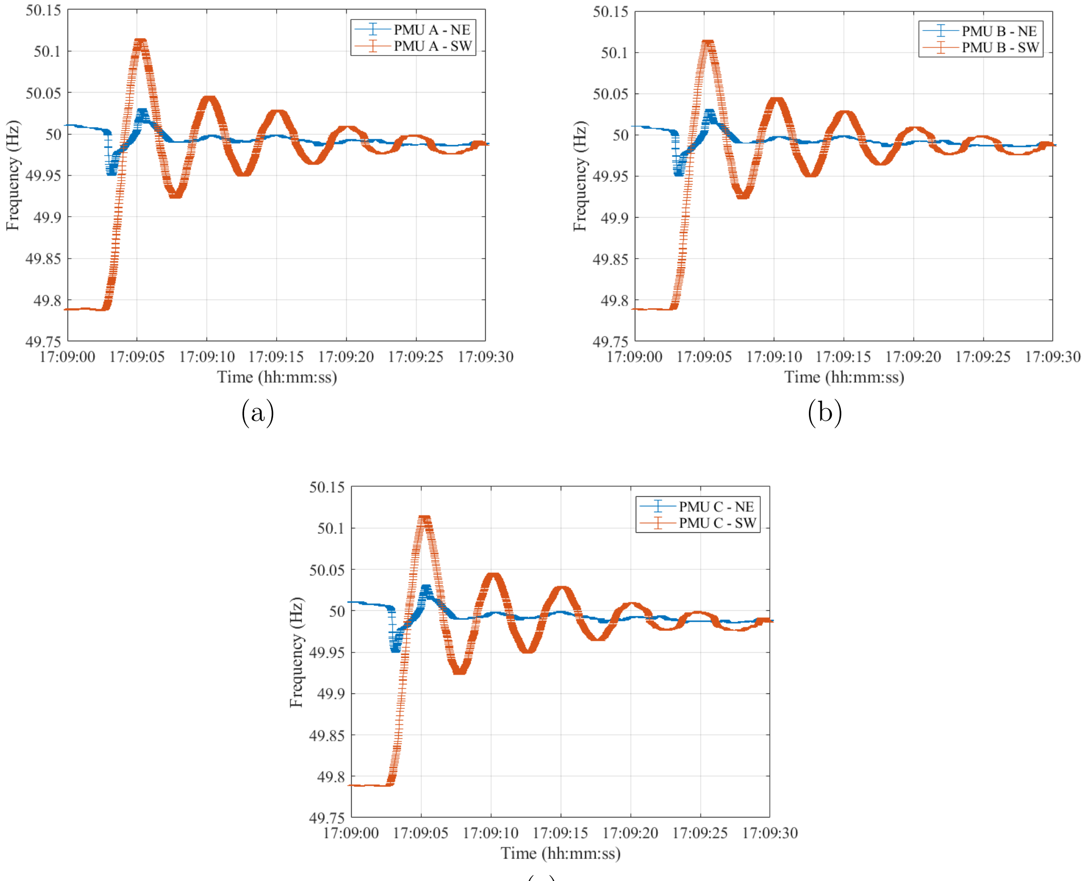

(a) (b)

(c)

Figure 4.20: Test Case II: Uncertainty on the frequency estimates recorded during the resynchronization phase using PMU A (a), B (b), and C (c) in P-class configuration according to the PMU Std in the NE and SW synchronous areas in blue and red, respectively. Source: [98].

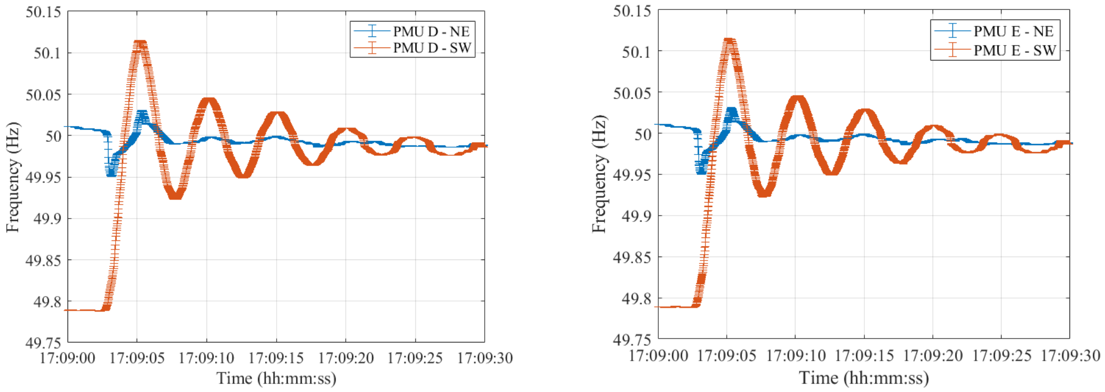

(a) (b)

Figure 4.21: Test Case II: Uncertainty on the frequency estimates recorded during the resynchronization phase using PMU D (a), and E (b), corresponding to the M-class configuration of PMU B and C, respectively, according to the PMU Std in the NE and SW synchronous areas in blue and red, respectively. Source: [98].

measurement point of view, it can be concluded that it is essential to evaluate the uncertainty to be associated with the frequency estimates. This is relevant, most importantly, during transient conditions since PMUs are prone to higher errors, thus significantly influencing their outcomes. In addition, Test Case II showed the results of performing reconnection when the frequencies in the two areas are far apart. In this case, when roughly 200 mHz can be assessed, this may produce strong frequency oscillations in the reconnecting area. Not only does this strain the mechanical parts of the synchronous machines but it also affects the operation of the loads and the electrical instrumentation which are not supplied at their rated frequency.

4.5 Discussion

This Chapter presented the three studies on the applications of PMUs in distribution and transmission power systems, in order to assess the reliability of PMU-based measurements when applied to typical IEEE benchmark grids and in the case of real-world contingencies.

The first study illustrated the feasibility and the advantages which can be derived from the inclusion of a reliability index, i.e., nRMSE, for PMU-based measurements in order to extend power quality assessment procedures at each node of power systems. This research pointed out how the proposed reliability index can guarantee a better description of the behavior of the system in terms of its state and how it can be a new and interesting tool for the investigation of comparability and interoperability of measurements taken from different sensors.

The second application, instead, is entirely devoted to MV distribution networks. They are characterized by different specifications with respect to transmission power systems, e.g., shorter line lengths and radial configurations, hence, if their measurement infrastructure is based on PMU devices, different requirements are needed. As a matter of fact, in this case, the objective consisted of the evaluation of target uncertainties to ensure correct and reliable measurements.

Based on the obtained outcomes, it emerges the substantial impact on the measurement uncertainty of the components constituting the measurement chain, in particular, the LPVTs. Comparing these results with the typical characteristics of distribution networks, the target uncertainty for voltage magnitude and phase angle are derived. More in detail, no major issues can be encountered when measuring the voltage variations in magnitude. Nevertheless, the same cannot be said for the phase displacements at the end of a typical MV line. Indeed, this measurement cannot be obtained despite the best achievable PMU-based measurement chain. The results of this study point out the need for defining performance targets for PMUs in distribution networks, still leaving ample space for further research.

Lastly, the third study analyzed the impact of the frequency estimates assessed by means of PMUs at the transmission level. Specifically, two real-world contingencies that involved the splitting of CE into separate synchronous areas were evaluated. By analyzing three different algorithms compliant with the P- and M-class of the PMU Std, it resulted that it is of the highest importance to associate an uncertainty with the frequency, especially during transient conditions. In fact, the first case study showed a perfect overlap between the frequency error bandwidths in the two synchronous areas after the resynchronization. In contrast, in the second case, the frequency of the area to be reconnected started oscillating around its rated value since the two frequencies were barely within ENTSO-E guidelines.

This study indicated that the ±200 mHz threshold suggested by the ENTSO-E policy could be insufficient to ensure a safe resynchronization. As proven by the results, comparing this threshold with the PMU frequency uncertainties, it is possible to derive that the frequencies should have overlapping error bandwidth in order to ensure a safe resynchronization. Therefore, the results of this research indicate the relevance of estimating the uncertainty to be associated with time-varying quantities before and after performing counteractions on HV transmission systems.

Chapter 5

Power System Inertia Fundamentals and Models

In the latest years, the ever-increasing installation of renewable-based generation at various levels is threatening the stability of traditional power systems. This is owing to power electronic converters which constitute an interface between such renewable-based sources and the rest of the system: in this way, modern generators do not contribute to the overall system inertia as old traditional synchronous machines did. As a result, the overall inertia has been progressively reducing, resulting in faster and more severe transients in case of contingencies. This Chapter provides an introduction to power system stability and a thorough literature review of the state-of-the-art of power system inertia. The main algorithms presented in the recent literature are briefly discussed and commented on, explaining the need for assessing inertia from a metrological point of view. Lastly, this is followed by the presentation of the two power system models used in the next Chapter for various applications.

5.1 Introduction and State-of-the-Art

With the aim of reducing emissions by 45 % by 2030 and reaching net zero by 2050, the increase in the installation of RES at various power system levels is ever-more increasing in a significant number of countries worldwide [109].

However, the wide penetration of DG is prompting many technical challenges that are required to be tackled. As an example, these resources cannot be connected directly to the grid, but rather they require dedicated power converters in order to be securely interconnected, constituting the so-called CIG. Besides the evident environmental benefits, DG promises to improve grid efficiency by increasing the proximity and the correlation between power generation and consumption [88, 110].

On the contrary, though, many challenges are posed from the operational and planning point of view. For instance, most of RES rely on weather conditions, e.g., solar irradiance, wind speed, and so on, which are volatile and uncontrollable. In this context, a peculiar situation is the one present in the South Australia State, of Australia. This region is strongly characterized by the presence of RES, in particular by wind turbines which have an overall capacity of 2437 MW produced by 23 facilities [111]. This region has already been subject in the past to a well-known blackout in 2016 which caused the disconnection of the entire area to the rest of the power system [12]. Indeed, this scenario is studied in Section 4.2 from the PMUs' measurement reliability point of view. It is of certain interest to observe a peculiar condition that was verified just recently. Indeed, it can be examined the generation profile, in MW, recorded during the week between July 26th and August 2nd, 2023. During

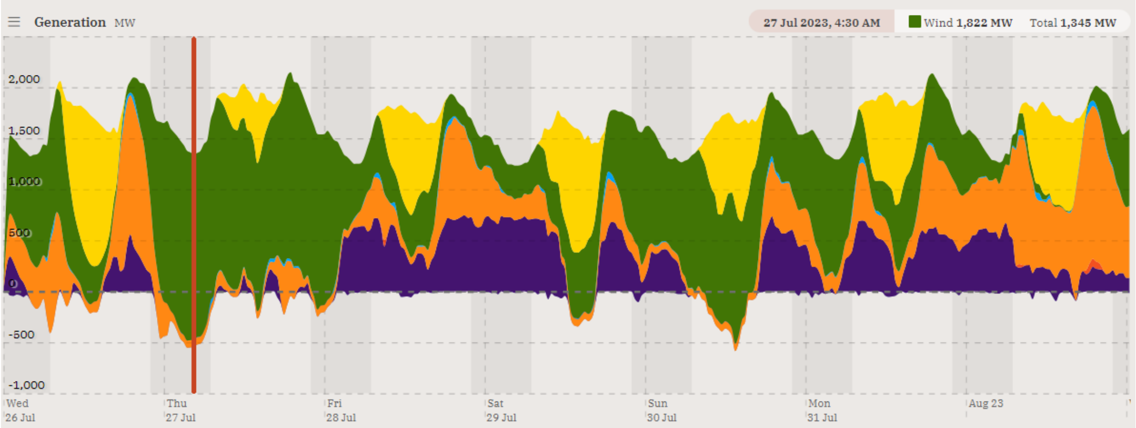

Figure 5.1: Energy generation mix, expressed in MW, in the South Australia region of Australia recorded during the week in between July 26th and August 2nd 2023. The vertical red bar indicates the time at which the wind power production peaked. Source: [111].

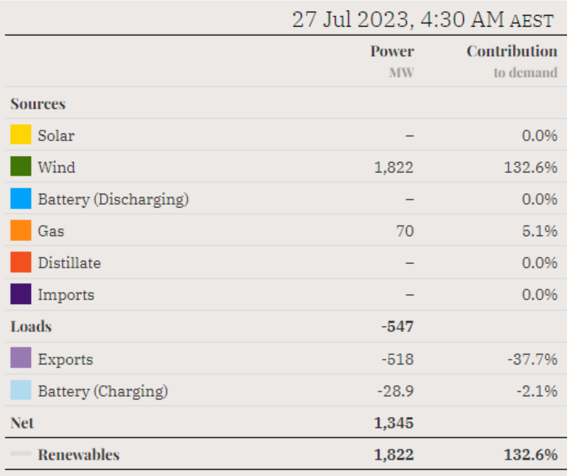

27 Jul 2023, 4:30 AM AEST

	Power MW	Contribution to demand
Sources		
🟨 Solar	–	0.0%
🟩 Wind	1,822	132.6%
🟦 Battery (Discharging)	–	0.0%
🟧 Gas	70	5.1%
🟥 Distillate	–	0.0%
🟪 Imports	–	0.0%
Loads	**-547**	
🟪 Exports	-518	-37.7%
🟦 Battery (Charging)	-28.9	-2.1%
Net	**1,345**	
Renewables	**1,822**	**132.6%**

Figure 5.2: Legend of the generation mix, indicating for each source of energy the generated power in MW and the contribution to the overall demand in %. This table refers to the data recorded on July 27th 2023 at 4:30 AM AEST, corresponding to the vertical red bar in Fig. 5.1. Source: [111].

this week, the energy generated by renewables was more than 100 % as shown in Fig. 5.1[1]. In correspondence with the vertical red bar, it is possible to notice that the generation reached even 132 %, most of which was produced by wind turbines for a total amount of 1832 MW, as depicted in the legend in Fig. 5.2. This scenario indicates the criticality of the operation of the power system in the South Australia State which is subject to volatility and, at the same time, the strong presence of RES which deeply affect the management of the power system.

Another significant challenge entails the consequent reduction of power system inertia, resulting from the replacement of traditional synchronous machines with CIG. More precisely, in such a condition the power system is more likely to be subjected to fast dynamics and transients [112]. Hence, protection schemes and counter-maneuvers are required to act in a prompter way for the same contingency. In this context, it is also worth highlighting that the PMU measurement infrastructure is also strongly affected. Indeed, they have been designed for traditional transmission power systems characterized by high-inertia conditions and little variations [74, 88]. Indeed, from a metrological perspective, this represents a critical aspect for PMUs since most of them rely on static and narrow-band signal models [88].

---

[1] It is worth clarifying that the reference value, i.e., 100 %, corresponds to the forecasted power demand by the South Australian TSO.

In a low-inertia context, the greatest criticality typically involves frequency and ROCOF measurements. In this regard, a Technical Specification has been recently published in July 2023. The aim of IEC TS 62786-41 is to provide a list of use cases, comprising synthetic inertia and anti-islanding detection, as well as the associated requirements to control DER and loads [113]. However, significant work is still required in terms of normative requirements and metrological infrastructures. For what concerns the first one, it is crucial to underline that inverters' requirements over time are slowly changing. In the past, they were required to disconnect from the grid when the frequency reached 50.2 Hz, working in the so-called "grid following" mode. Nowadays, they work in a "grid supporting" mode as they have fault-ride-through capabilities[2]. Normative requirements and testing specifications have been either recently issued or are expected to be published in 2024, such as the EN 50549-10 and the IEC 63409 series [115, 116]. In the future, instead, CIG is expected to provide a form of *synthetic inertia* and "grid forming" capabilities [117]. In this context, some works recently published in the scientific literature hypothesize a future grid comprising only of RES without any inertia [118–120].

On the other hand, with regard to the necessity of establishing metrological requirements and developing a suitable measurement infrastructure, one project has been recently funded and one has just finished in Spring 2023. The latter is EdgeFLEX which is a H2020 project that has recently come to an end. It aimed at the development of solutions based on renewable sources that provide flexibility to the energy system. It focused on the development of virtual power plants and on enhancements of the measurement infrastructure constituted by PMUs, also in low-inertia conditions [121]. The second project, which was only recently funded in October 2022 by the Swiss Federal Office of Energy, is called Measurement and QUantification of INertia on electrical power systems to supPORT integratION of renewables, briefly QUINPORTION. Among its objectives, it is worth mentioning the development of a novel PMU prototype, more resilient with respect to harmonic distortion and capable to cope with amplitude and phase fluctuations that are, as previously disclosed, ever more present in low-inertia power systems. It also focuses on the definition of new inertia measurement methods that rely on PMU measurements and account for their inherent uncertainty [122]. The latter is still strongly discussed as no International Standards are available, much research is yet to be performed in this regard, as it is better discussed in the next Sections. These projects are worth mentioning as they funded the research presented in this and in the next Chapter 6.

---

[2] Fault-Ride-Through can be defined as the ability of the generating units to ride through transmission system faults and disturbances whilst being connected to a healthy system circuit. This is a fundamental requirement to maintain the system's security and prevent a wider frequency collapse [114].

The next Sections 5.1.1 and 5.1.2 present in brief long-discussed topics such as power system stability and inertia, highlighting only the key concepts. The following Section 5.2 illustrates a literature review on the inertia estimation algorithms, based on their most common classification. It also shows the main challenges that are faced nowadays and it details the algorithm that is studied in the scenarios presented in the next Chapter 6. Lastly, in Section 5.3 the two power system models that are used for the evaluation of the algorithm are shown.

5.1.1 Power System Stability

The aim of this Section consists in presenting a simple overview of a broad topic such as power system stability and the key concepts of inertia. The focus of this Section, though, is mainly on the reasons for which inertia shall be assessed and on the measurement infrastructure that is required in order to do so.

Power system stability is a target that every TSO and DSO aim at achieving during their daily management of transmission and distribution power systems. The *stability* of an electric power system can be defined as its ability, for a given initial operating condition, to regain a state of operating equilibrium after being subjected to a physical disturbance, with most system variables bounded so that practically the entire system remains intact [123].

Three main typologies of stability can be identified in power systems. The first one entails *voltage*: voltage stability includes both short-term and long-term stability, for both small and large disturbances. The second, instead, deals with *rotor angle stability*: it includes transient stability and small-disturbance angle stability. Lastly, there is *frequency stability*. It can be further divided into short-term and long-term stability. The first refers only to the time frames up to tens of seconds and involves fast frequency deviations, occurring owing to the momentary power imbalances. Whereas long-term stability includes longer time frames, spanning from tens of seconds up to several minutes.

In order for a power system to work correctly, the amount of total active power, including both generated and imported ones, shall be equal to the total consumed and exported power, comprising the system losses. The index that is commonly used to represent this balance between *generation* and *load* is the *frequency*. When an active power imbalance occurs, i.e., there is a difference between the generation and the load following a disturbance, the frequency will deviate from its nominal value. Therefore, it can be directly derived a relation between active power and ROCOF: as long as the active power balance is not met, ROCOF cannot be equal to zero. Nevertheless, the frequency shall remain within a specified range centered around its nominal value which is specified in the relevant Standards such as [21] for LV and MV power systems and ENTSO-E guidelines for transmission power systems, as in [124]. It is also worth specifying that these guidelines typically indicate the required actions that should be taken in order to restore the nominal frequency and reduce the risk of damaging power system components and prevent blackouts.

A power system can be regarded as *frequency stable* when it is able to maintain its frequency in-between predefined limits after a disturbance, which causes an imbalance between generation and load. Frequency stability depends on three main factors that are detailed here as follows:

- Power imbalance: as already disclosed, it is the difference between generation and load after a disturbance. It can be caused by a sudden disconnection of a load or generator. However, in general, the larger the power imbalance, the greater the instantaneous frequency deviation.
- Reserves: they represent the additional power that can be provided to the system as frequency support, for instance via HVDC links.
- Inertia: it is the parameter that defines the behavior of the frequency just after a disturbance. The higher the inertia, the more power can be extracted from rotating masses to the grid. When a power deficit occurs, a higher inertia represents a higher resilience of the power system to a frequency decline.

Without loss of generality, two main scenarios can take place: either the power required by the loads is greater than the generated power or vice versa, i.e., the produced power is greater than the active power required by the loads. The latter is an *over frequency* event where the inertial response corresponds to the absorption of kinetic energy from the rotating masses of the synchronous machines. Hence, the speed of the machines increases and, consequently, the system frequency increases. Such events can be easily tackled by either reducing the generated power or transferring it via dedicated HVDC links when available. As an extreme countermeasure, Over-Frequency Generator Shedding (OFGS) can be performed.
On the other hand, in the case of *under frequency* events, the inertial response occurs as a release of kinetic energy stored in rotating masses of the synchronous machines to the grid. Consequently, synchronous machines slow down, and the system frequency declines. The generation should be increased, or, in case that is not feasible, the UFLS scheme should be activated, in order to reduce the active load power and prevent cascade effects or, in extreme conditions, power system blackouts.

5.1.2 Fundamentals on Power System Inertia

As previously disclosed, the ever-increasing installation of RESs at various levels of power systems is threatening their stability. As a matter of fact, most RESs do not have any rotating parts, such as PVs, or they are decoupled from the rest of the power systems, as WTs, therefore they provide little to no inertia[3].

As a consequence of the progressive reduction of power system inertia, following a disturbance, not only does the frequency drop by larger extents but it also occurs in shorter times, as shown in Fig. 5.3. The graph, indeed, shows the behavior of the frequency after a loss of production when the amount of kinetic energy in the system varies. Solid lines indicate the case in which the FCR begins to respond to the decreasing frequency, whilst dotted lines represent the same situation, but without FCR [125]. This also implies that protective schemes and counter maneuvers

---

[3] A behavior similar to inertia can be replicated only for high-rated power generators participating in frequency control. Additionally, suitable controls and extremely responsive algorithms on active power need to be implemented.

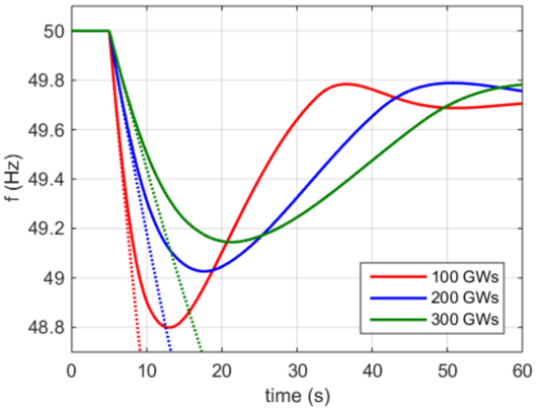

Figure 5.3: Frequency responses for three different amounts of kinetic energy after a loss of production. Solid lines represent the behavior with FCR, while dotted lines indicate the response without it. Source: [126].

shall be able to act prompter for the same contingency. Additionally, the primary response could be too slow to contain frequency deviations.

The governor response (also known as the primary control) corresponds to the power output adjustment of the synchronous generators required after a disturbance to arrest the declining system frequency. In case the governor's response is insufficient, the frequency decline will continue, leading to UFLS and generation outages. Lastly, in a low-inertia power system, the network itself is less capable of managing system losses: this results in an overall increase in ROCOF and great deviation from the operating point for given losses [127]. Hence, in the latest years, there has been an increase in the necessity of assessing power system inertia to evaluate the frequency response of a system in order to evaluate its behavior.

Proposed solutions able to provide fast frequency response to sustain power systems following transient events include the use of adaptive UFLS techniques as in [128–130]. Alternatively, storage activation could represent a valuable solution: the intermittent nature of RESs can be partially suppressed using ESSs, minimizing the impact on power systems. Lastly, synthetic or virtual inertia represents a promising solution. Especially for what regards WTs, virtual inertia can help in "buying time" for primary control [131, 132]. In the latest years, similar techniques have been developed also for PV plants, adopting specific control algorithms [133, 134].

In this context, it is worth specifying the typologies of interfaces that can be realized in order to connect the so-called CIG to the rest of the power system. In the past, RESs were typically interfaced via a Grid-Connected Converter (GCC) which was not designed to provide any virtual inertia. For this reason, the overall power system inertia kept on reducing throughout the years. Nevertheless, even though virtual inertia can be provided, this inertia is not entirely equivalent to the traditional one provided by synchronous rotating machines as GCCs behave similarly to ESSs distributed in the power system. Therefore, further studies should be conducted to find out the difference between the two types of inertia [135, 136].

On the other hand, a Grid-Forming Converter (GFC), when suitably controlled, is able to provide virtual inertia which resembles the traditional one. If there were only GFCs but no synchronous generator in the power system, then the way the power system frequency could be completely controlled and changed independently.

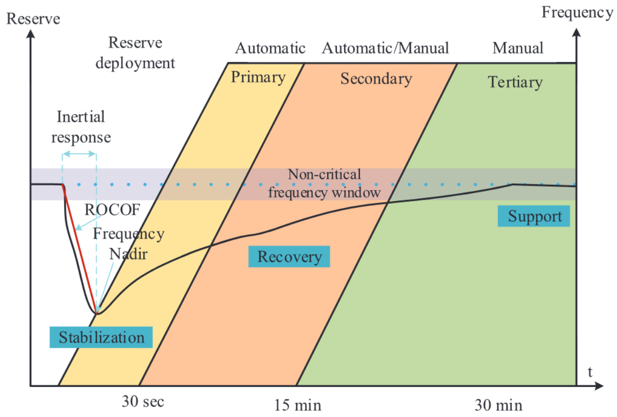

Figure 5.4: Frequency response in time, highlighting the activation stages of the three reserves. The stabilization, support, and recovery steps are emphasized, based on ENTSO-E data. Source: [142].

As a matter of fact, GFCs can control the frequency at a fixed value, similarly to a Uninterruptible Power Supply (UPS), hence there would be no need to have inertia [118–120]. Also in traditional GCCs, the energy stored in the DC-link of the power converter can support low-inertia events. However, due to the proportional relationship between the DC-link voltage and the grid frequency, the DC-link voltage cannot restore its nominal value after releasing the power required by inertia emulation as long as the grid frequency deviation exists. Furthermore, a low DC-link voltage may lead to an overmodulation of GCCs, in case another DC-link voltage drop is yielded by sudden load changes. Lastly, the GCCs cannot provide multiple inertia support in the face of cascading frequency events. However, different techniques are being developed in this context, especially for what concerns the restoration of the DC-link voltage involving the implementation of high-pass filters [136–140].

Nonetheless, the problem concerning RESs and synthetic inertia is still strongly debated and no state-of-the-art is yet available. This subject has been briefly introduced for the sake of completeness, however, it is out of the scope of this work. For this reason, in the following, the focus is only on traditional inertia.

For what concerns traditional inertia, indeed, after the occurrence of a disturbance, the protection system is triggered by either the ROCOF value or the Instantaneous Frequency Deviation (IFD), which is the maximum or minimum frequency nadir [127]. As described in the previous Section, the frequency (or ROCOF) of a power system is an index that represents the balance between generation and load. However, after an event, it does not change instantaneously due to power system inertia. As a matter of fact, the generation initially remains the same and it takes some time for frequency control actions, or governors, to react. Typically, governors start to react to a disturbance after at least 500 ms to 1 second [141]. For instance, if a disturbance causes a reduction in the generation, the kinetic energy stored in the rotating masses of the generators is released to the grid and the frequency begins to decrease as the speed of the generators decreases. After a while, the generator governors respond to this frequency drop. The inertial and the governor response constitute the so-called *frequency response*, as illustrated in Fig. 5.4.

In the following Section 5.2, a literature review on the main inertia estimation algorithms is presented.

5.2 Inertia Estimation Algorithms

The objective of this Section is to provide an overview of the main categories of inertia estimation algorithms present in the scientific literature, as well as their most significant characteristics and the main challenges that are still unsolved. A first clarification is worth mentioning: it must be noted that inertia can be generally *estimated*, rather than *computed* or *measured*. One of the reasons behind this stems from the fact that the inertia contribution of each generator unit must be included. Within each synchronous area, data exchange among TSOs is required, in order to assess inertia in large synchronous regions. Additionally, each TSO has a good, yet not complete, overview of the system state, including which large conventional power plants are in operation at each moment in time. Finally, to correctly estimate inertia, it is also important to have a good picture of the load composition and of their connection. However, it is difficult to know precisely these pieces of information since loads are both time-varying and stochastic [143].

5.2.1 Algorithms Classification

Two main categories of inertia estimation algorithms can be identified: the first one relies on swing-equation-based techniques, which are analyzed as follows. In this method, the inertia is estimated by observing the dynamics between the changes in active power (ΔP) and the resulting frequency deviations in time, i.e., ROCOF, (df/dt) during the normal operation of the power system. The well-known swing equation relates the system inertia to the dynamic changes in rotor angle and the generation load power mismatch [144].
A similar method relying on the same rationale, but based on small disturbances, can be employed. It allows for identifying the online inertia of a power system using a closed-loop method, based on small perturbations, so that inertia can be monitored nearly continuously in normal operating measurements [145]. In a similar way, [146] relies on an analogous method that represents an optimal solution for pre-assessing the system frequency behavior in response to hypothetical disturbances. However, limitations of such methods typically involve long time delays due to the heavy computation burden, and low accuracy of the measurements (errors barely lower than 20 % can be observed as in [146]). The system observability can represent an additional hurdle as well as multi-machine systems in which the so-called Center-Of-Inertia (COI) needs to be defined.

Before moving on to the second typology of estimation algorithms, it is worth detailing better the concept of COI. The COI represents the average system frequency, or inertia, for a highly meshed network, thus mostly referring to transmission grids, where all generators of the system are interconnected. This concept is widely used in inertia estimations, however, it suffers from some limitations.

First of all, in case PMUs are widely deployed, they could perform this kind of distributed measurement easily. In spite of the fact that a COI can be obtained, it cannot be regarded as a unique value throughout the power system. Since PMUs' performances are strongly dependent on the location of the measurement, their assessment of the COI may highly deviate [147]. The COI could be chosen as the location of the power grid showing the smallest oscillations, nevertheless, the

Authors in [125] proved that a single COI cannot represent all operating conditions, as errors higher than 50 % are observed. On the contrary, if data from only a single location is available, the time of the disturbance and the power system inertia could be estimated simultaneously. However, this method can work well only for small and/or homogeneous systems [148]. Lastly, the necessity of having complete observability using SCADA systems is required: the status of the generators' circuit breakers and overall power production and demand are mandatory inputs in order to assess inertia online from network status, as already done by Nordic TSOs [126]. In the same context, the use of historical data and events has proven to help in inertia estimation algorithms, as in [149].

The second method of inertia estimation, instead, involves recursive state-based techniques. Such routines rely on the recursive state-based estimation of the system inertia and investigate the states of statistical models of the power network whose parameters are updated in a recursive manner [144]. They require real-time observations of both system topology and measurements of selected system variables, such as power or frequency, which are needed for the purpose of online state updating. These methods are based, for instance, on historical data sets of inertia or frequency, machine-learning based algorithms, KFs, etc. ...).

Among their limitations, it is worth citing the need for algorithm training to learn the features relating to the steady-state average frequency variations and system inertia. Additionally, the complexities of the wide range of parameters that need to be updated can represent a challenge. Lastly, the identification of electromechanical modes, or aggregated models of the prime mover-governor dynamics, is another difficulty in the system model identification.

A further classification, as presented in [150], can be made based on the time at which the estimation takes place. More in detail, there exist offline, online, and prediction methods. The first ones provide a-posteriori information which can be useful in scheduling and planning stages but cannot be useful for preventive or corrective actions in real-time. Indeed, these techniques are used to study and evaluate the values of inertia constant in the network after events of contingencies. Online methods allow TSOs to estimate inertia continuously, thus reducing low-inertia conditions and enabling correct frequency response reserves. Most of the proposed methods exploit the distributed infrastructure realized by PMUs to record real-time measurements from the network, which are used for the online estimation of the inertia constant in different perspectives. Lastly, inertia prediction methods enable forecasting inertia values in the network, to determine when the network will be at risk and which appropriate measures can be taken in advance. Regarding the last category, only a very limited number of algorithms is present in the literature.

Offline Estimation Methods

The first method used by the Authors in [147, 151] consists in the estimation of the inertial frequency response of the transmission network of the United Kingdom, based on the rate of change of frequency, following an imbalance between supply and demand. The total inertia of the British power system was determined, by dividing the network into groups of generations, before combining it to get the total estimate for the whole network. The so-called RV and V-methods, instead, can approximate the power imbalance and the inertia of the system, without introducing errors in the estimation, starting from frequency and voltage variations [127]. A dynamic estimation algorithm, presented in [152], uses data from PMUs and is able to estimate the inertia of a system and its COI. It starts from the swing equation, then it uses a Butterworth filter to get rid of high-frequency noises and a clustering algorithm to estimate the COI and eliminate bias from the measurement location. In [153, 154], the Authors focus on estimating the values of the effective inertia of each area rather than the equivalent inertia of the entire system. They derive a mathematical relationship between the effective inertia of each area and the inter-area oscillation modes. Specifically, [154] points out that it is more reasonable to estimate the available inertia of generators in an area independently, followed by an aggregation to retrieve the system's total inertia. Therefore, it proposes a continuous online generator inertia monitoring method, including both large disturbance and ambient signals from PMUs. Indeed, this algorithm can be classified as an in-between online and offline methods. Lastly, a data-driven approach is shown in [155, 156] which is valid in normal operating conditions, with PMUs dedicated to measuring system data and estimating a dynamic model of the system.

Differently from all the presented works, it is worth citing [157]. In this study, the Authors present an analysis of different dynamic oscillations using data from a domestic supply side of PMUs in a Japanese island characterized by high penetration of PVs. Different tests are carried out based on weather conditions, computing the system frequency and ROCOF based on phasors measured by PMUs.
The results indicate that there exists a correlation between frequency and ROCOF with the high penetration of PVs. ROCOF increases significantly in line with a stronger presence of PVs. However, this is in contrast to the frequency, meaning that ROCOF could assist DSOs to analyze grids in which a low-inertia criticality is present. Nevertheless, in this research, no direct calculation of the power system inertia is performed.

Online Estimation Methods

Among online techniques, it is worth mentioning [145]. In [145], the Authors present a method for estimating power system inertia from ambient frequency and active power signals measured by PMUs. Not only can inertia be measured from disturbances, but it can also be assessed in near real-time, i.e., in time ranges spanning from minutes to tens of minutes. The concept of "effective inertia" is introduced: it defines the relationship between a change in the power balance of the system or area and the rate of change of frequency of that area, in contrast to the traditional definition of inertia related to physical spinning masses. The Authors in [158], instead, use the available electromechanical oscillation modes in the system, which are linked with system parameters, to determine inertia estimates. An algorithm that allows to estimate in real-time the inertia constant and the aggregated mechanical power set-point of a large-scale power system, as the ENTSO-E test system with 1013 machines, is presented in [159]. Conversely, the Authors in [160] present an analytical method based on the ROCOF measured by PMUs and relying on the swing equation to estimate simultaneously the loss of generation and the power system inertia. The proposed method also takes into account the reporting latency of PMUs. On the contrary, [161] illustrates an online estimation method for power system inertia constant under normal operating conditions. Finally, [162] presents an artificial neural network, using the power system variables measured by PMUs through WAMPAC, for estimation/forecasting of power system inertia with high penetration of wind farms. In the beginning, a correlation analysis is performed, aiming at identifying the best power system variables that can be used as inputs.

Inertia Prediction Methods

As already disclosed, prediction methods constitute only a small portion of all inertia estimation algorithms. It is worth mentioning [163] and [164] that present a forecasting-based virtual-inertial control that enables PVs to serve as an alternative inertia supplier without using any ESS. However, they are both specific for islanded microgrids that feature different characteristics and control strategies from traditional power systems. The Authors in [165], instead, propose the use of a decomposable time series model to short-term forecast the total kinetic energy of a power system. The choice of forecasting the latter rather than the rotational inertia was based on the fact that rotational inertia depends on the rated power of the generation unit. Hence, using the kinetic energy avoids referring to a common base for all the inertia constants. A system recording the total kinetic energy of the Nordic power system was already installed in 2020, therefore, there is a source of historical data that can be used for forecasting. The results are deemed promising, albeit up to 7 % errors can be observed for 24-hour forecasts. Lastly, [166] suggests an algorithm that optimizes system operation by scheduling the energy production, the spinning reserves, and the inertia-dependent fast frequency response simultaneously. It also evaluates the impact of wind uncertainty on system inertia.

5.2.2 Challenges in Inertia Estimation

As it could be inferred from the analysis of the main inertia estimation algorithms shown in the previous Section 5.2.1, there still exist numerous unsolved challenges in inertia estimation, besides the metrological ones that are rarely examined.

First of all, the identification of the exact moment of a disturbance is of utmost importance as it is crucial for ensuring a correct correlation between ROCOF and the power constituting the disturbance (ΔP_{dist}). Two main solutions are presented in literature: a moving average filter can be used to get rid of noise from the measured frequency transients and setting a threshold for ROCOF as in [167]. Nevertheless, disturbances do not propagate instantaneously in power systems, hence discrepancies between ROCOF and ΔP_{dist} can be observed. Plus, for some events such as the disconnection of generators at different times, this method does not apply [147]. In the same scenario, the power imbalance can be significantly different from ΔP_{dist}, owing to the voltage dependency of loads. This result worsens in case ROCOF at later stages is examined, since governors have already responded [127].

A second challenge entails the quality of frequency measurements: ROCOF is usually derived from frequency measurements, hence it is essential to measure frequency as accurately as possible. Possible solutions include the use of high-order polynomials to eliminate oscillations in measured data and the use of low-pass Butterworth filters [151]. In the same context, no research deeply analyzes both the system frequency and ROCOF against high RESs penetration [157]. Plus, the location can also constitute a significant hurdle in frequency estimation: as a matter of fact, frequency deviations are observed sooner in the regions of the grid closer to the disturbance. A possible solution can involve the wide deployment of PMUs to perform distributed frequency measurements in different locations to assess the system's average frequency. However, as described in Chapter 4, PMUs are still typically employed by TSOs at specific locations at the current stage.

It is also worth commenting that, nowadays, there is only one real-time measurement system to assess inertia. This project, which is still at a very preliminary stage and is adopted by the British TSO, intends to measure power system inertia, based on a distributed measurement system made up of devices similar to PMUs [168]. The measurements are performed by perturbing the system exploiting a battery storage system of a couple of MW and providing a sort of "power impulse" to the grid. In this way, it is possible to perform signal analysis on the power system frequency signals to estimate inertia.

Nevertheless, at present, no studies in the literature have attempted at considering the uncertainty to be associated with inertia estimates. However, many works are able to provide typical errors of their suggested algorithms[4]. This could stem from the high errors, which are already non-negligible in the estimation of inertia, i.e., around 5 to 7 %, can be observed in the best cases [169]. For what regards, distribution grids, instead, most of the works focus only on the computation of frequency and ROCOF as in [157]. Whereas, inertia in microgrids is better investigated [170, 171]. Nevertheless, they constitute a specific condition that features different characteristics from the rest of the power system, e.g., different load configurations, their own generators, and shorter line lengths.

To summarize, a common factor that can be found among all inertia estimation algorithms, regardless of their classification, is the simultaneous measurement of frequency, or its time variation, and power. As a matter of fact, independently from their complexity or the use of advanced routines, all algorithms require frequency and power measurements to produce results as accurately as possible. For this reason, the following Section 5.2.3 presents in detail the theoretical concepts behind the swing-equation-based approach. It is the foundation of all algorithms and it represents the simplest form of evaluation of inertia as well as COI. Therefore, in the following, this approach is used for the evaluation of power system inertia by means of PMUs at distribution and transmission levels.

5.2.3 Swing-Equation Based Approach

According to power system theory, the swing equation illustrates the electromechanical dynamics of the rotor of the i^{th} generator, namely how the electrical and mechanical parts of the rotor interact with each other [141].

---

[4] It is worth recalling that the *error* of an algorithm results from the measured value minus a reference value. Conversely, the *uncertainty* of inertia represents the dispersion of the values being attributed to the measurand according to the definitions of [15].

$$J_i \frac{d\omega_{mi}}{dt} = T_{mi} - T_{ei} \tag{5.1}$$

where J_i is the total moment of inertia of the turbine, shaft, and generator, expressed in kg $\cdot\, m^2$, and ω_{mi} is the mechanical rotating speed of the rotor in rad/s. T_{mi} is the mechanical torque, or torque of the turbine, expressed in Nm; while, T_{ei} is the electromagnetic torque, or torque of the generator, expressed in Nm.

The inertia constant H_i of a single i^{th} generator is given by:

$$H_i = \frac{J_i \omega_{mi}^2}{2S_{ni}} \tag{5.2}$$

where S_{ni} is the rated power of the generator in VA, whilst the other variables have already been introduced. Given the fact that during frequency events the speed ω_{mi} does not vary significantly from its rated value, then it is acceptable to replace ω_{mi} with the rated speed of the generator ω_{msi}. From a physical point of view, the inertia constant H_i of the i^{th} generator, expressed in seconds, represents the time that it takes to immobilize a generator that rotates at synchronous speed. Typically, this value ranges between 1 to 10 seconds [141].

Skipping some steps in introducing Eq. (5.2) into Eq. (5.1) and rewriting it for small changes around the operating point, Eq. (5.1) becomes:

$$2H \frac{df(t)}{dt} = \Delta P_{mi}(t) - \Delta P_{ei}(t) = \Delta P(t) \tag{5.3}$$

where H is the inertia constant, in s, of the generic i^{th} synchronous generator; f represents the frequency at its terminals, expressed in Hz. ΔP_{mi} and ΔP_{ei} are the mechanical and electrical power deviations, respectively, in W.

When evaluating the response of the power system after an electromechanical transient, as previously disclosed when treating ω_{mi}, the mechanical time constant can be regarded as much larger than the electrical one. For this reason, it is acceptable to neglect the mechanical contribution, i.e., $\Delta P_{mi} \approx 0$, and approximate the power variation only with the electrical one. This further simplifies Eq. (5.3) as:

$$2H \frac{df(t)}{dt} \approx -\Delta P_{ei}(t) = \Delta P(t) \tag{5.4}$$

Given a contingency occurring at the time instant $t = t_0$, Eq. (5.4) can be rewritten for the inertia constant H as:

$$H = \frac{P_e(t_0^+) - P_e(t_0^-)}{2\left[\frac{df(t_0^+)}{dt} - \frac{df(t_0^-)}{dt}\right]} \tag{5.5}$$

where t_0^- and t_0^+ indicate the time instant before and after the contingency, respectively. However, in general, it is necessary to study the electromechanical dynamics of the whole power system which comprises more than one single generator. Hence, the total inertia of a power system is calculated as:

$$H_{COI} = \frac{\sum_{i=1}^{n} H_i S_{ni}}{\sum_{i=1}^{n} S_{ni}} \tag{5.6}$$

where i is the i^{th} synchronous machine out of a total of n. H_{COI} corresponds to a weighted average of the inertia constants of all the synchronous machines over their rated power. H_{COI} is the overall inertia of the power system and it is associated with the COI. The inertia constant and the kinetic energy that is stored in the rotating masses of a system, E_k, are directly related as follows:

$$E_k = \sum_{i=1}^{n} H_i S_{ni} \tag{5.7}$$

As described in the aforementioned Sections, the frequency does not have a unique value throughout the whole power system, following a disturbance. If generators stay synchronized after an event, they will have a similar frequency trajectory with inter mutual swings. In order to apply the swing equation to an entire power system, a representative average frequency signal of the whole system needs to be defined. This signal is the frequency of the COI and is computed as follows:

$$f_{COI} = \frac{\sum_{i=1}^{n} \left(S_{ni} H_i\right) f_i}{\sum_{i=1}^{n} S_{ni} H_i} \tag{5.8}$$

It can be introduced to represent the average system frequency and it can be regarded as an imaginary bus, where all generators of the system are connected. For a highly meshed system, f_{COI} represents well the average frequency, however, the same cannot hold for radial, distributed systems.

Hence, the electromechanical dynamics of an n-machine power system are described by Eq. (5.9), which can be obtained by introducing in Eq. (5.3) the concept of COI as in Eq. (5.6) and Eq. (5.8):

$$\frac{2HS_n}{f_s} \frac{d\Delta f_{COI}(t)}{dt} = \Delta P_m(t) - \Delta P_e(t) = \Delta P(t) \tag{5.9}$$

where f_s is the power system rated frequency, in Hz, and S_n is the sum of the generators' rated powers in VA. ΔP_m and ΔP_e are the total mechanical and electrical power deviations, respectively. ΔP is the power imbalance which usually can be approximated with $\Delta P_e(t)$ only.

Eq. (5.9) can be rewritten using the per unit method, as:

$$2H \frac{d}{dt} \frac{\Delta f_{COI}(t)}{f_s} = \frac{\Delta P_m(t) - \Delta P_e(t)}{S_n} \approx \frac{\Delta P_e(t)}{S_n} \tag{5.10}$$

where $f_{COI}(t)/f_s$ is the frequency of the COI expressed in per unit and $\Delta P_e(t)/S_n$ is the power variation, approximated with only the electrical one, in per unit value.

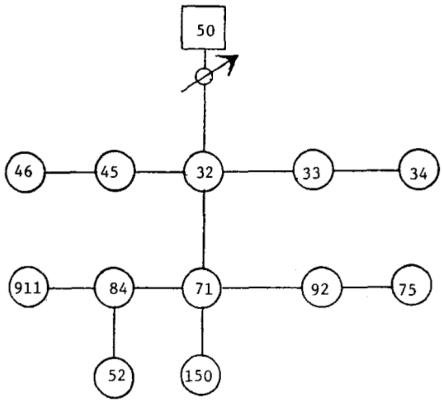

Figure 5.5: IEEE 13-bus system scheme, as illustrated in its original presentation. Source: [172].

In the following, the swing equation is applied in different forms, both at local and at a global level, in various scenarios using measurements retrieved from PMUs.

5.3 Low-Inertia Power System Models

As disclosed at the beginning of this Chapter, more precisely in Section 5.1, not only is the progressive installation of RES taking place at the transmission level, but it also occurs at lower levels in distribution grids[5]. For such a reason, two power system models have been considered: a transmission and a distribution one. Therefore, the aim of this Section is to present the two models and briefly disclose their corresponding low-inertia versions. The latter will be better specified for each application in the following Chapter 6, in order to specify only the additive components and modifications, e.g., RES models or particular test conditions.

5.3.1 Distribution Power System Model

As a distribution network, the well-known IEEE 13-bus power system, as shown in Fig. 5.5, is the simulated scenario considered in the following Chapter 6. It well represents a typical distribution grid comprising two feeders and a combination of single- and balanced/unbalanced three-phase loads, as well as both overhead and underground lines. However, some modifications have been performed with respect to the original data presented in [172].

Firstly, all line lengths have been multiplied by a factor of 10 in order to represent a wider distribution system. Second, the On-Load Tap Changer (OLTC) transformer connecting Bus 50 to Bus 32, as in Fig. 5.5, has been neglected. Afterward, since this model is well suitable for simulating the presence of RES at various levels, in Chapter 6, a combination of PV plants and ESSs at MV and LV levels are simulated. All

---

[5] Although power system inertia is still barely examined at low-voltage levels, it is evident how microgrids are more and more widespread. Such scenarios are particularly challenging from a design and control point of view, hence a MV power system model is considered in the following low-inertia studies.

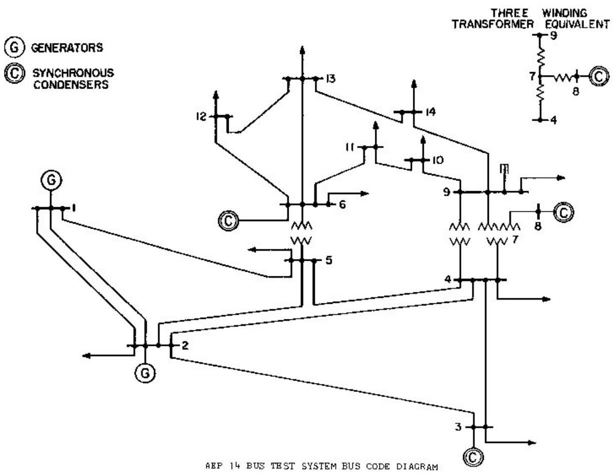

Figure 5.6: IEEE 14-bus system scheme, as illustrated in its original presentation. Source: [173].

modeled PV plants comprise time-varying solar irradiance cycles in order to recreate a time-varying output power that can constitute a reasonable scenario. Lastly, a Circuit Breaker (CB) is added and simulated in between Bus 71 and 92, in order to recreate additional transient conditions.

For the sake of completeness, the following Sections will detail the individual modifications that have been carried out for this distribution network under test.

5.3.2 Transmission Power System Model

As a transmission power system, the well-known IEEE 14-bus system is examined. It represents a portion of the American electric transmission system, in the Midwestern region, as of February 1962.

It comprises 14 buses, 11 constant-impedance loads, 8 transformers, 17 transmission lines, and 5 synchronous generators. The latter are respectively installed at Bus 1, 2, 3, 6, and 8. At Bus 7, a three-winding transformer is modeled, as it connects together Bus 4, 8, and 9. The power system scheme is shown in Fig. 5.6 and its original data can be found in [173].

This network is typically employed for voltage stability and line parameter estimation under different operating conditions [73, 174]. Hence, it represents an ideal candidate to investigate contingencies in the presence of different inertia levels. Since Chapter 6 focuses on low-inertia cases, two scenarios are examined: a high and low-inertia one, referred to as Scenario I and II, respectively.

In Scenario I, i.e., the high-inertia one, the nominal generator parameters are applied, as given by the original IEEE 14-bus model. By evaluating Eq. (5.6), the equivalent inertia results in $H_{COI} = 5.36$ s at rated conditions. Scenario II, instead, is intended to reproduce the same operation, but in a reduced inertia power system. To this end, the inertia constants of the synchronous generators at Bus 2 and 3 have been halved. The inertia of the COI is evaluated again, according to Eq. (5.6), and it results in $H_{COI} = 4.86$ s, thus implying a reduction of $-9.33\,\%$ with respect to the nominal conditions of Scenario I.

It is worth mentioning that the decision to simulate a low-inertia power system by

Table 5.1: Inertia constant values of the IEEE 14-bus system, expressed in s, in rated- and low-inertia conditions, indicated by Scenario I and II, respectively.

Synchronous Machine	Scenario I	Scenario II
1	5.15	5.15
2	6.54	3.27
3	6.54	3.27
6	5.06	5.06
8	5.06	5.06
H_{COI}	5.36	4.86

halving the inertia constants of some of its synchronous machines can be regarded as a strong approximation. However, it is deemed reasonable as a first evaluation for the study of this complex model. For the sake of completeness, Table 5.1 reports the inertia constants of each synchronous machine as well as their equivalent inertia, H_{COI} for the two scenarios under test, all expressed in seconds.

Specific modifications or details relative to this particular transmission system model are presented in the following Sections of Chapter 6 presenting its application.

5.4 Discussion

This Chapter presented the causes and the consequences of the progressive installation of CIG in power systems. In this scenario, the key concepts of power system stability and inertia are illustrated, as well as a classification of the most recent algorithms present in the scientific literature.

Some insights are also provided for what regards the most significant challenges that are still yet to be tackled from a technical and metrological perspective.

The last part is dedicated to the presentation of the swing-equation-based algorithm and of the two power system models that are used in the next Chapter for the application of PMUs and evaluation of the uncertainties.

Chapter 6

PMUs in Low-Inertia Power Systems: Local Assessment and Interoperability

Besides the evident environmental benefits that renewable-based sources bring, they also yield significant technical and metrological challenges in the field of power system inertia. They involve both the development of suitable algorithms and new devices able to provide reliable estimations of inertia. Additionally, from a normative perspective, there is little information available and still ample space for further developments, as presented in Chapter 5. In this context, this Chapter attempts at contributing to such a broad topic, by investigating the application of PMUs for the local assessment of power system inertia. First, an initial metrological requirement is derived, starting from the specifications of the instrumentation used in the field. Second, the evaluation of the swing-equation-based approach and the reliability of PMU measurements is established, still at a local level, with the aim of providing regional indices. Lastly, the interoperability between PMUs and other electric instrumentation is assessed, examining, among all of them, power quality meters.

6.1 Metrological Perspective on Inertia Measurements

As could be inferred from the literature review illustrated in Section 5.2, it is evident how, despite inertia being an essential quantity in power systems, it is seldom accompanied by an uncertainty that quantifies its goodness. In this regard, it is worth recalling that most of the algorithms are accompanied by an estimation error, however, for what concerns the uncertainty, there is still leeway for development. Hence, in this scenario, this work aims at providing an initial contribution by investigating the possibility of associating a CI to an inertia estimate. The latter is assumed to be obtained by means of a swing-equation-based approach, having as inputs in-field measurements, whose typical specifications are considered. This Section illustrates the work presented at the 12th International Workshop on Applied Measurements for Power Systems (AMPS) held in Cagliari, Italy in 2022 [175].

There exist some works published in the scientific literature which are worth considering in the measurement framework. For instance, the Authors in [176] compare the performances of the most known measurement-based inertia estimation techniques. However, this is performed by assessing the accuracy of the algorithm when the noise and the observation window length are changed. In [177], instead, the accuracy of the model is verified by means of real measurements. Nevertheless, such measurements are regarded as “true” values as their intrinsic uncertainty is neglected. The Authors in [169] evaluate the robustness of their inertia estimation algorithm by testing it against PMUs' measurement noise. To do so, three different values of TVE are considered (i.e., 1, 2, and 3 %). Yet, from these results, it is not possible to draw any significant conclusion about the uncertainty to be associated with the inertia estimate. Moreover, the choice of such high values of TVE is rather questionable given that most state-of-the-art PMU algorithms feature TVE values in the order of few $0.x$ % in dynamic test conditions. Finally, the Authors in [161] propose multiple inertia estimations and a 95 %-CI associated with the results, for both ambient data and large disturbance methods. However, this is still a simulation-based method that lacks instrumentation uncertainties. Therefore, based on this rationale, this Section presents an approach aimed at quantifying the uncertainty to be associated with inertia values, obtained from in-field measurements. The following Section 6.1.1 presents the testing conditions and the hypotheses are discussed and motivated. The results and the main conclusions are drawn in 6.1.2.

6.1.1 Testing Conditions

As detailed in Section 5.2, there are a number of algorithms published in the literature concerning the estimation of power system inertia. However, given the motivations presented in Section 5.2.3 and since this work aims at approaching the uncertainty evaluation, a basic case relying on the swing equation is examined. The inertia is evaluated starting from Eq. (5.5), considering a realistic scenario.

As disclosed in Chapter 5, power and frequency measurements are mandatory inputs for inertia estimation, regardless of the algorithm and its complexity. Moreover, it is crucial to remember that, at the current state, there exists neither a standardized way to compute inertia, nor its required uncertainty. Since this topic is still widely under research and no guidelines are yet available, this study does not attempt at providing plausible CIs but rather it aims at understanding the goodness and the reliability of inertia values in a realistic in-field configuration that can be found nowadays. In this regard, a typical instrumentation setup currently employed by TSOs comprises LPITs for the acquisition of voltage and current signals, as well as PMUs[1]. Their uncertainty contributions are presented and listed here as follows.

For what concerns LPITs, class 0.5 is considered. This choice stems from the fact that these devices are widely used in distribution and transmission networks; however, in the latter, sometimes better accuracy classes are used. Nevertheless, class 0.5 represents a good trade-off between accuracy and costs, as well as representing a realistic setting. Class 0.5 LPVTs feature a ratio error and a phase displacement of 0.5 % and ±0.6 crad, at rated voltage, respectively, as shown in Table 2.4 [66]. LPCTs, instead, are characterized by a ratio error and a phase displacement of 0.5 % and ±0.9 crad, at the rated current, respectively, as in Table 2.5 [65].

In the acquisition chain, the next component is the DAQ system. A generic commercial device has been considered, likewise to the one presented in Section 4.3.1. It is characterized by a 24-bit ADC, ±10 V full-scale voltage, a $70\,\mu V_{rms}$ input noise, ±0.03 % gain error, and ±0.008 % offset error, according to its datasheet.

---

[1] This setup represents a very good condition that can be found in the field. Indeed, capacitive VTs are the most popular VTs among TSOs despite being characterized by very poor dynamic performances.

Given the negligible contribution of the PMU algorithm to the overall uncertainty, as indicated by the three PMU models presented in Section 4.1.1, it is assumed that PMUs are only used for the frequency measurements. Despite the fact that it can represent a strong approximation, it is considered a reasonable assumption given the excellent performances of modern PMUs. Therefore, only the frequency error is considered: in view of a conservative approach, the worst-case scenario is considered. For an M-class PMU, measuring a steady-state signal, the frequency error is equal to ±5 mHz as indicated in the PMU Std [14].

The effect of the synchronization source on the PMU is also considered, as it is affected by a non-negligible contribution to the phase of the estimated synchrophasor. In worst-case conditions, a GPS source is characterized by a time uncertainty of ±500 ns [106]. In this context, it is worth explaining that all the listed sources of uncertainty are assumed as obtained from uniform distributions. This represents a worst-case, rather conservative scenario, but it is deemed to be quite realistic.

Having listed the set of variables under test, jointly with their uncertainty, then the MCM is applied to the swing equation shown in Eq. (5.5). The choice of applying the MCM has been made due to its simplicity and efficacy, as shown more in detail in Section 1.2.4. Furthermore, considering that this represents a first approach to the uncertainty evaluation of inertia, the MCM is a suitable candidate for performing a starting-point evaluation of the uncertainty, before moving to more complicated solutions. A total of $M = 10000$ Monte Carlo trials are performed, with the objective of establishing a 95 %-CI.

The powers and frequencies in Eq. (5.5) are corrupted by the sources of uncertainty of the complete measurement chain, starting from those stemming from voltages and currents measured by LPITs to obtain the active power, and the frequency value evaluated by the PMU. It is must be clarified that, for the sake of simplicity, the uncertainties of LPVTs and LPCTs are not included in frequency and ROCOF estimations. Despite being a strong approximation, it is reasonable to assume that the biggest effects will be observed only on power estimates.
In order to replicate plausible test conditions, another important choice involved attributing realistic values to the two differences at the numerator and denominator. These two are briefly referred to as ΔP and Δf, respectively, hereinafter. Realistic values of ΔP and Δf have been found in an official ENTSO-E report illustrating the requirements and impacting factors in the evaluation of frequency stability in CE [178, 179]. Consequently, the selected ΔP values range from 1 % to 40 %, whereas for Δf maximum values equal to 0.5, 1, 2, and 3 Hz/s are selected. Based on this information, a set of tests is created and applied to Eq. (5.5). It is worth noticing that, as pointed out by [178, 179], the reference scenario of CE for the future indicates that the system must be able to resist, under split scenarios, conditions characterized by power imbalances greater than 40%, which may lead to ROCOF values higher than 2 Hz/s. For these reasons, also such high values are examined in the following, in order to comprise possible present and future scenarios.

Lastly, the voltages and the currents needed to obtain such ΔP and Δf values are defined. With the purpose of selecting plausible values, one of the three synchronous

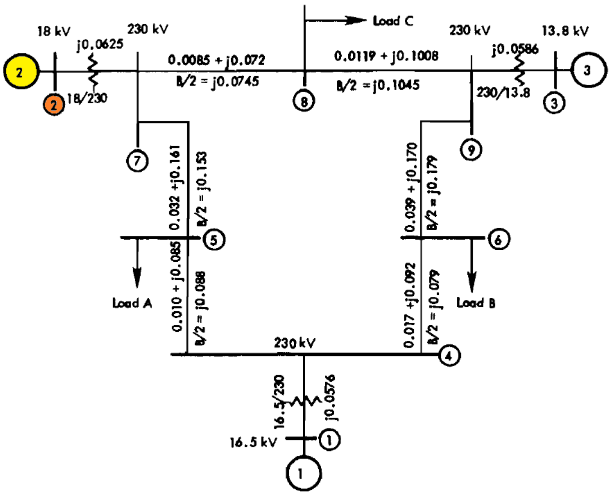

Figure 6.1: IEEE 9-bus power system scheme, indicating the impedances that are expressed in p.u. on a 100 MVA base. Generator 2, which is the generator whose parameters are examined in the following, is located in the upper-left corner and is indicated in yellow. Its corresponding bus at which measurements are performed is shown in orange. Adapted from [180].

generators of the IEEE 9-bus system is used, as illustrated in [180] and shown in Fig. 6.1. Without loss of generality, this choice has been made in order to examine data that is the most realistic as possible. It is not intended to be as a general rule, but rather as a reasonable example of what can be observed by TSOs. Generator 2 features a rated power of 192 MVA, a rated voltage of 18 kV, and a PF of 0.85. Its rated speed is equal to 3600 revolutions per minute (rpm) and its stored kinetic energy at rated speed equals 640 MWs. Based on this data, Eq. (5.2) is applied to Generator 2 so that it is possible to estimate its inertia constant in rated conditions, which results in $H = 3.333$ s. Its rated electrical power is also computed, as it is regarded as the output power of the synchronous generator before the contingency, after which ΔP is applied to replicate a disturbance. To apply MCM, it is assumed that power and frequency measurements are performed at the generator output terminals, as it is often done by TSOs.

6.1.2 Results Assessment and Discussion

This Section presents the results of the MCM previously detailed which are summarized in Tables 6.1 and 6.2. The first one includes, for every combination of ΔP, only Δf equal to 0.5 and 1.0 Hz/s. Table 6.2, instead, presents the same results but for more severe frequency variations, i.e., Δf corresponding to 2.0 and 3.0 Hz/s. In both tables, the mean value H_m is expressed in s, and the left and right extrema of the 95 %-CI, s_L, and s_R are indicated as lower and higher limits, respectively, are indicated in s as well.

Examining the results shown in the two Tables 6.1 and 6.2, it is possible to observe that the uncertainty associated with the mean value of the estimated inertia is not negligible. This is valid, especially for lower values of Δf, shown in Table 6.1. This can be deemed true for every ΔP value, ranging from 1 % to 40 %, in spite that they reflect events in the power network with increasing severity. Therefore, as expected, the inertia variation is higher as well as its associated uncertainty. Lastly, high values of ΔP associated with limited values of Δf reflect a realistic situation in

Table 6.1: Monte Carlo results for the inertia estimates, obtained considering all possible ΔP in %, but examining only Δf equal to 0.5 and 1.0 Hz/s. The mean value of the estimate is indicated as H_m, while the left and right extrema of the CI are indicated by s_L and s_R, respectively. Adapted from [175].

Δf (Hz/s)	0.5			1.0		
ΔP (%)	s_L (s)	H_m (s)	s_R (s)	s_L (s)	H_m (s)	s_R (s)
1	−0.13	0.42	0.96	−0.10	0.20	0.47
5	1.55	2.10	2.64	0.76	1.03	1.30
10	3.68	4.20	4.73	1.82	2.08	2.34
15	5.79	6.31	6.81	2.87	3.12	3.37
20	7.90	8.41	8.91	3.91	4.16	4.41
30	12.14	12.62	13.10	6.00	6.24	6.47
40	16.37	16.83	17.29	8.09	8.32	8.55

Table 6.2: Monte Carlo results for the inertia estimates, obtained considering all possible ΔP in %, but examining only Δf equal to 2.0 and 3.0 Hz/s. The mean value of the estimate is indicated as H_m, while the left and right extrema of the CI are indicated by s_L and s_R, respectively. Adapted from [175].

Δf (Hz/s)	2.0			3.0		
ΔP (%)	s_L (s)	H_m (s)	s_R (s)	s_L (s)	H_m (s)	s_R (s)
1	−0.04	0.10	0.24	−0.02	0.07	0.16
5	0.38	0.52	0.65	0.26	0.35	0.44
10	0.91	1.04	1.17	0.61	0.70	0.79
15	1.44	1.57	1.69	0.97	1.05	1.14
20	1.96	2.10	2.22	1.31	1.40	1.49
30	3.02	3.14	3.26	2.03	2.11	2.19
40	4.07	4.18	4.30	2.73	2.81	2.89

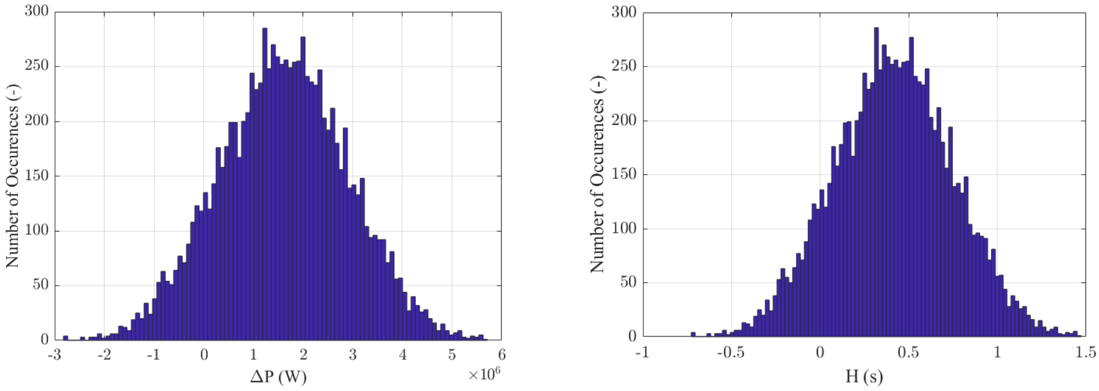

(a) (b)

Figure 6.2: Low-severity case illustrating the ΔP (a) and H (b) distributions obtained applying the MCM for a $\Delta P = 1\%$ and a $\Delta f = 0.5$ Hz.

which a power variation affects less the system frequency.

In a similar way, when a low value of ΔP is associated with an extensive Δf, this results in a strong variation of the system frequency. Some interesting comments can be made for what concerns the sign of H_m in both Tables. It is worth underlying that having considered either a positive or negative ΔP has no impact on the uncertainty associated with inertia. Indeed, from an uncertainty perspective, the presented research is valid for all ΔP and Δf cases, regardless of their signs. Hence, H_m represents the mean value of a variation which could be positive or negative. The sign will be reflected in an increase or in a decrease in the overall inertia. Therefore, in the first row of both Tables 6.1 and 6.2, the uncertainty associated with H_m varies from positive to negative terms. This is clearly not happening during a fault, but it emphasizes the importance of the uncertainty assessment process. Finally, for low ΔP values, the uncertainty associated with H_m is comparable to it. Hence, TSOs should properly assess such information before taking any countermeasures.

In the following, given the significant amount of data presented in the previous Tables 6.1 and 6.2, only three cases are shown in more detail. A low-severity case having a $\Delta P = 1\,\%$ and $\Delta f = 0.5$ Hz/s, an intermediate one characterized by a $\Delta P = 15\,\%$ and $\Delta f = 1.0$ Hz/s, and a severe one, based only on perspective data from ENTSO-E having a $\Delta P = 40\,\%$ and $\Delta f = 3.0$ Hz/s. They are respectively illustrated in Fig. 6.2, 6.3, and 6.4. The distributions of ΔP and H obtained from the MCM are shown, for each case, in subfigure (a) and (b) respectively.

As it can be seen, in all three cases regardless of their severity, the distribution of the estimated inertia follows the ΔP one, concluding that ΔP contribution is clearly the more impacting one on the overall estimation of H. In light of the presented results an important conclusion applies: with this first analysis on the uncertainty related to power system inertia, it is still not yet possible to prescribe limits on the accuracy values to be attributed to it. However, it is evident how the LPIT class affects the ΔP measurement, especially for low values of power variations. Hence, this is reflected in the estimation of H as in Fig. 6.2. Conversely, future more severe cases envisioned by ENTSO-E could represent an easier scenario from a measurement perspective since higher power variations can be assessed straightforwardly, besides being characterized by smaller CIs as shown in Fig. 6.4.

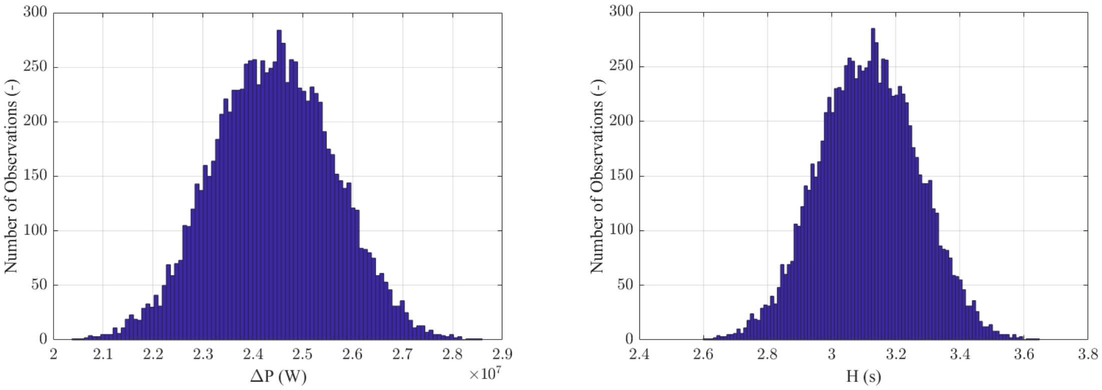

(a) (b)

Figure 6.3: Intermediate case illustrating the ΔP (a) and H (b) distributions obtained applying the MCM for a $\Delta P = 15\%$ and a $\Delta f = 1.0$ Hz. Adapted from [175].

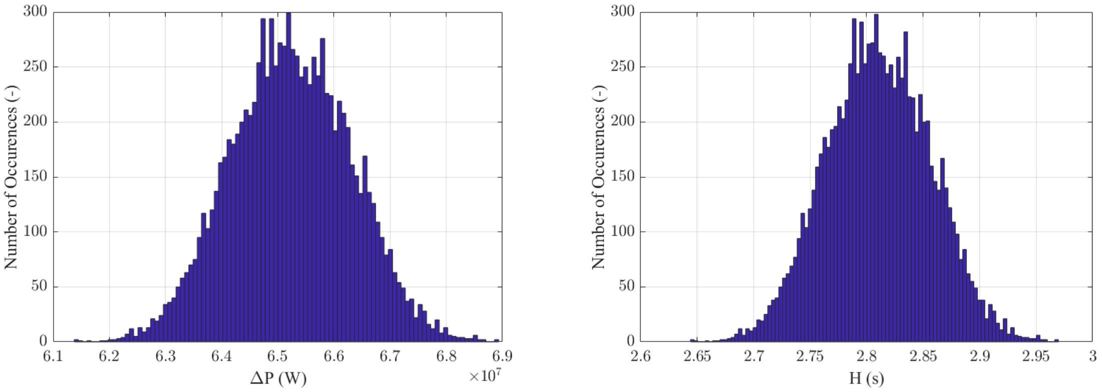

(a) (b)

Figure 6.4: High-severity case illustrating the ΔP (a) and H (b) distributions obtained applying the MCM for a $\Delta P = 40\%$ and a $\Delta f = 3.0$ Hz.

6.2 Local Evaluation of Inertia Variations

Having illustrated a first investigation of the measurement requirements needed when assessing inertia, the remaining Sections of this Chapter illustrate a different approach. It entails the feasibility of assessing a local inertia index based on PMUs with the aim of establishing regional indices.

In this regard, the objective of this study consists in proposing an added feature to PMUs. It includes the computation of a new indicator that is representative of local inertia, as a function of active power and ROCOF variations. For the reasons presented in 5.2.3, this approach also relies on the swing equation. This Section illustrates the work presented at the International Instrumentation and Measurement Technology Conference (I2MTC) held in Kuala Lumpur, Malaysia in 2023, for which I received a Student Travel Grant [181].

The definition of a local inertia variation index, indicated as dH, is computed in a single node, hence it is based only on local measurements of phasors and ROCOF. Without loss of generality, this is not supposed to replace the traditional inertia definition but is intended to provide a prompter detection of anomalous or unstable operation. The objective, indeed, does not intrinsically involve a re-definition of inertia from a power system perspective. It rather entails the definition of a new stability index that can be used at a local level, contrarily to inertia which inherently refers to large power system areas.
In this regard, it is worth clarifying that such a stability indicator can be calculated in any operating condition, regardless of contingencies or particular power system structures. It means that its results can help in discerning steady-state from dynamic conditions, in every power system scenario, without having to make a distinction from distribution to transmission power systems. The latter, of course, are characterized by higher interconnections by their configurations. However, despite this consideration, it is assumed to be worth assessing local conditions at the most critical buses of the power system under test.

When properly aggregated, the new inertia indicators may allow for more robust and effective algorithms for fault detection and system restoration. As a matter of fact, PMUs could experience phase drifting because of either a contingency or due to their own measuring issues. For this reason, the new index includes both power and ROCOF variations. It is validated by simulating different contingencies in two inertia levels, to assess whether the proposed indicator represents a reliable solution for local inertia assessment. The power system model is presented in Section 6.2.1 in which the IEEE 14-bus system is equipped at each node with two PMU models, compliant with the P-class requirements of the PMU Std. The results, instead, are discussed in Section 6.2.2.

6.2.1 Power System Scenario

The PMU model as well as the power system scenarios are thoroughly detailed in this Section, jointly with the theoretical background on which the definition of the new local inertia indicator is founded.

PMU model: In order to reproduce a distributed monitoring system, a simulated

PMU model is deployed at each node of the power system under test. For this analysis, PMU A and B are considered as detailed in the previous Section 4.1.1. Both PMU A and B are compliant with the P-class indicated in the PMU Std, they adopt a sampling rate of 18 kSa/s, an observation interval of 3 nominal cycles of the rated power system frequency, and a reporting rate of 120 fps. The choice of the maximum allowed reporting rate is not so common in real-world applications. Nevertheless, it allows for investigating whether this new approach involving local PMU-based inertia estimation is affected by the selected time resolution. Additionally, according to the PMU Std specifications, PMU estimates are associated with the positive sequence component and are referred to the midpoint of the observation interval. Not only are the PMU models designed in order to provide the traditional phasor, frequency, and ROCOF associated with voltage and current positive sequences, but also a local indicator of inertia variation (dH) at each reporting time instant t_i. In particular, the voltage and current phasors ($\overline{U}$ and $\overline{I}$, respectively) allow for defining the instantaneous complex power $\overline{P}_e$ injected at the bus under test, whereas the ROCOF ($\overline{R_f}$) accounts for the frequency variation. By combining these parameters, it is possible to evaluate Eq. (6.1) in the considered node as follows:

$$\begin{aligned} \overline{P}_e(t_i) &= \Re\Big\{\overline{U}(t_i) \cdot \overline{I}^*(t_i)\Big\} \\ \overline{R_f}(t_i) &= \frac{df}{dt}(t_i) \simeq \frac{\overline{f}(t_i) - \overline{f}(t_{i-1})}{t_i - t_{i-1}} \\ dH(t_i) = \left|\frac{\Delta \overline{P}_e}{\Delta \overline{R_f}}\right| &= \left|\frac{\overline{P}_e(t_i) - \overline{P}_e(t_{i-1})}{2 \cdot \Big[\overline{R_f}(t_i) - \overline{R_f}(t_{i-1})\Big]}\right| \end{aligned} \tag{6.1}$$

for the i^{th} reporting instant t_i. The new inertia indicator dH is expressed in s, in accordance with the definition in Eq. (5.5), and accounts for the variation of inertia as perceived at the PMU terminals in a specific node. Contrarily to Eq. (5.4), Eq. (6.1) assesses variations of inertia based on local phasor estimates. At this preliminary level, the model does not account for the IT stage nor for the synchronization error [182, 183]. Nevertheless, based on the previous analysis in Section 6.1, it is more than reasonable to assume that both these aspects represent significant uncertainty contributions in the estimation of local inertia variations and shall be properly investigated and quantified in a second stage [175]. However, to account for the noise introduced by the PMU analog front-end, the input waveforms of voltage and current are distorted by an additive uncorrelated white Gaussian noise with a SNR of 80 dB.

Power System Model: As a validation test case, the well-known IEEE 14-bus system is considered, whose data is illustrated in Section 5.3.2. For this reason, most of its original data is omitted here for the sake of brevity, however, the relative modifications are carefully described in the following.
To investigate the impact of different inertia losses' locations, the network is divided into five non-overlapping regions. In a first approximation, it is reasonable to affirm that the selected regions are characterized by a unique frequency since each region contains only a Synchronous Generator (SG). All the machines are equipped with an Automatic Voltage Regulator, but only the ones at Bus 1 and 2 are equipped with a Turbine Governor (TG).

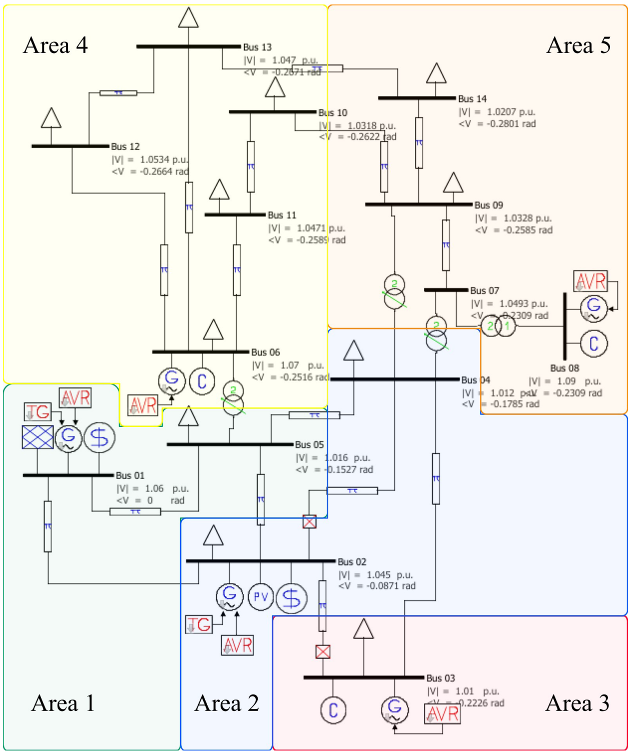
Area 4
Area 5
Bus 13
|V| = 1.047 p.u.
<V = -0.2671 rad
Bus 14
|V| = 1.0207 p.u.
<V = -0.2801 rad
Bus 10
|V| = 1.0318 p.u.
<V = -0.2622 rad
Bus 12
|V| = 1.0534 p.u.
<V = -0.2664 rad
Bus 11
|V| = 1.0471 p.u.
<V = -0.2589 rad
Bus 09
|V| = 1.0328 p.u.
<V = -0.2585 rad
Bus 07
|V| = 1.0493 p.u.
<V = -0.2309 rad
AVR
G
C
Bus 08
|V| = 1.09 p.u.
<V = -0.2309 rad
Bus 06
|V| = 1.07 p.u.
<V = -0.2516 rad
Bus 04
|V| = 1.012 p.u.
<V = -0.1785 rad
TG
AVR
AVR
G
$
Bus 05
|V| = 1.016 p.u.
<V = -0.1527 rad
Bus 01
|V| = 1.06 p.u.
<V = 0 rad
Bus 02
|V| = 1.045 p.u.
<V = -0.0871 rad
PV
TG
AVR
Bus 03
|V| = 1.01 p.u.
<V = -0.2226 rad
Area 1
Area 2
Area 3

Figure 6.5: IEEE 14-bus system developed in MATLAB/Simulink environment using PSAT toolbox [184]. The model shows the load flow results and the five non-overlapping areas, each of them comprising a synchronous generator. Source: [181].

As shown in Fig. 6.5, the five regions are identified as follows.

- Area 1 (green): Bus 1 (SG+TG) and 5.
- Area 2 (blue): Bus 2 (SG+TG) and 4.
- Area 3 (red): Bus 3 (SG).
- Area 4 (yellow): Bus 6 (SG), 10, 11, 12, and 13.
- Area 5 (orange): Bus 8 (SG), 7, 9, and 14.

The model has been realized in MATLAB/Simulink environment by means of the Power System Analysis Toolbox (PSAT) toolbox [184]. For the sake of completeness, Fig. 6.5 also reports the load flow results in terms of voltage phasor magnitude and angle expressed per unit and rad, respectively.

Given the network and PMU models, two plausible scenarios are reproduced as detailed in Section 5.3.2: in the first one, i.e., Scenario I, the nominal generator parameters are considered as given by the original IEEE 14-bus model [173]. The second scenario, instead, referred to as Scenario II, is intended to reproduce the same operation in a reduced inertia power system. To this end, the inertia constants of the SGs in Area 2 and 3 are halved. All the inertia constants can be found in Table 5.1. It is worth recalling that the new low-inertia configuration results in equivalent inertia $H_{COI} = 4.86$ s, hence implying a reduction of $-9.33\,\%$ with respect to nominal power system conditions having $H_{COI} = 5.36$ s.

A time-domain simulation is performed, characterized by a discrete resolution of $\Delta t = 5$ ms and an overall duration of 5 s. It is worth specifying that a subsequent

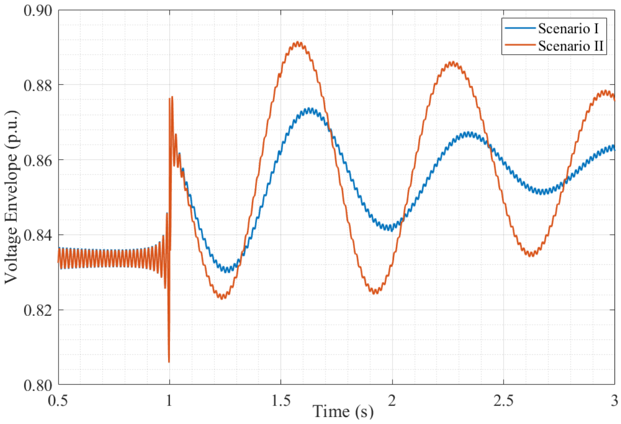

Figure 6.6: Comparison of the magnitude envelopes of the voltage waveform for Scenario I and II in blue and red, respectively. Source: [181].

interpolation at 18 kSa/s is performed after the complete simulation has taken place. This is carried out in order to ensure reasonable results for both PMUs under test. At $t = 1$ s, both CBs, indicate as squares with a red cross in Fig. 6.5, at Bus 2 and Bus 3 open. Based on the CBs' locations, it is reasonable to expect that this will mostly impact Areas 2 and 3, whereas the neighboring partitions should be less affected independently by the inertia constant of the respective SG.

6.2.2 Results Discussion and Conclusions

In this Section, the PMU measurement results are presented as obtained in the two scenarios. Lastly, the feasibility of a local PMU-based estimation of inertia variations is discussed. For the sake of brevity, the following figures present only the results relative to Bus 2, as this is the closest to the opening CB, but similar results can be obtained in other buses.

First of all, Fig. 6.6 presents the magnitude envelope of the voltage positive sequence waveform as acquired at Bus 2 for both the considered scenarios. It is worth clarifying that this is performed for the sake of completeness. The PSAT simulation provides as outputs time-varying samples of three-phase voltage and current signals. For both sets of signals, the Fortescue theorem is applied to retrieve the positive sequence only. Afterward, for this analysis, the Hilbert Transform is computed in MATLAB: the magnitude envelope is obtained as the module of the analytic signal associated with the fundamental component only.
In Scenario I, the system undergoes a dampened oscillation that nearly vanishes after 3 s. A similar trend is noticeable in Scenario II but with a much slower dampening factor and larger oscillation depth.

Fig. 6.7 presents the active power $\overline{P}_e$ in subfigure (a) and ROCOF estimates $\overline{R}_f$, in subfigure (b), as obtained by PMU A (dark and light red shades) and PMU B (dark and light blue shades) in the two scenarios. For what concerns $\overline{P}_e$, the PMU estimates are quite consistent in both cases. In the case of ROCOF, instead, more significant discrepancies are noticeable. Both ROCOF present different trends in the two scenarios, namely a reduced inertia produces long-lasting oscillations, confirming the results of Fig. 6.6. However, the estimates of PMU A and B are inconsistent. More in detail, it is interesting to observe how PMU A estimates are

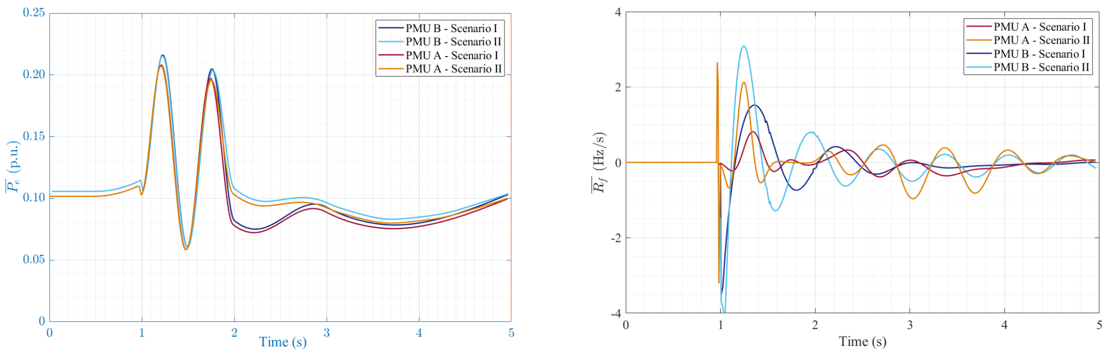

(a) (b)

Figure 6.7: Active power $\overline{P_e}$ in (a) and ROCOF $\overline{R_f}$ (b) comparison in Scenario I and II for PMU A and B at Bus 2, indicated by red and blue shades respectively. Source: [181].

slightly delayed and low-pass filtered if compared to the PMU B ones.
This is reasonably due to the different ROCOF computations of the two models. It is worth recalling, as described in Section 4.1.1, that PMU A adopts a finite difference formulation, in which the ROCOF is the ratio between two frequency estimates. Whereas, PMU B adopts a TFT model, which allows to computing the instantaneous ROCOF from the first two time derivatives (in this case, the ROCOF corresponds to the second-order derivative) of the estimated synchrophasor. Hence, it is reasonable to expect that a derivative filter minimizes the estimation delay, albeit showing higher sensitivity to sudden frequency variations.

Having analyzed the active power and the ROCOF in both scenarios, the new local indicator dH can be evaluated according to Eq. (6.1). Fig. 6.8 compares the estimates of dH and $\Delta\overline{R_f}$ as provided by PMU B in the Scenario I in (a) and in Scenario II in (b). It is worth mentioning that $\Delta\overline{R_f}$ is computed as a finite difference of subsequent ROCOF estimates provided by the PMU under test. Before the contingency (i.e., for $t < 1$ s), both quantities remain stable around their stationary values of 0.001 s and 0.001 mHz/s, respectively. The only noticeable variability is to be associated with the additive measurement noise. In both scenarios, in correspondence with the CBs' opening, the estimated ROCOF exhibits a step change and then a dampened oscillation, compatible with the trend observed in Fig. 6.6. This variation is reflected also on the local inertia indicator dH: first, a step change is detected of nearly 3 orders of magnitude, then, a strongly non-linear trend whose variation range is much larger than the pre-contingency one.

In a similar way, Fig. 6.8(b) presents the results relative to Scenario II. In this case, some comments hold true as for Scenario I, meaning that a noticeable step of a few orders of magnitude can be observed for both dH and $\Delta\overline{R_f}$. However, in this case, it is interesting to observe how $\overline{R_f}$ presents a time trend that tends to fade out in a longer time interval. As a matter of fact, at the end of the simulation ($t = 5$ s), there exists a difference of 2 orders of magnitude between $\Delta\overline{R_f}$ measured in Scenario I and in Scenario II.
This clearly indicates how a reduced inertia condition affects the time constants of a power system, making them more susceptible and less resilient for the same contingency. With regards to dH, instead, it can be concluded that, as already disclosed, dH is not an exact definition of the inertia variation. However, from a

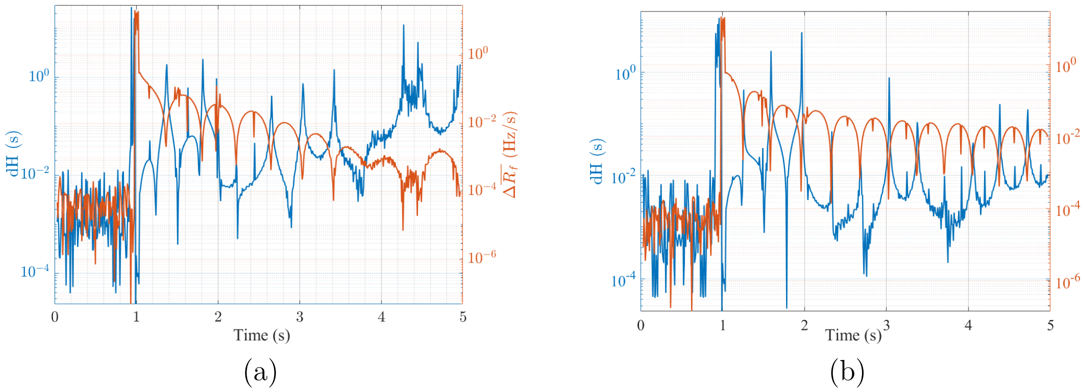

Figure 6.8: Indicator of local inertia variation dH and variations of ROCOF $\Delta\overline{R_f}$ as provided by PMU B at Bus 2 in blue and red, respectively. Scenario I is shown in (a), while Scenario II is in (b). Adapted from [181].

network perspective, it can be used to detect transient conditions and assess when the system comes back to a quasi-stable operation.

Given that from the results of dH of Fig. 6.8 cannot be distinctively discerned which variable plays a major role, the purpose of the following is to determine which quantity is affecting more directly the definition of dH. To this end, the mean μ and standard deviation σ of both $\overline{P_e}$ and $\overline{R_f}$ are computed over a moving window of 10 consecutive and non-overlapping reporting periods. This is repeated twice, for both Scenario I and II. In more detail, in Fig. 6.9(a) the mean value of the active power $\mu(\overline{P_e})$ is shown on the left axis in blue, while its corresponding standard deviation $\sigma(\overline{P_e})$ is depicted in red on the right axis. Similarly, Fig. 6.9(b) presents the same quantities but relative to the ROCOF. These results are valid for Scenario I and they are obtained using P-class PMU B. Analogously, Fig. 6.10 illustrates the same quantities, but they are referred to Scenario II.

It is interesting to observe how the ROCOF is very sensitive to the contingency in both scenarios, but then it goes rapidly back to quasi-stationary conditions as indicated by its standard deviation. On the contrary, the active power presents an increased variability which tends to persist. This is evident even after a few seconds from the contingency as the pre-contingency level is not reached at the end of the simulation neither in rated nor in low-inertia conditions.
For what concerns Scenario II, analyzing the results of Fig. 6.10, it can be also concluded that the ROCOF has a much wider and long-lasting oscillation in comparison to the rated condition. Based on these observations, it is evident once again how a lower inertia condition corresponds to a longer time to converge to a new quasi-stable operation in case of events or contingencies.

So far, dH has been used as an indicator of a contingency in a power system node. However, only data retrieved from Bus 2 is examined for the sake of conciseness. Nevertheless, in the following, it is investigated whether dH is also able to provide any useful indications for what concerns the proximity to the fault location.
Apart from Bus 2, Bus 10 is considered in this analysis. It is located in Area 4 which is roughly on the other side of the power system, with reference to Fig. 6.5. Hence it is reasonable to assume that the effects of the contingency occurring on this bus are minimal in contrast to what can be observed on Bus 2. Nonetheless, it is plausible to assume that every node located in either Area 4 or 5 can represent

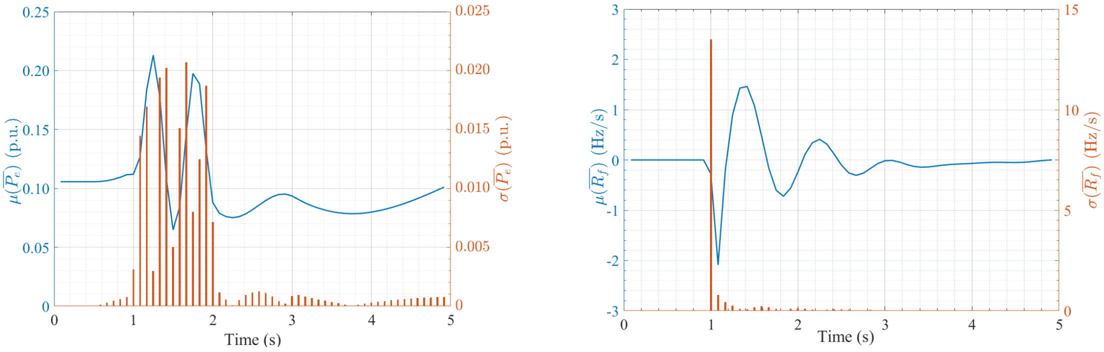

(a) (b)

Figure 6.9: $\overline{P_e}$ mean value μ and standard deviation σ in (a) and $\overline{R_f}$ mean value μ and standard deviation σ in (b) as computed by PMU B at Bus 2 in Scenario I. Source: [181].

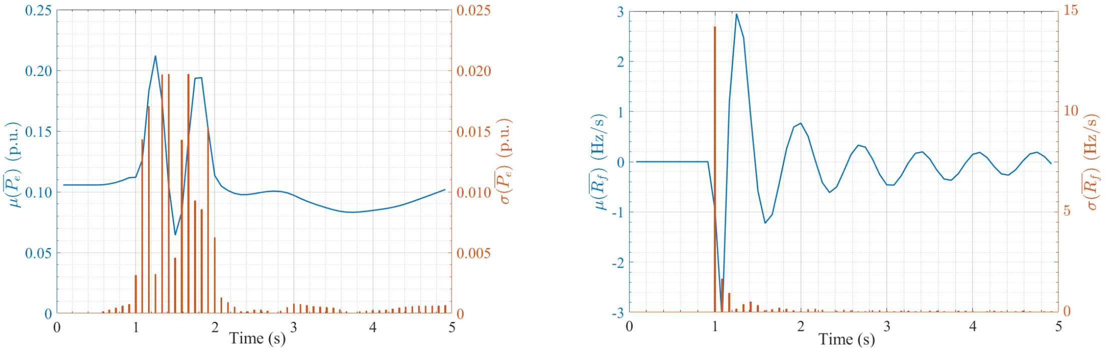

(a) (b)

Figure 6.10: $\overline{P_e}$ mean value μ and standard deviation σ in (a) and $\overline{R_f}$ mean value μ and standard deviation σ in (b) as computed by PMU B at Bus 2 in Scenario II. Source: [181].

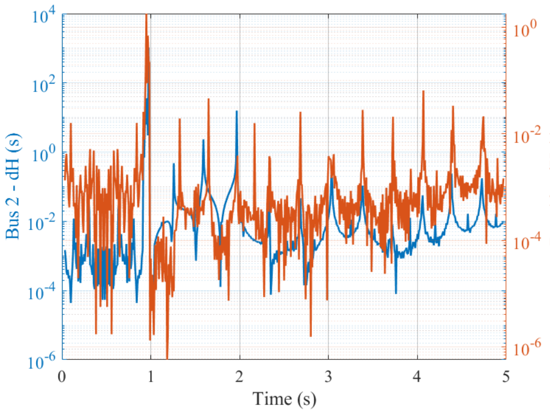

Figure 6.11: Indicator of local inertia variation dH as provided by PMU B in Scenario II at Bus 2 and at Bus 10 in red and blue, respectively. Source: [181].

a valid candidate for this analysis, as long as located sufficiently far away from the bus at which the contingency occurs.

Fig. 6.11 illustrates dH computed at Bus 2, indicated in blue on the left axis, and the same index assessed at Bus 10 and shown in red on the right axis. The results show that not only is dH able to identify a contingency, but its magnitude can also be a significant indicator of the proximity to the fault location. Indeed, there is a difference of 4 orders of magnitude between dH measured closely to the contingency (i.e., at Bus 2) and dH on the other side of the power system, at Bus 10. As a matter of fact, the latter is barely affected by any transients as foreseen. From this result, it can be concluded that the most influencing factor is represented by power variations and dH should be considered more as a local stability indicator rather than an inertia quantification.

In order to provide a more quantitative comparison of the two scenarios, Table 6.3 reports the Pearson correlation coefficients computed between the standard deviations of power and ROCOF in three different buses, namely 2, 3, and 10. The first two are in close proximity to the contingency location, while the latter is regarded as the farthest bus from the fault location as for the previous investigation.

For this analysis, the estimates obtained with both PMU models are compared in the two scenarios. In the areas directly affected by the CBs' opening, the correlation is nearly negligible independently of the considered scenario (i.e., inertia level) or PMU model (i.e., ROCOF computation method). This confirms how the two quantities are statistically independent and account for different phenomena: the ROCOF is mainly an index of stability, while the active power depends on the re-distribution of power flows after the contingency. However, at Bus 10, a slightly higher correlation is noticed, at least for what regards PMU B. The motivation can be found in the more accurate performance of PMU B in transient conditions with respect to the finite-difference method adopted by PMU A.

The most significant conclusion that can be drawn from this work is that the most influencing factor is represented by power variations. Therefore, dH should be considered more as a *stability*, or *transient*, indicator rather than an inertia quantification. Additionally, it has been proven that a lower inertia level corresponds to a longer time to converge to a new quasi-stable operation. Lastly, despite the fact that it is not possible to derive global information from a single PMU, the proposed

Table 6.3: Correlation coefficients between active power and ROCOF measured by PMU A and B, in Scenario I and II. Three different buses are considered as Bus 2 and 3 are in close proximity to the contingency, while Bus 10 is the farthest available. Source: [181].

Bus	PMU A		PMU B	
	Scenario I	Scenario II	Scenario I	Scenario II
2	2.96	3.79	2.03	6.88
3	0.42	2.10	2.79	6.01
10	6.72	5.55	15.96	16.99

metric can be used to detect power system transients and its magnitude can indicate the proximity to the region in which the contingency occurs.

6.3 Local Data Aggregation and Reliability

Following the first two applications dedicated to the measurement requirements and the local assessment of inertia, this Section and the following one 6.4 do not aim at assessing it. Instead, they rather focus on checking how PMUs would behave in such a condition. For this reason, the objective of this study consists in the utilization of the reliability index (i.e., the nRMSE, presented in the previous Section 4.1.2) in order to decide whether it is suitable and metrologically significant to aggregate measurements coming from neighboring nodes.

In this way, it would be possible to produce an average estimate of the system state in small grid partitions. In addition to this, they could also help in detecting unexpected inconsistencies between adjacent nodes, that may trigger prompt counteractions to be taken by DSOs and TSOs. To this purpose, Section 6.3.1 presents the examined low-inertia distribution grid, characterized by a strong presence of RESs. The results are evaluated and discussed in Section 6.3.2. In the following, the results of the work presented at the 4$^{\text{th}}$ International Conference on Smart Grid Metrology (SMAGRIMET) held in Cavtat, Croatia in 2023 are presented, for which I won the Best Student Paper Award [185].

6.3.1 PMU Model and Power System Simulations

PMU Model: In this study, it has been decided to utilize PMU C whose theoretical background has been presented in Section 4.1.1. Following the parameter setting presented in [49], the number of times to compensate for the long- and short-range spectral leakage contributions have been set equal to 2 and 16, respectively. Voltage and current waveforms are sampled at a sampling frequency f_s of 18 kSa/s and, given that the power system rated frequency f_n is equal to 60 Hz, the PMU reporting rate has been picked to be equal to 60 fps. It is worth noting that a higher reporting rate, i.e., 120 fps, could be used. Nevertheless, this is implausible to be found for in-field applications nowadays as it represents one of the latest addition to the PMU Std [14]. The observation window N_c spans over 3 nominal cycles, as it is a typical value for P-class PMUs, hence, based on the chosen N_c and f_n, it results that the PMU windowing time is equal to 0.05 s.

Following the acquisition of the samples by the PMU and the synchrophasor reconstruction, then Eq. (4.6) is applied in order to evaluate the nRMSE. It is worth

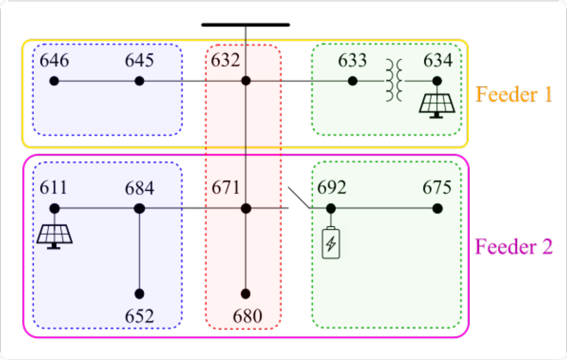

Figure 6.12: Model of the IEEE 13-bus system developed in MATLAB/Simulink, including the local area partitions and the two feeders under test in yellow and in pink, respectively. Source: [185].

reminding that, in an ideal condition, the result of Eq. (4.6) is approximately zero, since the mismatch between the real and the estimated phasor is minimal. However, in such a simulated scenario, higher values are expected owing to both transient conditions (i.e., the opening and re-closing of the CB) and to the high penetration of PV plants that pollute the power system introducing harmonic and inter-harmonic components. Therefore, the rationale behind this entails the aggregation of local measurements only in the case of nRMSE presents low values, implying the trustworthiness of the measurement itself.

Power System Simulations: As a distribution grid, the IEEE 13-bus power system presented in Section 5.3.1 is examined. However, with respect to its original formulation illustrated in [172], some modifications have been performed. First of all, with the objective of representing a low-inertia scenario, two PV plants and an ESS have been simulated. It has been decided to model different RES with the aim of reproducing diversified sources ever more present in modern distribution feeders. The first PV is a three-phase system, characterized by a rated power of 250 kW and it is installed at Bus 634. The second PV plant, instead, represents a single-phase, transformer-less household system with a rated power of 3.5 kW and it is simulated at Bus 611. On the other hand, the ESS is simulated with a battery having a rated power of 500 kW and a rated capacity of 100 kWh. Fig. 6.12 represents the described distribution power system.

In order to recreate plausible variations of solar irradiance, two different cycles have been simulated for each PV plant. They are shown in Fig. 6.13, where it is also worth noticing that the variations in the value of the solar irradiance are set to occur at time instants that do not correspond to the zero-crossing of the voltage and current waveforms. First of all, this has been done with the aim of avoiding facilitating the performances of the PMU model. Additionally, though, not only does this simulate a realistic condition that can be found in-field, as it is reasonable to assume that different portions of the power system can be affected by a different irradiance, but it also implies variations in the generated current and, consequently, in the output power of the PV. As a matter of fact, the generated output power of the two PV is adjusted by changing the solar irradiance from 100 % to a minimum of 50 % of the rated value (i.e., 1000 W/m^2), corresponding to the inverters' rated power. It must be highlighted that lower values, i.e., below 25 %, have been discarded in order to avoid strong harmonic and interharmonic emissions as shown in [186].

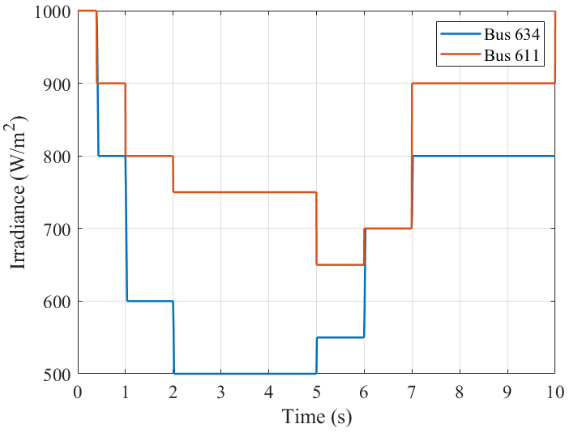

Figure 6.13: Time-varying irradiance cycles on PV power plants simulated at Bus 634 and 611 of the IEEE 13-bus system in blue and red, respectively. Source: [185].

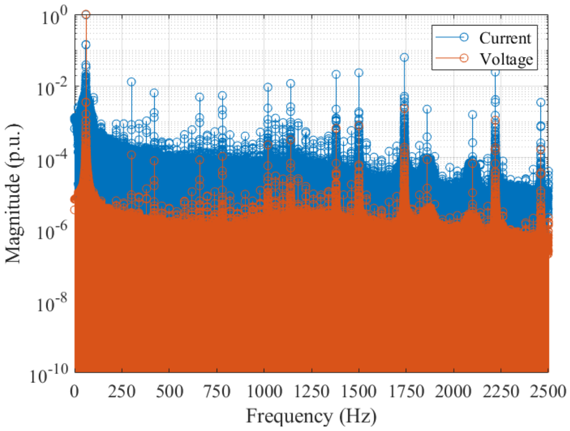

Figure 6.14: Voltage and current frequency spectra illustrating the first 40 harmonics measured on phase A at Bus 634, shown in red and blue respectively. Source: [185].

Before analyzing the other time-varying condition and the simulation specifications, it is worth assessing the noise and the harmonic levels present in voltage and current signals, for instance at Bus 634 since it hosts a PV plant. From Fig. 6.14, which illustrates the first 40 harmonics, it is clear that a non-negligible amount of harmonic pollution is present in both voltage (red) and current (blue) signals. Nevertheless, it is interesting to observe that low-order harmonics up to 240 Hz are characterized by small magnitudes which are nearly comparable with the noise floor. Hence, it is reasonable to expect that they will not cause significant interferences with the PMU estimation results. Conversely, higher-order harmonics are evident in both voltage and current spectra, but the utilization of PMU C which relies on windowing functions with fast-decaying side lobes allows for minimizing their impact on the synchrophasor estimates as presented in Section 4.1.1.

The second time-varying condition is simulated by generating a transient induced by the opening a CB located between Bus 671 and Bus 692. This results in a disconnection of Bus 692 and 675 from the main grid. However, the latter is still supplied by the ESS installed at Bus 692. This resembles a typical working condition, similar to those that can be observed in microgrids. The CB opens all three phases simultaneously at $t = 3.5$ s, subsequently, all phases are re-connected all at once at $t = 7.5$ s. It is worth underlying that such a long disconnection is not to be intended as a realistic scenario, but rather it aims at better visualizing the disconnection and the re-connection transients, as well as the behavior of the power system during the islanding operation.

Lastly, some comments are worth for what regards the power system simulation. The distribution network is modeled in MATLAB/Simulink environment and a time-domain simulation with a time step equal to $\Delta t = 2\ \mu$s is performed. The simulation lasts for 10 s, in order to ensure the complete ending of all transients. To replicate a realistic scenario, both voltage and current signals have been corrupted with white Gaussian noise of 75 and 60 dB, respectively, as assessed in [82]. Being the referenced work about measurements on a distribution microgrid, it is reasonable to assume that it can provide coherent values for this study.

As this research aims at performing a local aggregation of PMU measurements coming from neighboring nodes in proximity to each other, the power system under study has been divided into different parts. First, two main feeders, Feeder 1 and Feeder 2, can be identified as they are illustrated in Fig. 6.12 in yellow and pink, respectively. In addition, a finer subdivision aims at identifying even smaller areas. The three main vertical buses are highlighted in red, whereas western buses (W) are shown in blue and eastern buses (E) in green, as illustrated in Fig. 6.12.

6.3.2 Results Evaluation

This Section illustrates the most significant results obtained from performing the simulations previously described. For the sake of completeness, all individual partitions are analyzed, but greater detail is provided for those in which there are buses hosting either PV plants or an ESS.

The first area under test is the West region of Feeder 1. In these buses, the nRMSE is approximately zero. The negligible discrepancies in voltage and current waveforms are produced just by the superimposed noise on the signals. The results concerning Bus 646 and 645 are presented as follows. Fig. 6.15(a) shows the nRMSE at Bus 646 of the voltage ($nRMSE_V$, in blue) and of the current ($nRMSE_I$, in red) expressed in per unit of their rated values, and computed on phase A. Similarly, Fig. 6.15(b) illustrates the results concerning Bus 645. Small nRMSE values indicate the reliability of these measurements, in spite of the transients and the RES installed in other areas of the network. These results were expected, considering that buses in this area are distant from all RES and in proximity to the generator.

The East area in Feeder 1, instead, is strongly affected by the presence of the three-phase PV power plant installed at Bus 634. Not only does it produce variable power depending on the solar irradiance but it also introduces harmonic and inter-harmonic components. For this reason, the results refer to Bus 634 only but similar outcomes can be obtained for Bus 633. Fig. 6.16 reports the nRMSE in per unit computed on phase A of voltage and current signals. With respect to the results of Feeder 1-W shown in Fig. 6.15, in this case, the results are not negligible at all. Indeed, $nRMSE_V$ follows the applied solar irradiance cycle and shows 7 different plateaux corresponding to the different power levels. Similar considerations are valid for $nRMSE_I$ that presents also six spikes that can be clearly identified. Comparing Fig. 6.15 with Fig. 6.13, it is evident that these peaks occur at the same time instants as the irradiance step changes. In this case, though, the plateaux in $nRMSE_I$ are

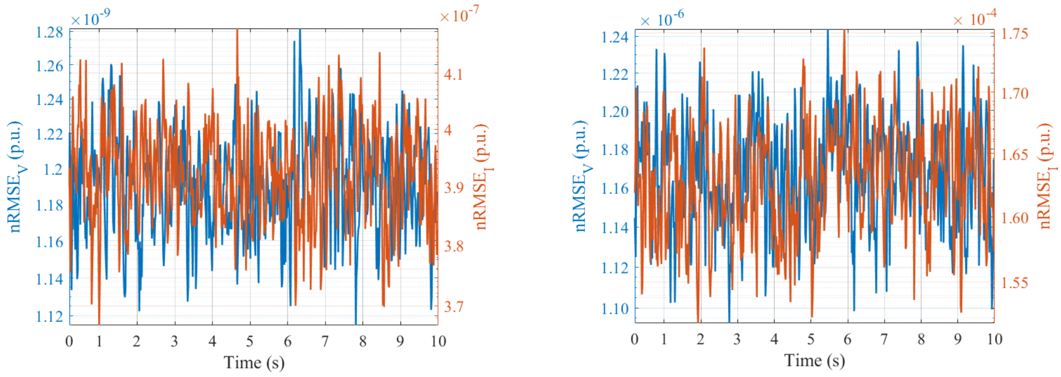

(a) (b)

Figure 6.15: Results of nRMSE evaluated on Feeder 1 - W. The nRMSE on phase A of voltage ($nRMSE_V$) and current ($nRMSE_I$) waveforms are shown in blue and red, respectively. They are obtained at Bus 646 (a) and at Bus 634 (b). Adapted from [185].

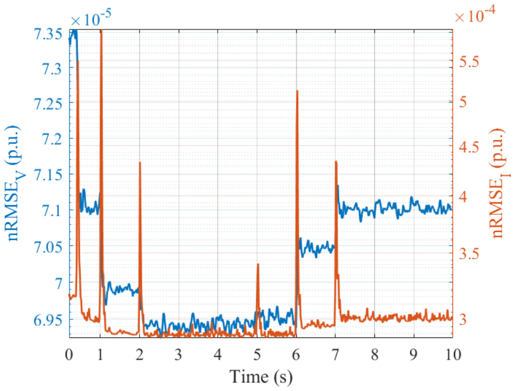

Figure 6.16: The nRMSE of voltage ($nRMSE_V$) and current ($nRMSE_I$) waveforms are shown in blue and red, respectively. They are obtained in Feeder 1 - E at Bus 634. Source: [185].

much less evident than those observed in $nRMSE_V$.

In the following, instead, the results regarding the West and East areas of Feeder 2 are analyzed. This is a single-phase area, in which a PV power plant is simulated as well as a diverse mix of single-phase loads.

First of all, the results of the West area are examined. The outcomes attained at Bus 611 are shown in Fig. 6.17. Similar comments can be made to what has been observed in Fig. 6.16 which is also characterized by the presence of a PV plant. As a matter of fact, also in this case it can be noted a clear correspondence between peaks in $nRMSE_I$ and step changes in the irradiance cycle, by comparing Fig. 6.13. Furthermore, in this case, two additional spikes can be distinguished. They occur at 3.5 and 7.5 s, which correspond to the time instants of the opening and re-closing of the CB installed in the same feeder. Despite its physical distance from the fault location, corresponding to roughly 2 km, noticeable effects influence the signals at this bus. Therefore, the measurements are made less reliable at multiple instants during the simulation. As regards $nRMSE_V$, instead, a nearly constant trend is noticed, apart from the spikes related to the CB opening and re-closing. In this case, the irradiance variations are smaller and their contribution to the overall nRMSE is limited and practically hidden by the wide-band noise.

The neighboring buses, namely Bus 684 and Bus 652, are affected just by the switch-

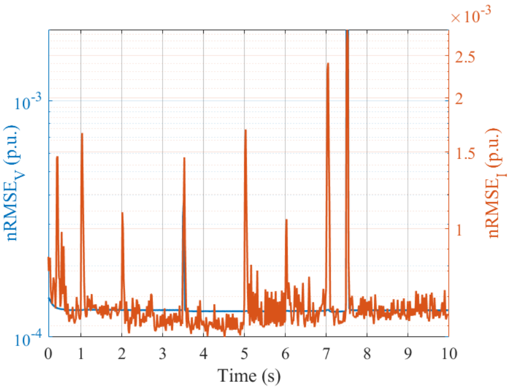

Figure 6.17: The nRMSE of voltage ($nRMSE_V$) and current ($nRMSE_I$) waveforms are shown in blue and red, respectively. They are obtained in Feeder 2 - W at Bus 611. Source: [185].

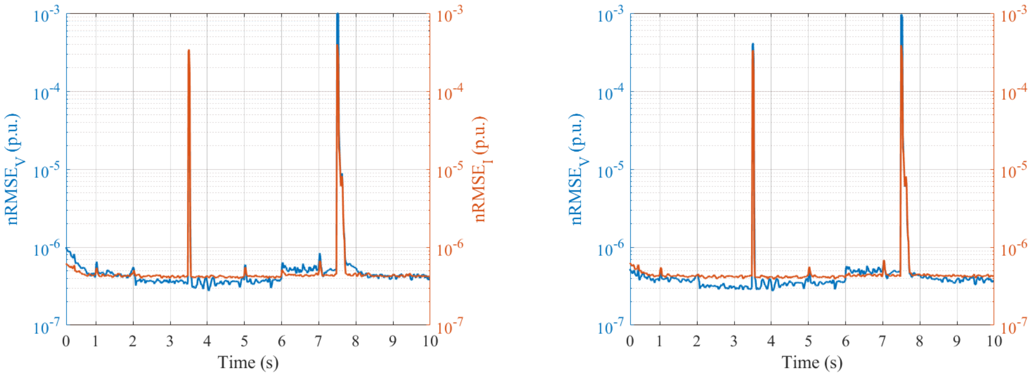

(a) (b)

Figure 6.18: Results of nRMSE evaluated on Feeder 2 - W. The nRMSE on voltage ($nRMSE_V$) and current ($nRMSE_I$) waveforms are shown in blue and red, respectively. They are obtained at Bus 684 (a) and at Bus 652 (b). Source: [185].

ing of the CB. On the contrary, the contribution of the PV is still present but much less visible, as shown in Fig. 6.18 depicting in (a) the nRMSE indices assessed at Bus 684 and in (b) those relative to Bus 652. Moreover, the signals are less corrupted by harmonics and inter-harmonics, since the variability of nRMSE is minimal in comparison to the results retrieved from the previous buses. In this area, it is not appropriate to aggregate measurements despite their physical proximity given by short line lengths, because these nodes need to be monitored independently as each of them is characterized by peculiar conditions.

The East partition of the same Feeder is of particular interest given the presence of the ESS at Bus 692 and the switching of the CB leading to a brief islanding operation. Indeed, in between 3.5 and 7.5 seconds these two buses get disconnected from the main grid but, in spite of that, they are still supplied thanks to the ESS. For this reason, it is very significant to assess the reliability of PMU measurements in these conditions. Indeed, the nRMSE is shown in Fig. 6.19, illustrating data relative to Bus 675 in (a) which is the farthest from the CB and to Bus 692 which hosts the ESS in (b). Before and after the switching, both voltage and current nRMSE show low values in the order of 10^{-6} per unit. Nevertheless, during the microgrid operation, despite being still supplied by the ESS, both nRMSE values increase by roughly three orders of magnitude. This indicates the scarce reliability of such PMU measurements in this low-inertia condition.

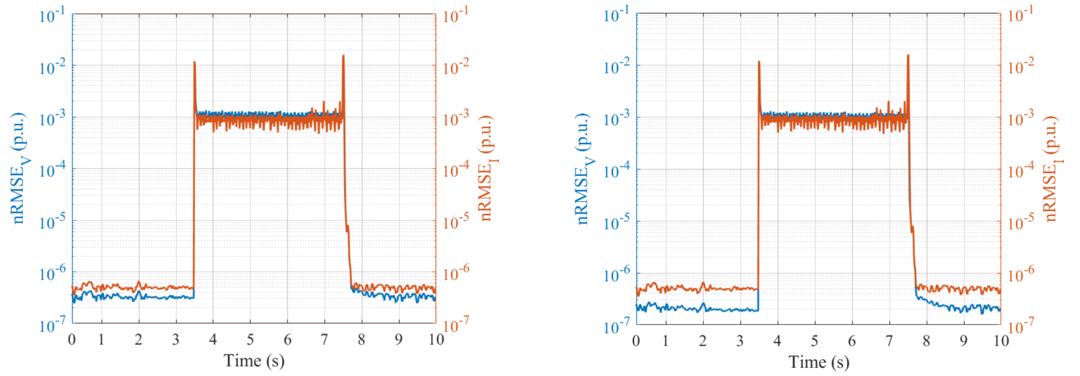

(a) (b)

Figure 6.19: Results of nRMSE evaluated on Feeder 2 - E. The nRMSE on voltage ($nRMSE_V$) and current ($nRMSE_I$) waveforms are shown in blue and red, respectively. They are obtained at Bus 675 (a) and at Bus 692 (b). Source: [185].

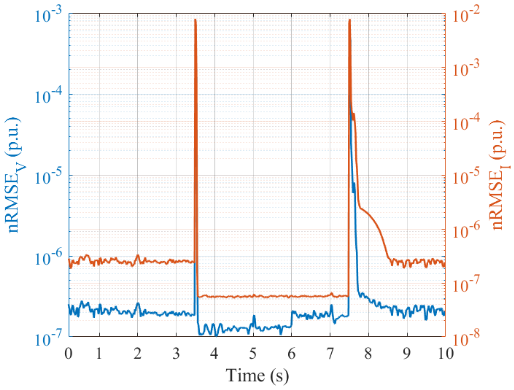

Figure 6.20: The nRMSE of voltage ($nRMSE_V$) and current ($nRMSE_I$) waveforms are shown in blue and red, respectively. They are obtained in Connection 1-2 at Bus 671. Source: [185].

The last partition to be analyzed is the Connection 1-2 highlighted in red in Fig. 6.12 that links Feeder 1 to Feeder 2. All three buses are affected, in a stronger or weaker way, by the opening/re-closing of the CB on Feeder 2. For the sake of clarity, just the outcomes of Bus 671 are shown since it is the closest in proximity to the CB. Bus 680 is discarded since no load is connected here, so it could only be possible to assess the voltage nRMSE. While Bus 632 is not considered owing to the less visibility of nRMSE variations in comparison to those on Bus 671.

Fig. 6.20 illustrates the nRMSE trends relative to Bus 671. In this case, the behavior is comparable to the one observed in Fig. 6.19(a) and (b) for what concerns the two steady-state conditions, i.e., before and after the CB switching. Moreover, two peaks can be noted at the switching time instants, as before. During the disconnection of the two buses, in this case, PMU measurements performed on this bus are still reliable nonetheless. This can be deduced from the low nRMSE values between 3.5 and 7.5 s which are in the same range as those in steady-state. However, this result could have been foreseen as this bus is still supplied by the main voltage generator of the feeder. Therefore, it is not subject to a microgrid, or a low-inertia condition, which would have made it more susceptible to power and frequency variations.

Having presented the nRMSE trend in each of the partitions that divide the distribution network, it is then examined how the nRMSE can be integrated into the PMU measurement aggregation process. At a PDC level, this would allow the com-

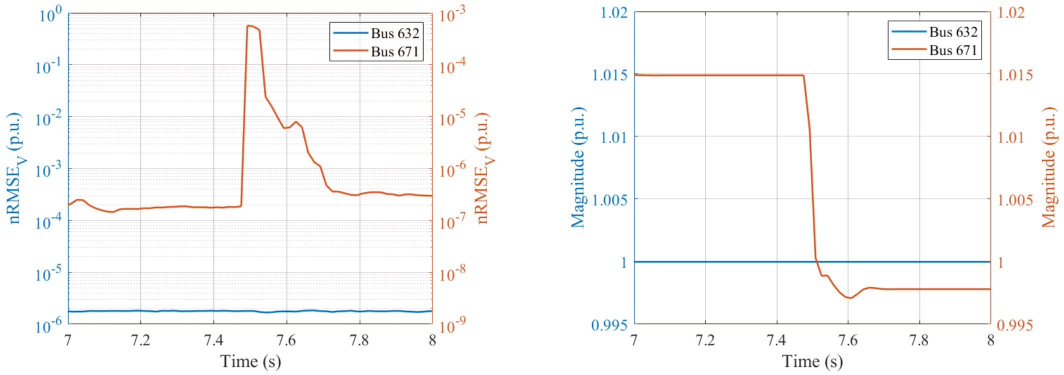

(a) (b)

Figure 6.21: Comparison of nRMSE in (a) and of voltage magnitudes (b) obtained on Connection 1-2 at Bus 632 and 671 in blue and red, respectively. Source: [185].

parison of consistent measurements and hence the definition of a local area estimate of the frequency and magnitude associated with voltages and currents.

As a case study, the Connection 1-2 area is considered and only voltage measurements are examined, namely $nRMSE_V$ and phase A, on Bus 632 and 671. The first one is directly connected to the reference voltage generator: it is then reasonable to expect that both the observed quantities are nearly time-invariant. The second one, instead, is affected by the CB opening and re-closing as well as by the power output variations of the PV at Bus 611. In this context, Fig. 6.21(a) presents the $nRMSE_V$ as computed on the two buses in a zoomed portion of the time simulation in between 7 and 8 s. It is worth recalling that the CB re-closing occurs at $t = 7.5$ s. As expected, Bus 632 is characterized by a nearly constant trend, where the only contribution is represented by the additive wide-band noise. Conversely, Bus 671 shows a clear transition in correspondence with the CB re-closing, but the transient effects persist during the following 0.3 s. In a similar way, Fig. 6.21(b) compares the voltage magnitude estimates on the two selected buses. Once more, Bus 632 voltage is constantly equal to 1 p.u., whereas Bus 671 presents a step change variation. It is interesting to observe how the voltage magnitude keeps oscillating for the following 0.3 s, in line with what has been observed in the previous nRMSE analysis.

Based on this analysis, it can be concluded that nRMSE can be used as a flag of measurement reliability. When PMUs present a low nRMSE, it is reasonable to aggregate their measurement results and merge them to define a local area estimate of the voltage magnitude and frequency. On the contrary, when one or more PMUs present a non-negligible variation in their nRMSE, a deeper insight is required, and it is preferable to consider each measurement data stream individually. The outcomes also point out a significant reduction in the PMUs' measurements reliability in proximity to RES and in low-inertia conditions.

6.4 nRMSE for Renewable-Based Power Systems

The previous Section 6.3 presented interesting results obtained in the assessment of local regions based on their nRMSE value. For this reason, it is worth proceeding in this regard and assessing the capability of nRMSE to specifically identify contingencies in both high- and low-inertia power systems. Therefore, this Section presents a study on the nRMSE, which is still regarded as a local index of measurement reliability for PMU measurements, applied in two well-known IEEE benchmark grids that have been suitably modified in order to account for the presence of RES.

The objective of this work consists in detecting anomalous conditions by means of a simple threshold comparison. First of all, the expected nRMSE is defined as the mean value over 0.2 s of nominal operating conditions. Afterward, an anomalous condition, such as a fault or a CB opening, is detected as soon as the nRMSE exceeds the expected value by 3 orders of magnitude. It is worth noticing that this value stems from the results presented in Section 6.2.2 in which a discrepancy between roughly 3 order of magnitude was observed in dH in case of faults. In the following, the nRMSE latency is also assessed. Indeed, it is quantified as the time elapsed from the passing of the threshold, comprising acquisition and processing latencies, similarly to what is presented in Section 4.2.

The following Section 6.4.1 illustrates the PMU model and the specifications of the two power systems under test, while Section 6.4.2 presents the most significant results and draws some conclusions of this work. This work is an extension of what is illustrated in Section 4.2 and it summarizes the main results of [88].

6.4.1 Simulated Scenarios

This Section illustrates the power system scenarios under test, at transmission and distribution levels, both characterized by the presence of RESs. The simulated scenarios are inspired by well-known benchmark grids as detailed in Section 5.1. In the following, the PMU model, as well as the simulation details and the introduced modifications, are illustrated and motivated.

PMU model: it is based on PMU B that is presented in Section 4.1.1. More specifically, since in these two scenarios, the power system rated frequency is 60 Hz, the sampling rate of the PMU is chosen equal to 18 kSa/s. The windowing time corresponds to three cycles of nominal system frequency, i.e., 50 ms for 60-Hz signals. As one of the objectives of this Section involves the investigation of the effects of the PMU reporting rate on the identification of events by means of the nRMSE, all possible reporting rates, according to the PMU Std, for a 60-Hz PMU are considered, i.e., $10, 30, 60, 120$ fps [14]. Lastly, the considered model is compliant with P-class as it is reasonable to expect P-class compliant devices in these applications which are characterized by fast transient and contingencies. For the sake of brevity, the description of the computation of the nRMSE is omitted as the same steps presented in Section 4.1.2 are still valid.

Power System I: As a first assessment, the well-known IEEE 14-bus system is examined. Its original data and its main characteristics are presented in Section 5.3.2. More specifically in this application, the time-domain simulation lasts 5 seconds and includes the opening of the CB connecting Bus 2 to Bus 3, and the CB connecting Bus 2 to Bus 4, both simultaneously at $t = 1$ s. Despite no re-closing is involved, noticing the topology of the grid shown in Fig. 6.22, it can be observed that all the loads can still be supplied by the generators present in the network. For the sake of brevity, the following analysis is focused only on Bus 2 which is the most affected by

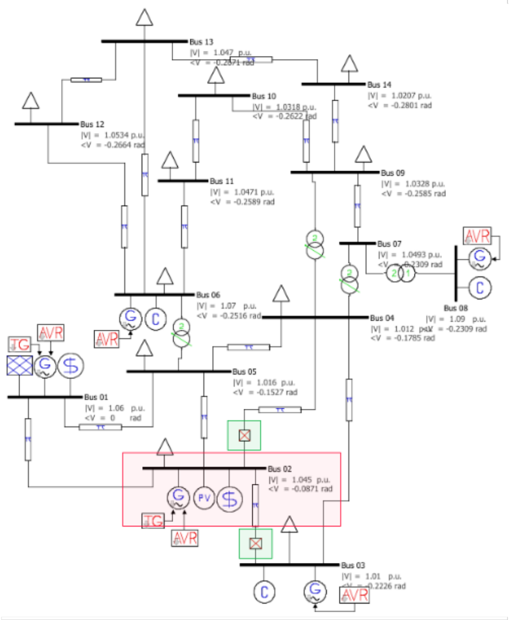
Bus 13
|V| = 1.047 p.u.
<V = -0.2671 rad
Bus 14
|V| = 1.0207 p.u.
<V = -0.2801 rad
Bus 10
|V| = 1.0318 p.u.
<V = -0.2622 rad
Bus 12
|V| = 1.0534 p.u.
<V = -0.2664 rad
Bus 11
|V| = 1.0471 p.u.
<V = -0.2589 rad
Bus 09
|V| = 1.0328 p.u.
<V = -0.2585 rad
Bus 07
|V| = 1.0493 p.u.
<V = -0.2309 rad
AVR
G
C
Bus 08
|V| = 1.09 p.u.
<V = -0.2309 rad
Bus 06
|V| = 1.07 p.u.
<V = -0.2516 rad
Bus 04
|V| = 1.012 p.u.
<V = -0.1785 rad
TG
AVR
G
$
AVR
G
C
Bus 05
|V| = 1.016 p.u.
<V = -0.1527 rad
Bus 01
|V| = 1.06 p.u.
<V = 0 rad
Bus 02
|V| = 1.045 p.u.
<V = -0.0871 rad
G
PV
$
TG
AVR
Bus 03
|V| = 1.01 p.u.
<V = -0.2226 rad
C
G
AVR
2
1

Figure 6.22: Power System I: Model of the IEEE 14-bus system developed in MATLAB/Simulink using PSAT Toolbox [184]. The two CBs which open at $t = 1$ s are indicated by green squares, while the red rectangle indicates Bus 2 which is the bus under test. Source: [88].

the CB opening. However, similar results can be observed in the other nodes.

The second simulation, instead, consists of the same contingency, but the inertia constants of the synchronous machines hosted at Bus 2 and 3 have been halved, as illustrated in Table 5.1, in order to replicate a low-inertia power system. This corresponds to a reduction of $-9.33\,\%$ of the overall power system inertia with respect to the rated power system's conditions.

The model of the IEEE 14-bus system has been developed using the PSAT toolbox for MATLAB/Simulink environment [184]. Fig. 6.22 presents the topology of the power system under study, highlighting in red Bus 2 whose results are examined in the following. The two green squares indicate the CBs which open simultaneously generating the transient condition.

It is worth noticing that in this model no uncorrelated white Gaussian noise has been added to either voltage or current signals. Therefore, the results are affected only by numerical simulation or model errors, but they do not include any form of noise on the acquired signals.

Power System II: The second scenario is based on another well-known power system benchmark grid that, differently from the previous scenario, replicates a typical distribution power system. It relies on the IEEE 13-bus system data which was originally presented in [172] and whose most significant specifications are shown in Section 5.3.1. However, significant changes have been introduced in order to take into account the ever-growing DG also at low-voltage levels.

For this purpose, three new buses have been added with respect to the original distribution feeder. They are located at the original Bus 611, which hosts a single-phase PV with a rated power of 3.5 kW which resembles a typical household plant. Whereas, Bus 652 hosts two single-phase PV plants with a rated power of 3.5 kW each. It is worth highlighting that all PV plants are transformer-less, in a similar

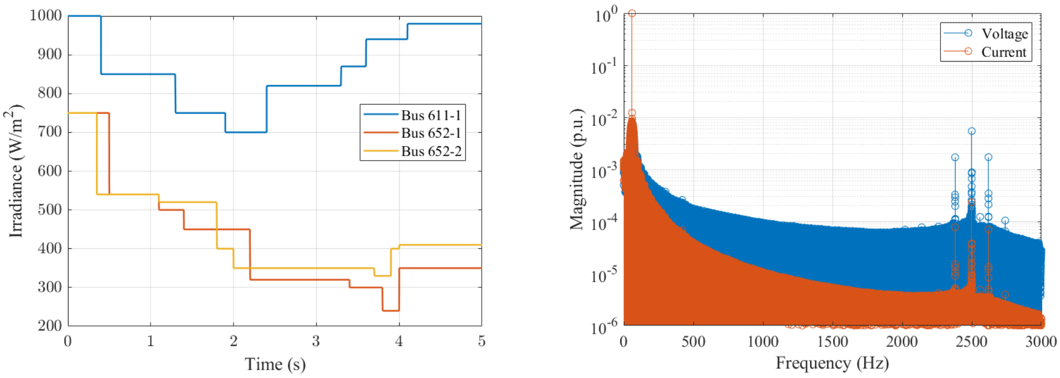

(a) (b)

Figure 6.23: Power System II: In (a) the solar irradiance trends are shown for the three PV plants simulated in the power system at Bus 611-1, 652-1, and 652-2, respectively in blue, red, and yellow. In (b): Amplitude spectrum of the first 50 harmonics of the voltage and current signals measured at Bus 652 in blue and red, respectively. Source: [88].

way to household devices. Additionally, to introduce plausible levels of harmonic content and time-varying output power generated by the PV, three different irradiance cycles having low levels of irradiance have been recreated, as shown in Fig. 6.23(a). Similarly to the study carried out in Section 6.3, the time instants at which the solar irradiance changes its value do not correspond to any of the zero-crossing of the power system signals. Furthermore, the choice of having such low levels has been proven to introduce a non-negligible level of harmonics and inter-harmonics [186]. This is confirmed by the voltage and current amplitude spectra assessed at Bus 652 and shown in Fig. 6.23(b). Additionally, both voltage and current signals have been corrupted with white Gaussian noise of 75 and 60 dB, respectively. This noise level presents a plausible amount introduced by the analog front-end and by the in-field transducers as evaluated in [82].

In more detail, Bus 611-1 is connected to the original Bus 611 with a 3000 ft line, whereas Bus 652-1 and 652-2 are connected to the preexisting Bus 652 via a 10000 and a 15000 ft lines, respectively. In this feeder, specifically along the line connecting Bus 684 to Bus 652, a phase-to-ground fault occurs at $t = 2.220$ s and it is cleared at $t = 2.255$ s. This scenario replicates the typical response of a low-voltage CB, which has a clearance time below 3 cycles of nominal system rate. The simulation is performed in MATLAB/Simulink environment. The total duration is 5 s, while the discrete time step Δt is equal to $2\,\mu$s.

6.4.2 Results Assessment

Power System I: without loss of generality, the following graphs refer only to the minimum ($R_r = 10$ fps) and maximum reporting rates ($R_r = 120$ fps). For this analysis, the nRMSE is considered on both voltage and current signals, respectively indicated by subscript V and I, at Bus 2 in order to assess whether significant differences can be observed on the two signals. The rationale behind the choice of Bus 2, among all power system buses, relies on the fact that this bus is the closest to the CB opening. As proven by the results of Section 6.2 and 6.3, the variations of inertia dH and the nRMSE are more sensitive as the distance between the measuring point and the fault location is minimized. In this regard, Fig. 6.25

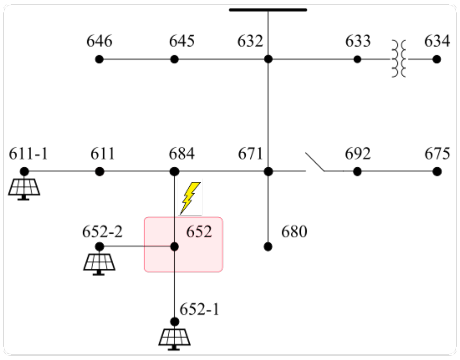

Figure 6.24: Power System II: Model of the IEEE 13-bus system developed in MATLAB/Simulink environment, including three additional buses hosting a 3.5 kW PV each. Bus 652 is the bus under test and it is highlighted in red, while the fault location is indicated by a lightning bolt. Source: [88].

presents the resulting nRMSE in the time domain, in rated inertia conditions for the two R_r under test, respectively in subfigures (a) and (b). Similarly, Fig. 6.26 illustrates the time trend results for the same simulated power system model, but in low-inertia conditions (i.e., Scenario II). In both cases, the CB opening corresponds to a sharp transition of a few orders of magnitude in the nRMSE values in both Fig. 6.25 and 6.26. Additionally, comparing both subfigures, it is evident how the highest R_r allows for better tracking of the nRMSE oscillations caused by the transient. As a matter of fact, when the R_r is the lowest, the first values of nRMSE exceeding the threshold could be misinterpreted as outliers, hence leading to longer times in counteracting. On the other hand, the reduction of inertia is evident in Fig. 6.26 in the irregular and more oscillatory trend with respect to the results of Fig. 6.25. Similar comments can be made also in this case. Indeed, for a $R_r = 10$ fps, the tracking of the nRMSE is much less accurate, and the first values could be misinterpreted. Additionally, comparing these results with the previous ones, it is evident how a low-inertia case is heavily subjected to longer and deeper oscillations in the time domain which are clearly reflected on the nRMSE, in a similar way to the power and ROCOF oscillations observed in the dH assessment. Nevertheless, it is interesting to observe that the nRMSE in the two Scenarios are characterized by the same order of magnitude, meaning that a low-inertia condition cannot be discerned from a rated one, just by analyzing the absolute value itself. But rather it is necessary to assess the whole time-domain trend of the quantities under test. In a similar way, it is not possible to forecast the response of the power system to a contingency, as the steady-state nRMSE in both high- and low-inertia conditions are in the same order of magnitude.

In this regard, it is worth recalling that values of $nRMSE_V$ and $nRMSE_I$ in the order of 10^{-15} p.u. have to be intended as ideal values, owing only to the numerical errors and to the fact that no additional noise has been added to the voltage and current signals. Such values indicate the correct estimation of the synchrophasor by means of the PMU used for the simulations, but they do not have to be expected for in-field conditions. In terms of latency, instead, all the reporting rates allow for prompt detection. However, in the presence of a CB opening, the use of higher reporting rates implies some, but limited advantages (i.e., a latency reduction of less than 1 nominal cycle). Nevertheless, as previously described, it allows for better tracking of the nRMSE oscillations, especially in the low-inertia scenario.

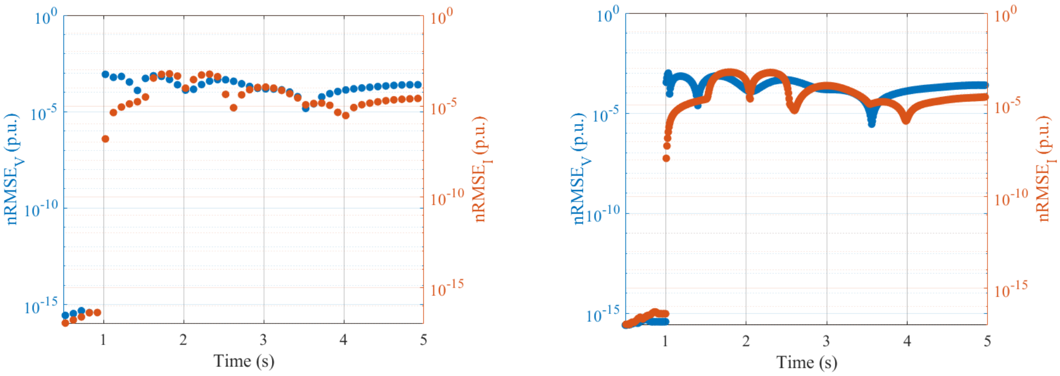

(a) (b)

Figure 6.25: Power System I: voltage and current nRMSE indicated by the subscripts V and I, respectively, measured at Bus 2 in rated inertia conditions. In both cases, PMU B is used, but only the lowest and the highest reporting rates are studied: (a) $R_r = 10$ fps, (b) $R_r = 120$ fps.

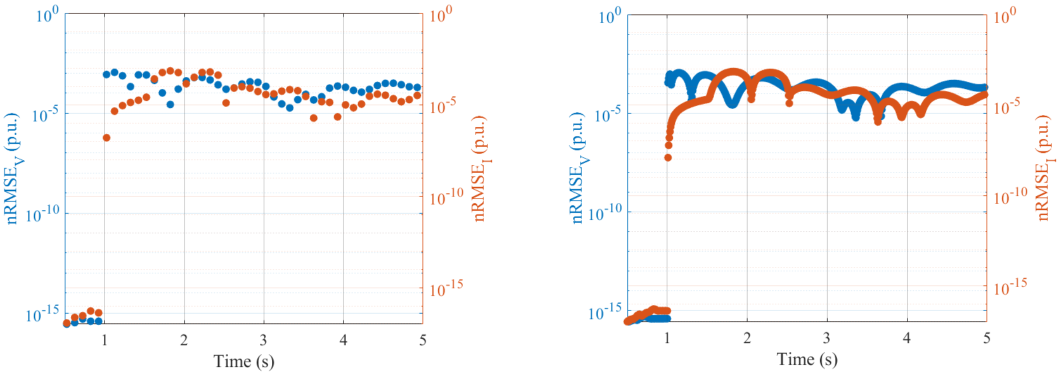

(a) (b)

Figure 6.26: Power System I: voltage and current nRMSE indicated by the subscripts V and I, respectively, measured at Bus 2 in low-inertia conditions. In both cases, PMU B is used, but only the lowest and the highest reporting rates are studied: (a) $R_r = 10$ fps, (b) $R_r = 120$ fps.

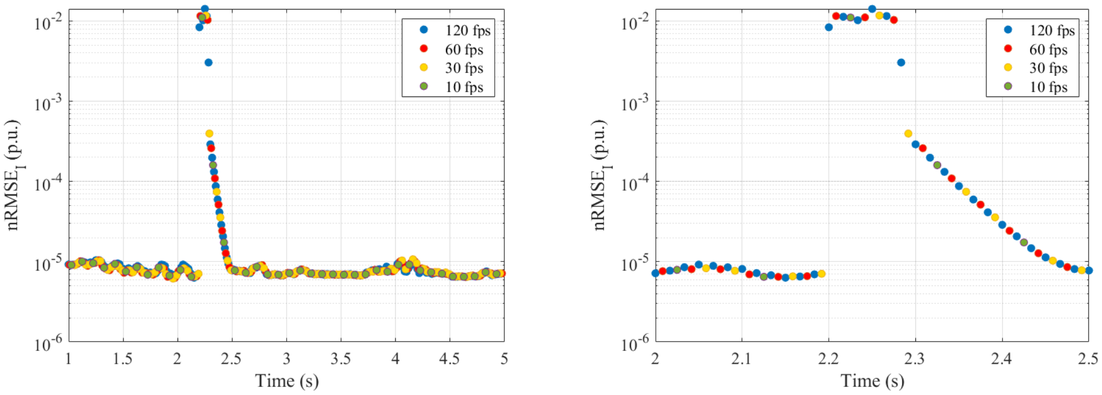

(a) (b)

Figure 6.27: Power System II: current nRMSE indicated by subscript I measured at Bus 652 using all possible R_r available for a 60-Hz PMU B. Different time lengths are illustrated: (a) Entire simulation duration, (b) Only during the contingency. Adapted from [88].

Power System II: in this case, instead, the clearance of a single phase-to-ground fault is considered, simulated by the opening and re-closing of a CB after less than 3 nominal cycles. Hence, it is interesting to evaluate the nRMSE response in the presence of two consecutive transients. In this context, Fig. 6.27 presents the nRMSE profiles of the current signal recorded at Bus 652 for all the possible reporting rates available for a 60-Hz PMU according to the PMU Std. More in detail, Fig. 6.27(a) illustrates the results recorded during the entire simulation duration, while Fig. 6.27(b) presents a zoomed portion focusing on the contingency, highlighting the occurrence of the CB opening and re-closing. Analyzing Fig. 6.27(b), it is clear how the first transition is easily detected by all reporting rates: as in the previous scenario, higher reporting rates allow for an enhancement in terms of detection latency. On the other hand, with an excessively low reporting rate ($R_r = 10$ fps), the threshold is exceeded only once and it could be easily misinterpreted as an outlier. Conversely, the highest reporting rate ($R_r = 120$ fps) allows for quantifying the contingency duration and accurate tracking of the progressive restoration of normal operating conditions. Whereas, just two and three points are recorded in the latter transient when a reporting rate of $R_r = 10$ and $R_r = 30$ fps are selected, respectively. In this simulation, it is also interesting to observe how the results can clearly identify three different states: a steady-state state before the contingency, a short time during which the fault occurs, and a last state when the system restores to its original pre-fault values. The first and the latter are characterized by a nRMSE of the current in the order of 10^{-5} p.u. having added white Gaussian noise to the simulated signals. On the contrary, during the contingency, a jump of 3 orders of magnitude is recorded since a nRMSE is approximately 10^{-2} p.u. These results confirm how the selected threshold can be a good trade-off between ideal and realistic conditions, such as this one, in which the noise can significantly worsen the PMU measurements and, hence any further analysis.

For the sake of completeness, Table 6.4 presents a summary of the detection latencies, in ms, for the two power systems under test. Once again, it can be easily derived that the latency is inversely proportional to the PMU reporting rate.

Additionally to the results presented in Section 4.2.2, this study on specific RES-based power systems highlighted the necessity of assessing the reliability of PMU

Table 6.4: nRMSE detection latency measured in low-inertia scenarios presented in Power System I and II, expressed in ms, as a function of the PMU reporting rate R_r. Source: [88].

R_r (fps)	Power System I	Power System II
10	55	65
30	47	55
60	45	38
120	38	30

measurements. Besides finding a good trade-off between the R_r and a suitable threshold for detecting possible contingencies, what is most significant is the need for evaluating the entire trend in the time domain for the nRMSE in low-inertia conditions. As the results pointed out, the value itself does not provide sufficient information on the low resiliency of the power system, but rather it does its time trend characterized by longer and stronger oscillations that need to be tackled.

6.5 Electric Instrumentation Interoperability in Low-Inertia Conditions

The previous parts of this Chapter presented the metrological aspects related to the inertia estimation and a feasibility study on a local assessment based on PMUs. Still regarding the same instrumentation, this was followed by the reliability evaluation and possible aggregation of PMU measurements in low-inertia systems.

However, there exist several typologies of electrical instrumentation installed in modern power systems. Therefore, in view of a more comprehensive study on various devices, this Section investigates the interoperability between two of the different measurement systems that can be found in the field.

Based on the previous outcomes and on the evident convenience of using PMUs, they are still considered in this study. The second typology of electrical instrumentation, instead, is represented by PQ meters. Both of these have already been proven to enhance power system observability and real-time control of the network [187–190]. However, given the different characteristics, requirements, and working principles of these two devices, this Section focuses only on their interoperability. As a matter of fact, the objective consists of the investigation of the possible challenges related to the proper aggregation and comparison of the two data streams.

To achieve this, the distribution network presented in Section 5.3.1, including an extensive penetration of RES is simulated, jointly with PMU and PQ meters models. The correlation of their measurements is studied, investigating the consistency between their measurements. Furthermore, the feasibility of merging the corresponding data streams is assessed, presenting the possible challenges related to the proper aggregation and comparison of the two data streams.

This Section illustrates the work presented at the International Instrumentation and Measurement Technology Conference (I2MTC) held in Kuala Lumpur, Malaysia in 2023 [191]. The power system model is presented in Section 6.5.1 in which the IEEE 13-bus system is equipped at each node with two PMU models, compliant with the

P-class requirements of the PMU Std, and a PQ meter. The results, instead, are discussed in Section 6.5.2.

6.5.1 Simulation Specifications and Models

This Section illustrates in the first part the adopted PMU and PQ models for this study, presenting their characteristics and the relevant Standard requirements. On the other hand, the second part focuses only on the modifications performed on the distribution system model presented in Section 5.3.1.

PMU and PQ models: first of all, it is worth highlighting that PMUs and PQ meters are different devices that refer to two different standards, respectively the IEC/IEEE 60255-118-1 and the IEC 61000-4-30 and IEC 62586-2 [14, 192, 193]. Consequently, they shall comply with different performance requirements in terms of measurement accuracy and synchronization source. Among all of them, it is worth citing that, PMUs must refer their time stamps to a UTC-traceable time source, with a resolution typically included within 1μs. On the contrary, PQ meters' time-stamps are rounded to the nearest ms. In the same context, PMUs exploit the external time reference to discipline their ADC stage, whereas PQ meters take as reference the zero-crossing of the signal under test. Lastly, as briefly disclosed previously, PMUs and PQ meters adopt quite different measurement time intervals and reporting rates. Given a nominal system frequency of 60 Hz, a typical PMU setup considers a measurement time interval of three to six nominal cycles, with a reporting rate of 10, 30, 60, or 120 fps. Conversely, a PQ meter relies on a measurement time interval of 12 nominal cycles and a reporting rate of half-cycle corresponding to 120 fps. From the measurement point of view, it is also important to point out that PMUs and PQ meters have different noise rejection and filtering capabilities. The first ones exploit advanced signal processing algorithms to estimate the dynamic behavior of the fundamental component phasor, frequency, and ROCOF. They consider any other narrow- or wide-band component as spurious contributions to be mitigated and potentially compensated. PQ meters, instead, are designed to estimate both the fundamental component and the harmonic and supra-harmonic ranges. As a consequence, they rely on much less selective estimation filters, for what concerns the fundamental, and are characterized by larger equivalent noise bandwidths.

From the model point of view, instead, for what concerns PMU measurements, PMU B is considered. It is described in Section 4.1.1 and relies on the algorithm presented in [100]. It is worth recalling that PMU B is compliant with both P- and M-class requirements of the PMU Std [14]. The reporting rate is chosen equal to 60 fps as the power system rated frequency (f_n) is 60 Hz. In order to guarantee a fair and consistent comparison between PMU and PQ measurements, the window length is set equal to 12 cycles, corresponding to a time window of 0.2 s, based on the previous description. For all voltage and current phasors, their rms values, frequency, and ROCOF are extracted and post-processed in MATLAB environment.

On the other hand, for what regards PQ measurements, the Electrical Power Quality toolbox in LabVIEW is used, as it already performs PQ calculations in compliance with the relevant Standard [192, 194]. Similarly to what is done for PMUs, voltage and current rms values are computed, together with the phasor frequencies.

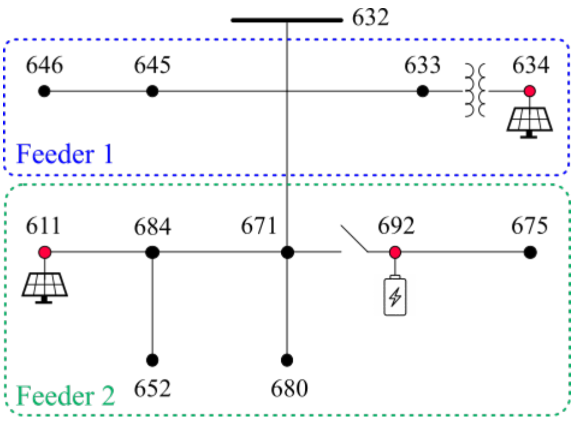

Figure 6.28: Model of the IEEE 13-bus system developed in MATLAB/Simulink environment, including two additional PV plants at Bus 634 and 611, and an ESS at Bus 692. The distribution network is divided into two feeders indicated by Feeder 1 and 2, in blue and green, respectively. Red dots indicate the buses whose measurements are examined in the following. Source: [191].

Power System Model: In order to model a distribution power system, the IEEE 13-bus network is developed in MATLAB/Simulink environment. However, starting from its original description presented in Section 5.3.1, according to [172], some modifications have been introduced and they are listed here as follows.

In Feeder 1, a three-phase 250 kW PV is introduced at Bus 634. Whereas, in Feeder 2 a single-phase transformer-less 3.5 kW PV power plant is added at Bus 611. Additionally, an ESS is located at Bus 692. The ESS features a rated power and capacity of 500 kW and 100 kWh, respectively. Fig. 6.28 represents the simulated distribution grid described above, where Feeders 1 and 2 are highlighted by blue and green dashed rectangles, respectively. Despite performing power measurements with PMUs and PQ meters at all nodes, red dots in Fig. 6.28 indicate which power measurements are considered in the following Section.

Before performing time-domain simulations, power flow is computed once again to start from steady-state conditions. Simulations are run for 10 seconds and are performed with a discrete-time resolution Δt equal to 2 μs.

To simulate a dynamic and realistic scenario, a time-varying irradiance cycle has been created, as shown in Fig. 6.29, considering data presented in [186]. Changing the irradiance implies that the current generated by the two PV power plants changes in time and, consequently, the PV output power. Similarly to the previous analysis and without loss of generality, the variations of the irradiance value occur at time instants not corresponding to the zero crossing of the power system waveforms.

The second dynamic condition is simulated by opening the CB connecting Bus 671 to Bus 692 in Feeder 2. At $t = 5$ s all three phases are opened simultaneously, and they are re-closed at $t = 7$ s. During this time, the ESS installed at Bus 692 still supplies Bus 675, replicating an operation typically employed in microgrids.

As already disclosed, only three measuring locations are examined, which correspond to the nodes at which the DG is added, namely Bus 634, Bus 611, and Bus 692. However, for the sake of simplicity, in the following, only phase A is analyzed, yet similar results can be obtained for the other phases.

In order to reproduce plausible operating conditions, voltage and current waveforms

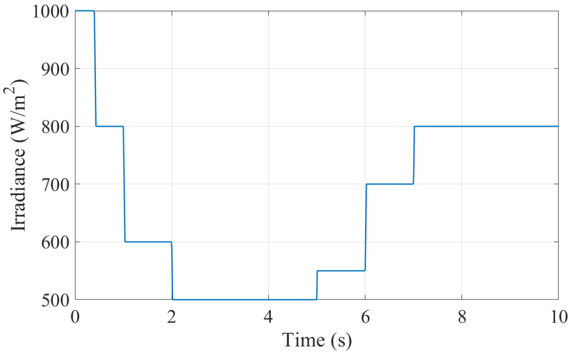

Figure 6.29: Solar irradiance cycle applied to both PV plants simulated at Bus 634 and Bus 611, added to the distribution system under test. Source: [191].

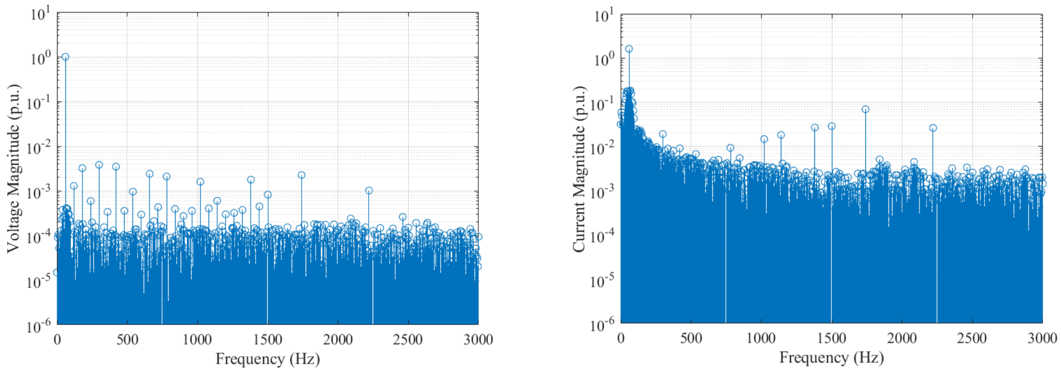

(a)

(b)

Figure 6.30: Amplitude spectrum of the first 50 harmonics of the voltage (a) and current signals (b) measured at Bus 634 and computed on a 200 ms interval. Source: [191].

have been corrupted by means of uncorrelated white Gaussian noise and harmonic components. Based on real-world measurements performed by the Authors on a real distribution grid in [82, 195], it is likely to expect that the current waveforms are characterized by higher levels of distortion. For the sake of reproducibility, Table 6.5 reports the THD and SNR for both voltage and current waveforms. In this regard, Fig. 6.30(a) and 6.30(b) show the module of the Discrete Fourier Transform for the first 50 harmonics, as computed on 200 ms interval, for current and voltage waveform at Bus 634, respectively. In particular, it can be observed a higher noise floor on the current waveform and a larger bandwidth of the fundamental component, which is a clear indicator of larger phase noise and frequency instability.

6.5.2 Results Analysis

The first result illustrates the difference between the reporting frames of PMUs and PQ meters. It is worth recalling that PMUs provide one measurement every cycle,

Table 6.5: Power quality indices of the voltage and current signals assessed at Bus 634, which hosts a PV plant. The PQ indices are presented in terms of THD and SNR, expressed in % and in dB, respectively. Source: [191].

Signal	THD (%)	SNR (dB)
Voltage	0.75	45
Current	14.50	35

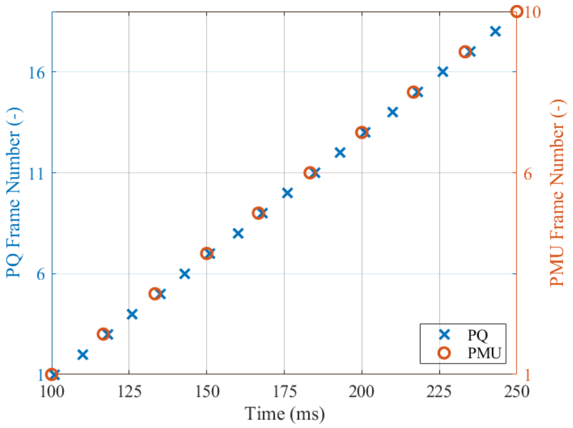

Figure 6.31: Reporting frame difference observed in a 250 ms time interval between PMUs and PQ meters. The firsts are indicated by red circles on the right axis, while the latter by blue crosses on the left axis. Source: [191].

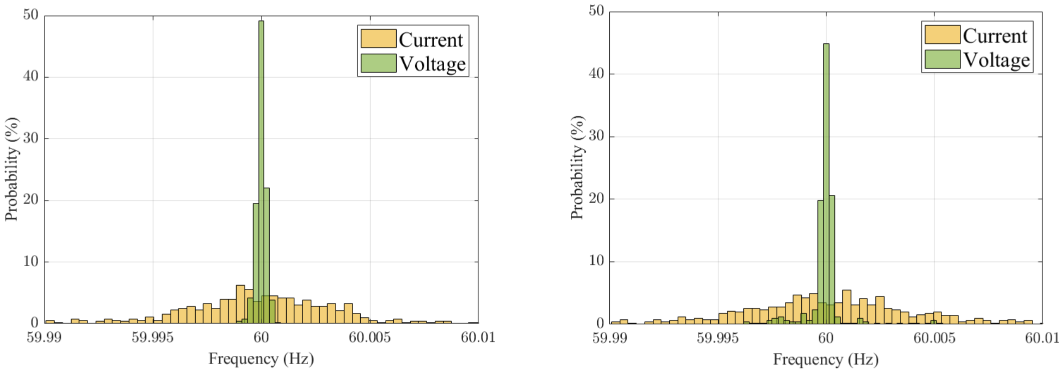

(a)

(b)

Figure 6.32: Statistical distribution of the frequency measurements obtained on phase A voltage (green) and current (yellow) signals, as provided by the PMU at Bus 634 (a) and in Bus 611 (b). Adapted from [191].

hence corresponding to every $1/60 = 16.67$ ms for a 60-Hz rated system signal, which is referred to the UTC[2]. On the contrary, PQ meters provide one rms measure every half cycle, thus every $(1/60)/2 = 8.33$ ms. In this case, it is important to underline that these measurements are synchronized to the signal zero-crossing but they are not referred to any UTC-based system. For the sake of clarity, Fig. 6.31 shows the reporting rates for a small time-domain portion equal to 250 ms. PQ and PMU frame numbers are shown by blue crosses and red circles, respectively. What can be clearly denoted is that the reporting never occurs exactly at the same time, but there is always a discrepancy, owing to the inconsistent synchronization sources as expected by the devices' operating principles.

In the following analysis, instead, a particular focus is given to Bus 634 and 611, since they host the two PV units. Hence, they are representative of reduced inertia and high-distorted conditions. In particular, the frequency distributions measured by PQ and PMUs are evaluated, based on the results attained on phase A of both voltage and current phasors.

---

[2] For the sake of simplicity, the synchronization error is neglected in this first study.

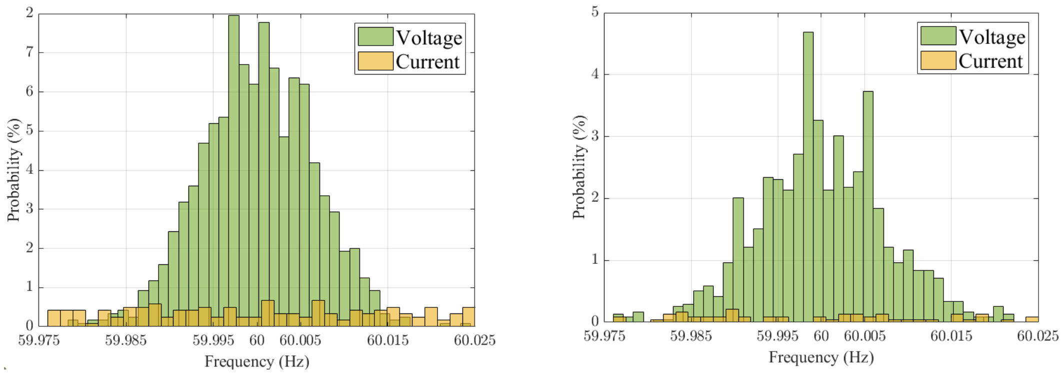

(a) (b)

Figure 6.33: Statistical distribution of the frequency measurements obtained on phase A voltage (green) and current (yellow) signals, as provided by the PQ meters at Bus 634 (a) and in Bus 611 (b). Adapted from [191].

Fig. 6.32 shows the probability histogram of the frequency measured by PMU B at Bus 634 in (a) and 611 in (b). Voltage and current frequencies are shown in green and in yellow hereinafter, respectively. For the sake of clarity, the following figures present just a zoomed portion of the frequency spectrum centered around $f_n = 60$ Hz, even if the entire distributions span over a much wider range in particular for the current signals. It is also worth remarking that the size of the bins has been properly adjusted, independently in each subfigure, in order to fit the two distributions within the same vertical and horizontal limits as far as possible.

The PMU results show that the voltage is characterized by few harmonics, whereas the current includes lots of them owing to the switching of the power converter interfacing the PV to the power grid. It is worth clarifying that a PMU cannot intrinsically detect harmonics. It has rather to be intended that a stronger or weaker harmonic content is more or less reflected in the PMU estimates, as in this particular scenario. Comparing the results shown in (a) and (b) in Fig. 6.32, it can be concluded that neither the proximity to the CB nor the power rating of the PV plays any significant role in the histograms.

The same frequency measurement is repeated using PQ meters in LabVIEW environment. Fig. 6.33 shows the histograms corresponding to the frequency measurements at Bus 634 in (a) and at Bus 611 in (b). If compared with the PMU counterparts of Fig. 6.32, it can be observed that PQ meters perform much less effective filtering and are much more affected by narrow- and wide-band disturbances, as expected based on their operating principle. More precisely, the voltage is still mostly centered around f_n, whereas the current exhibits a much wider and flatter distribution, resembling a uniform one, in the same frequency range.

Based on these results, it is noticeable how the aggregation and comparison of PMU and PQ frequency measurements are not straightforward. As a matter of fact, it is necessary to account for the different measurement procedures and the different rejection capabilities against spurious disturbances of the two devices. From a long-scale statistical perspective, the mean values may be consistent but the instantaneous values may differ by tens of mHz.

Having assessed the frequency distributions obtained using two different devices, the following part focuses on investigating whether the variability of the system

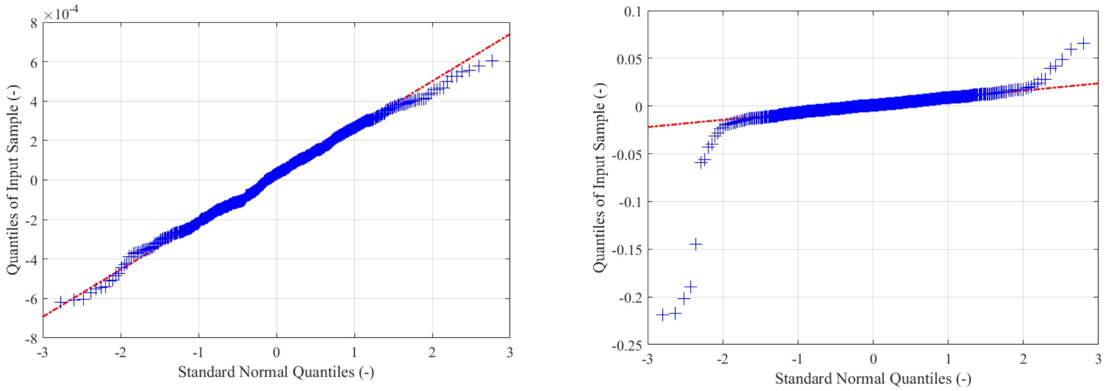

(a) (b)

Figure 6.34: Voltage residuals r_v in (a) and current residuals r_i in (b) evaluated at Bus 634 over the entire simulation duration. Source: [191].

is reflected in other parameters. As a matter of fact, the system dynamics are reproduced in two ways: on one side, the time-varying profile of the irradiance; on the other, the CB opening and consequent re-closing. For this analysis, the voltage and current rms values are considered, as they are a quantity of interest for both the computation of the power flows and protection schemes control.

This analysis is based on the evaluation of the signal residuals. The normalized residuals r, expressed in per unit value, are computed as follows:

$$r_v = \frac{v_{pmu} - v_{pq}}{\overline{v}_{pmu}} \tag{6.2}$$

where the voltage phasor rms values obtained by the PMU and PQ meter are defined as v_{pmu} and v_{pq}, both expressed in V. $\overline{v}_{pmu}$, instead, indicates the mean value of the voltage rms computed by the PMU over the entire simulation time, which is regarded as a reference value. It is worth remarking that the formulation illustrated in Eq. (6.2) is valid for the current just by replacing the subscript v with i.

In Feeder 1, no significant variation neither in voltage nor current signals can be observed in correspondence with the CB opening. This is reasonable because the CB is simulated on the other feeder. In this context, it can be considered Bus 634, for instance, whose voltage and current residuals are investigated as follows.

The quantile-quantile plot (qqplot) of Fig. 6.34 shows the voltage in (a) and the current residuals in (b) for the node under test, respectively.

In spite of the distance from the fault location, the two subfigures present very different trends. In Fig. 6.34(a), the voltage residuals r_v at Bus 634 are characterized by a nearly ideal normal distribution, whose mean and standard deviation are compatible with the simulation settings presented in Table 6.5. This result is in line with what has been observed in Fig. 6.30(a) where the additive noise covers almost all the harmonic components. Moreover, r_v are very small, in the order of 10^{-4} p.u., proving the consistency between PMU and PQ estimates. On the contrary, Fig. 6.34(b) illustrates that the current residuals r_i at the same bus are much larger. Indeed, they present a discrepancy of two orders of magnitude, roughly. Furthermore,

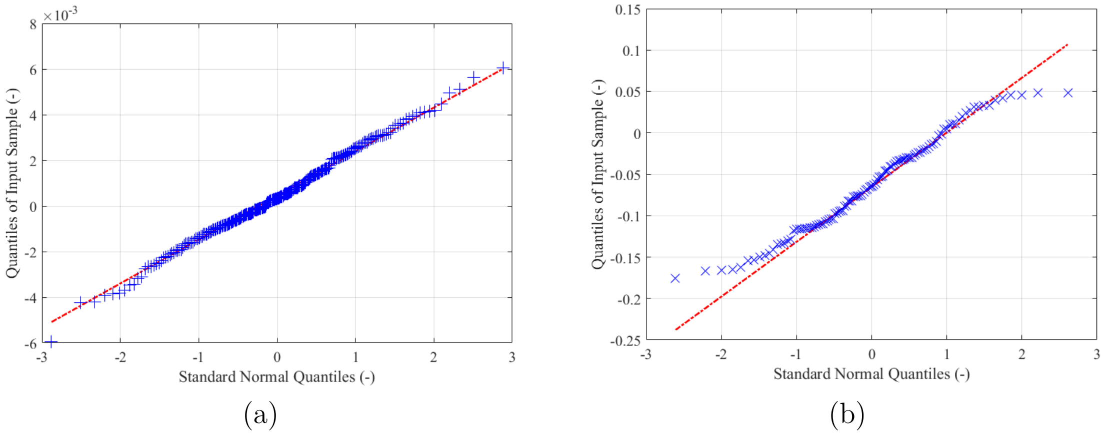

(a) (b)

Figure 6.35: Current residuals r_i before in (a), and after the opening of the CB in (b) evaluated at Bus 692 over the entire simulation duration. Source: [191].

r_i do not follow a Gaussian distribution, due to the non-negligible distortion of the harmonic components on the PQ estimates, as shown in Fig. 6.30(b). The latter means that the bad performances of PQ meters are strongly reflected in Eq. (6.2) in the i_{pq} term. This results in a non-Gaussian distribution of the current residuals, with respect to the voltage ones.

For what concerns Feeder 2, instead, the residuals obtained at Bus 692 are assessed, since it hosts an ESS and is close to the CB. At this node, any harmonics can be barely noticed because both PV plants are far away. Additionally, this bus supplies a very highly unbalanced three-phase load. The opening of the CB results in a transient that identifies three operating conditions: before the opening, during the opening, and after the re-closing of the CB. The focus of the following analysis is on the first two intervals since the last one represents a new steady-state condition that should be similar to the pre-opening condition.

Moreover, it is interesting to observe the behavior of Bus 692 in correspondence with the CB opening, as the loads at this node are still supplied thanks to the ESS. This resembles a typical operating condition of a low-inertia microgrid: this branch continues to be supplied despite being separated from the rest of the distribution grid in an islanded mode. The residuals are computed according to Eq. (6.2) and the results of r_i in these two scenarios are illustrated in Fig. 6.35.

Before the opening, r_i are extremely small in the order of 10^{-3} and they overall present a Gaussian trend, as illustrated in Fig. 6.35(a). The effect of harmonics is minimal because neither of the PV plants is located in proximity to this bus. When the CB opens, instead, r_i present a totally different behavior. Indeed, in Fig. 6.35(b), it can be seen a noticeable increase in the current residuals by two orders of magnitude. In addition, they are not anymore normally distributed.

As obtained investigating the frequency measurements distributions, also the study on the rms, or more specifically on its residuals, demonstrates how PMU and PQ measurements are characterized by different variation ranges and responses to transient conditions. In this regard, in view of enhanced versions of WAMPAC systems in which data streams coming from different devices are merged together, this study presents an interesting conclusion. Before combining two or more typologies of measurement data, first, it is important to consider the spectral content of the waveform under test which is highly dependent on the installed RES. Second, it is also necessary to evaluate the reliability of the data streams based on the adopted PMU and PQ configurations. More importantly, the outcomes pointed out how in the ever-increasing microgrid and low-inertia power systems which both represent weak network conditions, such measurements are less and less reliable, in spite of their compliance with the relevant Standards. This has to be regarded as valid, especially for fast and strong dynamics and contingencies.

6.6 Discussion

In spite of the numerous and ever-increasing amount of studies on power system inertia, there is a lack of research works focusing on inertia from a measurement perspective. In this context, this Chapter attempted at presenting the main challenges and contributing to this field by investing some application of PMUs.

Overall, these results do not attempt at providing a definitive solution to the real-time assessment of inertia. They rather intend to provide some initial guidelines and points that can be further investigated in such a complex scenario that is yet to be fully comprehended and standardized. As a matter of fact, most of the research presented in this Chapter falls within the framework of QUINPORTION project that, as presented in Chapter 5, aims at the development of new inertia measurement methods and at the definition of their uncertainty.

First, owing to the lack of international Standard requirements, a preliminary study has been presented with the aim of establishing CIs for power system inertia assessed using modern in-field instrumentation. The results showed the relevance of assigning a CI to the inertia estimates: not only must the goodness of the estimation algorithm be considered, as already widely done in the literature. But also the measurement uncertainty contributions cannot be disregarded, as their role is not negligible in the final estimate. This is valid, especially for small power variations which are more difficult to assess, albeit less threatening for the power system itself.

Still relying on PMUs, the feasibility of a local assessment of inertia is evaluated. First, similarly to the previous case, an initial metrological requirement is derived, starting from the specifications of the instrumentation used in the field. Second, the evaluation of the swing-equation-based approach and the reliability of PMU measurements is established, again at a local level, with the aim of providing regional indices. The outcomes illustrated that, at the present stage, it is not possible to derive global information from a single PMU. However, the proposed metric can be used to detect power system transients and its magnitude can provide information on the proximity to contingency location. Moreover, active power and ROCOF variations proved to be strongly uncorrelated: a stability analysis based only on ROCOF measurements might be limited and neglect significant phenomena.

In the context of local assessment and measurement reliability in low-inertia power systems, the feasibility of aggregating PMU-based measurements performed in different nodes is evaluated. An online reliability index already presented in the previous Chapters, the nRMSE, is considered. Analyzing the nRMSE permitted to extrapolate information not only on the trustworthiness of the measurements but also on possible transient conditions. Indeed, three different transients were detected: output power variations where PV plants were hosted, the opening/re-closing of a CB, and a low-inertia condition in which the only source of energy was an ESS. The results highlighted how it is hence possible to get a deeper insight into the measurement data stream and promptly detect anomalies or inconsistencies.

However, a deeper study on the target requirements in the performances of PMUs was carried out with the aim of assessing whether the nRMSE can correctly track power system transients and discern them from normal steady-state operation in low-inertia scenarios. More specifically, the dependence between the nRMSE and the PMU reporting rate was analyzed, spanning over the entire set of values provided by the PMU Std. As could be expected, the results indicated that the higher the reporting rate, the lowest the time latency in the identification of contingencies and possible system oscillations. Moreover, the time-trend of the nRMSE can provide useful data about the inertia of the power system. Nevertheless, little information can be derived prior to a contingency since nRMSE values are in the same order of magnitude for both high- and low-inertia scenarios.

Lastly, in view of a more complex system comprising various typologies of electrical instrumentation, a study on the interoperability between PMUs and PQ meters was presented. The results of numerical simulations carried out in MATLAB/Simulink and in LabVIEW demonstrated the discrepancies between the two measurement data streams both in terms of time-stamp and measured values. However, this result was envisaged, based on the different Standards which regulate the performance of such devices. Nevertheless, this discrepancy became more and more relevant with the distortion level due to reduced inertia conditions such as harmonics injections produced by PV panels and frequency instability caused by an ESS. As a consequence, a preliminary evaluation of the PMU and PQ data reliability can be envisioned as a necessary improvement for many control room applications.

Conclusions

The recent years have been characterized by a progressive upgrading of power systems in terms of automation and identification of contingency events. The so-called *smart grids* are indeed a clear consequence of the rapid growth of DG, at various system levels, which requires enhanced levels of control and planning.
As a matter of fact, they pose several technological challenges ranging from the continuous reduction of inertia owing to the replacement of traditional machines to the worsening of power quality, resulting in increased levels of harmonic content.
As examined in this Thesis, PMUs represent a suitable tool in the context of power system measurements. Indeed, they can definitely contribute to the delineation of an overall picture of the real-time system state which can be used by the DSOs and TSOs in their daily activities.

This Thesis, falling within this framework, investigated the requirements, the performance and the possible applications of PMUs in power systems which are ever-more characterized by dynamic and distorted conditions.
More in detail, the infrastructure of the PMU calibrator present at the Swiss NMI was illustrated and thoroughly characterized. In this sense, both its generating and acquisition stages were examined, as well as the effects on the time synchronization for various sources. The more evident result of this work consisted of the evaluation of the performances in terms of uncertainty intervals and, consequently, the identification of the possible areas of improvement.

Afterward, two different applications of PMUs were considered: one at transmission and one at distribution level. Concerning the latter, a typical MV measurement chain was illustrated, including the most common pieces of equipment present in the field. The aim of retrieving a target uncertainty in such a scenario was driven by the increasing installation of CIG at low-voltage levels which, hence, require further monitoring similar to high-voltage ones. On the other hand, the application at the transmission level involved a very specific case in which the accuracy of frequency measurements is essential when performing counter-maneuvers. As a matter of fact, the current policies developed by ENTSO-E do not involve any uncertainty when dealing with the re-synchronization of power system areas after a split event. However, as pointed out by the results, the uncertainty represents an important indicator that should taken into account, especially during dynamic conditions.

On the other hand, the second part of the Thesis was dedicated to the application of PMUs in low-inertia power systems. The results of the prior literature review pointed out many algorithms concerning the estimation of inertia, some of them relying also on PMUs. Nevertheless, little to nothing could be found for what concerns the measurement aspects or standard requirements. To contribute to this gap, a first study focused on the establishment of CIs based on the characteristics of modern in-field devices, by applying the MCM. As a preliminary result, the obtained intervals proved to be non-negligible, especially for the smaller power/frequency disturbances which are more challenging to assess. Afterward, the focus was on the local assessment of inertia based only on single-node PMU measurements. A new indicator was developed and tested accordingly in two scenarios, one of which was characterized by low inertia. The results proved how the indicator might be helpful in discerning an event from a steady-state condition; plus, its magnitude was representative of the proximity to the fault location. The other studies concerning inertia were mostly focused on the investigation of the reliability of PMU measurements in such conditions and on the possibility of providing values for local areas. The dependency on the PMU parameters, i.e., the reporting rate, was examined for different rated frequencies and different power systems. As a result, the inertia assessment by means of PMUs could not be deemed as straightforward, especially in case different pieces of electrical instrumentation come into play.

Future Outlook

The results illustrated in this Thesis do not intend to propose any decisive solution in the context of wide-area measurements and PMU-based inertia estimation. They rather summarize a three-year work and leave ample space for further improvements, some of which are suggested as follows.

For what concerns the PMU calibrator, the complete characterization should be envisioned in view of possible calibrations of customer PMUs in the future. As a matter of fact, at the current state, the PMU Std does not require any certification of the devices, but this cannot be fully excluded in the future. Having a complete characterization of the infrastructure would allow for a better understanding of the performance and trigger consequent actions on the various components.

Regarding the applications of PMUs in distribution systems, it is envisaged that their need will grow in the next years. This will be prompted by the increasing number of microgrids and installation of RES which would require further monitoring.

Lastly, the inertia estimation represents the topic that will require the most extensive studies. As a matter of fact, the presented outcomes represent some initial starting points which can need to be further investigated in such a complex scenario that is yet to be fully comprehended and standardized as already disclosed. In fact, most of the results presented in the last Chapter fell within the QUINPORTION project which started at the end of 2022 and aims at the development of new inertia measurement methods and at the definition of their uncertainty.

List of Acronyms

ADC Analog to Digital Converter.

CB Circuit Breaker.
CD Capacitive Divider.
CE Continental Europe.
CET Central European Time.
CI Confidence Interval.
CIG Converter-Interfaced Generation.
CLT Central Limit Theorem.
COI Center-Of-Inertia.
CS-TFM Compressive Sensing Taylor-Fourier Model.
CT Current Transformer.

DAQ Data Acquisition Board.
DER Distributed Energy Resources.
DFT Discrete Fourier Transform.
DG Distributed Generation.
DSO Distribution System Operator.

ENTSO-E European Network of Transmission System Operators for Electricity.
ESS Energy Storage System.

FACTS Flexible Alternating Current Transmission System.
FCR Frequency Control Response.
FE Frequency Error.
FIR Finite Impulse Response.
FRACSEC Fraction of a Second.

GCC Grid-Connected Converter.
GFC Grid-Forming Converter.
GoF Goodness of Fit.
GPS Global Positioning System.

GUM Guide to the expression of Uncertainty in Measurements.

HEPR Hard Grade Ethylene Propylene Rubber.
HV High Voltage.
HVDC High Voltage Direct Current.

i-IpDFT Iterative Interpolated Discrete Fourier Transform.
IFD Instantaneous Frequency Deviation.
IRIG-B Inter-Range Instrumentation Group timecode B.
ISO International Organization for Standardization.
IT Instrument Transformer.

KF Kalman Filter.

LPCT Low-Power Current Transformer.
LPIT Low-Power Instrument Transformer.
LPU Law of Propagation of Uncertainties.
LPVT Low-Power Voltage Transformer.
LV Low Voltage.

MCM Monte Carlo Method.
MV Medium Voltage.

NMI National Metrology Institute.
nRMSE Normalized Root Mean Square Error.

OFGS Over-Frequency Generator Shedding.
OLTC On-Load Tap Changer.
OOBI Out-Of-Band Interference.

PD Partial Discharge.
PDC Phasor Data Concentrator.
pdf Probability Density Function.
PEVs Plug-In Electric Vehicles.
PF Power Factor.
PLL Phase-Locked Loop.
PMU Phasor Measurement Unit.

PPS Pulse Per Second.

PQ Power Quality.

PTP Precision Time Protocol.

PV Photovoltaic Unit.

r.v. Random Variable.

RC Rogowski Coil.

RES Renewable Energy Sources.

RFE ROCOF Error.

rms Root-Mean Square.

ROCOF Rate Of Change Of Frequency.

SCADA Supervisory Control And Data Acquisition.

SE State Estimation.

SG Synchronous Generator.

SNR Signal-to-Noise Ratio.

SOC Second Of Century.

TFT Taylor Fourier Transform.

TG Turbine Governor.

THD Total Harmonic Distortion.

TOV Temporary Overvoltage.

TSO Transmission System Operator.

TVE Total Vector Error.

UFLS Under-Frequency Load Shedding.

UPS Uninterruptible Power Supply.

UTC Coordinated Universal Time.

VIM International Vocabulary of Metrology.

VT Voltage Transformer.

WAMPAC Wide Area Monitoring, Protection, Automation and Control.

WR White Rabbit.

WT Wind Turbine.

XLPE Cross-linked Polyethylene.

List of Figures

1 Objectives of the Climate Energy Plan promoted by the European Commission, showing the targets to be achieved by 2050 in various sectors. Source: [3]. 1
2 Energy consumption levels recorded in Italy in January 2023 by the Italian Transmission System Operator (TSO), Terna. It is worth highlighting that only 28.2% of the overall power production was based on renewable sources. Source: [7]. 2
3 Energy consumption levels recorded in Italy in June 2023 by the Italian TSO, Terna. It is worth underlying that 44.3% of the overall power production was based on renewable sources. Source: [8]. 2

1.1 Distribution of the true value D1 and distribution of one of the means D2, in blue and red respectively. Their corresponding expected value μ and mean value m are represented by dashed blue and red lines. . . 12
1.2 Ideal instrument behavior represented by a bisector, as a solid blue line, and real instrument behavior illustrated by a dotted red line. The angular coefficient between the two represents the gain, or reading, error. 13
1.3 Ideal instrument behavior represented by a bisector, as a solid blue line, and real instrument measurements illustrated by solid red circles. The difference between each ideal and actual measurement is represented by a dotted red line. 13
1.4 Traceability sequence illustrating the uninterrupted chain of comparison, starting from the NMI up to the generic industry instrument. . . 20

2.1 Example of a smart grid, including DERs and a wide-area monitoring system. Source: [23] 22
2.2 Block diagram of a PMU including its main components. Dashed blue blocks and thin arrows indicate analog/digital inputs/outputs, whereas the green dashed block highlights the DAQ components. . . . 23
2.3 Graphical representation of TVE real and imaginary components in red: the ideal and the measured phasor components are illustrated in blue and green, respectively. Source: [14]. 27
2.4 Model of an ideal transformer, omitting all parasitic parameters. . . . 29
2.5 Model of a real transformer, including longitudinal primary and secondary parameters as well as non-idealities in the ferromagnetic core represented by the transversal parameters on the primary side. 29
2.6 Structure of an ideal LPVT made up of a capacitive divider, comprising only two ideal capacitors C_a and C_b and no parasitic components. The input and output voltages and indicated by subscripts 1 and 2, respectively. 33
2.7 Structure of a Rogowski coil, having a radius R and a cross-section S. The output voltage at the terminals $u_s(t)$ is proportional to the derivative of the measured current $i(t)$. Source: [68]. 35

3.1 Simplified block diagram of the PMU calibrator infrastructure present at the Swiss Federal Institute of Metrology (METAS) in Bern, Switzerland. Voltage signals and related components are shown in blue, current-related ones in red, and timing ones are in orange. The PMU acquisition stage is shown as a simplified dotted block in green. . . . 40
3.2 PMU Calibrator infrastructure present at the Swiss Federal Institute of Metrology (METAS) in Bern, Switzerland. Only some of its components are shown: a signal analyzer (top shelf), a real-time controller including time and analog input/output modules (middle shelf), and an external ADC (bottom shelf). 42
3.3 Frequency as a function of time (solid blue line) during dynamic ramp tests for a 50-Hz signal, as illustrated in [14]. Blue markers indicate an idle time of 1 s, while red ones of 2 s. P-class frequency ramp is shown in (a), whereas M- one in (b). The horizontal dashed black line indicates the nominal system frequency. 45
3.4 Heaviside function for positive values of time only, computed for five increasing values of k. The dashed black line represents the vertical asymptote. 46
3.5 Block diagram of the fundamental steps and devices required for the evaluation of the generating stage of the PMU calibrator. 49
3.6 Results of the magnitude sweep in regard to the frequency. The mean value of the error (in ppm) is indicated by solid bars, while the corresponding uncertainty intervals are shown by smaller vertical bars on top (in ppm). The results of phase A are shown in blue, those of phase B in red, and phase C in green, as a function of the excitation expressed in % of the rated value. 52
3.7 Results of the magnitude sweep in regard to the frequency. The 95 % confidence intervals are shown as vertical bars (in ppm). The results of phase A are shown in blue, those of phase B in red, and phase C in green, as a function of the excitation expressed in % of the rated value. 53
3.8 Results of the magnitude sweep illustrating the uncertainty intervals of the voltage magnitude. The 95 % confidence intervals are shown as vertical bars (in ppm). The results of phase A are shown in blue, those of phase B in red, and phase C in green, as a function of the excitation expressed in % of the rated value. 53
3.9 Results of the magnitude sweep illustrating the uncertainty intervals of the current magnitude. The 95 % confidence intervals are shown as vertical bars (in ppm). The results of phase A are shown in blue, those of phase B in red, and phase C in green, as a function of the excitation expressed in % of the rated value. 53
3.10 Results of the magnitude sweep illustrating the uncertainty intervals of the phase difference $\Delta\varphi$. The 95 % confidence intervals are shown as vertical bars (in ppm). The results of phase A are shown in blue, those of phase B in red, and phase C in green, as a function of the excitation expressed in % of the rated value. 54

3.11 Results of the frequency sweep in regard to the frequency. The 95 % confidence intervals are shown as vertical bars (in ppm). The results of phase A are shown in blue, those of phase B in red, and phase C in green, as a function of the frequency expressed in Hz. 55
3.12 Results of the frequency sweep illustrating the uncertainty intervals of the voltage magnitude. The 95 % confidence intervals are shown as vertical bars (in ppm). The results of phase A are shown in blue, those of phase B in red, and phase C in green, as a function of the frequency expressed in Hz. 56
3.13 Results of the frequency sweep illustrating the uncertainty intervals of the current magnitude. The 95% confidence intervals are shown as vertical bars (in ppm). The results of phase A are shown in blue, those of phase B in red, and phase C in green, as a function of the frequency expressed in Hz. 56
3.14 Results of the frequency sweep illustrating the uncertainty intervals of the phase difference $\Delta\varphi$. The 95 % confidence intervals are shown as vertical bars (in ppm). The results of phase A are shown in blue, those of phase B in red, and phase C in green, as a function of the frequency expressed in Hz. 57
3.15 Phase delay mean values expressed in ns as a result of the magnitude sweep in (a) and of the frequency sweep in (b). All results of phase A are in blue, those of phase B in red, and phase C in green, as a function of the excitation expressed in % of the rated value in (a) and of the frequency in Hz in (b). 57
3.16 Block diagram of the fundamental steps and devices required for the evaluation of the acquisition stage of the PMU calibrator. 58
3.17 Results of the frequency sweep in regard to the frequency. The 95 % confidence intervals are shown as vertical bars (in ppb). The results of phase A are shown in blue, those of phase B in red, and phase C in green, as a function of the frequency expressed in Hz. 60
3.18 Results of the frequency sweep illustrating the uncertainty intervals of the voltage magnitude. The 95 % confidence intervals are shown as vertical bars (in ppm). The results of phase A are shown in blue, those of phase B in red, and phase C in green, as a function of the frequency expressed in Hz. 61
3.19 Results of the frequency sweep illustrating the uncertainty intervals of the current magnitude. The 95 % confidence intervals are shown as vertical bars (in ppm). The results of phase A are shown in blue, those of phase B in red, and phase C in green, as a function of the frequency expressed in Hz. 61
3.20 Phase error of the voltage as a result of the frequency sweep. In (a) the uncertainty on the phase is expressed in ppb, instead (b) presents the errors as mean values in %. In addition, the black and red dotted line indicates a linear trend. All results of phase A are in blue, those of phase B in red, and phase C in green. 62

3.21 Complete block diagram of the fundamental steps and devices required in a PMU calibrator. While the generation and acquisition stages shown in green have been already presented in the previous Sections, in this part the focus is on the time synchronization blocks illustrated in orange. 63
3.22 Distribution of the time reference in the PMU calibrator showing in (a) how the NI 6653 board can be disciplined by an external reference. Then, it distributes the time information in terms of trigger signals and time-bases. In more detail, (b) presents the interaction between the NI 6653 and NI 4461 cards in terms of the 10 MHz time base and effective clock. Adapted from [76]. 64
3.23 Block diagram of the basic working principle of the NI 6653 time module when a PLL is used to generate an equivalent 10 MHz time base from a generic external reference. 64
3.24 Block diagram of the basic working principle and settings adopted in Test A (upper) and B (lower), highlighting the specific external clock reference in the green-shaded block. 66
3.25 Block diagram of the basic working principle and settings adopted in Test C (upper) and D (lower), both traceable to UTC(CH), highlighting the specific external clock reference in the green-shaded block. An additional step is included to clarify the different settings between the two tests. 66
3.26 Dissemination of time reference in METAS, tracing back to the physical realization of the second. Blue, red, and yellow areas represent the realization, distribution, and final exploitation of the time itself, respectively. Blue and red arrows concern PPS and 10 MHz signals, respectively, while green ones account for fiber optic connections. Adapted from [76]. 67
3.27 Block scheme illustrating the measurement setup employed for the phase noise in (a) and time skew assessment in (b). Source: [76]. . . . 67
3.28 In (a), the power spectral density of the phase noise is shown as a function of the frequency of the 10 MHz time base supplied to the PMU calibrator in Tests A, B, C, and D. In addition, (b) illustrates the noise floor (filled area) only for Tests A and D. Source: [76]. . . . 68
3.29 Statistical distribution of the PPS skew measurements with respect to UTC(CH) assessed in Tests A and D. The black vertical bar represents the variability between WR01 (the device under test) and WR02 (the reference one). Source: [76]. 69
3.30 Allan deviation of the PPS skew measurements with respect to UTC(CH) in Tests A and D. The black line indicates the results of the WR against WR comparison. Source: [76]. 70
3.31 PPS skew measurements in the time domain assessed for Test A in (a), Test D in (b), and for the WR to WR comparison in (c). Source: [76]. 70

4.1 Portion of the frequency profile recorded during the South Australia blackout on September 28th, 2016. The contingency occurs at $t = 3.75$ s. Source: [12, 99]. 81

4.2 Results of the real-world scenario I: **(a)** Portion of the frequency profile recorded during the South Australia blackout on September 28th, 2016. **(b)** nRMSE expressed in % and computed using PMU B in P-class configuration for four different reporting rates R_r. Source: [12, 99]. 82
4.3 Results of the real-world scenario II: Voltage and active power variations, indicted as ΔV and ΔP in blue and red, respectively. They are both expressed in per-unit values. 83
4.4 Results of the real-world scenario II: ROCOF expressed in Hz/s, measured during the entire sequence of events using P-class PMU B. . . . 83
4.5 Results of the real-world scenario II: **(a)** Voltage profile in per unit value recorded during the contingency events in the modified IEEE 39-bus system. **(b)** nRMSE expressed in % and computed using PMU B in P-class configuration for four different reporting rates R_r. Source: [99]. 84
4.6 Measurement data packet structure as defined in [105]. Source: [99]. . 85
4.7 Configuration of a simplified π model of a distribution grid, including only longitudinal resistive and inductive parameters. Source: [91]. . . 88
4.8 Results of the $\Delta\varphi$, in rad, measured for the eight cable configurations shown in Table 4.3 having an ampacity A of 100%, for PF = 0.8 in (a) and for PF = 1 in (b). Results for D1 cable length are shown on the left vertical axis (blue dots), while D2 and D3 lengths are on the right vertical axis (yellow and red dots, respectively). Source: [91]. . . 92
4.9 Results of the $\Delta\varphi$, in rad, measured for the eight cable configurations shown in Table 4.3 having an ampacity A of 50%, for PF = 0.8 in (a) and for PF = 1 in (b). Results for D1 cable length are shown on the left vertical axis (blue dots), while D2 and D3 lengths are on the right vertical axis (yellow and red dots, respectively). Source: [91]. . . 92
4.10 Results of the ΔV, in %, measured for the eight cable configurations shown in Table 4.3 having an ampacity A of 100%, for PF = 0.8 in (a) and for PF = 1 in (b). Results for D1 cable length are shown on the left vertical axis (blue dots), while D2 and D3 lengths are on the right vertical axis (yellow and red dots, respectively). Source: [91]. . . 92
4.11 Results of the ΔV, in %, measured for the eight cable configurations shown in Table 4.3 having an ampacity A of 50%, for PF = 0.8 in (a) and for PF = 1 in (b). Results for D1 cable length are shown on the left vertical axis (blue dots), while D2 and D3 lengths are on the right vertical axis (yellow and red dots, respectively). Source: [91]. . . 93
4.12 Synchronous areas resulting from the transmission power system split that occurred on January 8th, 2021. Two areas can be identified: a Northwest and a Southeast one, indicated in blue and red, respectively. Source: [96, 98]. 96
4.13 Time-varying frequency trends obtained from the interpolation algorithm in the North-West (NW) and South-East (SE) synchronous areas for the entire contingency duration, shown in blue and red, respectively. Source: [96, 98]. 96

4.14 Synchronous areas resulting from the transmission power system split that occurred on July 24th, 2021. Two areas can be identified: a North-East and a South-West one, indicated in blue and red, respectively. Source: [97, 98]. 98
4.15 Test Case I: Distribution of the frequency error obtained using P-class PMU A and B, in green and pink, respectively. Such errors have been computed in the SE synchronous area during the resynchronization to CE. Source: [98]. 99
4.16 Test Case I: Uncertainty on the frequency estimates recorded during the resynchronization phase using PMU A (a), B (b), and C (c) in P-class configuration according to the PMU Std in the NW and SE synchronous areas in blue and red, respectively. Source: [98]. 100
4.17 Test Case I: Uncertainty on the frequency estimates recorded during the resynchronization phase using PMU D (a), and E (b), corresponding to the M-class configuration of PMU B and C, respectively, according to the PMU Std in the NW and SE synchronous areas in blue and red. Source: [98]. 100
4.18 Test Case II: Distribution of the frequency error obtained using PMU A and B, in green and pink, respectively. Such errors have been recorded during the fault sequence leading to the splitting of CE. Source: [98]. 101
4.19 Test Case II: Uncertainty on frequency estimates obtained using PMU A and B during the 2nd and 3rd faults, leading to the system separation in both SW and NE synchronous areas. Source: [98]. 102
4.20 Test Case II: Uncertainty on the frequency estimates recorded during the resynchronization phase using PMU A (a), B (b), and C (c) in P-class configuration according to the PMU Std in the NE and SW synchronous areas in blue and red, respectively. Source: [98]. 103
4.21 Test Case II: Uncertainty on the frequency estimates recorded during the resynchronization phase using PMU D (a), and E (b), corresponding to the M-class configuration of PMU B and C, respectively, according to the PMU Std in the NE and SW synchronous areas in blue and red, respectively. Source: [98]. 103

5.1 Energy generation mix, expressed in MW, in the South Australia region of Australia recorded during the week in between July 26th and August 2nd 2023. The vertical red bar indicates the time at which the wind power production peaked. Source: [111]. 108
5.2 Legend of the generation mix, indicating for each source of energy the generated power in MW and the contribution to the overall demand in %. This table refers to the data recorded on July 27th 2023 at 4:30 AM AEST, corresponding to the vertical red bar in Fig. 5.1. Source: [111]. 108
5.3 Frequency responses for three different amounts of kinetic energy after a loss of production. Solid lines represent the behavior with FCR, while dotted lines indicate the response without it. Source: [126]. . . 112

5.4 Frequency response in time, highlighting the activation stages of the three reserves. The stabilization, support, and recovery steps are emphasized, based on ENTSO-E data. Source: [142]. 113
5.5 IEEE 13-bus system scheme, as illustrated in its original presentation. Source: [172]. 121
5.6 IEEE 14-bus system scheme, as illustrated in its original presentation. Source: [173]. 122

6.1 IEEE 9-bus power system scheme, indicating the impedances that are expressed in p.u. on a 100 MVA base. Generator 2, which is the generator whose parameters are examined in the following, is located in the upper-left corner and is indicated in yellow. Its corresponding bus at which measurements are performed is shown in orange. Adapted from [180]. 128
6.2 Low-severity case illustrating the ΔP (a) and H (b) distributions obtained applying the MCM for a $\Delta P = 1\%$ and a $\Delta f = 0.5$ Hz. . . . 130
6.3 Intermediate case illustrating the ΔP (a) and H (b) distributions obtained applying the MCM for a $\Delta P = 15\%$ and a $\Delta f = 1.0$ Hz. Adapted from [175]. 131
6.4 High-severity case illustrating the ΔP (a) and H (b) distributions obtained applying the MCM for a $\Delta P = 40\%$ and a $\Delta f = 3.0$ Hz. . . 131
6.5 IEEE 14-bus system developed in MATLAB/Simulink environment using PSAT toolbox [184]. The model shows the load flow results and the five non-overlapping areas, each of them comprising a synchronous generator. Source: [181]. 134
6.6 Comparison of the magnitude envelopes of the voltage waveform for Scenario I and II in blue and red, respectively. Source: [181]. 135
6.7 Active power $\overline{P_e}$ in (a) and ROCOF $\overline{R_f}$ (b) comparison in Scenario I and II for PMU A and B at Bus 2, indicated by red and blue shades respectively. Source: [181]. 136
6.8 Indicator of local inertia variation dH and variations of ROCOF $\Delta\overline{R_f}$ as provided by PMU B at Bus 2 in blue and red, respectively. Scenario I is shown in (a), while Scenario II is in (b). Adapted from [181]. . . . 137
6.9 $\overline{P_e}$ mean value μ and standard deviation σ in (a) and $\overline{R_f}$ mean value μ and standard deviation σ in (b) as computed by PMU B at Bus 2 in Scenario I. Source: [181]. 138
6.10 $\overline{P_e}$ mean value μ and standard deviation σ in (a) and $\overline{R_f}$ mean value μ and standard deviation σ in (b) as computed by PMU B at Bus 2 in Scenario II. Source: [181]. 138
6.11 Indicator of local inertia variation dH as provided by PMU B in Scenario II at Bus 2 and at Bus 10 in red and blue, respectively. Source: [181]. 139
6.12 Model of the IEEE 13-bus system developed in MATLAB/Simulink, including the local area partitions and the two feeders under test in yellow and in pink, respectively. Source: [185]. 141
6.13 Time-varying irradiance cycles on PV power plants simulated at Bus 634 and 611 of the IEEE 13-bus system in blue and red, respectively. Source: [185]. 142

6.14 Voltage and current frequency spectra illustrating the first 40 harmonics measured on phase A at Bus 634, shown in red and blue respectively. Source: [185]. 142
6.15 Results of nRMSE evaluated on Feeder 1 - W. The nRMSE on phase A of voltage ($nRMSE_V$) and current ($nRMSE_I$) waveforms are shown in blue and red, respectively. They are obtained at Bus 646 (a) and at Bus 634 (b). Adapted from [185]. 144
6.16 The nRMSE of voltage ($nRMSE_V$) and current ($nRMSE_I$) waveforms are shown in blue and red, respectively. They are obtained in Feeder 1 - E at Bus 634. Source: [185]. 144
6.17 The nRMSE of voltage ($nRMSE_V$) and current ($nRMSE_I$) waveforms are shown in blue and red, respectively. They are obtained in Feeder 2 - W at Bus 611. Source: [185]. 145
6.18 Results of nRMSE evaluated on Feeder 2 - W. The nRMSE on voltage ($nRMSE_V$) and current ($nRMSE_I$) waveforms are shown in blue and red, respectively. They are obtained at Bus 684 (a) and at Bus 652 (b). Source: [185]. 145
6.19 Results of nRMSE evaluated on Feeder 2 - E. The nRMSE on voltage ($nRMSE_V$) and current ($nRMSE_I$) waveforms are shown in blue and red, respectively. They are obtained at Bus 675 (a) and at Bus 692 (b). Source: [185]. 146
6.20 The nRMSE of voltage ($nRMSE_V$) and current ($nRMSE_I$) waveforms are shown in blue and red, respectively. They are obtained in Connection 1-2 at Bus 671. Source: [185]. 146
6.21 Comparison of nRMSE in (a) and of voltage magnitudes (b) obtained on Connection 1-2 at Bus 632 and 671 in blue and red, respectively. Source: [185]. 147
6.22 Power System I: Model of the IEEE 14-bus system developed in MATLAB/Simulink using PSAT Toolbox [184]. The two CBs which open at $t = 1$ s are indicated by green squares, while the red rectangle indicates Bus 2 which is the bus under test. Source: [88]. 149
6.23 Power System II: In (a) the solar irradiance trends are shown for the three PV plants simulated in the power system at Bus 611-1, 652-1, and 652-2, respectively in blue, red, and yellow. In (b): Amplitude spectrum of the first 50 harmonics of the voltage and current signals measured at Bus 652 in blue and red, respectively. Source: [88]. . . . 150
6.24 Power System II: Model of the IEEE 13-bus system developed in MATLAB/Simulink environment, including three additional buses hosting a 3.5 kW PV each. Bus 652 is the bus under test and it is highlighted in red, while the fault location is indicated by a lightning bolt. Source: [88]. 151
6.25 Power System I: voltage and current nRMSE indicated by the subscripts V and I, respectively, measured at Bus 2 in rated inertia conditions. In both cases, PMU B is used, but only the lowest and the highest reporting rates are studied: (a) $R_r = 10$ fps, (b) $R_r = 120$ fps. 152

6.26 Power System I: voltage and current nRMSE indicated by the subscripts V and I, respectively, measured at Bus 2 in low-inertia conditions. In both cases, PMU B is used, but only the lowest and the highest reporting rates are studied: (a) $R_r = 10$ fps, (b) $R_r = 120$ fps. 152
6.27 Power System II: current nRMSE indicated by subscript I measured at Bus 652 using all possible R_r available for a 60-Hz PMU B. Different time lengths are illustrated: (a) Entire simulation duration, (b) Only during the contingency. Adapted from [88]. 153
6.28 Model of the IEEE 13-bus system developed in MATLAB/Simulink environment, including two additional PV plants at Bus 634 and 611, and an ESS at Bus 692. The distribution network is divided into two feeders indicated by Feeder 1 and 2, in blue and green, respectively. Red dots indicate the buses whose measurements are examined in the following. Source: [191]. 156
6.29 Solar irradiance cycle applied to both PV plants simulated at Bus 634 and Bus 611, added to the distribution system under test. Source: [191]. 157
6.30 Amplitude spectrum of the first 50 harmonics of the voltage (a) and current signals (b) measured at Bus 634 and computed on a 200 ms interval. Source: [191]. 157
6.31 Reporting frame difference observed in a 250 ms time interval between PMUs and PQ meters. The firsts are indicated by red circles on the right axis, while the latter by blue crosses on the left axis. Source: [191]. 158
6.32 Statistical distribution of the frequency measurements obtained on phase A voltage (green) and current (yellow) signals, as provided by the PMU at Bus 634 (a) and in Bus 611 (b). Adapted from [191]. . . 158
6.33 Statistical distribution of the frequency measurements obtained on phase A voltage (green) and current (yellow) signals, as provided by the PQ meters at Bus 634 (a) and in Bus 611 (b). Adapted from [191].159
6.34 Voltage residuals r_v in (a) and current residuals r_i in (b) evaluated at Bus 634 over the entire simulation duration. Source: [191]. 160
6.35 Current residuals r_i before in (a), and after the opening of the CB in (b) evaluated at Bus 692 over the entire simulation duration. Source: [191]. 161

List of Tables

2.1 Voltage ratio error ε_u and phase displacement $\Delta\varphi$ in % and in crad, respectively, for inductive VTs as defined in IEC 61869-3. Adapted from [61]. 30

2.2 Voltage ratio error ε_u and phase displacement $\Delta\varphi$ in % and in crad, respectively, for capacitive VTs as defined in IEC 61869-5. Adapted from [62]. 31

2.3 Current ratio error ε_i and phase displacement $\Delta\varphi$ in % and in crad, respectively, for CTs as defined in IEC 61869-2. Adapted from [64]. . . 32

2.4 Voltage ratio ε_u and phase errors $\Delta\varphi$ in % and in crad, respectively, for LPVTs as defined in IEC 61869-11. Adapted from [66]. 34

2.5 Current ratio ε_i and phase errors $\Delta\varphi$ in % and in crad, respectively, for LPCTs as defined in IEC 61869-10. Adapted from [65]. 37

3.1 Calibration routine tests performed for the generation stage. Based on all possible excitation levels expressed in %, reference voltage V_{ref} and current I_{ref} values are determined. The reference frequency is set at 50 Hz, while both phases are set to 0 min. 51

3.2 Calibration routine tests performed for the generation stage based on all possible test frequencies included in the PMU Std for M-class PMUs. The excitation level is considered equal to 100%, hence voltage and current reference values are the nominal ones, prior to their corresponding amplification stages. Both reference phases are equal to 0 min. 55

3.3 Calibration routine tests performed for the acquisition stage based on possible test frequencies included in the PMU Std for M-class PMUs. Five different excitation levels are considered, hence the corresponding voltage and current reference values are computed, prior to their corresponding amplification stages. Both reference phases are equal to 0 min. 59

4.1 nRMSE detection latency, expressed in ms, as a function of the PMU reporting rate R_r in the two real-world scenarios under test. Source: [88]. 84

4.2 Test configurations comprising different combinations of the sources of uncertainty under test. 87

4.3 Characteristics of MV cables considered for a typical distribution network scenario. 89

4.4 Results of the 10^5 trials obtained applying MCM considering each source of uncertainty individually in a typical MV measurement chain. Source: [91]. 90

4.5 Results of the 10^5 trials obtained applying MCM considering the six configurations, as detailed in Table 4.2, including a combination of the sources of uncertainty in a typical MV measurement chain. Source: [91]. 91

5.1 Inertia constant values of the IEEE 14-bus system, expressed in s, in rated- and low-inertia conditions, indicated by Scenario I and II, respectively. 123

6.1 Monte Carlo results for the inertia estimates, obtained considering all possible ΔP in %, but examining only Δf equal to 0.5 and 1.0 Hz/s. The mean value of the estimate is indicated as H_m, while the left and right extrema of the CI are indicated by s_L and s_R, respectively. Adapted from [175]. 129
6.2 Monte Carlo results for the inertia estimates, obtained considering all possible ΔP in %, but examining only Δf equal to 2.0 and 3.0 Hz/s. The mean value of the estimate is indicated as H_m, while the left and right extrema of the CI are indicated by s_L and s_R, respectively. Adapted from [175]. 129
6.3 Correlation coefficients between active power and ROCOF measured by PMU A and B, in Scenario I and II. Three different buses are considered as Bus 2 and 3 are in close proximity to the contingency, while Bus 10 is the farthest available. Source: [181]. 140
6.4 nRMSE detection latency measured in low-inertia scenarios presented in Power System I and II, expressed in ms, as a function of the PMU reporting rate R_r. Source: [88]. 154
6.5 Power quality indices of the voltage and current signals assessed at Bus 634, which hosts a PV plant. The PQ indices are presented in terms of THD and SNR, expressed in % and in dB, respectively. Source: [191]. 157

Bibliography

[1] United Nations. *Kyoto Protocol*. Online. Aug. 2023. URL: `https://unfccc.int/kyoto_protocol`.

[2] European Commission. *2030 Climate Target Plan*. Online. 2020. URL: `https://climate.ec.europa.eu/eu-action/european-green-deal/2030-climate-target-plan_en`.

[3] International Energy Agency. *Net Zero by 2050: A Roadmap for the Global Energy Sector*. Online. May 2021. URL: `https://www.iea.org/reports/net-zero-by-2050`.

[4] European Commission. *SET Plan: progress report 2022*. Online. Nov. 2022. URL: `https://setis.ec.europa.eu/set-plan-progress-report-2022_en`.

[5] European Commission. *Directive (EU) 2018/2001 of the European Parliament and of the Council on the promotion of the use of energy from renewable sources*. Online. June 2022. URL: `https://eur-lex.europa.eu/eli/dir/2018/2001/2022-06-07`.

[6] Terna. *Pubblicazioni Statistiche 2022*. Online. Dec. 2022. URL: `https://www.terna.it/it/sistema-elettrico/statistiche/pubblicazioni-statistiche`.

[7] Terna. *Electricity Consumption - January 2023*. Online. Feb. 2023. URL: `https://www.terna.it/en/media/press-releases/detail/electricity-consumption-january-2023`.

[8] Terna. *Electricity Consumption - June 2023*. Online. July 2023. URL: `https://www.terna.it/en/media/press-releases/detail/electrical-consumption-june-2023`.

[9] European Commission. *EU Emissions Trading System (EU ETS)*. Online. Aug. 2023. URL: `https://climate.ec.europa.eu/eu-action/eu-emissions-trading-system-eu-ets_en`.

[10] Harold R. Chamorro et al. "Power system coherency recognition and islanding: Practical limits and future perspectives". In: *IET Energy Systems Integration* 5.1 (2023), pp. 1–14. DOI: `https://doi.org/10.1049/esi2.12081`.

[11] FERC and NERC. *Arizona-Southern California Outages on September 8, 2011 Causes and Recommendations*. Online. Apr. 2012. URL: `https://www.nerc.com/pa/rrm/ea/September%5C%202011%5C%20Southwest%5C%20Blackout%5C%20Event%5C%20Document%5C%20L/AZOutage_Report_01MAY12.pdf`.

[12] AEMO. *Black System South Australia 28 September 2019 - Final Report*. Online. Mar. 2017. URL: `https://www.aemo.com.au/-/media/Files/Electricity/NEM/Market_Notices_and_Events/Power_System_Incident_Reports/2017/Integrated-Final-Report-SA-Black-System-28-September-2016.pdf`.

[13] North-American Electric Reliability Corporation (NERC). *2022 Odessa Disturbance. Texas Event: June 4, 2022. Joint NERC and Texas RE Staff Report.*

Online. Dec. 2022. URL: `https://www.nerc.com/comm/RSTC_Reliability_Guidelines/NERC_2022_Odessa_Disturbance_Report%20(1).pdf`.

[14] "IEEE/IEC International Standard - Measuring relays and protection equipment - Part 118-1: Synchrophasor for power systems - Measurements". In: *IEC/IEEE 60255-118-1:2018* (2018), pp. 1–78. DOI: `10.1109/IEEESTD.2018.8577045`.

[15] International Organization of Legal Metrology (OIML). *International Vocabulary of Metrology - Basic and General Concepts and Associated Terms (VIM)*. online. 2007. URL: `https://www.oiml.org/en/files/pdf_v/v002-200-e07.pdf`.

[16] Joint Committee for Guides in Metrology (JCGM). *Evaluation of measurement data - Guide to the expression of uncertainty in measurement (GUM)*. online. 2008. URL: `https://www.bipm.org/documents/20126/2071204/JCGM_100_2008_E.pdf/cb0ef43f-baa5-11cf-3f85-4dcd86f77bd6`.

[17] Kenneth L. Lange, Roderick J. A. Little, and Jeremy M. G. Taylor. "Robust Statistical Modeling Using the t-Distribution". In: *Journal of the American Statistical Association* 84.408 (1989), pp. 881–896. DOI: `10.1080/01621459.1989.10478852`.

[18] Joint Committee for Guides in Metrology (JCGM). *Evaluation of measurement data - Supplement 1 to the "Guide to the expression of uncertainty in measurement" - Propagation of distributions using a Monte Carlo method*. online. 2008. URL: `https://www.bipm.org/documents/20126/2071204/JCGM_101_2008_E.pdf/325dcaad-c15a-407c-1105-8b7f322d651c`.

[19] ISO/IEC. *Guide 2:2004 - Standardization and related activities - General vocabulary*. online. 2004. URL: `https://www.iso.org/standard/39976.html`.

[20] ISO. *9001:2015 Quality management systems - Requirements*. online. 2015. URL: `https://www.iso.org/standard/62085.html`.

[21] BSI Standards. *EN 50160:2022 Voltage characteristics of electricity supplied by public electricity networks*. online. 2022.

[22] "IEEE Standard for Harmonic Control in Electric Power Systems". In: *IEEE Std 519-2022 (Revision of IEEE Std 519-2014)* (2022), pp. 1–31. DOI: `10.1109/IEEESTD.2022.9848440`.

[23] General Electric. *GE Smart Grid At a Glance*. online. 2022. URL: `https://www.gegridsolutions.com/gesmartgrid.htm`.

[24] Shun-Hsien Huang et al. "Voltage control challenges on weak grids with high penetration of wind generation: ERCOT experience". In: *2012 IEEE Power and Energy Society General Meeting*. 2012, pp. 1–7. DOI: `10.1109/PESGM.2012.6344713`.

[25] Federica Costa. *Real-time PMU monitoring of an IEEE 5-Bus Network implemented on OPAL system*. online. Oct. 2020. URL: `http://amslaurea.unibo.it/21405`.

[26] Matija Naglic et al. "Synchronized Measurement Technology Supported Online Generator Slow Coherency Identification and Adaptive Tracking". In: *IEEE Transactions on Smart Grid* 11.4 (2020), pp. 3405–3417. DOI: `10.1109/TSG.2019.2962246`.

[27] Federico Milano, Álvaro Ortega, and Antonio J. Conejo. "Model-Agnostic Linear Estimation of Generator Rotor Speeds Based on Phasor Measurement

Units”. In: *IEEE Transactions on Power Systems* 33.6 (2018), pp. 7258–7268. DOI: `10.1109/TPWRS.2018.2846737`.

[28] Marco Pignati et al. “Fault detection and faulted line identification in active distribution networks using synchrophasors-based real-time state estimation”. In: *2017 IEEE Manchester PowerTech*. 2017, pp. 1–1. DOI: `10.1109/PTC.2017.7981276`.

[29] Marco Pignati et al. “Fault Detection and Faulted Line Identification in Active Distribution Networks Using Synchrophasors-Based Real-Time State Estimation”. In: *IEEE Transactions on Power Delivery* 32.1 (2017), pp. 381–392. DOI: `10.1109/TPWRD.2016.2545923`.

[30] Ye Shi et al. “PMU Placement Optimization for Efficient State Estimation in Smart Grid”. In: *IEEE Journal on Selected Areas in Communications* 38.1 (2020), pp. 71–83. DOI: `10.1109/JSAC.2019.2951969`.

[31] Sudipta Ghosh et al. “Optimal PMU Allocation Strategy for Completely Observable Networks With Enhanced Transient Stability Characteristics”. In: *IEEE Transactions on Power Delivery* 37.5 (2022), pp. 4086–4102. DOI: `10.1109/TPWRD.2022.3144462`.

[32] Md. Ariful Islam et al. “Modeling and Performance Evaluation of ANFIS Controller-Based Bidirectional Power Management Scheme in Plug-In Electric Vehicles Integrated With Electric Grid”. In: *IEEE Access* 9 (2021), pp. 166762–166780. DOI: `10.1109/ACCESS.2021.3135190`.

[33] Marco Faifer et al. “Characterization of Voltage Instrument Transformers Under Nonsinusoidal Conditions Based on the Best Linear Approximation”. In: *IEEE Transactions on Instrumentation and Measurement* 67.10 (2018), pp. 2392–2400. DOI: `10.1109/TIM.2018.2806949`.

[34] Marco Faifer et al. “Harmonic Distortion Compensation in Voltage Transformers for Improved Power Quality Measurements”. In: *IEEE Transactions on Instrumentation and Measurement* 68.10 (2019), pp. 3823–3830. DOI: `10.1109/TIM.2019.2906990`.

[35] Antonio Cataliotti et al. “Compensation of Nonlinearity of Voltage and Current Instrument Transformers”. In: *IEEE Transactions on Instrumentation and Measurement* 68.5 (2019), pp. 1322–1332. DOI: `10.1109/TIM.2018.2880060`.

[36] Antonello Monti, Carlo Muscas, and Ferdinanda Ponci. *Phasor Measurement Units and Wide Area Monitoring Systems: From the Sensors to the System*. Elsevier, 2016. DOI: `doi/10.1016/C2014-0-03907-X`.

[37] “IEEE Standard for Phasor Data Concentrators for Power Systems”. In: *IEEE Std C37.247-2019* (2019), pp. 1–44. DOI: `10.1109/IEEESTD.2019.8830511`.

[38] Xian-Chang Guo, Chung-Shou Liao, and Chia-Chi Chu. “Enhanced Optimal PMU Placements With Limited Observability Propagations”. In: *IEEE Access* 8 (2020), pp. 22515–22524. DOI: `10.1109/ACCESS.2020.2967066`.

[39] Nikolaos M. Manousakis and George N. Korres. “Optimal Allocation of Phasor Measurement Units Considering Various Contingencies and Measurement Redundancy”. In: *IEEE Transactions on Instrumentation and Measurement* 69.6 (2020), pp. 3403–3411. DOI: `10.1109/TIM.2019.2932208`.

[40] Riccardo Andreoni et al. “Tri-Objective Optimal PMU Placement Including Accurate State Estimation: The Case of Distribution Systems”. In: *IEEE Access* 9 (2021), pp. 62102–62117. DOI: `10.1109/ACCESS.2021.3074579`.

[41] Francesco Conte et al. “Fault Detection and Localization in Active Distribution Networks Using Optimally Placed Phasor Measurements Units”. In: *IEEE Transactions on Power Systems* 38.1 (2023), pp. 714–727. DOI: `10.1109/TPWRS.2022.3165685`.

[42] Chongyu Wang et al. “MILP-Based Fault Diagnosis Model in Active Power Distribution Networks”. In: *IEEE Transactions on Smart Grid* 12.5 (2021), pp. 3847–3857. DOI: `10.1109/TSG.2021.3071871`.

[43] Xiaoyang Tong et al. “Robust Fault Location Method for Transmission Lines Using PMUs”. In: *IEEE Transactions on Power Delivery* 38.4 (2023), pp. 2338–2347. DOI: `10.1109/TPWRD.2023.3240717`.

[44] Guglielmo Frigo, Paolo Attilio Pegoraro, and Sergio Toscani. “Tracking power system events with accuracy-based PMU adaptive reporting rate”. In: *International Journal of Electrical Power & Energy Systems* 153 (2023), p. 109384. ISSN: 0142-0615. DOI: `https://doi.org/10.1016/j.ijepes.2023.109384`.

[45] “IEEE Guide for Synchronization, Calibration, Testing, and Installation of Phasor Measurement Units (PMUs) for Power System Protection and Control”. In: *IEEE Std C37.242-2021 (Revision of IEEE Std C37.242-2013)* (2021), pp. 1–98. DOI: `10.1109/IEEESTD.2021.9574625`.

[46] Farrokh Aminifar et al. “Synchrophasor Measurement Technology in Power Systems: Panorama and State-of-the-Art”. In: *IEEE Access* 2 (2014), pp. 1607–1628. DOI: `10.1109/ACCESS.2015.2389659`.

[47] Alessandro Mingotti et al. “On the Importance of Characterizing Virtual PMUs for Hardware-in-the-Loop and Digital Twin Applications”. In: *Sensors* 21.18 (2021). ISSN: 1424-8220. DOI: `10.3390/s21186133`. URL: `https://www.mdpi.com/1424-8220/21/18/6133`.

[48] Daniel Belega and Dario Petri. “Accuracy Analysis of the Multicycle Synchrophasor Estimator Provided by the Interpolated DFT Algorithm”. In: *IEEE Transactions on Instrumentation and Measurement* 62.5 (2013), pp. 942–953. DOI: `10.1109/TIM.2012.2236777`.

[49] Asja Derviškadić, Paolo Romano, and Mario Paolone. “Iterative-Interpolated DFT for Synchrophasor Estimation: A Single Algorithm for P- and M-Class Compliant PMUs”. In: *IEEE Transactions on Instrumentation and Measurement* 67.3 (2018), pp. 547–558. DOI: `10.1109/TIM.2017.2779378`.

[50] Tao Jin and Weifeng Zhang. “A Novel Interpolated DFT Synchrophasor Estimation Algorithm With an Optimized Combined Cosine Self-Convolution Window”. In: *IEEE Transactions on Instrumentation and Measurement* 70 (2021), pp. 1–10. DOI: `10.1109/TIM.2020.3033073`.

[51] Tianshu Bi et al. “Dynamic Phasor Model-Based Synchrophasor Estimation Algorithm for M-Class PMU”. In: *IEEE Transactions on Power Delivery* 30.3 (2015), pp. 1162–1171. DOI: `10.1109/TPWRD.2014.2353816`.

[52] Masoud Karimi-Ghartemani, Boon-Teck Ooi, and Alireza Bakhshai. “Application of Enhanced Phase-Locked Loop System to the Computation of Synchrophasors”. In: *IEEE Transactions on Power Delivery* 26.1 (2011), pp. 22–32. DOI: `10.1109/TPWRD.2010.2064341`.

[53] Matteo Bertocco et al. “Compressive Sensing of a Taylor-Fourier Multifrequency Model for Synchrophasor Estimation”. In: *IEEE Transactions on Instrumentation and Measurement* 64.12 (2015), pp. 3274–3283. DOI: `10.1109/TIM.2015.2450295`.

[54] Roberto Ferrero, Paolo Attilio Pegoraro, and Sergio Toscani. “Synchrophasor Estimation for Three-Phase Systems Based on Taylor Extended Kalman Filtering”. In: *IEEE Transactions on Instrumentation and Measurement* 69.9 (2020), pp. 6723–6730. DOI: `10.1109/TIM.2020.2983622`.

[55] Anamika Dubey, Saikat Chakrabarti, and Vladimir Terzija. “Testing and validation of a dynamic estimator of states in OPAL-RT real time simulator”. In: *2017 IEEE Power & Energy Society General Meeting*. 2017, pp. 1–5. DOI: `10.1109/PESGM.2017.8273954`.

[56] Carlo Muscas et al. “New Kalman Filter Approach Exploiting Frequency Knowledge for Accurate PMU-Based Power System State Estimation”. In: *IEEE Transactions on Instrumentation and Measurement* 69.9 (2020), pp. 6713–6722. DOI: `10.1109/TIM.2020.2977744`.

[57] S. Xu et al. “An improved Taylor weighted least squares method for estimating synchrophasor”. In: *International Journal of Electrical Power & Energy Systems* 120 (2020), p. 105987. ISSN: 0142-0615. DOI: `https://doi.org/10.1016/j.ijepes.2020.105987`.

[58] Cheng Qian and Mladen Kezunovic. “A Power Waveform Classification Method for Adaptive Synchrophasor Estimation”. In: *IEEE Transactions on Instrumentation and Measurement* 67.7 (2018), pp. 1646–1658. DOI: `10.1109/TIM.2018.2803938`.

[59] Innocent Kamwa, S. R. Samantaray, and Geza Joos. “Wide Frequency Range Adaptive Phasor and Frequency PMU Algorithms”. In: *IEEE Transactions on Smart Grid* 5.2 (2014), pp. 569–579. DOI: `10.1109/TSG.2013.2264536`.

[60] Yassine Amirat et al. “Phasor Estimation for Grid Power Monitoring: Least Square vs. Linear Kalman Filter”. In: *Energies* 13.10 (2020). ISSN: 1996-1073. DOI: `10.3390/en13102456`.

[61] IEC 61869-3. *Instrument transformers - Part 3: Additional requirements for inductive voltage transformers*. online. 2018. URL: `https://webstore.iec.ch/publication/6051`.

[62] IEC 61869-5. *Instrument transformers - Part 5: Additional requirements for capacitor voltage transformers*. online. 2011. URL: `https://webstore.iec.ch/publication/6054`.

[63] IEC 61869-1. *Instrument transformers - Part 1: General requirements*. online. 2023. URL: `https://webstore.iec.ch/publication/34049`.

[64] IEC 61869-2. *Instrument transformers - Part 2: Additional requirements for current transformers*. online. 2012. URL: `https://webstore.iec.ch/publication/6050`.

[65] IEC 61869-10. *Instrument transformers - Part 10: Additional requirements for low-power passive current transformers*. online. 2017. URL: `https://webstore.iec.ch/publication/27276`.

[66] IEC 61869-11. *Instrument transformers - Part 11: Additional requirements for low power passive voltage transformers*. online. 2017. URL: `https://webstore.iec.ch/publication/27484`.

[67] Alessandro Mingotti et al. “Modeling Capacitive Low-Power Voltage Transformer Behavior over Temperature and Frequency”. In: *Sensors* 21.5 (2021). ISSN: 1424-8220. DOI: `10.3390/s21051719`.

[68] Alessandro Mingotti et al. “External Magnetic Fields Effect on Harmonics Measurements with Rogowski coils”. In: *2021 IEEE 11th International Workshop on Applied Measurements for Power Systems (AMPS)*. 2021, pp. 1–6. DOI: `10.1109/AMPS50177.2021.9586003`.

[69] Alessandro Mingotti et al. “Effects on the Accuracy Performance of Rogowski Coils Due to Temperature and Humidity”. In: *2022 IEEE International Instrumentation and Measurement Technology Conference (I2MTC)*. 2022, pp. 1–6. DOI: `10.1109/I2MTC48687.2022.9806638`.

[70] Federica Costa et al. “Combined Effect of Temperature and Humidity on Distorted Currents Measured by Rogowski Coils”. In: *2022 20th International Conference on Harmonics & Quality of Power (ICHQP)*. 2022, pp. 1–6. DOI: `10.1109/ICHQP53011.2022.9808485`.

[71] Alessandro Mingotti et al. “Accuracy Type Test for Rogowski Coils Subjected to Distorted Signals, Temperature, Humidity, and Position Variations”. In: *Sensors* 22.4 (2022). ISSN: 1424-8220. DOI: `10.3390/s22041397`.

[72] Matthew Rhodes and Ryan Quint. *Integrating Synchrophasor Technology into Power System Protection Applications*. [Online] available at: `https://www.naspi.org/`. Sept. 2016.

[73] Sanjay Kumar et al. “PMU-Based Voltage Stability Measurement Under Contingency Using ANN”. In: *IEEE Transactions on Instrumentation and Measurement* 71 (2022), pp. 1–11. DOI: `10.1109/TIM.2021.3129210`.

[74] Guglielmo Frigo et al. “PMU-Based ROCOF Measurements: Uncertainty Limits and Metrological Significance in Power System Applications”. In: *IEEE Transactions on Instrumentation and Measurement* 68.10 (2019), pp. 3810–3822. DOI: `10.1109/TIM.2019.2907756`.

[75] Jean-Pierre Braun, Christian Mester, and Marc-Olivier André. “Requirements for an advanced PMU calibrator”. In: *2016 Conference on Precision Electromagnetic Measurements (CPEM 2016)*. 2016, pp. 1–2. DOI: `10.1109/CPEM.2016.7540656`.

[76] Federica Costa et al. “Comparison of Time Synchronization Sources for PMU Calibration Infrastructures”. In: *2023 IEEE International Symposium on Precision Clock Synchronization for Measurement, Control, and Communication (ISPCS)*. 2023, pp. 1–6.

[77] Daniele Colangelo et al. “Architecture and characterization of a calibrator for PMUs operating in power distribution systems”. In: *2015 IEEE Eindhoven PowerTech*. 2015, pp. 1–6. DOI: `10.1109/PTC.2015.7232792`.

[78] G. Frigo et al. “Characterization of uncertainty contributions in a high-accuracy PMU validation system”. In: *Measurement* 146 (2019), pp. 72–86. ISSN: 0263-2241. DOI: `https://doi.org/10.1016/j.measurement.2019.06.013`.

[79] R. Razzaghi, A. Derviskadic, and M. Paolone. “A white rabbit synchronized PMU”. In: *2017 IEEE PES Innovative Smart Grid Technologies Conference Europe (ISGT-Europe)*. 2017, pp. 1–6. DOI: `10.1109/ISGTEurope.2017.8260178`.

[80] Gert Rietveld et al. “Measurement Infrastructure to Support the Reliable Operation of Smart Electrical Grids”. In: *IEEE Transactions on Instrumentation and Measurement* 64.6 (2015), pp. 1355–1363. DOI: `10.1109/TIM.2015.2406056`.

[81] Yi-hua Tang, Gerard N. Stenbakken, and Allen Goldstein. “Calibration of Phasor Measurement Unit at NIST”. In: *IEEE Transactions on Instrumentation and Measurement* 62.6 (2013), pp. 1417–1422. DOI: `10.1109/TIM.2013.2240951`.

[82] G. Frigo et al. “Statistical Model of Measurement Noise in Real-World PMU-based Acquisitions”. In: *2019 International Conference on Smart Grid Synchronized Measurements and Analytics (SGSMA)*. 2019, pp. 1–8. DOI: `10.1109/SGSMA.2019.8784581`.

[83] R. Lapuh and B. Jeckelmann. *Sampling with 3458A*. Left Right, 2018. ISBN: 9789619447604.

[84] Mari Löper, Tarmo Trummal, and Jako Kilter. “Analysis of the Applicability of PMU Measurements for Power Quality Assessment”. In: *2018 IEEE PES Innovative Smart Grid Technologies Conference Europe (ISGT-Europe)*. 2018, pp. 1–6. DOI: `10.1109/ISGTEurope.2018.8571618`.

[85] Lina He and Chen-Ching Liu. “Parameter Identification With PMUs for Instability Detection in Power Systems With HVDC Integrated Offshore Wind Energy”. In: *IEEE Transactions on Power Systems* 29.2 (2014), pp. 775–784. DOI: `10.1109/TPWRS.2013.2283656`.

[86] Nihal Mohan et al. “Synchronized Phasor Measurement Unit-Based Central Controller for Normal and Contingent Operation of a High-Capacity HVDC Macrogrid for the Continental US”. In: *IEEE Transactions on Power Systems* 36.1 (2021), pp. 680–688. DOI: `10.1109/TPWRS.2020.3027262`.

[87] Yihui Zuo et al. “Impact of Synchrophasor Estimation Algorithms in ROCOF-Based Under-Frequency Load-Shedding”. In: *IEEE Transactions on Power Systems* 35.2 (2020), pp. 1305–1316. DOI: `10.1109/TPWRS.2019.2936277`.

[88] Federica Costa, Guglielmo Frigo, and Federico Grasso Toro. “PMU-based Reliability Index for Renewable-Based Power Systems”. In: *ACTA IMEKO* (2023).

[89] Miles H.F. Wen et al. “Phase identification in distribution networks with micro-synchrophasors”. In: *2015 IEEE Power & Energy Society General Meeting*. 2015, pp. 1–5. DOI: `10.1109/PESGM.2015.7286066`.

[90] Jean-Pierre Braun and Christian Mester. “Metrolgy for smart grids”. In: *2018 First International Colloquium on Smart Grid Metrology (SmaGriMet)*. 2018, pp. 1–4. DOI: `10.23919/SMAGRIMET.2018.8369826`.

[91] F. Costa et al. “Revision of target uncertainty for PMU-based distributed measurement systems in MV networks”. In: *2022 IEEE 12th International Workshop on Applied Measurements for Power Systems (AMPS)*. 2022, pp. 1–6. DOI: `10.1109/AMPS55790.2022.9978864`.

[92] Mohammad Gholami et al. “Detecting the Location of Short-Circuit Faults in Active Distribution Network Using PMU-Based State Estimation”. In: *IEEE Transactions on Smart Grid* 11.2 (2020), pp. 1396–1406. DOI: `10.1109/TSG.2019.2937944`.

[93] Paulo M. De Oliveira-De Jesus et al. “PMU-Based System State Estimation for Multigrounded Distribution Systems”. In: *IEEE Transactions on Power Systems* 36.2 (2021), pp. 1071–1081. DOI: `10.1109/TPWRS.2020.3017543`.

[94] Alberto Borghetti et al. “Synchronized Phasors Monitoring During the Islanding Maneuver of an Active Distribution Network”. In: *IEEE Transactions on Smart Grid* 2.1 (2011), pp. 82–91. DOI: `10.1109/TSG.2010.2094213`.

[95] Tianshu Bi et al. “The Impact of Time Synchronization Deviation on the Performance of Synchrophasor Measurements and Wide Area Damping Control”. In: *IEEE Transactions on Smart Grid* 8.4 (2017), pp. 1545–1552. DOI: `10.1109/TSG.2015.2489384`.

[96] ENTSO-E. *Continental Europe Synchronous Area Separation on 08 January 2021.* Online. July 2021. URL: `https://www.entsoe.eu/news/2021/07/15/final-report-on-the-separation-of-the-continental-europe-power-system-on-8-january-2021/`.

[97] ENTSO-E. *Continental Europe Synchronous Area Separation on 24 July 2021.* Online. Mar. 2022. URL: `https://www.entsoe.eu/news/2022/03/28/final-report-on-the-power-system-separation-of-iberia-from-continental-europe-on-24-july-2021/`.

[98] Federica Costa, Lorenzo Peretto, and Guglielmo Frigo. “Impact of Estimation Uncertainty in PMU-Based Resynchronization of Continental Europe Synchronous Areas”. In: *Sensors* 23.5 (2023). ISSN: 1424-8220. DOI: `10.3390/s23052705`.

[99] G. Frigo, F. Costa, and F. Grasso Toro. “PMU-based metrics for Power Quality Assessment in Distributed Sensor Networks”. In: *25th IMEKO TC4 Symposium and 23rd International Workshop on ADC and DAC Modelling and Testing (IWADC).* 2022, pp. 1–6. DOI: `https://doi.org/10.21014/tc4-2022.09`.

[100] G. Frigo et al. “Taylor-Fourier PMU on a Real-Time Simulator: Design, Implementation and Characterization”. In: *2019 IEEE Milan PowerTech.* 2019, pp. 1–6. DOI: `10.1109/PTC.2019.8810660`.

[101] Guglielmo Frigo and Federico Grasso Toro. “On-line performance assessment for improved sensor data aggregation in power system metrology”. In: *Measurement: Sensors* 18 (2021), p. 100186. ISSN: 2665-9174. DOI: `https://doi.org/10.1016/j.measen.2021.100186`.

[102] Guglielmo Frigo and Federico Grasso Toro. “Metrological Significance and Reliability of On-Line Performance Metrics in PMU-based WLS State Estimation”. In: *2022 International Conference on Smart Grid Synchronized Measurements and Analytics (SGSMA).* 2022, pp. 1–6. DOI: `10.1109/SGSMA51733.2022.9806016`.

[103] T. Athay, R. Podmore, and S. Virmani. “A Practical Method for the Direct Analysis of Transient Stability”. In: *IEEE Transactions on Power Apparatus and Systems* PAS-98.2 (1979), pp. 573–584. DOI: `10.1109/TPAS.1979.319407`.

[104] “Load representation for dynamic performance analysis (of power systems)”. In: *IEEE Transactions on Power Systems* 8.2 (1993), pp. 472–482. DOI: `10.1109/59.260837`.

[105] "IEEE Standard for Synchrophasor Data Transfer for Power Systems". In: *IEEE Std C37.118.2-2011 (Revision of IEEE Std C37.118-2005)* (2011), pp. 1–53. DOI: `10.1109/IEEESTD.2011.6111222`.

[106] Ravi Shankar Singh, Hossein Hooshyar, and Luigi Vanfretti. "Assessment of time synchronization requirements for Phasor Measurement Units". In: *2015 IEEE Eindhoven PowerTech*. 2015, pp. 1–6. DOI: `10.1109/PTC.2015.7232728`.

[107] ENTSO-E. *P5 – Policy 5: Emergency Operations*. Online. Sept. 2015. URL: `https://eepublicdownloads.entsoe.eu/clean-documents/Publications/SOC/Continental_Europe/oh/20150916_Policy_5_Approved_by_ENTSO-E_RG_CE_Plenary.pdf`.

[108] ENTSO-E. *Commission Regulation (EU) 2017/1485 of 2 August 2017 establishing a guideline on electricity transmission system operation - Article 3: Definitions*. online. 2017. URL: `https://www.entsoe.eu/network_codes/sys-ops/`.

[109] United Nations. *For a livable climate: Net-zero commitments must be backed by credible action*. Online. Aug. 2023. URL: `https://www.un.org/en/climatechange/net-zero-coalition#:~:text=To%20keep%20global%20warming%20to,reach%20net%20zero%20by%202050.`.

[110] Jassim Ahmed Ahmed, H. Alkhafaji Mohammed, and Jafer Mahdi Ali. "Performance enhancement of a low-voltage microgrid by measuring the optimal size and location of distributed generation". In: *ACTA IMEKO* 11.3 (2022). DOI: `10.21014/acta_imeko.v11i3.1270`.

[111] OpenNEM. *OpenNEM: Energy - South Australia*. online. 2023. URL: `https://opennem.org.au/energy/sa1/?range=7d&interval=30m`.

[112] Mario Paolone et al. "Fundamentals of power systems modelling in the presence of converter-interfaced generation". In: *Electric Power Systems Research* 189 (2020), p. 106811. ISSN: 0378-7796. DOI: `https://doi.org/10.1016/j.epsr.2020.106811`.

[113] PD IEC TS 62786-41. *Distributed energy resources connection with the grid. Requirements for frequency measurement used to control distributed energy resources (DER) and loads*. online. July 2023. URL: `https://webstore.iec.ch/publication/64241`.

[114] National Grid ESO. *Stage 01: Workgroup Report GC0062 – Fault-Ride-Through*. online. Aug. 2023. URL: `https://www.nationalgrideso.com/document/13246/download`.

[115] BS EN 50549-10. *Requirements for generating plants to be connected in parallel with distribution networks Tests for conformity assessment of generating units*. online. Nov. 2022. URL: `https://shop.electrosuisse.ch/de/Normen-und-Produkte/Normen/EN-50549-10_2022_E_-397612.html`.

[116] IEC 63409-6. *Photovoltaic power generating systems connection with grid - Conformity assessment for power conversion equipment - Part 6: Power control functions and grid support*. online. 2024.

[117] Christof Bucher. *Bern University of Applied Sciences: Webinar - PV IEC 63409*. Mar. 2023.

[118] Saeed DaneshvarDehnavi et al. "Can 100 % renewable power system be successfully built". In: *Renewable Energy* 177 (2021), pp. 715–722. ISSN: 0960-1481. DOI: `10.1016/j.renene.2021.06.002`.

[119] Thomas Ackermann et al. “Paving the Way: A Future Without Inertia Is Closer Than You Think”. In: *IEEE Power and Energy Magazine* 15.6 (2017), pp. 61–69. DOI: `10.1109/MPE.2017.2729138`.

[120] Junru Chen et al. “100 % Converter-Interfaced generation using virtual synchronous generator control: A case study based on the Irish system”. In: *Electric Power Systems Research* 187 (2020), p. 106475. ISSN: 0378-7796. DOI: `10.1016/j.epsr.2020.106475`.

[121] H2020 EdgeFLEX. *Managing future grids with the new VPP Concept.* online. Aug. 2023. URL: `https://www.edgeflex-h2020.eu/`.

[122] QUINPORTION. *QUINPORTION – Measurement and quantification of inertia on electrical power systems to support integration of renewables.* online. Aug. 2023. URL: `https://www.aramis.admin.ch/Grunddaten/?ProjectID=50638&Sprache=de-CH`.

[123] P. Kundur et al. “Definition and classification of power system stability IEEE/CIGRE joint task force on stability terms and definitions”. In: *IEEE Transactions on Power Systems* 19.3 (2004), pp. 1387–1401. DOI: `10.1109/TPWRS.2004.825981`.

[124] ENTSO-E. *Frequency ranges - ENTSO-E guidance document for national implementation for network codes on grid connection.* Online. Sept. 2018. URL: `https://eepublicdownloads.entsoe.eu/clean-documents/Network%20codes%20documents/NC%20RfG/IGD_Frequency_ranges_final.pdf`.

[125] M. Kuivaniemi, K. Laasonen, and A. Elkington. “Estimation of System Inertia in the Nordic Power System Using Measured Frequency Disturbances”. In: *Cigre Conference, Lund, Sweden.* 2015, pp. 1–5.

[126] E. Ørum, M. Kuivaniemi, and A. M. Laasonen. *Future System Inertia.* European Network of Transmission System Operators for Electricity (ENTSOE) Report, 2015. URL: `https://eepublicdownloads.entsoe.eu/clean-documents/Publications/SOC/Nordic/Nordic_report_Future_System_Inertia.pdf`.

[127] Dimitrios Zografos. “Power System Inertia Estimation and Frequency Response Assessment”. PhD thesis. KTH, School of Electrical Engineering, Computer Science (EECS), Electrical Engineering, Electric Power, and Energy Systems, 2019. URL: `https://kth.diva-portal.org/smash/record.jsf?pid=diva2:1369967`.

[128] Changgang Li et al. “Continuous Under-Frequency Load Shedding Scheme for Power System Adaptive Frequency Control”. In: *IEEE Transactions on Power Systems* 35.2 (2020), pp. 950–961. DOI: `10.1109/TPWRS.2019.2943150`.

[129] Seyed Sohrab Banijamali and Turaj Amraee. “Semi-Adaptive Setting of Under Frequency Load Shedding Relays Considering Credible Generation Outage Scenarios”. In: *IEEE Transactions on Power Delivery* 34.3 (2019), pp. 1098–1108. DOI: `10.1109/TPWRD.2018.2884089`.

[130] Qiteng Hong et al. “A New Load Shedding Scheme With Consideration of Distributed Energy Resources’ Active Power Ramping Capability”. In: *IEEE Transactions on Power Systems* 37.1 (2022), pp. 81–93. DOI: `10.1109/TPWRS.2021.3090268`.

[131] Tong Wang et al. “Adaptive Damping Control Scheme for Wind Grid-Connected Power Systems With Virtual Inertia Control”. In: *IEEE Transac-*

tions on Power Systems 37.5 (2022), pp. 3902–3912. DOI: `10.1109/TPWRS.2021.3140086`.

[132] Haoshu Shao et al. “Equivalent Modeling and Comprehensive Evaluation of Inertia Emulation Control Strategy for DFIG Wind Turbine Generator”. In: *IEEE Access* 7 (2019), pp. 64798–64811. DOI: `10.1109/ACCESS.2019.2917334`.

[133] Qiao Peng et al. “Event-Triggering Virtual Inertia Control of PV Systems With Power Reserve”. In: *IEEE Transactions on Industry Applications* 57.4 (2021), pp. 4059–4070. DOI: `10.1109/TIA.2021.3080227`.

[134] Qiao Peng et al. “Coordination of virtual inertia control and frequency damping in PV systems for optimal frequency support”. In: *CPSS Transactions on Power Electronics and Applications* 5.4 (2020), pp. 305–316. DOI: `10.24295/CPSSTPEA.2020.00025`.

[135] Jingyang Fang et al. “Distributed Power System Virtual Inertia Implemented by Grid-Connected Power Converters”. In: *IEEE Transactions on Power Electronics* 33.10 (2018), pp. 8488–8499. DOI: `10.1109/TPEL.2017.2785218`.

[136] Ke Guo, Jingyang Fang, and Yi Tang. “Autonomous DC-Link Voltage Restoration for Grid-Connected Power Converters Providing Virtual Inertia”. In: *2018 IEEE Energy Conversion Congress and Exposition (ECCE)*. 2018, pp. 6387–6391. DOI: `10.1109/ECCE.2018.8557440`.

[137] Stefania Cuoghi et al. “Dual-Active-Bridge Model and Control for Supporting Fast Synthetic Inertial Action”. In: *Energies* 15.6 (2022). ISSN: 1996-1073. DOI: `10.3390/en15062295`.

[138] Mostafa Farrokhabadi et al. “Microgrid Stability Definitions, Analysis, and Examples”. In: *IEEE Transactions on Power Systems* 35.1 (2020), pp. 13–29. DOI: `10.1109/TPWRS.2019.2925703`.

[139] James Amankwah Adu et al. “Virtual Inertia in a Microgrid with Renewable Generation and a Battery Energy Storage System in Islanding Transition”. In: *2019 1st International Conference on Energy Transition in the Mediterranean Area (SyNERGY MED)*. 2019, pp. 1–5. DOI: `10.1109/SyNERGY-MED.2019.8764108`.

[140] Juan Diego Rios Penaloza et al. “A Power Control Scheme for the Islanding Transition of a Microgrid with Battery Energy Storage Systems”. In: *2019 IEEE International Conference on Environment and Electrical Engineering and 2019 IEEE Industrial and Commercial Power Systems Europe (EEEIC / I&CPS Europe)*. 2019, pp. 1–6. DOI: `10.1109/EEEIC.2019.8783275`.

[141] P. Kundur. *Power System Stability and Control*. McGraw-Hill, 1994.

[142] Umer Akram et al. “Sizing HESS as inertial and primary frequency reserve in low inertia power system”. In: *IET Renewable Power Generation* 15.1 (2021), pp. 99–113. DOI: `10.1049/rpg2.12008`.

[143] European Commission et al. *Penetration of renewables and reduction of synchronous inertia in the European power system: analysis and solutions*. Publications Office, 2020. DOI: `10.2833/35606`.

[144] E.M. Carlini et al. “Online analysis and prediction of the inertia in power systems with renewable power generation based on a minimum variance harmonic finite impulse response filter”. In: *International Journal of Electrical Power & Energy Systems* 131 (2021), p. 107042. ISSN: 0142-0615. DOI: `https://doi.org/10.1016/j.ijepes.2021.107042`.

[145] Kaur Tuttelberg et al. “Estimation of Power System Inertia From Ambient Wide Area Measurements”. In: *IEEE Transactions on Power Systems* 33.6 (2018), pp. 7249–7257. DOI: `10.1109/TPWRS.2018.2843381`.

[146] B. Berry et al. “Inertia Measurements in the GB Power System used for Operations and Planning Improvements”. In: *Cigre Science & Engineering* 27.1 (2023), pp. 1–13. URL: `https://cse.cigre.org/cse-n027/c2-inertia-measurements-in-the-gb-power-system-used-for-operations-and-planning-improvements`.

[147] P. M. Ashton et al. “Application of phasor measurement units to estimate power system inertial frequency response”. In: *2013 IEEE Power & Energy Society General Meeting*. 2013, pp. 1–5. DOI: `10.1109/PESMG.2013.6672671`.

[148] Peter Wall and Vladimir Terzija. “Simultaneous Estimation of the Time of Disturbance and Inertia in Power Systems”. In: *IEEE Transactions on Power Delivery* 29.4 (2014), pp. 2018–2031. DOI: `10.1109/TPWRD.2014.2306062`.

[149] Sandip Sharma, Shun-Hsien Huang, and N.D.R. Sarma. “System Inertial Frequency Response estimation and impact of renewable resources in ERCOT interconnection”. In: *2011 IEEE Power and Energy Society General Meeting*. 2011, pp. 1–6. DOI: `10.1109/PES.2011.6038993`.

[150] Peter Makolo, Ramon Zamora, and Tek-Tjing Lie. “The role of inertia for grid flexibility under high penetration of variable renewables - A review of challenges and solutions”. In: *Renewable and Sustainable Energy Reviews* 147 (2021), p. 111223. ISSN: 1364-0321. DOI: `https://doi.org/10.1016/j.rser.2021.111223`.

[151] Phillip M. Ashton et al. “Inertia Estimation of the GB Power System Using Synchrophasor Measurements”. In: *IEEE Transactions on Power Systems* 30.2 (2015), pp. 701–709. DOI: `10.1109/TPWRS.2014.2333776`.

[152] Mingjian Tuo and Xingpeng Li. “Dynamic Estimation of Power System Inertia Distribution Using Synchrophasor Measurements”. In: *2020 52nd North American Power Symposium (NAPS)*. 2021, pp. 1–6. DOI: `10.1109/NAPS50074.2021.9449713`.

[153] Deyou Yang et al. “Ambient-Data-Driven Modal-Identification-Based Approach to Estimate the Inertia of an Interconnected Power System”. In: *IEEE Access* 8 (2020), pp. 118799–118807. DOI: `10.1109/ACCESS.2020.3004335`.

[154] Hongbo Ye et al. “Generator Available Inertia Estimation Based on Various Disturbance Measurements of PMU”. In: *2021 22nd IEEE International Conference on Industrial Technology (ICIT)*. Vol. 1. 2021, pp. 605–610. DOI: `10.1109/ICIT46573.2021.9453654`.

[155] Peter Makolo, Ramon Zamora, and Tek-Tjing Lie. “Heuristic Inertia Estimation Technique for Power Networks with High Penetration of RES”. In: *2020 2nd International Conference on Smart Power & Internet Energy Systems (SPIES)*. 2020, pp. 356–361. DOI: `10.1109/SPIES48661.2020.9242923`.

[156] Peter Makolo et al. “Data-driven inertia estimation based on frequency gradient for power systems with high penetration of renewable energy sources”. In: *Electric Power Systems Research* 195 (2021), p. 107171. ISSN: 0378-7796. DOI: `https://doi.org/10.1016/j.epsr.2021.107171`.

[157] Thongchart Kerdphol et al. “Application of PMUs to monitor large-scale PV penetration infeed on frequency of 60 Hz Japan power system: A case study from Kyushu Island”. In: *Electric Power Systems Research* 185 (2020),

p. 106393. ISSN: 0378-7796. DOI: https://doi.org/10.1016/j.epsr.2020.106393.

[158] Peter Makolo, Ramon Zamora, and Tek-Tjing Lie. "Online inertia estimation for power systems with high penetration of RES using recursive parameters estimation". In: *IET Renewable Power Generation* 15.12 (2021), pp. 2571–2585. DOI: https://doi.org/10.1049/rpg2.12181.

[159] Johannes Schiffer, Petros Aristidou, and Romeo Ortega. "Online Estimation of Power System Inertia Using Dynamic Regressor Extension and Mixing". In: *IEEE Transactions on Power Systems* 34.6 (2019), pp. 4993–5001. DOI: 10.1109/TPWRS.2019.2915249.

[160] Rasoul Azizipanah-Abarghooee et al. "A New Approach to the Online Estimation of the Loss of Generation Size in Power Systems". In: *IEEE Transactions on Power Systems* 34.3 (2019), pp. 2103–2113. DOI: 10.1109/TPWRS.2018.2879542.

[161] Fanhong Zeng et al. "Online Estimation of Power System Inertia Constant Under Normal Operating Conditions". In: *IEEE Access* 8 (2020), pp. 101426–101436. DOI: 10.1109/ACCESS.2020.2997728.

[162] E. S. N. Raju Paidi et al. "Development and Validation of Artificial Neural Network-Based Tools for Forecasting of Power System Inertia With Wind Farms Penetration". In: *IEEE Systems Journal* 14.4 (2020), pp. 4978–4989. DOI: 10.1109/JSYST.2020.3017640.

[163] Jiaming Chang et al. "Forecasting Based Virtual Inertia Control of PV Systems for Islanded Micro-Grid". In: *2019 29th Australasian Universities Power Engineering Conference (AUPEC)*. 2019, pp. 1–6. DOI: 10.1109/AUPEC48547.2019.211843.

[164] Jiaming Chang et al. "Coordinated Frequency Regulation Using Solar Forecasting Based Virtual Inertia Control for Islanded Microgrids". In: *IEEE Transactions on Sustainable Energy* 12.4 (2021), pp. 2393–2403. DOI: 10.1109/TSTE.2021.3095928.

[165] F. Gonzalez-Longatt et al. "Short-term Kinetic Energy Forecast using a Structural Time Series Model: Study Case of Nordic Power System". In: *2020 International Conference on Smart Systems and Technologies (SST)*. 2020, pp. 173–178. DOI: 10.1109/SST49455.2020.9264087.

[166] Fei Teng, Vincenzo Trovato, and Goran Strbac. "Stochastic Scheduling With Inertia-Dependent Fast Frequency Response Requirements". In: *IEEE Transactions on Power Systems* 31.2 (2016), pp. 1557–1566. DOI: 10.1109/TPWRS.2015.2434837.

[167] T. Inoue et al. "Estimation of power system inertia constant and capacity of spinning-reserve support generators using measured frequency transients". In: *IEEE Transactions on Power Systems* 12.1 (1997), pp. 136–143. DOI: 10.1109/59.574933.

[168] Reactive Technologies. *Accurate Grid Inertia Measurements - Providing the foundation for resilient renewable grids*. Online. July 2023. URL: https://reactive-technologies.com/accurate-grid-inertia-measurements-grid-operators/.

[169] Bendong Tan et al. "Decentralized data-driven estimation of generator rotor speed and inertia constant based on adaptive unscented Kalman filter". In: *International Journal of Electrical Power & Energy Systems* 137 (2022),

p. 107853. ISSN: 0142-0615. DOI: `https://doi.org/10.1016/j.ijepes.2021.107853`.

[170] Chitaranjan Phurailatpam et al. "Measurement-Based Estimation of Inertia in AC Microgrids". In: *IEEE Transactions on Sustainable Energy* 11.3 (2020), pp. 1975–1984. DOI: `10.1109/TSTE.2019.2948224`.

[171] Pritam Bhowmik et al. "Vector Measurement-Based Virtual Inertia Emulation Technique for Real-Time Transient Frequency Regulation in Microgrids". In: *IEEE Transactions on Power Electronics* 36.6 (2021), pp. 6685–6698. DOI: `10.1109/TPEL.2020.3034699`.

[172] W.H. Kersting. "Radial distribution test feeders". In: *IEEE Transactions on Power Systems* 6.3 (1991), pp. 975–985. DOI: `10.1109/59.119237`.

[173] IEEE. *14 Bus Power Flow Test Case*. online. Aug. 1993. URL: `http://labs.ece.uw.edu/pstca/pf14/pg_tca14bus.htm`.

[174] Paolo Attilio Pegoraro et al. "PMU-Based Estimation of Systematic Measurement Errors, Line Parameters, and Tap Changer Ratios in Three-Phase Power Systems". In: *IEEE Transactions on Instrumentation and Measurement* 71 (2022), pp. 1–12. DOI: `10.1109/TIM.2022.3165247`.

[175] F. Costa et al. "A Simple Approach to Quantify Accuracy of Power Systems Inertia". In: *2022 IEEE 12th International Workshop on Applied Measurements for Power Systems (AMPS)*. 2022, pp. 1–5. DOI: `10.1109/AMPS55790.2022.9978840`.

[176] Eleftherios O. Kontis et al. "Estimation of power system inertia: A Comparative assessment of measurement-Based techniques". In: *Electric Power Systems Research* 196 (2021), p. 107250. ISSN: 0378-7796. DOI: `https://doi.org/10.1016/j.epsr.2021.107250`.

[177] Bahman Alinezhad Osbouei et al. "Impact of Inertia Distribution on Power System Stability and Operation". In: *2019 IEEE Milan PowerTech*. 2019, pp. 1–6. DOI: `10.1109/PTC.2019.8810689`.

[178] ENTSO-E. *Frequency Stability Evaluation Criteria for the Synchronous Zone of Continental Europe – Requirements and impacting factors*. Online. Mar. 2016. URL: `https://eepublicdownloads.entsoe.eu/clean-documents/SOC%20documents/RGCE_SPD_frequency_stability_criteria_v10.pdf`.

[179] ENTSO-E. *Inertia and Rate of Change of Frequency (RoCoF) - Version 17 SPD – Inertia TF*. Online. Dec. 2020. URL: `https://eepublicdownloads.azureedge.net/clean-documents/SOC%20documents/Inertia%20and%20RoCoF_v17_clean.pdf`.

[180] Paul M. Anderson and A. A. Fouad. *Power System Control and Stability*. Wiley-IEEE Press, 2003. URL: `https://ieeexplore.ieee.org/servlet/opac?bknumber=5264012`.

[181] Federica Costa, Lorenzo Peretto, and Guglielmo Frigo. "PMU-Based Estimation of Inertia Variation: Proposed Metric and Feasibility Analysis". In: *2023 IEEE International Instrumentation and Measurement Technology Conference (I2MTC)*. 2023, pp. 1–6. DOI: `10.1109/I2MTC53148.2023.10176065`.

[182] Roberto Ferrero, Paolo Attilio Pegoraro, and Sergio Toscani. "Impact of Capacitor Voltage Transformers on Phasor Measurement Units Dynamic Performance". In: *2018 IEEE 9th International Workshop on Applied Measurements for Power Systems (AMPS)*. 2018, pp. 1–6. DOI: `10.1109/AMPS.2018.8494899`.

[183] A. Derviškadić, G. Frigo, and M. Paolone. "Impact of Time Dissemination Technologies on Synchrophasor Estimation Accuracy". In: *2019 International Conference on Smart Grid Synchronized Measurements and Analytics (SGSMA).* 2019, pp. 1–8. DOI: `10.1109/SGSMA.2019.8784496`.

[184] "An open source power system analysis toolbox". In: *IEEE Transactions on Power Systems* 20.3 (2005), pp. 1199–1206. DOI: `10.1109/TPWRS.2005.851911`.

[185] Federica Costa and Guglielmo Frigo. "Local Aggregation of PMU Measurements in a Low-Inertia Distribution Power System". In: *2023 4th International Conference on Smart Grid Metrology (SMAGRIMET).* 2023, pp. 1–6. DOI: `10.1109/SMAGRIMET58412.2023.10128654`.

[186] Roberto Langella et al. "Experimental-Based Evaluation of PV Inverter Harmonic and Interharmonic Distortion Due to Different Operating Conditions". In: *IEEE Transactions on Instrumentation and Measurement* 65.10 (2016), pp. 2221–2233. DOI: `10.1109/TIM.2016.2554378`.

[187] Kostyantyn Koziy, Bei Gou, and Joel Aslakson. "A Low-Cost Power-Quality Meter With Series Arc-Fault Detection Capability for Smart Grid". In: *IEEE Transactions on Power Delivery* 28.3 (2013), pp. 1584–1591. DOI: `10.1109/TPWRD.2013.2251753`.

[188] Fernando Bambozzi Bottura et al. "Optimal Positioning of Power Quality Meters for Monitoring Potential Conditions of Harmonic Resonances in a MV Distribution System". In: *IEEE Transactions on Power Delivery* 34.5 (2019), pp. 1885–1897. DOI: `10.1109/TPWRD.2019.2923365`.

[189] Robert Ferdinand, Marco Cupelli, and Antonello Monti. "Multipoint Synchronized Recordings in Offshore Wind Farms With Continuous Measurement Power Quality Meters". In: *IEEE Transactions on Instrumentation and Measurement* 67.12 (2018), pp. 2785–2795. DOI: `10.1109/TIM.2018.2829489`.

[190] Mihaela M. Albu, Mihai Sănduleac, and Carmen Stănescu. "Syncretic Use of Smart Meters for Power Quality Monitoring in Emerging Networks". In: *IEEE Transactions on Smart Grid* 8.1 (2017), pp. 485–492. DOI: `10.1109/TSG.2016.2598547`.

[191] Federica Costa and Guglielmo Frigo. "Interoperability Issues in PQ and PMU Measurements for Reduced Inertia Power Systems". In: *2023 IEEE International Instrumentation and Measurement Technology Conference (I2MTC).* 2023, pp. 01–06. DOI: `10.1109/I2MTC53148.2023.10176036`.

[192] IEC 61000-4-30. *Electromagnetic compatibility (EMC) - Part 4-30: Testing and measurement techniques - Power quality measurement methods.* online. 2021. URL: `https://webstore.iec.ch/publication/68642`.

[193] IEC 62586-2. *Power quality measurement in power supply systems - Part 2: Functional tests and uncertainty requirements.* online. 2017. URL: `https://webstore.iec.ch/publication/29675`.

[194] National Instrument. *LabVIEW Electrical Power Toolkit.* online. 2023. URL: `https://www.ni.com/en-us/shop/product/labview-electrical-power-toolkit.html`.

[195] G. Frigo et al. "Harmonic Phasor Measurements in Real-World PMU-Based Acquisitions". In: *2019 IEEE International Instrumentation and Measure-*

ment Technology Conference (I2MTC). 2019, pp. 1–6. DOI: `10.1109/I2MTC.2019.8826988`.